Engineering Elastic and Functional Electrospun Nano-Fibers for Potential Heart Repair

By Alan Mark Taylor

A Dissertation Submitted to the Graduate School of the University of Texas at Arlington in
Partial Fulfillment of the Requirements for the Degree of Doctor of Philosophy

Arlington, Texas

August 2022

Engineering Elastic and Functional Electrospun Nano-Fibers for Potential Heart Repair

By

Alan Mark Taylor

Approved:

Yi Hong (Primary Advisor)

Jun Liao (Co-advisor)

Zui Pan (Committee Member)

Kytai Nguyen (Committee Member)

Matthias Peltz (Committee Member)

Georgios Alexandrakis (Graduate Advisor)

Dedication

I would like to dedicate this to my parents, Mark and Pam Taylor, and my brother, Bryan Taylor. Without their endless support and care throughout life, I would not be here. I also dedicate this to the numerous past and current friends who have impacted me meaningfully.

Acknowledgment

I would like to acknowledge many people for their support, both financially and morally, during the tenure of my Ph.D. career. Firstly, Dr. Yi Hong, my PI, and advisor who provided extensive insight and guidance over the years, driving motivation and funding from NSF CAREER (DMR #1554835, YH) and NIH R15 HL140503 (YH). Through his advice and encouragement, I never would have pushed myself to come this far in the Ph.D. process. Secondly, I would like to thank Dr. Kytai Nguyen and the NIH (T32 HL134613, KN) for their moral and financial support. With her support and the T32 program, I have improved my work ethic both in and out of the field. The NIH T32 program has been an excellent resource for expanding my network, providing me with a group of like-minded, driven students in advancing the scientific field. I would also like to acknowledge Dr. Jun Liao for his input and guidance and for introducing me to research during my master's career. Without his encouragement, I would not have considered pursuing a Ph.D.

I want to extend my gratitude to Dr. Zui Pan for providing access to her lab equipment and always providing aid. Without the help of her lab, specifically Dr. Yan Chang, many of the cell data collected would not have been possible. I wish to express my deep gratitude to Dr. Matthias Peltz. He has taken time out of his hectic schedule to offer his expertise as a medical doctor. His perspective provides valuable insight into conventional treatments and the transition from research to clinical applications. Dr. Hyejin Moon also contributed significantly by allowing the use of her contact angle measurement instrument. I also would like to express profound thanks to my helpful lab mates and colleagues. First, Jiazhu, who has my most profound appreciation for his work on all the cell studies, devoting much of his time to culturing and imaging my fibers. His expertise and knowledge of culturing have allowed the studies to go smoothly. He has also been a plentiful supply of suggestions for various studies, making the investigations more complex and in-depth. Without him, all the cell studies would not have been possible.

Secondly, Huikang has sacrificed much of his time synthesizing the plethora of polymers I request. His efforts have made the fabrication of the scaffolds much quicker. His experience with synthesis has allowed for consistent polymer preparation that would not have been possible if I had done it. Sara and Karla have given me an endless supply of moral support throughout the turbulent times. They both taught me about heart dissections and the digestion of ECM. Without their friendship, I would not have made it this far. Lastly, I want to thank Lia Molina Cortez, without her dedicated help in the lab, I wouldn’t have been able to accomplish as much as I have in the last year. The countless times she has offered her time to help progress my research cannot be understated, and she has my endless thanks.

I would like to acknowledge all the funding that made this possible; many thanks to NSF CAREER (DMR #1554835, YH), NIH R15 HL140503 (YH), and NIH (T32 HL134613, KN).

Abstract

In the United States and around the world, cardiovascular disease (CVD) has been one of the main causes of death since 1921, responsible for approximately 1 in 4 deaths domestically. Myocardial infarction (MI), or commonly called a heart attack, is a subset of CVD that often ends in heart failure (HF). Cardiac cells are incapable of regeneration, leading to severe impacts on quality of life. Current treatments for MI fail to target left ventricular remodeling and therefore do little to address the progression towards HF. Cardiac scaffolds for tissue engineering (TE) are a prominent solution in recent research. Developing various biomaterials to promote regaining function has narrowed down critical aspects for a successful scaffold. Trends in development show that biomaterials consisting of bioactive, conductive, elastic, and robust mechanical properties provide good environmental niches for cardiac cells. We aim to develop biomaterial blends that improve the bioactivity and conductivity of biodegradable polyurethane (PU) to study their structural, mechanical, and material characteristics and their interaction with cells.

In Aim 1, we integrated digested porcine cardiac extracellular matrix (ECM) into PU at varying concentrations, incorporating biomolecules found natively in cardiac tissue to supply biological cues in cardiac myocyte development. Interaction with the surrounding environment through integrins modulates the development of cardiomyocytes; ECM provides binding sites for integrins not found in synthetic polymers like PU. Aligned electrospinning (ES) of PU-ECM fibers was characterized and compared to the outer wall of a porcine left ventricle (LV). Fabricated fibers displayed highly aligned nanofibrous structures maintained throughout simulated body conditions. The resulting fiber diameter was 650-980 nm after simulated conditions. PU-ECM fibers exhibited anisotropic shrinkage after hydration due to swelling and the release of residual stress from the aligned electrospinning process. The hydrophilicity of fibers was improved through the incorporation of ECM, with PU displaying a contact angle of 107 ± 9° while PU-20%ECM was 70 ± 9°. Improvement of hydrophilicity originated from blending ECM. *In vitro* degradation of PU-20%ECM fibers showed accelerated degradation retaining a mass of 34.2 ± 2.8% over two weeks in

an enzymatic solution; comparatively, PU retained 54.8 ± 7.3% of its mass. Mechanically the LV porcine tissue had a failure stress of 0.36 ± 0.095 MPa, while PU-20%ECM was 15.0 ± 1.3 MPa. The superior mechanical properties of these fibers ensure resistance to failure when bearing forces applied to a heart. Viscoelastic and anisotropic mechanical properties were noted across all fibrous blends. Mouse HL-1 cells and neonatal rat ventricular cardiomyocytes (NNRCM) were seeded on blended fibers. HL-1 cells are organized unidirectionally on aligned fibers, and no significant toxicity to cells. Higher expression of α-actinin and f-actin was noted on PU-20%ECM scaffolds. NNRCM cells displayed significant improvement to viable counted cells in PU-20%ECM. Markers for maturity such as sarcomere and Z-line length were enhanced in PU-20%ECM fibers.

In Aim 2, we designed various conductive PU blends with reduced graphene oxide (rGO) to fabricate a potential muscle scaffold to improve electromechanical coupling. Uniformity of contractions is improved by coupling the myocytes, which is critical for practical myocyte function. PU-rGO blends were processed into aligned nanofibrous scaffolds through aligned ES. Initially, PU-rGO blends the highest rGO concentration of 4% w/w. During initial conductivity testing, poor results were obtained. To correct this, we fabricated a PU-10%rGO scaffold. Additionally, fiber size was impacted by rGO blending; PU-10%rGO's fiber diameter was 689 ± 226 nm, compared to PU, which was 464 ± 87 nm. The contact angle of PU-10%rGO was more hydrophobic than PU, with a contact angle of 132 ± 5° and 120 ± 7°, respectively. The conductivity of fibrous scaffolds was unobtainable, so membranes were made for 4-point probe instrumentation. Dry PU-10%rGO membranes displayed superior conductivity of 0.149 ± 0.035 S/m compared to PU-4%rGO, whose conductivity was 2 magnitudes less, at only 0.006 ± 0.001 S/m. Wet conductance gave erroneous results due to PBS masking bulk conductivity readings. PU-10%rGO displayed vastly reduced failure stresses along and across the fiber preferred direction. However, mechanical properties were still superior along the fiber preferred direction and comparable across the fiber preferred direction to LV tissue. Elasticity curves from cyclic loading revealed no change in trend due to rGO doping; similarly, anisotropic characteristics were consistent with native LV trends. *In vitro* cell culturing with mouse C2C12 and NNRCM displayed modulation of cell behavior. C2C12 cells were highly aligned on PU-10%rGO fibers, with interconnected cytoskeletal proteins of myosin heavy chain and f-actin. NNRCM displayed highly aligned morphologies, with maturity markers such as sarcomere length, Z-line length, and aspect ratio, which were significantly improved on the PU-10%rGO fibers. In contrast to PU, the expression for connexin-43 (Cx-43) was noted more peripherally, suggesting improved electromechanical coupling.

In Aim 3, we built upon the previous two objectives to fabricate a bioactive, conductive, elastic, and robust scaffold for improved biomimicry of native cardiac ECM. Previously found optimal blends of PU-20%ECM and PU-10%rGO were combined to fabricate a composite PU-20%ECM-10%rGO biomaterial blend. PU-20%ECM-10%rGO fibers were produced similarly to the previous iterations. Morphological characteristics of PU-20%ECM-10%rGO were similar to PU-20%ECM and PU-10%rGO, with highly aligned nanofibers, with a fiber diameter of 438 ± 158 nm. Shrinkage of PU-20%ECM-10%rGO (82.4 ± 1.5%) was similar to PU-10%rGO (83.0 ± 2.4%), shrinking less than its PU-20%ECM counterpart (78.0 ± 0.8%). The contact angle of PU-20%ECM-10%rGO was vastly improved compared to PU10%rGO, with the droplet fully absorbing within the first 15 seconds of placement. A unique interaction between ECM and rGO was displayed during conductivity testing. PU-20%ECM-10%rGO was 5-fold more conductive, at 0.92 ± 0.038 S/m compared to PU-10%rGO, at 0.174 ± 0.005 S/m. This improved conductivity may be caused by an improved dispersal of rGO throughout the membrane. Mechanically, PU-20%ECM-10%rGO was superior or comparable to the native LV tissue. A slight increase in failure stress was noticed across the fiber preferred direction in the PU-20%ECM-10%rGO fibers compared to PU-10%rGO. Cyclic loading curves showed similar trends. Biaxial testing revealed PU-20%ECM-10%rGO maintained anisotropic mechanical behavior. NNRCM *in vitro* studies displayed aligned cell morphologies across all fiber blends. PU-20%ECM-10%rGO sarcomere length was significantly higher than its counterparts. PU-20%ECM-10%rGO Z-line lengths were like PU-20%ECM and were superior to PU and PU-10%rGO.

Following the above three aims, future studies should focus on improving various limitations and challenges. Integrating mechanical and electrical stimulation during *in vitro* studies should promote functionality. Fabrication of a bioreactor capable of mechanical and electrical stimulation has been completed for this purpose. Initial calibrations of mechanical parameters of the bioreactor are ongoing. Secondly, an improvement to diminishing shrink of aligned scaffolds through annealing has also initially been explored. Releasing residual stress before removing the scaffold from the mandrel reduces shrinkage. Thirdly, incorporating a higher concentration of ECM may result in higher bioactivity. Another direction is sourcing and synthesizing monolayer rGO. Issues with aggregation of rGO and the need for high concentrations concern the robustness of mechanical properties and cell viability. Monolayer rGO should reduce the required rGO for improved conductivity while minimizing effects on mechanical properties. Lastly, finite element analysis modeling biomaterial mechanical behavior could reveal scaffold responses in physiological conditions. Computational modeling of the designed biomaterials could offer predictive powers to minimize time and money waste.

This dissertation has demonstrated several novel approaches to designing and fabricating new biomaterial blends of biodegradable PU as a potential cardiac scaffold. The approaches for functionalization focused on bioactivity and conductivity separately and combined. Firstly, incorporating bioactive ECM provides environmental cues to modulate cell maturation. Secondly, the incorporation of rGO improves electromechanical coupling by facilitating action potentials. Lastly, we created an improved biomimetic material and scaffold for optimized cell signaling by building upon the previous improvements. These various blends of PU offer a new selection of potential biomaterials for cardiac tissue regeneration and skeletal muscle regeneration.

TABLE OF CONTENTS

Dedication iv

Acknowledgment v

Abstract.. vii

LIST OF FIGURES xvii

LIST OF TABLES xxiii

CHAPTER I: Introduction and Rationale for Dissertation Research 1

1.1 Cardiac Layer Development, Structure, and Function 2

1.1.1 Epicardium 3

1.1.2 Myocardium 4

1.1.3 Endocardium 5

1.2 Cardiovascular Disease (CVD) 5

1.2.1 Cellular Pathology in LV Remodeling due to MI 8

1.2.2 Humoral Pathology in LV Remodeling due to MI 8

1.2.3 LV Mechanical Changes due to MI Remodeling 9

1.3 Current MI Treatments and Complications 9

1.4 Cardiac Scaffolds and Biomaterial Design Considerations 10

1.4.1 Poly (ε-caprolactone) 13

1.4.2 Poly (lactic-co-glycolic acid) 14

1.4.3 Poly (glycerol sebacic acid) (PGS) 16

1.4.4 Polyurethane 17

1.4.5 Polyethylene glycol ... 20

1.4.6 Decellularized Extracellular Matrix ... 21

1.4.7 Other Biomaterials ... 23

1.5 Knowledge Gap on Cardiac Tissue-Focused Biomaterials and Rationale for Dissertation Research ... 25

CHAPTER II: Electrospun Elastic Polyurethane/Extracellular Matrix Nanofiber Scaffold for Cardiomyocyte Culture ... 37

2.1 Introduction ... 38

2.2 Materials and Methods ... 41

2.2.1 Materials ... 41

2.2.2 Biodegradable Polyurethane Synthesis ... 41

2.2.3 ECM Extraction and Digestion ... 41

2.2.4 Electrospun Aligned, Hybrid Scaffold Fabrication ... 42

2.2.5 Scaffold Characterization ... 43

2.2.6 Cell Compatibility and Behavior ... 45

2.2.7 Statistical Analyses ... 48

2.3 Results ... 49

2.3.1 Sample fabrication ... 49

2.3.2 ATR-FTIR Surface Characterization ... 50

2.3.3 Scaffold Morphology Analysis ... 51

2.3.4 Contact Angle ... 53

2.3.5 In Vitro Enzymatic Degradation ... 54

2.3.6 Mechanical Testing 55

2.3.7 *In vitro* Cell Compatibility and Behavior 61

2.4 Discussion 65

2.5 Conclusions 70

2.6 Outcomes 70

CHAPTER III: Electrospun Elastic Nanofiber Polyurethane Scaffold Incorporated with Conductive Reduced Graphene Oxide for Muscle Cell Culture 72

3.1 Introduction 73

3.2 Materials and Methods 75

3.2.1 Materials 75

3.2.2 Biodegradable Polyurethane Synthesis 75

3.2.3 Electrospun rGO Doped Scaffold Fabrication 76

3.2.4 Scaffold Characterization 77

3.2.5 Cell Compatibility and Behavior 79

3.2.6 Statistical Analyses 82

3.3 Results 83

3.3.1 Scaffold Fabrication 83

3.3.2 ATR-FTIR Surface Characterization 83

3.3.3 Scaffold Morphology Analysis 84

3.3.4 Contact Angle 86

3.3.5 *In vitro* Enzymatic Degradation 87

3.3.6 Conductivity 88

3.3.7 Mechanical Testing 89

3.3.8 *In vitro* Cell Compatibility and Behavior 94

3.4 Discussion 98

3.5 Conclusions 101

3.6 Outcomes 102

CHAPTER IV: Fabrication of an Elastic Conductive Bioactive Electrospun Nanofiber Scaffold for Cardiomyocyte Culture 103

4.1 Introduction 104

4.2 Material and Methods 105

4.2.1 Materials 105

4.2.2 Biodegradable Polyurethane Synthesis 106

4.2.3 ECM Extraction and Digestion 106

4.2.4 Electrospun Conductive Hybrid Scaffold Fabrication 107

4.2.5 Scaffold Characterization 108

4.2.6 Cell Compatibility and Behavior 110

4.2.7 Statistical Analyses 112

4.3 Results 113

4.3.1 Scaffold Fabrication 113

4.3.2 ATR-FTIR 114

4.3.3 Scaffold Morphology 114

4.3.4 Contact Angle 117

4.3.5 In vitro Enzymatic Degradation 118

4.3.6 Conductivity 119

4.3.7 Mechanical Testing 120

4.3.8 *In vitro* Cell Compatibility and Behavior 125

4.4 Discussion 126

4.5 Conclusions 132

CHAPTER V: Summary and Future Studies 133

5.1 Summary 134

5.1.1 Chapter II: Electrospun Elastic Polyurethane/Extracellular Matrix Nanofiber Scaffold for Cardiomyocyte Culture 134

5.1.2 Chapter III: Electrospun Elastic Nanofiber Polyurethane Scaffold Incorporated with Conductive Reduced Graphene Oxide for Muscle Cell Culture 135

5.1.3 Chapter IV: Fabrication of an Elastic Conductive Bioactive Electrospun Nanofiber Scaffold for Cardiomyocyte Culture 135

5.2 Limitations 136

5.3 Future Works and Preliminary Study 137

5.3.1 *In vitro* Cell Functionality Quantification 137

5.3.2 Mechanical and Electrical Stimulation Bioreactor 138

5.3.3 Annealing of Aligned Electrospun Scaffolds 139

5.3.4 Increasing ECM Concentration in Hybrid Scaffolds 139

5.3.5 Exchanging Multilayer rGO Flakes for Monolayer rGO or Carbon Derivatives 140

5.3.6 Finite Element Analysis 140

5.3.7 *In vivo* Evaluation of Cardiac Repair 140

Appendix A 142

Appendix B 145

Abbreviations 146

REFERENCES 150

Biographical Information 186

LIST OF FIGURES

Figure 1.1: The distinct layers found in the ventricle of the heart [3] 2

Figure 1.2: A) The healthy human heart and B) post-ischemic human heart [3]....................................... 7

Figure 1.3: A) Healthy Ventricle Wall and B) Thinning of the ventricle wall [3] 7

Figure 1.4: Illustration of ischemic heart with a cardiac scaffold attached to the defect site [3, 68] 11

Figure 2.1: Schematic of aligned electrospinning setup; electrospinning took place over 8 hours with an extrusion rate of 1 ml/hr. The rotating mandrel was 15 cm away from the blunt tip rotating at 2500 rpm.42

Figure 2.2: Electrospun PU, PU-5%ECM, PU-10%ECM, and PU-20%ECM scaffolds. PU was the smoothest. Roughness increased with ECM. 49

Figure 2.3: ATR-FTIR of PU, PU-5%ECM, PU-10%ECM, PU-20%ECM scaffolds, and digested ECM. The wavelength range was 4000-600 cm^{-1}. 50

Figure 2.4: A-D) PU, PU-5%ECM, PU-10%ECM, and PU-20%ECM SEM images before and E-H) after immersion in PBS. I) Summary of fiber analysis PU, PU-5%ECM, PU-10%ECM, and PU-20%ECM before immersion in PBS and J) after immersion in PBS at 37°C for 24 hours. Scale bar length is 10 µm. 51

Figure 2.5: A) PU, PU-5%ECM, PU-10%ECM, and PU-20%ECM contact angle images at time points of 15, 30, 60, 90, and 120 seconds after water droplet application B) Dynamic contact angle for PU, PU-5%ECM, PU-10%ECM, and PU-20%ECM. C) Summary of contact angles for PU, PU-5%ECM, PU-10%ECM, and PU-20%ECM at each time point. 53

Figure 2.6: In vitro Enzymatic Degradation of PU, PU-5%ECM, PU-10%ECM, and PU-20%ECM. A) % remaining weight over the 14-day study. B) Summary of % remaining weight at each time point. The degradation solution was composed of PBS and 100 U/mL lipase; samples were incubated with the solution for 14 days. 54

Figure 2.7: A) Stress relaxation in PD for PU, PU-5%ECM, PU-10%ECM, PU-20%ECM, and LV porcine wall B) Stress relaxation in XD for PU, PU-5%ECM, PU-10%ECM, PU-20%ECM, and LV porcine wall C) Stress relaxation summary PU, PU-5%ECM, PU-10%ECM, PU-20%ECM, and LV porcine wall..... 55

Figure 2.8: A) PD Creep for PU, PU-5%ECM, PU-10%ECM, PU-20%ECM, and LV porcine wall B) XD creep for PU, PU-5%ECM, PU-10%ECM, PU-20%ECM, and LV porcine wall C) Summary of creep values for PU, PU-5%ECM, PU-10%ECM, PU-20%ECM, and LV porcine wall. 56

Figure 2.9: A) PD failure testing for PU, PU-5%ECM, PU-10%ECM, PU-20%ECM, and LV porcine wall B) XD failure testing for PU, PU-5%ECM, PU-10%ECM, PU-20%ECM, and LV porcine wall. C) Failure stress and strain values for PU, PU-5%ECM, PU-10%ECM, PU-20%ECM, and LV porcine wall. 57

Figure 2.10: Cyclic test to 30% strain over 10 cycles for A) PU B) PU-5%ECM C) PU-10%ECM D) PU 20%. The darker coloration denotes later cycles of testing, with the darkest representing the tenth cycle. 59

Figure 2.11: A) PD and XD biaxial testing of PU, PU-5%ECM, PU-10%ECM, PU-20%ECM, and B) LV porcine wall in the PD and XD direction. Scaffolds and LV porcine walls exhibited apparent anisotropic properties. 60

Figure 2.12: A) Live/Dead Staining of HL-1 cells on scaffolds on days 1, 4, and 7 for PU, PU-5%ECM, PU-10%ECM, PU-20%ECM, and B) Cell count from CCK-8 of HL-1 cells on days 1, 4, and 7 for PU, PU-5%ECM, PU-10%ECM, PU-20%ECM 61

Figure 2.13: HL-1 cell morphology at 500x, 1000x, 2000x, and 5000x on days 7 and 14 of culture on PU, PU-5%ECM, PU-10%ECM, and PU-20%ECM obtained by SEM. 61

Figure 2.14: Immunofluorescence staining for α-actinin, F-actin, DAPI, and the merged images at day 7 of differentiation of HL-1 cells seeded on PU, PU-5%ECM, PU-10%ECM, and PU-20%ECM. 62

Figure 2.15: Immunofluorescence Staining for α-actinin, F-actin, DAPI, and the merged images at day 14 of differentiation of HL-1 cells seeded on PU, PU-5%ECM, PU-10%ECM, and PU-20%ECM. 62

Figure 2.16: A) Aspect ratio and immunofluorescence intensity of B) α-actinin and C) F-actin of HL-1 cells on TCP, PU, PU-5%ECM, PU-10%ECM, and PU-20%ECM. 63

Figure 2.17: Cell viability of NNRCM on PU, PU-10%ECM, and PU-20%ECM, with A) Live/Dead staining and B) cell counting from CCK-8 results on days 1, 4, and 7. 64

Figure 2.18: Morphology of NNRCM on PU, PU-10%ECM, and PU-20%ECM on days 1, 4, and 7. Variable magnifications of 500x, 1000x, and 2000x were used during SEM. 64

Figure 2.19: A) Immunofluorescence staining for α-actinin, Cx-43, and DAPI on PU and PU-5%ECM, PU-10%ECM, and PU-20%ECM on day 7. B) Table summary of sarcomere length, Z-line length, and aspect ratio of NNRCM on scaffolds. 65

Figure 3.1: Schematic of aligned electrospinning setup 76

Figure 3.2: Electrospun image of PU, PU-0.5%rGO, PU-1%rGO, PU-2%rGO, PU-4%rGO, and PU-10%rGO. Scaffolds retained a shine across all rGO concentrations and darker coloration with increasing rGO. 83

Figure 3.3: ATR-FTIR spectra of PU, PU-0.5%rGO, PU-1%rGO, PU-2%rGO, PU-4%rGO, PU-10%rGO scaffolds, and rGO flakes in the wavelength range of 4000-600 cm^{-1}. 83

Figure 3.4: A-F) Images taken with SEM of PU, PU-0.5%rGO, PU-1%rGO, PU-2%rGO, PU-4%rGO, and PU-10%rGO before and G-L) after immersion in PBS at 37°C for 24 hours. M) Fiber analysis table before and N) after immersion in PBS at 37°C for 24 hours for PU, PU-0.5%rGO, PU-1%rGO, PU-2%rGO, PU-4%rGO, and PU-10%rGO and O) rGO flakes used in scaffold fabrication SEM image. Scale bar length is 10 μm. 84

Figure 3.5: A) Droplet at 15, 30, 60, 90, and 120 seconds after application for PU, PU-0.5%rGO, PU-1%rGO, PU-2%rGO, PU-4%rGO, and PU-10%rGO B) Change of contact angle with time for PU, PU-0.5%rGO, PU-1%rGO, PU-2%rGO, PU-4%rGO, and PU-10%rGO. C) Contact angle values over 120 seconds for PU, PU-0.5%rGO, PU-1%rGO, PU-2%rGO, PU-4%rGO, and PU-10%rGO. 86

Figure 3.6: A) % remaining weight of in vitro enzymatic degradation of PU, PU-1%rGO, PU-4%rGO, and PU-10%rGO over the course of the 14-day study. B) Summary of values for % remaining weight at each time point. The degradation solution was composed of PBS and 100 U/mL lipase; samples were incubated with the solution for 14 days. 87

Figure 3.7: A) PD stress-relaxation of PU, PU-0.5%rGO, PU-1%rGO, PU-2%rGO, PU-4%rGO, PU-10%rGO, and LV porcine wall B) XD stress-relaxation of PU, PU-0.5%rGO, PU-1%rGO, PU-2%rGO,

PU-4%rGO, PU-10%rGO, and LV porcine wall C) Table of stress relaxation values of PU, PU-0.5%rGO, PU-1%rGO, PU-2%rGO, PU-4%rGO, and PU-10%rGO and LV porcine wall in the PD and XD........... 89

Figure 3.8: A) PD creep testing of PU, PU-0.5%rGO, PU-1%rGO, PU-2%rGO, PU-4%rGO, PU-10%rGO, and LV porcine wall B) XD creep testing of PU, PU-0.5%rGO, PU-1%rGO, PU-2%rGO, PU-4%rGO, PU-10%rGO, and LV porcine myocardium C) Summary table of creep testing values of PU, PU-rGO scaffolds and LV porcine wall. 90

Figure 3.9: A) PD failure testing of PU, PU-0.5%rGO, PU-1%rGO, PU-2%rGO, PU-4%rGO, PU-10%rGO, and LV porcine wall B) XD failure testing of PU, PU-0.5%rGO, PU-1%rGO, PU-2%rGO, PU-4%rGO, PU-10%rGO, and LV porcine wall C) Table of failure stress and strain values for PU, PU-0.5%rGO, PU-1%rGO, PU-2%rGO, PU-4%rGO, PU-10%rGO, and LV porcine wall in the PD and XD. 91

Figure 3.10: Cyclic test to 30% strain over 10 cycles with the various scaffolds; A) PU B) PU-0.5%rGO C) PU-1%rGO D) PU-2%rGO E) PU-4%rGO F) PU-10%rGO 93

Figure 3.11: A) Biaxial testing of PU, PU-0.5%rGO, PU-1%rGO, PU-2%rGO, PU-4%rGO, PU-10%rGO, and B) LV porcine wall.. 93

Figure 3.12: A) Live/Dead Staining of C2C12 cell seeded on PU, PU-1%rGO, PU-4%rGO, PU-10%rGO, and TCP on days 1, 4, and 7, and B) cell count from CCK-8 of C2C12 Cells on PU, PU-1%rGO, PU-4%rGO, PU-10%rGO on day 1, 4, and 7. 94

Figure 3.13: Images of C2C12 cell differentiation at 500x, 1000x, and 2000x magnification on days 3 and 7 of culture for PU, PU-1%rGO, PU-4%rGO, PU-10%rGO taken with SEM. 95

Figure 3.14: Immunofluorescence Staining for MHC, F-actin, DAPI, and the merged images on days 3 and 7 of differentiation of C2C12 cells for PU, PU-1%rGO, PU-4%rGO, PU-10%rGO................................ 95

Figure 3.15: Cell viability of NNRCM for PU, PU-4%rGO, PU-10%rGO, and TCP, A) Live/dead staining of NNRCM on PU, PU-4%rGO, 10%rGO, and TCP, B) Cell counting results from CCK-8 of PU, PU-4%rGO, and PU-10%rGO scaffolds. 96

Figure 3.16: NNRCM morphology on PU, PU-4%rGO, and PU-10%rGO scaffolds, at 500x, 1000x, and 2000x magnification. Images were taken on days 1, 4, and 7 with SEM. 97

Figure 3.17: A) Immunofluorescence staining of NNRCM for a-actinin, Cx-43, and DAPI on PU, PU-4%rGO, PU-10%rGO, and TCP on day 7. B) Summary table of sarcomere length, Z-line length, and aspect ratio of NNRCM on scaffolds. 97

Figure 4.1: Schematic of aligned electrospinning setup 107

Figure 4.2: The obtained electrospun PU, PU-20%ECM, PU-10%rGO, and PU-20%ECM-10%rGO, with evident changes in color due to rGO and ECM inclusion. 113

Figure 4.3: ATR-FTIR Surface Characteristics of PU, PU-20%ECM, PU-10%rGO, and PU-20%ECM-10%rGO scaffolds with pure ECM and rGO flakes in the wavelength range of 4000-600 cm^{-1}. 114

Figure 4.4: A-D) Images of PU, PU-20%ECM, PU-10%rGO, and PU-20%ECM-10%rGO before immersion and E-H) after submersion in PBS at 37°C for 24 hours taken with SEM. I) rGO flakes used in scaffold fabrication. J) Table of fiber analysis of PU, PU-20%ECM, PU-10%rGO, and PU-20%ECM-10%rGO scaffolds before immersion in PBS and K) after submersion in PBS at 37°C for 24 hours. Scale bar length is 10 µm. 115

Figure 4.5: A) Contact angle images for PU, PU-20%ECM, PU-10%rGO, and PU-20%ECM-10%rGO scaffolds at time points of 15, 30, 60, 90, and 120 seconds after water droplet application B) Dynamic contact angle measurement for PU, PU-20%ECM, PU-10%rGO, and PU-20%ECM-10%rGO. C) Table of contact angles for PU, PU-20%ECM, PU-10%rGO, and PU-20%ECM-10%rGO at each time point. ... 117

Figure 4.6: A) The % remaining weight of in vitro enzymatic degradation for PU, PU-20%ECM, PU-10%rGO, and PU-20%ECM-10%rGO over the course of the 14-day study. B) Table of % remaining weight at each time point for PU, PU-20%ECM, PU-10%rGO, and PU-20%ECM-10%rGO. The degradation solution was composed of PBS and 100 U/mL lipase; samples were incubated with the solution for 14 days. 118

Figure 4.7: A) PD stress-relaxation for PU, PU-20%ECM, PU-10%rGO, PU-20%ECM-10%rGO, and LV porcine wall B) XD stress-relaxation for PU, PU-20%ECM, PU-10%rGO, PU-20%ECM-10%rGO, and LV

porcine wall C) Table of stress-relaxation values for PU, PU-20%ECM, PU-10%rGO, PU-20%ECM-10%rGO, and LV porcine wall 120

Figure 4.8: A) PD creep for PU, PU-20%ECM, PU-10%rGO, PU-20%ECM-10%rGO, and LV porcine wall B) XD creep for PU, PU-20%ECM, PU-10%rGO, PU-20%ECM-10%rGO, and LV porcine wall C) Table of creep values for PU, PU-20%ECM, PU-10%rGO, PU-20%ECM-10%rGO, and LV porcine wall 121

Figure 4.9: A) PD failure testing for PU, PU-20%ECM, PU-10%rGO, PU-20%ECM-10%rGO, and LV porcine wall B) PD failure testing for PU, PU-20%ECM, PU-10%rGO, PU-20%ECM-10%rGO, and LV porcine wall C) Table of failure stress and strain values for PU, PU-20%ECM, PU-10%rGO, PU-20%ECM-10%rGO, and LV porcine wall 122

Figure 4.10: Cyclic test to 30% strain over 10 cycles for A) PU B) PU-20%ECM C) PU-10%rGO D) PU-20%ECM-10%rGO. The darker coloration denotes later cycles of testing, with the darkest representing the tenth cycle. 123

Figure 4.11: A) Biaxial testing in the PD and XD of PU, PU-20%ECM, PU-10%rGO, PU-20%ECM-10%rGO, and B) the porcine left ventricle wall in PD and XD direction. 124

Figure 4.12: Cell viability on PU, PU-20%ECM, PU-10%rGO, PU-20%ECM-10%rGO scaffolds, A) Live/Dead staining, and B) cell counting from CCK-8 on days 1, 4, and 7. 125

Figure 4.13: NNRCM morphology on PU, PU-20%ECM, PU-10%rGO, PU-20%ECM-10%rGO scaffolds, at 500x, 1000x, and 2000x magnification taken with SEM. 125

Figure 4.14: A) Immunofluorescence staining of NNRCM for α-actinin, Cx-43, and DAPI on PU, PU-20%ECM, PU-10%rGO, PU-20%ECM-10%rGO scaffolds on day 7. B) Summary table of sarcomere length, Z-line length, and aspect ratio of NNRCM on scaffolds. 126

Figure 5.1: Bioreactor capable of mechanical stretch and electronic stimulation.................................. 138

Figure 5.2: A) Annealed PU and PU scaffolds with SEM images at 500x, 1000x, 2500x, and 5000x magnification. B) Comparison of PU to annealed PU scaffold shrinkage. C) Summary of % shrinkage for PU and annealed PU scaffolds. 139

LIST OF TABLES

Table 1.1: List of investigated biomaterials and their effects on cardiomyocyte behavior 28

Table 2.1: Summary of shrinkage of PU, PU-5%ECM, PU-10%ECM, and PU-20%ECM after immersion in PBS at 37°C for 24 hours. 51

Table 3.1: Summary of shrinkage of PU, PU-0.5%rGO, PU-1%rGO, PU-2%rGO, PU-4%rGO, and PU-10%rGO after immersion in PBS at 37°C for 24 hours 84

Table 3.2: Conductivity of PU, PU-1%rGO, PU-4%rGO, and PU-10%rGO Films 88

Table 4.1: Summary of shrinkage of PU, PU-20%ECM, PU-10%rGO, and PU-20%ECM-10%rGO after immersion in PBS at 37°C for 24 hours 114

Table 4.2: Conductivity of PU, PU-20%ECM, PU-10%rGO, and PU-20%ECM-10%rGO Films......... 119

KEYWORDS: Myocardial Infarction, Tissue Engineering, Decellularized ECM, Biodegradable Polyurethane, Reduced Graphene Oxide, Cardiomyocytes

CHAPTER I: Introduction and Rationale for Dissertation Research

1.1 Cardiac Layer Development, Structure, and Function

In the United States and the world cardiovascular disease (CVD) is the one of the main causes of death. An estimated 1 in 4 people die from a cardiovascular-related disease costing the United States around $219 billion yearly from medical expenses and loss of productivity from recovery and death [1]. CVD is a progressive disease caused by various environmental and genetic factors; myocardial infarction (MI), colloquially known as a heart attack, is a large subset of CVD that leads to heart failure (HF). Understanding cardiac layers and their structural and biological effects on cardiomyocytes (CM) are vital for determining the efficacy of current and future treatments. The heart has three distinct layers: the epicardium, myocardium, and endocardium. Structurally the extracellular matrix (ECM) changes morphology from layer to layer for its unique mechanical requirements (**Figure 1.1**) [2]. The most studied protein in cardiac ECM is collagen, which is present throughout all three layers, with different compositions of naturally occurring structural proteins in each layer. Understanding the characteristics of the three cardiac layers and their interactions during development is paramount in crafting an effective treatment for regeneration.

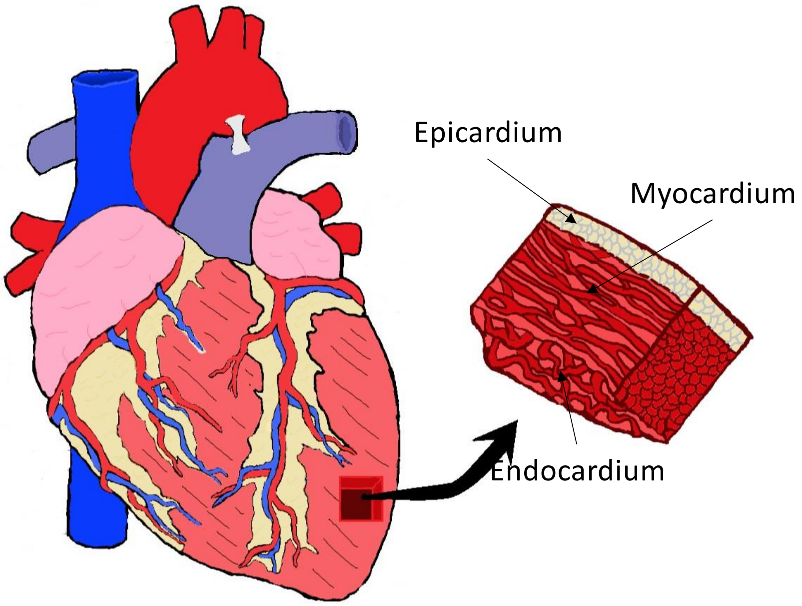

Figure 1.1: The distinct layers found in the ventricle of the heart [3]

1.1.1 Epicardium

The epicardium is the outermost epithelial layer of the heart. Anatomically, it is a part of the pericardium, a bi-layered fibrous sac that protects the heart and anchors it in the body [4]. Developmentally the epicardium forms separately from the myocardium and endocardium, originating from a primarily extracardiac primordium, the proepicardial serosa [4, 5]. The proepicardial serosa contains various mesenchymal and endothelial cell types, which are responsible for the maturation of the epi/myocardium and the production of ECM [5]. The developing epicardium contributes to myocardial development via epithelial to mesenchymal transition (EMT), a process that reduces the expression of transmembrane adhesion proteins like E-cadherin and zonula occudens-1 on the epithelial cells [4, 5]. The morphology of endothelial cells subsequently changes to be spindle-shaped with an increased expression of fibronectin, N-cadherin, and matrix metalloproteases (MMP) [4]. Quickly after development, the epicardium goes dormant, showing rapid downregulation of WT1, Raldh2, and Tbhx18 genes [4]. In the adult epicardium, the primary function of the ECM is to provide a protective layer for the heart with the pericardium [2, 6]. The epicardium is composed of mostly elastin and collagen. This elastin-rich matrix provides a passive constriction that can withstand deformation due to the elastin network [7]. In response to damage, particularly from ischemic heart disease such as MI, the epicardium reactivates its’ regenerative properties via upregulation of WT1, Raldh2, and Tbhx18 genes [4]. The partial reactivation of these genes occurs across the entirety of the epicardium, not localized exclusively to the area of defect. The wide reactivation of the developmental properties is thought to be caused by signals transmitted via pericardial fluid [4]. The epicardium shifts from a single cell layer into a multilayered cell sheet, most layering occurs around the defect [4]. The multilayered sheets recapitulated neonatal activity with the presence of EMT through upregulation of transcription factors like *Snail, Smad1, Twist, and Slug* in MI models [4]. Models primed for EMT, through the injection of thymosin β4, exhibited more migration and improved cardiac function [4]. Evidence indicates the EMT cells differentiated into fibroblasts, smooth muscle cells, and cardiomyocytes; the majority differentiated into fibroblasts which highly express collagen-I, elastin, and fibronectin [4]. Signals derived from EMT cells help contribute to the development and repair of the myocardium.

1.1.2 Myocardium

The myocardium is the mid-layer of the heart, comprised of densely compacted cardiomyocytes responsible for most of the contractile forces of the heart. Developmentally the myocardium originates from the splanchnic mesoderm [8]. During the initial tubular heart formation, the myocardium and endocardium appear, separated by an acellular matrix called the cardiac jelly [8]. The majority of the early cardiac jelly is composed of hyaluronic acid (HA) and proteoglycans (PG), producing a malleable hydrated matrix for easy remodeling and infiltration [9]. The myocardium is made of mainly collagen I and III in adult hearts with a relatively affluent composure of glycosaminoglycans (GAGs), such as HA and PG, for lubricated contractions [10]. This initial myocardium layer is dubbed the 'primary myocardium,' characterized by a low density of gap junctions, a craniocaudal gradient expression of acetylcholinesterase, and sarcoplasmic reticulum calcium ATPase [11]. Smooth muscle α actin is expressed throughout the length of the primary myocardium, which is replaced later in development by skeletal and cardiac isoforms of actin [11]. As the tubular heart starts to loop towards the right, the atrial and ventricular segments become distinct. The ventricular segment begins trabeculation, regulated by the endocardial cell signaling [8, 12]. Signaling from the endocardium leads to the degradation of structural proteins in the cardiac jelly region, with some cell migration from the myocardium layer into the acellular cardiac jelly [12-14]. Trabeculation allows for nutrient transfer to the thickening myocardium, and the development of fibril patterns occurs due to integrins interacting with the ECM of the myocardium [15-17]. Compaction starts with EMT migration into the myocardium, flattening the trabeculation or developing capillaries for nutrient delivery to the myocardium [17-20]. During the initial compaction phases, the myocardium's ECM aids intracellular interactions by transferring forces from cell to cell, maximizing uniformity of contractions [21]. The organized patterning of the myocardium ECM enables efficient contractions, and the presence of gap junctions in early heart development provides a mechanism for the electro-mechanical activation of cardiomyocytes in the myocardium [11, 15]. In myocardium development, there is a dependency on integrin presence to avoid fibrosis in the early heart [22]. As established in the prior section, the epicardium-derived cells contribute to myocardium development through paracrine signaling [4].

1.1.3 Endocardium

The endocardium is derived from the splanchnic mesoderm and can be identified as a distinct layer during the tubular heart stage of development [8]. The endocardium is structurally slick and helps regulate trabeculation [14, 22]. The ECM is composed of collagen and elastin, giving it the slick texture and ability to undergo deformity [10, 23]. The endocardium's prominent role in heart development depends on growth factor release and contributes to cell migration into the cardiac jelly [12, 24-26]. Remodeling the ECM in the cardiac jelly is temporally sensitive to signaling [23, 24, 27]. The early developing endocardium upregulates neuregulin-1 (NRG-1), stimulating $ErbB_2$ and Erb_4 to initiate ECM remodeling for trabeculation. Simultaneously signals cardiac jelly infiltrating cells to differentiate into the base electrical framework [12, 28, 29{Smith, 2007 #270]. NRG-1 regulates chamber morphogenesis via insulin-like growth factor 1 (IGF-1) by activating phosphatidylinositol 3-kinase [24]. The endocardial cells receive signals from the myocardium to initiate endocardial cushion formation by stimulating ECM production into the cardiac jelly; endocardium cells migrate into the cardiac jelly and differentiate into pre-valve tissue components [24, 30]. The release of neurofibromin (Nf1) from the endocardium modulates endocardial cushion formation, regulating the size of the cushions; limited Nf1 activation leads to gestational lethality [24, 31]. Expansion and myocardial cell growth in the trabeculae are activated by fibroblast growth factors (FGFs), mainly FGF-9, -16, and -29 [24]. Adverse remodeling of the adult heart due to MI interrupts the native ECM structure, which impacts the specific functionality of the cardiac ECM.

1.2 Cardiovascular Disease (CVD)

Myocardial infarctions (MI) are one of the main initiators of ventricular remodeling. MI's are characterized by a lack of nutrient and oxygen flow to heart sections leading to myocyte death and weakening the hearts' ability to function (**Figure 1.2**) [33]. Alterations to the ECM occur in 3 distinct overlapping phases for MI: the inflammatory and proliferative phases and the maturation phase [32]. During the inflammatory phase, degradation of the matrix proteins acts as an inflammatory factor [32]. These inflammatory factors attract macrophages to the injured area and act as a conduit for inflammatory cell infiltration [32-35]. Clearing out the dead cells from the tissue requires the destruction of the surrounding ECM, damaging the present complex structure. Clearing the ECM releases anti-inflammatory mediators, signaling the transition to the second phase of ECM alterations [32]. In the proliferation phase, the ECM comprises matricellular proteins that do not provide much structural support, alter the cellular phenotype of infiltrating cells, and activate various growth factors [36, 37]. Infiltrating fibroblasts replace the non-regenerative cardiomyocytes [38]. The fibroblasts then produce a significant amount of structural ECM proteins. The rate of phagocytosis and fibrotic tissue deposition does not always lead to thinning of the left ventricle (LV) wall [39-41]. Thinning increases the chance of LV wall rupture (**Figure 1.3**) [42, 43]. After ECM deposition, the maturation phase begins. In this phase, the ECM is reinforced by crosslinking, and the fibroblasts are deactivated with vascular infiltration to produce stable scar tissue [32, 36].

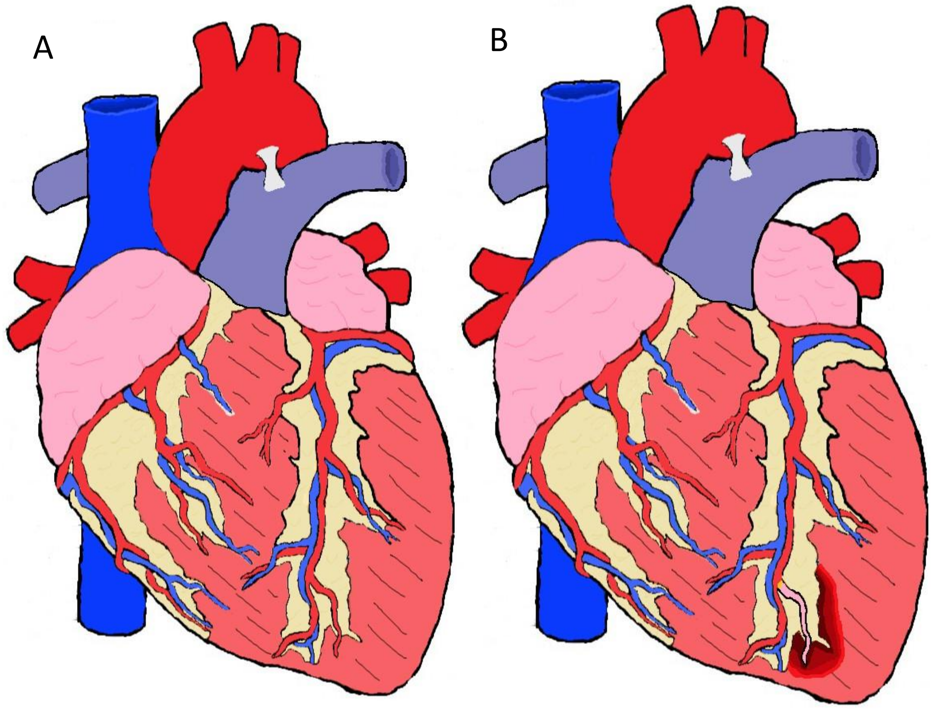

Figure 1.2: A) The healthy human heart and B) post-ischemic human heart [3]

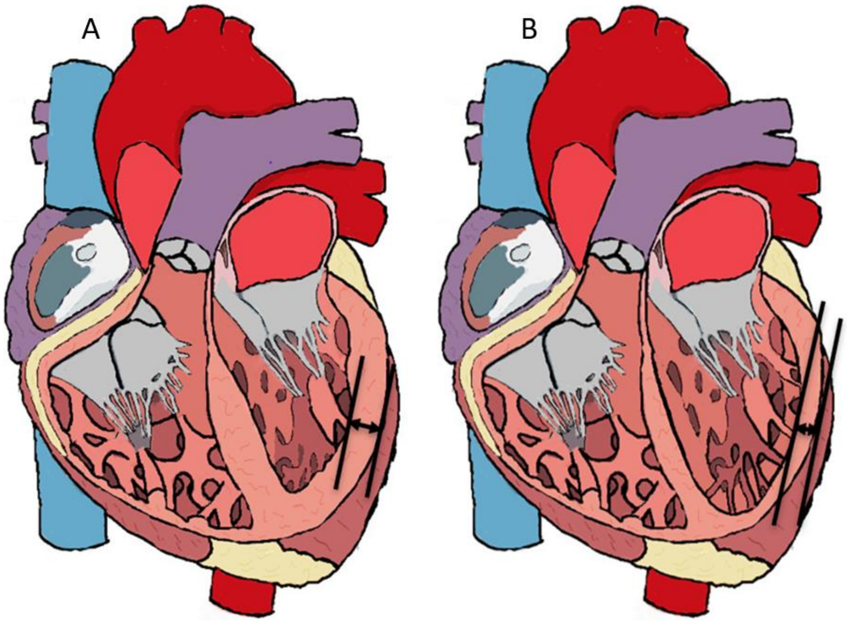

Figure 1.3: A) Healthy Ventricle Wall and B) Thinning of the ventricle wall [3]

MI leads to HF through LV remodeling, which gets progressively worse due to feedback loops. The progression from MI to HF is a gestalt, meaning cursory knowledge of the different mechanisms is needed to understand how they are interconnected. There are three understood pathways: cellular, humoral, and mechanics based.

1.2.1 Cellular Pathology in LV Remodeling due to MI

A typical location for blockage is in the left anterior descending coronary artery (LAD), where downstream suffocation of cardiomyocytes heavily affects the left ventricle (LV). The ischemic myocardium releases pro-inflammatory factors, a precursor to left ventricle remodeling [44]. Macrophages and neutrophils, attracted to the pro-inflammatory factors, clear away the necrotic tissue [44]. Collagen deposits in the perivascular space to replace necrotic tissue. Fibrotic tissue cannot aid myocyte contractions, leading to further heart complications [45-47]. During these changes, released factors exacerbate remodeling through the humoral pathway.

1.2.2 Humoral Pathology in LV Remodeling due to MI

The humoral pathway is mainly affected by the renin-angiotensin-aldosterone system (RAAS), which is responsible for the regulation of blood pressure and hydro electrolytic balance [48]. The buildup of angiotensin-converting enzyme (ACE) and angiotensin (AGT), produced in both infarcted and surrounding myocardium, from inflammatory and endothelial cells leads to worsening heart conditions. Excessive ACE and AGT disrupt blood pressure regulation and promote fibrosis, intensifying LV remodeling and blood pressure, which increases the risk of HF [48]. Activating the AGT_1 receptor increases aldosterone production in the infarction tissue, promoting fibrosis and myocyte hypertrophy [48]. Excess ACE and aldosterone elicit spontaneous fibrosis in non-infarcted areas [48, 49]. The increase in collagen deposition in non-infarcted myocardium alters the mechanics of the heart. The change in LV mechanics also plays a role in the remodeling process and eventual HF due to the feedback looping effect.

1.2.3 LV Mechanical Changes due to MI Remodeling

There are two main mechanical components to consider, stress and strain experienced by the LV wall [50]. The LV wall stress is calculated from the LV tension, the resistive force that prevents cavity dilation, and the LV pressure, the force for blood pumping [51]. This tension predominately comes from active myocardial contractions and passive support from the interstitial tissue in a healthy LV wall. In infarcted tissue, the tension is reliant on passive support. Lacking the active contractions of the myocardium, infarcted tissue cannot compensate for the change in pressure, stimulating hypertrophy of the surrounding cardiomyocytes to compensate, further impacting the heart's structure [52]. The LV must dilate to compensate for the hypertrophy to maintain a consistent stroke volume. The strain of the LV wall is impacted by the infarcted tissues' inability to cope with the changes in stress, leading to further deformation [44]. Based on the current understanding of MI pathology and HF progression, treatments to target the different pathways have been used clinically. Examination of current treatments aids in finding weaknesses and solutions.

1.3 Current MI Treatments and Complications

Current treatments for MI interventions focus more on prevention, doing little to combat remodeling. The less invasive treatments require long-term beta-blockers and blood thinners with exercise and dietary changes [53, 54]. More extreme cases require invasive treatment, ranging from balloon angioplasty for stent placement and coronary artery bypass to implanting a left ventricle assent device [55-57]. Total heart transplants are available in only the most extreme circumstances; however, the limited access to donor’s hearts, the cost of lifelong immunosuppressants, and a chance for organ rejection create a need for better treatment alternatives [58, 59]. Biomaterials have developed several prosthetic wraps that provide passive mechanical support limiting ventricular dilation [60, 61]. Clinical results from the prosthetic wraps are promising with left ventricle function improvement [60]. These therapies offer some symptom relief for patients with HF rather than provide renewed function, and long-term gains are due to the knowledge gap.

In recent years, tissue engineering (TE) has been a focal point in developing new MI treatments [62-64]. TE is the marriage of biology and engineering to produce artificial tissues or cellular products that manage or repair injuries sustained within the body [65, 66]. Tissue-engineered cardiac patches aim to treat the underlying issues in patients suffering from MI by providing a scaffold to preserve myocardium functionality, reverse remodeling, and mechanical support to prevent further remodeling. Traditionally TE cardiac scaffolds integrate cells into their construction before implantation to form the artificial tissues; the effects of acellular scaffolds on injury repair post-MI have been evaluated [66]. Regardless of cell-laden or acellular scaffolds, cardiac scaffolds require a biomaterial with many characteristics to mimic the native pre-MI heart [67]. The development of new complex biomaterials needs further investigation to maximize the effectiveness of future tissue-engineered scaffolds.

1.4 Cardiac Scaffolds and Biomaterial Design Considerations

Cardiac scaffolds are a relatively simplistic yet revolutionary idea widely researched due to their potential as a regenerative tool that can combat adverse remodeling through mechanical support. Mechanical support of the weakened tissue is an essential aspect of cardiac scaffolds that is rarely addressed in current treatment protocols. The scaffold is attached to the surface of the defect, supplying additional structural support and aiding in the restoration of cardiac function. These scaffolds can be loaded with cells or biomolecules; introducing cells and biomolecules promotes functional tissue production over restrictive fibrotic tissue by modifying biological cues. Biomaterials required in cardiac scaffolds must be mechanically like the native tissue, biocompatible, biodegradable, elastic, and conductive to act as an adequate scaffold (**Figure 1.4**) [68, 69]. Synthetic and natural polymers or a combination of both compose the biomaterials of tissue engineering scaffolds. Scaffolds are tailored to suit various applications of tissues by either functionalizing the polymers or including additives to augment the physical and chemical properties of the scaffold [70, 71]. Tailoring scaffold biomaterials enables a highly personalized treatment plan for patients, maximizing therapeutic effectiveness.

Fabrication is as crucial as biopolymer selection. Creating a porous, physiological-relevant microstructure is essential in promoting cell growth and differentiation [72, 73]. Cardiac scaffolds have various fabrication methods, including salt leaching, phase separation, electrospinning, gelation of hydrogels, 3D printed structures, and others [74-76].

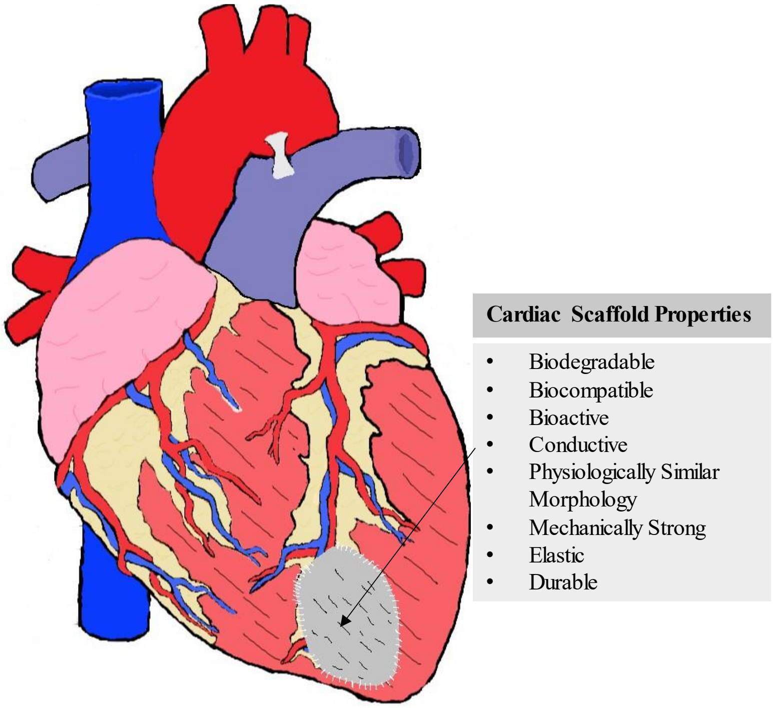

Figure 1.4: Illustration of ischemic heart with a cardiac scaffold attached to the defect site [3, 68]

Ideally, implanted scaffolds with a high degree of biomimicry integrate with the host tissue and encourage the migration and differentiation of host cells [68, 77, 78]. Cells should gradually degrade the implanted scaffold to be replaced with a newly formed ECM. The conductivity of the scaffold is vital for promoting uniform contractions due to easier electrical signaling to cells within the scaffold [79]. Injectable hydrogels have been explored as a possible alternative due to their 3D microstructure and ease of application, with the drawback of relatively mechanically weak support [80, 81]. Mechanically robust scaffolds are required for cardiac tissue-engineered scaffolds due to the continuous physical demands of a pumping heart [68]. A scaffold that is elastic and robust and withstands excessive cyclic fatigue while meeting all previous requirements highlights the importance of continued exploration into new biomaterial blends for improved cardiac tissue engineering [78].

Cardiac scaffolds previously investigated exemplify the possibilities of blends and the degree of functionalization to overcome the current hurdles they face. Most often, successful scaffolds have demonstrated several vital components. Firstly, they exhibited a high degree of cytocompatibility, capable of encouraging cells' growth and avoiding adverse immune reactions. Secondly, the scaffolds demonstrated mechanics that structurally reinforced the infarcted tissue with a degree of elasticity to mimic the elastic nature of the heart. Thirdly, the scaffolds could integrate with host tissue through well-timed degradation that matches the growth of cells. Fourthly, scaffolds enabled strong electrical signaling for improved contractions. Lastly, the scaffolds mimicked the native morphology of cardiac ECM to improve integration with host tissue.

Current research aims to develop synthetic polymers that fulfill all requirements. Synthetic polymers can be tuned at the molecular level, allowing them to incorporate several critical components needed for successful application as a cardiac scaffold. As a biomaterial, synthetic polymers can have reduced cell adhesion and poor integration with host tissue. Modifications and additions of other components such as growth factors or natural polymers can compensate for their weaknesses and help maintain their popularity as potential scaffolding material. Popular biodegradable synthetic polymers used as scaffolding for cardiac TE applications include poly (lactic-co-glycolic acid) (PLGA), poly (ε-caprolactone) (PCL), biodegradable polyurethane (PU), and poly (glycerol sebacate) (PGS). To completely understand the influences polymeric scaffolds have on cardiac repair, an investigation into cardiomyocyte behavior on various fibrous blends and the correlation between these behaviors in in vivo experiments must be performed. Below summarizes the response CMs have when grown on various polymers and polymeric blends.

1.4.1 Poly (ε-caprolactone)

PCL is a semicrystalline biodegradable polymer commonly investigated because of its structural strength, ready availability, and low price [82, 83]. The mechanical properties of PCL are determined by the degree of crystallinity and molecular weight [84]. This variability has made it an excellent synthetic polymer for various uses in the biomedical field [85]. It is synthesized via ring-opening polymerization (ROP) [85]. Researchers have attempted to capitalize on PCL's variability to produce cardiac scaffolds [86-90]. Earlier iterations of scaffoldings made with PCL supported cardiomyocytes that could contract after only a few days of growth. However, PCL's slow degradation led to low cell growth within the scaffold from limited nutrient flow [91]. Like other synthetic polymers, PCL has low hydrophilicity and no natural binding sites for cellular attachment. Guex et al. found that plasma functionalized PCL improved stable cardiac function [87]. Stem cell presence within the scaffold and scar tissue was increased compared to no treatment and non-functionalized PCL [87]. The effects of the morphology of the PCL scaffolds on CM behavior were investigated by Rath et al. [88]. Neonatal and adult CM were isolated from rats and seeded on nanofibrous aligned PCL scaffolds. The CMs exhibited greatly improved organization and development of well-striated sarcomeres [88]. The neonatal sarcomeres developed perpendicularly to the fibers in the scaffold while they developed parallel in the adult CMs [88]. The freshly isolated adult CM maintained its highly organized sarcomere system and grew perpendicular to fibers in the scaffold to minimize resistance to cell shortening. In contrast, the neonatal CM lacked an organized sarcomere system and thus developed sarcomeres perpendicular to the stress [88].

Shifts away from pure PCL cardiac scaffolds to an amalgam of polymers containing gelatin, collagen, elastin, and PCL, aim to combat the shortcomings of pure PCL [92]. A core/shell electrospun scaffold composed of a gelatin shell and a PCL core by Kai et al. exhibited improved CM maturity compared to pure PCL scaffolds [89]. CM's on the PCL/gelatin scaffolds upregulated troponin-T (cTnT) and α-actinin with a highly organized striated structure compared to the PCL scaffold [89]. Improved expression of CM markers further emphasizes the benefits of incorporating natural polymers into cardiac scaffolds. Liu et al.

also found a beneficial effect on cellular attachment, proliferation, and elasticity [92]. Within a mouse animal model, the area of the defect was significantly decreased by the composite scaffold [92]. The mechanical properties improved by incorporating these natural polymers to more than 50% natural polymer concentration [92]. The beneficial effects of the scaffolding were enhanced further with the incorporation of seeded cells on the scaffold compared to the acellular scaffold [92]. The ejection fraction, fractional shortening, and wall thickness significantly improved compared to non-blended scaffoldings [92]. Improvements to PCL's conductivity have also been tested to account for the electrical impulses the heart produces. Borriello et al. improved the conductivity by including polyaniline (PAni) [93]. The PCL: PAni (90%:10%) produced a scaffold with 1E-5 S/cm, improving cell signaling in the scaffold for better contractile strength [93]. Cardiomyocyte growth on the conductive scaffolding was significantly higher compared to the non-conductive scaffolding [93]. O. Gil-Castell et al. fabricated a PCL/Gelatin/PAni fibrous scaffold and investigated the effects on cardiomyocyte behavior [90]. The CM exhibited greatly improved proliferation in the high gelatin composition, further improved by incorporating PAni [90]. Cardiomyocytes grown on the PCL/Gel/PAni scaffold exhibited propagated beating on the scaffolds, with cells congregating around the PANi nanoparticles dispersed throughout the scaffold [90]. Consistently composite PCL-based scaffolds exhibited significantly improved growth and repair of the infarcted tissue, supporting the rationale for developing composite biomaterials.

1.4.2 Poly (lactic-co-glycolic acid)

Another popular polymer used as a cardiac scaffold material is poly (lactic-co-glycolic acid) (PLGA). PLGA is a block copolymer that is biodegradable, biocompatible, and customizable, made of poly(lactic acid) (PLA) and poly(glycolic acid) (PGA) [94]. Another benefit of PLGA is its acceptance of biomedical devices in clinical application by the US Food and Drug Administration (FDA). A change in ratios between the block copolymer enables tunable mechanical properties of the scaffold without additives. PLGA is typically synthesized via ROP, opening the cyclic dimer rings of D, L-lactide, and glycolide; altering the ratio of monomers is how different PLGA compositions are made [95]. The relatively low hydrophilicity paired with an absence of recognition sites for cells limits its cellular affinity [96]. Chen et al. fabricated micro-patterned films of PLGA to investigate CM behavior with electrical stimulation [97]. Grooved PLGA films organized CM growth; the production of ECM was parallel to the grooves, and electrical stimulation upregulated connexin-43 (Cx-43) expression throughout the scaffold [97]. Adding gelatin functionalized by adenosine improved PLGA's cellular affinity and wound healing [98]. The hybridized scaffolds had lower levels of inflammation, with a significant decrease in inflammatory cell infiltration [98]. After three months, scaffoldings scaffolds were highly cellularized, with no indication of fibrosis from scaffold implantation [98]. Yu et al. functionalized a PLGA scaffold with peptides for cellular attachment [99]. Cellular attachment to the peptide-treated scaffolds was significantly enhanced with striated α-actinin and improved contractibility [99]. The laminin-coated scaffold and YIGSR functionalized scaffolds had a higher degree of synchronized beating, and the beating was consistent over two weeks compared to the non-functionalized scaffolds [99]. Li et al. further augmented PLGA using a co-electrospinning technique of gelatin and elastin with PLGA [100]. Composite scaffolds exhibited improved cardiomyocyte proliferation and cellular penetration into the scaffold [100]. Prabhakaran et al. explored hybridized natural and synthetic polymer blends with collagen and PLGA [101]. The composite scaffolds upregulated striation of α-actinin compared to pure PLGA scaffolds, and the presence of Cx-43 was similarly upregulated in hybrid scaffolds [101]. The results of hybridized scaffolds indicate mature ECM development and improved cell proliferation. Mature ECM development is likely due to incorporating binding sites on the natural polymers and receptor-mediated intracellular processes from cell binding to these binding points [74, 99, 102]. Stout et al. improved the conductivity of scaffolds via blending carbon nanofibers with PLGA [103]. There was vastly increased conductivity and improved cytocompatibility [103]. Conductive scaffolds also exhibited higher cell density compared to their non-conductive counterparts. Hsiao et al. blended PLGA with PAni as a conductive scaffold for cardiomyocyte growth [104]. Cells cultured on the conductive scaffolds upregulated Cx-43 and cardiac troponin-I (cTnI) compared to the non-conductive scaffolds [104]. Upregulation of Cx-43 improved cell-to-cell communication beaause it is a critical protein in gap junction formation [104]. This was further validated by the synchronous beating of cells on the conductive scaffolds

[104]. Lesman et al. fabricated a PLGA: PLLA porous scaffold [105]. A tri-culture on the scaffold was capable of synchronous beating [105]. Transplanted scaffolds in hearts exhibited improved vascularization in the defect [105]. Vascularization within the scaffolding could integrate with the host's vascular post-implantation. Results of the examined literature highlight the importance of investigating polymeric blends to overcome weaknesses in current biomaterials.

1.4.3 Poly (glycerol sebacic acid) (PGS)

PGS is a synthetic, elastic, and crosslinked polymer that is attractive due to the control over the mechanical parameters and degradability through varying glycerol and sebacic acid [106]. The typical synthesis of PGS occurs by two-step synthesis through polycondensation and crosslinking [107-109]. It has similar mechanical properties to the myocardium, making it a perfect candidate as a cardiac scaffold. Engelmayr et al. made a patterned PGS scaffold with a laser [110]. The laser-patterned scaffold exhibited anisotropic behaviors and improved the alignment of cardiomyocytes [110]. Marsano et al. produced a PGS scaffold loaded with vascular endothelial growth factors that improved cardiac function [111]. Implanted scaffolds improved the vascularization of the defect after four weeks [111]. Improved ventricle wall thicknesses were noted, with thickening prevalent in scaffolds seeded with rat cardiomyocytes [111]. Hybridized scaffolds have also been extensively investigated with PGS-based scaffolds [112, 113]. Kharaziha et al. made an aligned nanofibrous scaffold of PGS and gelatin [112]. The CMs on PGS/gelatin scaffolds had enhanced synchronous beating. The upregulated expression of troponin-I (cTnI) and Cx-43 suggested gap junction formation [112]. The incorporation of gelatin into scaffolds led to higher elastic moduli, corresponding to the improved maturity of CMs on the scaffold [112]; utilizing a core-shell fabrication method, Ravichandran et al. generated nanofibrous PGS/fibrinogen scaffolds [113, 114]. CM behavior on their scaffolds revealed improvements in ECM production, with α-actinin forming striated bands, upregulation of β-myosin heavy chain (β-MHC), cTnT, and Cx-43 [113]. The upregulation of Cx-43 led to better functional activity via the increased formation of gap junctions [113]. Implanted scaffolding seed with mesenchymal stem cells exhibited improved left ventricle function compared to the sham [114].

The presence of cardiac markers within the scaffolding indicated improved differentiation of cells due to scaffolding. Ravichandran et al. also investigated a PGS/collagen core/shell scaffold as a potential cardiac scaffold [109]. Core/shell scaffolds improved cellular adhesion and proliferation of CM compared to its pure collagen counterpart [109]. Similarly, co-culturing with human mesenchymal stem cells improved the cardiogenic marker expression on the scaffolds (α-actinin, cTnT) [109]. 3D immunofluorescence imaging showed enhanced cell penetration throughout the PGS/Collagen scaffolds compared to pure collagen scaffolds, reinforcing the benefits of hybridized scaffolds [109]. Chen et al. made a PGS scaffold laden with stem cells, producing active beating cells [115]. Implanted scaffolds maintained their structure over two weeks, with no detrimental impact on cardiac function. Improvements to PGS's conductive properties have been investigated by Zanjanizadeh et al., producing a PGS/collagen/polypyrrole (PPy) scaffold capable of drug release [116]. The scaffold exhibited long-term drug release with no burst release and increased proliferation of cardiomyocytes over 21 days. Hu et al. improved conductivity incorporating aniline trimer (AT) into their film casted PGS scaffolds [117]. PGS-AT films improved cell proliferation compared to TCP, and upregulated α-actinin and Cx-43 [117]. Grooved films improved striation of ECM archicture [117]. Functional testing of CMs on scaffolds showed synchronized calcium transients and beating throughout scaffold and an increase in intracellular calcium [117]. Fakhrali et al. improved the conductivity of their PGS/PCL scaffold by incorporating graphene into their scaffold [118]. Graphene containing scaffolds improved cell migration into the scaffold compared to the nonconductive scaffolds, similarly proliferation was also improved in the presence of graphene [118]. The inclusion of graphene also improved cell viability, with 1% (w/w) showing the best viability [118]. Improvements to PGS through blending of various polymers has consistently led to more developed CMs compared to pure polymeric scaffolds, continuing to prove more material blends need investigating.

1.4.4 Polyurethane

Polyurethane is one of the most investigated polymers in cardiac repair, with a variety of types of biodegradable polyurethanes, such as poly (ester urethane urea) (PEUU), poly (carbonate urethane) urea

(PCUU), and poly (ester carbonate urethane) urea (PECUU) [119-122]. PU is often used due to its durable elastic mechanical properties and biocompatibility [123]. The wide variety of types of PU attracts attention for its cardiovascular applications. Varying types of PU allow for highly tailored chemical and physical properties. Like other synthetic polymers, poor hydrophilicity and lack of natural binding sites for cells are drawbacks. Studies aimed at overcoming its follies have been done. PU and silk fibroin blends were fabricated, and results indicated improved gene expression in maturing cardiomyocytes while maintaining good mechanical properties [124]. D'Amore et al. investigated a bi-layered PU scaffold with an ECM hydrogel [125]. The bi-layered scaffold exhibited thicker ventricle walls in the defect area compared to pure PU and sham treatments. Treated groups had lower end-systolic and end-diastolic areas than the untreated groups. Porous scaffolds composed of PU and PCL were investigated by Asadpour et al. and showed improvements in metabolic activity of the CMs compared to control scaffolds [126]. The PU-PCL scaffold upregulated α-actinin, cTnT, Cx-43, and cytoplasm distribution of Gata4 compared to the control group [126]. Hashizume et al. investigate the variety of types of PU, varying in degradation rates [127]. The PECUU treated group, with the longest degradation time, had significantly better cardiac output. Elastin content in the defect site was measured, showing increased elastin in the PECUU scaffold, improving the elasticity of the infarcted heart. Left ventricle wall thickness was improved across all PU scaffolds compared to the sham treatment. Functionalization of PU scaffold surface with laminin-1 was investigated [128]. Implanted scaffolds exhibited improved infiltration by host cells. No signs of an inflammatory response to implantation were noticed either. Tao et al. implanted their PU reinforced fibrin scaffold into rat models to explore ventricle replacement [129]. Vascularization of the implanted scaffold was measured with α-smooth muscle actin (α-SMA) with both cell laden and acellular implants exhibiting no significant difference in expression of α-SMA, with a significant increase in capillary presence with the expression of vWF in the cell laden implant [129]. Inflammatory response of leukocyte infiltration due to implantation of the scaffold was significantly decreased in the pre-vascularized scaffolds compared to the acellular scaffold group, with a significant increase in M2 macrophage infiltration in the cell-laden scaffolds [129]. Vascularization of the implanted scaffold has shown improved integration with host tissues through paracrine signaling of angiogenesis, preventing apoptosis of cardiomyocytes from preserving their contractile strength [129]. Improvements to PU's cell adhesiveness were explored by Carson et al. by functionalizing PU with RGD peptides and how nano-topography affected cellular behavior [130]. Scaffolds treated with RGD exhibited similar cellular adhesion as those treated with fibronectin, and scaffolds with grooves at 800 nm spacing exhibited the highest cell area coverage [130]. The ECM produced by cultured cells on the 800 nm spacing exhibited mature markers compared to other patterned scaffolds [130]. Improvements in PU's conductivity have also been investigated, a blend of PU and graphene was made, and results indicated vastly improved conductivity of doped scaffolds compared to pure PU [131]. Ganji et al. improved conductivity with gold nanotube/ nanowires [132, 133]. The porous scaffolds were made via salt leeching upregulated ANF, Nkx2.5, Mef2c, and NPPB expression of the CMs [132, 133]. The CMs were subjected to electrical stimulation, improving the organization of the seeded cells to align with the direction of the current [133]. Baheiraei et al. investigated PU/siloxane as a conductive medium for CM growth [134]. PU/siloxane scaffolds upregulated Cx-43, cTnT, and SERCA of CMs compared to tissue culture plastic (TCP) cultures [134]. Cell clusters on scaffolds were able to communicate with other clusters utilizing the conductive medium of the scaffold, allowing for improved cell-to-cell communication [134]. The development of stimuli-responsive PU has seen application as a cardiac scaffold. Yao et al. synthesized a reactive oxygen species (ROS)-sensitive PU for drug release in the infarcted tissue [135]. ROS responsive scaffolds exhibited improved vascularization in the scaffold and enhanced cardiac function compared to the no-treatment group. LV remodeling was limited in the scaffold treated groups compared to no treatment, with a decreased presence of fibrotic tissue. Ahmadi et al. explored a polymeric blend of PU/Chitosan and carbon nanotubes, investigating the effects of incorporating both natural polymers and conductive doping agents to cardiac scaffolds [136]. The seeded CMs exhibited further improved proliferation on the conductively doped scaffolds compared to the PU/Chitosan scaffolds, lending evidence that electrically conductive environments improve CM growth [136]. Consistently literature has shown that amalgamations of natural and synthetic polymers have enhanced the therapeutic effects of scaffolds on limiting ventricular remodeling post-ischemic heart injuries.

1.4.5 Polyethylene glycol

Another investigated polymer for cardiac tissue engineering is polyethylene glycol (PEG) [137]. It is desirable for research due to its nontoxic, non-immunogenic, and non-antigenic properties and its FDA approval [137, 138]. Often PEG was investigated as coatings aimed at modulating surface properties of materials; expanding upon this, and it is now used to help modulate cell interactions with the surface of scaffolds [137, 139]. Kim et al. investigated nanostructured PEG-dimethacrylate (DMA) hydrogel coated with collagen as a medium to culture functional 3D cardiomyocytes that can be removed and used as implanted cell sheets [89]. The cardiomyocytes on the patterned substrate exhibited improved functionality with increased beating speeds compared to cells grown on flat plates [89]. The patterned cultured CMs action potential threshold was decreased, leading to more robust beating properties [89]. Contractile forces on the patterned substrates were weaker than the flat controls due to the weaker cell binding [89]. Utilizing PEG's ability to functionalize materials, a PEG-fibrinogen hydrogel was investigated by Kerscher et al. [140]. The inclusion of PEG into fibrinogen hydrogels modulated the degradation rate and developed an environment that promotes migration into the structure; the fabrication method allowed for the direct encapsulation of hiPSC-CM into their scaffold for unformal distribution [140, 141]. The 3D culture environment created by the hydrogel could form spontaneous uniform contractions by upregulating peripheral Cx-43 expression of seeded cells [141]. Similarly, early cardiac cell markers like β-MHC and cTnT were upregulated in the PEG-fibrinogen scaffolds, forming mature structured sarcomeres [141]. Laura R. Geuss et al. also investigated PEG-fibrinogen hydrogels with HL-1 cells to examine how cardiac function was impacted by the scaffolding [142]. The study compared 2D and 3D culturing and explored how layering 2D cultures affected functionality. Studies indicated improved maturity of cell behavior in scaffolds that were mechanically compliant, with 2D cultures having the best contractile profiles [142]. The 3D culture exhibited less functionality than 2D cultures due to cell aggregation and poor structural hierarchy; with stacked 2D cultures, a 3D culture could be made without any impact on contractile functionality [142]. Another approach to hybridization with PEG is poly (lactic acid) (PLA)-PEG-collagen fibrous scaffold produced by Cesur et al. [143]. Fibrous scaffolds were nanofibrous to the near nanofibrous range to organize the seeded cells for consistent contractions [143]. High levels of PEG in the scaffolds negatively impacted cell viability, with the majority of effects on cardiomyocyte behavior impacted by collagen content [143]. The change in mechanics of the scaffold for more elastic and compliant parameters led to improvements to cellular maturity [143]. Research focused on conductivity improvements, like with other polymers, and has been investigated with PEG. Basara et al. 3D printed $Ti_3C_2T_x$ MXene-PEG hydrogel, and the inclusion of $Ti_3C_2T_x$ MXene into PEG based hydrogel improved the maturity of cultured hiPSCs [144]. Cells cultured on patterned conductive scaffolds upregulated cardiac markers such as myosin-7 (MYH7), troponin T2 (TNNT2), and Cx-43 compared to control scaffolds [144]. Upregulation of Cx-43 indicates the formation of gap junctions in the scaffold correlating to the mature beating pattern expressed by the conductive scaffolds [144]. Dobner et al. explored a PEG hydrogel in a rat animal model to examine the in vivo effects a non-biodegradable scaffold had on remodeling of the heart post MI [145]. Treatment with PEG hydrogel delayed LV in the animal model initially with remodeling occurring 3 months after induction of MI and treatment [145]. Animals treated with PEG maintained a thicker ventricle wall for four weeks before thinning occurred [145]. The suspected cause for delayed adverse remodeling is due to the delayed buildup of stresses on the cardiomyocytes in the border zone of the PEG scaffold [145]. Literatures continuously show beneficial effects of CM behaviors with scaffolds that were hybridized or blended with bioactive or conductive materials. These results re-enforce the boon of hybridization of natural and synthetic polymers.

1.4.6 Decellularized Extracellular Matrix

Examining cardiomyocytes' growth and development displays the importance of physiological, biological, and electrical cues to arrive at mature functioning tissues. The existing ECM in the heart provides the proper biological and physiological cues, leading researchers to explore the incorporation of native ECM into cardiac scaffolds. Some studies have focused on basing their scaffolds on decellularized slices of cardiac ECM or through digestion of cardiac ECM to form hydrogels. An ECM-chitosan construct was investigated by Pourfarhangi et al. [146]. Human cardiac progenitor cells (hCPCs) exhibited improved proliferation on ECM-containing scaffolds compared to the control [146]. Cell growth was shown to be impacted by the mechanical characteristics of the scaffolding, with more robust scaffolds having improved growth [146]. Pok et al. investigated an earlier iteration of an ECM-chitosan hydrogel as a basis for a full-thickness heart scaffold [147]. ECM-containing scaffolds significantly increased the attachment of seeded cells compared to pure gelatin scaffolds, and important cardiac proteins myosin-6 (MYH6) and Cx-43 were significantly upregulated [147]. Upregulation of Cx-43 led to ECM-containing scaffolds exhibiting higher conduction velocities and contractile stresses, indicating the maturity of seeded cells [147]. Another approach with decellularized ECM has been using it directly as a scaffold; one such study from Wang et al. investigated seeding bone marrow mononuclear cells on a slice of decellularized porcine myocardium [75]. Cardiac markers such as α-actinin, MHC, and cTnT were upregulated by the cells after seeding the scaffold. Cells were also shown to have penetrated deep into the scaffold [75]. Interestingly, scaffolds also indicated vessel formation throughout the study, with vessel-like structures seen throughout the scaffold [75]. Investigations of decellularized porcine ECM have progressed to animal studies to assess in vivo efficacy of such scaffolds [148]. Shah et al. implanted their decellularized porcine ECM into rat MI models over 4 weeks to assess impacts on cardiac function [148]. The originally non-populated scaffolds exhibited high host cell infiltration over 4 weeks, forming new vessels into the scaffold [148]. Sundaramurthy et al. investigated a catheter-deliverable ECM hydrogel in rat models [149]. Rat groups treated with the ECM hydrogel exhibited increased CM islands in the infarcted area and improved LV function. [149]. These promising results led the same group to investigate a porcine model. Seif-Naraghi et al. implemented the injectable ECM hydrogel in a porcine MI model examining heart functionality, building upon their rat model results [150]. Treatment with injected ECM hydrogel exhibited an improved significant increase in vascularization into the infarcted area and a significant increase in cardiac muscle area three months after treatment [150]. The echocardiographic global wall motion index measured the functionality of infarcted hearts, typically used as an indicator of mortality post-acute myocardial infarction; with a significant increase in hydrogel-treated pigs, the best indicator of heart repair was the average decrease in end-systolic volume [150]. Testing of vascularizing whole hearts has also been attempted in a few studies [151, 152].

Carvalho et al. used iPSC to vascularize a whole rat heart with some notable success [151]. The seeded cells exhibited an upregulation of cardiac marker genes compared to the cells seeded on Matrigel, along with improvements in cell proliferation [151]. A loss of pluripotency on the seeded cells is indicated to promote desired differentiation and reduce the chance of teratoma formation [151]. Guyette et al. similarly explored whole heart revascularization using human hearts [152]. Initial results examining populating strips of myocardium yielded promising results with hiPSCs, with constructs spontaneously beating within 4 to 7 days of culturing and upregulation of typical cardiac gene markers [152]. The construct could be reasonably paced with 1 Hz or 2 Hz, with immunofluorescent staining revealing well organized striated sarcomeres [152]. Whole heart revascularization was carried out in a custom whole heart bioreactor, providing perfusion and mechanical stimulation simultaneously; metabolic measurements taken during the study revealed ongoing metabolic activity, with a decreased presence of glucose and an increase in lactate formation [152]. Contractions were measurable across the whole heart, detected by the depolarization that occurred throughout the heart [152]. A clinical study of MI patients treated with an injectable ECM hydrogel has been carried out by Christman's group [153]. In this study, determining efficacy was not the focus, with Traverse et al. noting no adverse responses to injection of hydrogel [153]. The only examination of efficacy was noted by the 6 minute walk test, noting the hydrogel treated group exhibited significantly longer distances 3 and 6 months after operation compared to the control [153]. Overall, the current ongoing experimentations with decellularized native ECM indicate a distinct boon from the incorporation of such materials into cardiac scaffolds. These results drive the need to further explore ECM incorporation into future scaffold development.

1.4.7 Other Biomaterials

While many more blends of materials deserve their dedicated section, it is nearly impossible to encompass all studies in detail. As such, this section aims to glance at various researched material blends to detail further the benefits of hybridization and doping that were explored for cardiac tissue repair. Kerscher et al. explored a gelatin methacryloyl hydrogel for cardiac tissue engineering by directly capturing hiPSC-derived CM [154]. Captured cells upregulated various cardiac gene markers such as Cx-43, cTnT, and β-MHC; this led to improved contraction patterns through the scaffold [154]. Captured cells underwent morphological changes over the culture period, producing elongated actin filaments and larger nuclei, which were expected trends as the hiPSC differentiated into cardiomyocytes [154]. Extrinsic stimulation of cell-laden scaffold affected beating patterns similarly across all tested scaffolds, indicating a well-interconnected tissue formation with reliable cell-to-cell communication throughout the scaffold. Two other groups exploring gelatin-based scaffolds doped their gelatin scaffolds with GO or rGO to improve the mechanics and conductivity of scaffolds for improved beating patterns of seeded CM [155, 156]. Zhang et al. fabricated GO-doped gelatin hydrogels on patterned surfaces to produce scaffolds organizing seeded cells into a unidirectional arrangement [155]. Gel-GO patterned scaffolds exhibited upregulated expression of cTnT and Cx-43 compared to other scaffolds; improvements in α-actinin and sarcomere striation were most notable in the patterned Gel-GO scaffolds [155]. The beating velocity of contracting scaffolds was highest in the patterned Gel-GO scaffold indicating the alignment and improved conductivity from GO doping positively impacted tissue functionality [155]. Fibrinogen is another commonly explored biomaterial in cardiac scaffold literature [157]. Fibrinogen is a blood-borne glycoprotein that plays a vital role in the blood clotting process; fibrinogen is enzymatically cleaved by thrombin and converted to fibrin, with its high compatibility and biodegradability are what have motivated exploration as a biomaterial [158]. P. Balasubramanian et al. made a fibrinogen/gelatin (fib/gel) nanofiber scaffold via electrospinning to explore its viability as a biomaterial for myocardial regeneration [157]. The mechanics of various scaffolds fib/gel (2:3), fib/gel (1:4), and pure fibrinogen indicated increased failure stresses and strains in the fib/gel (1:4) scaffold. Scaffolds composed of fib/gel (1:4) also exhibited the best cardiac marker expression of α-actinin and cTnI compared to the pure fibrinogen samples. Indicating the mechanics' effects on influencing cardiomyocyte behavior [157]. Cell proliferation on scaffolds revealed a significant increase in growth on fib/gel (1:4) compared to the pure fibrinogen scaffold, indicating that gelatin played a part in cell adhesion and growth [157]. Silk fibroin (SF) has also been investigated as a scaffolding material [159, 160]. SF is most known for its use in the textile industry as silk, dating back thousands of years. More recently, its use has expanded past textiles into biomaterial research due to its availability, biocompatibility, and mechanics [161]. Yang et al. produced an SF-HA scaffold composed of compressed spray dried beads and seeded with rat mesenchymal stem cells (rMSCs) with CD44 surface markers to see if cardiac marker expression of cells could be achieved [160]. The positively stained CD44 was associated with improved cardiac expression, with CD44 blockage treatment significantly decreasing the amount of cardiac differentiation occurring [160]. The SF-HA scaffolds exhibited statistically upregulated Tnnt2, Nkx2.5, and Actc1 expression compared to pure SF scaffolds when induced with 5-aza [160]. The results continue to suggest that biomaterial blending is beneficial in most cases and the importance of cell membrane interactions on proper differentiation and growth [160]. A more complex SF scaffolding blend was fabricated via electrospinning [159]. The scaffold was composed of SF/PLA fibrous base loaded with carbon quantum dots (CQDs); the CQD-loaded scaffolds improved CM elongation compared to the control and improved Cx-43 presence seen on staining [159]. Improved maturity of developing CMs was noted through improved calcium management, which was further validated by ATPa2a expression [159]. As shown throughout the literature, advancements in biomaterials have consistently led to improved CM development and functionality.

1.5 Knowledge Gap on Cardiac Tissue-Focused Biomaterials and Rationale for Dissertation Research

Biomaterials are one of the critical components in the creation of tissue engineering scaffolds. The vast number of materials to choose and mix between leaves a near-infinite number of possibilities of potential biomaterials to explore. Tailoring a biomaterial toward myocardium regeneration has various mechanical and biochemical requirements. Biodegradable polyurethane (PU) is a synthetic polymer with a history in cardiac tissue engineering research [162-164]. PU is investigated mainly as a possible biomaterial due to its elastic and sturdy mechanical properties. The heart, a soft tissue, exhibits viscoelastic properties; viscoelasticity refers to the material property that has both viscous and elastic behavior in response to mechanical loading [165]. The extracellular matrix structure allows for elongation of the tissue with little to no deformity, enabling the heart to resist fatigue from cyclic stretching [166]. The continuous beating the heart undergoes applies constant cyclic extension to the ECM. If the biomaterial used in cardiac scaffolds were not elastic, scaffolds would be prone to deformation and failure caused by contractions. Stiff material cannot respond to changing pressures failing to provide proper support. Similarly, high pressure is exhibited in the heart due to the pumping of blood [166]. Scaffolding made of biomaterials incapable of withstanding high pressures is inadequate for structural support. An effective biomaterial needs physical similarities.

An essential aspect of biomaterials for tissue engineering is the interactions between seeded cells and the scaffold materials used. In the previous sections, a detailed examination of various commonly used biomaterials was undertaken; these results and more were condensed into **Table 1.1** to evaluate CMs behavior in response to the variety of biomaterials used as scaffolding. Synthetic polymers often lack critical binding sites for various cell types, with an emphasis on CMs, leading to poor performance of the materials. Adding bioactive components into synthetic polymers has improved cell growth and differentiation [128, 167]. As discussed in the previous sections and **Table 1.1**, the inclusion of bioactive components positively influenced CM growth and maturity. Scaffolds incorporating some natural polymer exhibited upregulation of early CM markers such as cTnT, cTnI, α-actinin, and Cx-43 [97, 104, 168-170].

Incorporating elements found in the native ECM in scaffolds allows cells to grow in an environment closer in biological and physiological nature like the native ECM. The ECM in cardiac tissue comprises a lattice-like network of structural proteins and biomolecules encompassed by a glycosaminoglycan (GAG) and proteoglycans gel [171]. Extensively in literature, results of hybridized scaffolds strongly suggest improvements to cell adhesion and proliferation compared to purely synthetic polymeric scaffolds [97, 104, 168-170]. The natural polymers have binding spots that CMs can bind to, whereas synthetic polymers lack binding sites [97, 104, 168-170]. Natively, cardiomyocytes interact with the surrounding collagen network via integrins [171]. Integrins are signal mechano-transducers that receive physiological cues to control cell growth and differentiation [15]. While the exact mechanism of how integrating natural polymers into scaffolds improves CM differentiation, it can be reasoned that the cell's interaction with the myriad of structural proteins exhibits different signals on integrins [15]. Integrating these myriads of proteins and GAGs into a scaffold provides an extensive range of differentiation cues. Various studies working with PU have integrated components like collagen or, in one case, incorporated a bilayer of digested ECM. The literature on incorporating natural polymers into scaffolds provides clear evidence of the beneficial effects. However, these studies fail to address issues such as fostering a conductive environment for cell signaling [125, 172]. The electrical aspect needs to be incorporated into the developed scaffolds to mimic the natural environment of the heart.

Table 1.1: List of investigated biomaterials and their effects on cardiomyocyte behavior

Fabrication	Scaffold Morphology	Material Composition	Cell Line	Observed Response	Functional Result	Reference
Aligned ES	Fibrous; Fiber Diameter: 420 ± 370 nm; Fiber Spacing: 120 ± 70 nm	PCL	Neonatal and Adult Rat CM	NRCM: Elongated parallel to fibers, Sarcomas perpendicular to fibers, exhibited larger aspect ratio; ARCM: aligned perpendicular to fibers, sarcomas were parallel to fibers, preserved aspect ratio	Alignment improved organization of striation, reduced cell shortening	[88]
Random Coaxial ES	Fibrous; Fiber Diameter: 2.39 ± 0.66 µm; Porosity: 82.5 ± 6.2%	PCL core, Gel shell	hiPSC-CM	2D Culture: upregulation of SIRPA and ISL-1↑, MHC6, and TNNT2 ↑↑; 3D Culture: SIRPA and ISL-1 ↑↑, MHC6 and TNNT2 ↑	Spontaneous macroscopic contractions in both 2D and 3D cultures Improved Cardiac Progenitor associated gene expression in 3D compared to 2D, 3D culture closer mimics in vivo mechanisms	[168]
Random and Aligned ES	Fibrous; Aligned: Fiber Diameter: 269 ± 33 nm; Random: 236 ± 37 nm	PCL/Gel blend; 50:50 Blend	Rabbit Primary CM	The gel-containing fibers had improved CM growth and attachment, CM's organized, aligned fiber direction, better alignment in PCL/Gel than PCL fibers, alpha-ACT and TP-T were directionally organized on aligned fibers, and Greater Cell spread on PCL/Gel compared to PCL scaffolds	Aligned: Striated and organized sarcoma formation, better expression of striation in PCL/Gel Blends compared to PCL fibers	[89]
Melt-based Electro-hydrodynamic 3D Printing	Grid Patterned; Filament Width: 18.4 ± 3.4 µm; Filament Height: 396 ± 8.3 µm	PCL/MWCNT	Rat CM, H9C2	No significant difference in proliferation between PCL and PCL/MWCNT scaffold	Short term study with PCL/MWCNT exhibited no significant adverse effects of MWCNT on cell growth	[173]
Melt-based Electro-hydrodynamic 3D Printing	Micro-lattice; Layer Height: 200-800 µm	PCL/Collagen	Rat primary CM, H9C2	CMs could align themselves in a collagen matrix, Upregulated α-actinin, and Cx-43; each layer can be independently aligned in different directions, Exhibiting a mature CM phenotype.	CMs exhibited synchronized beating on each layer; Consistent ~120Bpm was exhibited throughout the 8-day culture	[169]
Random ES	Fibrous; Fiber Diameter: <300 nm	PCL/GEL/PAni ; 50:50 Blend, 1% wt PAni	Rat HL-1	Cardiomyocyte proliferation increased with increased Gel concentration, PAni doping exhibited improved proliferation at a high level of Gel concentration, and Improved cell spread in PAni containing scaffolds with clustering around PAni NP	Cell clustering around PAni for successful beat propagation, non-significant stress factor release from higher gel composition.	[90]
Aligned ES	Fibrous; Fiber Diameter: < 200 nm	PLGA/PAni	Rat Neonatal CM	Upregulation of Cx-43 and cTnI, Increased protein absorption of positively charged scaffold surface, and Improved cell adhesion with electrical doping of scaffold.	Synchronized cell beating in the high-conductivity scaffold, organized cell orientation and beating due to aligned fibers and elongated cells.	[104]
Random ES	Fibrous; Fiber Diameter: < 1000 nm	PLGA/PRP	hiPSC-CM	Upregulation of Gata4 and troponin-T in PLGA/PRP scaffolds, upregulation of MLCA2, ANF, and MLC2V, and alpha-tubulin increased on PLGA/PRP compared to PLGA scaffold	PRP acted as a growth factor release for improved cardiomyocyte growth and proliferation	[170]
Film Casting	Grooved Film; Width x ridge width x groove depth: 15 x 5 x 6 um	PLGA	hESC-VCM	Upregulation of Cardiac troponin-T in PLGA grooves, F-actin expression and ECM production parallel to grooves, wide dispersion of Cx-43 expression	Synchronized cell beating and grooved scaffolds had a more stable and reliable response to premature electrical stimulation.	[97]
Aligned and Random ES	Fibrous; Fiber diameter: 500-800 nm	PLGA-RGD/YIGSR	Rat Primary Cardiomyocytes	α-actinin and f actin striation on Laminin coated, and PLGA-YIGSR functionalized scaffolds, Cells grew elongated and parallel on the aligned scaffold, Positive Yellow N-cadherin found on laminin-coated and PLGA-YIGSR scaffolds, ANF, β-tubulin, and α-MHC upregulated on PLGA-YIGSR scaffold	Synchronized beating in all functionalized PLGA scaffolds, a higher degree of synchronized beating in aligned scaffolding, and long-term consistent beating speed in laminin-coated and PLGA-YIGSR scaffolds compared to other scaffolds after 2 weeks.	[99]

Random ES	Fibrous; Fiber Diameter: 300 - 800 nm	PLGA/Collagen	Mouse ESC	Striated Pattern of α-actinin more visible on PLGA/Col scaffold than PLGA scaffold, Expression of Cx-43 upregulated on PLGA/Col compared to PLGA and TCP, Spindle like CM morphology present in PLGA and PLGA/Col scaffolds.	The beating of CM cultured on PLGA/Col scaffolds, differentiation into cardiomyocytes from embryonic stem cells.	[101]
Film Casting	Grooved Film; Groove/Ridge: 50/50 um and 50/100 µm	PGS/AT	Rat CM, H9C2	PGS-AT scaffolds exhibited improved proliferation, Upregulation of α-actinin and Cx-43 on PGS-AT scaffolds, Well-formed cross-striated sarcomeric structure, highly organized cell structure on 50/50 um groove/ridge scaffold, Synchronized calcium transients on PGS-AT scaffold.	Improved synchronized beating and more vigorous beating of CM on PGS-AT scaffold (Higher levels of intercellular Calcium), Improved maturity of CM grown on PGS-AT scaffolds compared to PGS scaffolds.	[117]
Random Coaxial ES	Fibrous; Fiber Diameter: ~1000 nm	PGS/Fibrinogen Core/Shell	Rat Neonatal CM	Striation bands of actinin and phalloidin on PGS/Fibrinogen scaffolds, expression of the β-myosin heavy chain, improved expression of α-actinin, Troponin- T, and Cx-43 in PGS/Fibrinogen scaffold compared to TCP.	Improved cell dispersity on the scaffold with PGS/Fibrinogen compared to Fibrinogen, Increased pore size from core-shell fabrication allowed for further penetration of CM, and Increased functional activity (gap junction formation) on PGS/Fibrinogen scaffold.	[113]
Aligned ES	Fibrous; Fiber Diameter: < 400 nm	PGS/Gelatin	Rat CM and CF	Cytoskeletal was more organized and developed in aligned fibers, thinner stress fiber formation in higher elasticity scaffolds, the sarcomeric organization in aligned fibers, homogenous distribution of gap junctions, and upregulation of Troponin I.	More synchronized beating on the aligned scaffold, a higher rate of beating on the PGS:2Gelatin scaffold compared to all other scaffolds, and more elastic scaffolds exhibited more synchronized beating.	[112]
Random ES	Fibrous; Fiber Diameter: < 500 nm	PCL/PGS/Graphene	Human CM	Improved cell compatibility with graphene incorporation, increased cell viability with increased hydrophilicity of PGS inclusion.	Cell proliferation increased with an increase in relative conductivity and improved cell adhesion due to hydrophilicity.	[118]
3D Printing	Grid Pattern; Filament Diameter: 350 µm, Porosity: 56-60%	PGS/PCL	Rat CM, H9C2	The slightly higher proliferation of CM in PGS/PCL scaffold compared to pure PGS or PCL scaffolds, upregulation of alpha-smooth muscle actin, upregulation of vascular formation in the PGS/PCL group, decrease in the rate of apoptosis of cells in PGS/PCL scaffold.	Implanted PGS/PCL scaffold improved LV ejection fraction and decreased in the infarcted area.	[174]
Random Patterned ES	Fibrous Grooves; Groove Spacing: 200 µm, Groove Depth: 10 µm	PGS/PCL	Rat Neonatal CM	Upregulation of Cx-43 in evenly spaced grooved scaffolds compared to control improved sarcomeric striation in evenly spaced groove scaffolds.	It improved cell-to-cell communication with a structured scaffold and synchronized beating due to improved cell-to-cell communication.	[82]
Random Coaxial ES	Fibrous; Fiber Diameter: < 1200 nm	PGS/Collagen Core/Shell	Human MSC and Cardiac Cells; 1:1 seeding ratio	Increase in proliferation and adhesion of cells on scaffolds compared to TCP and pure collagen scaffolds, Upregulation of α-actinin and cTnT in co-culture and on PGS/Collagen scaffold, Enhanced cell penetration into scaffold on PGS/Collagen.	MSCs and cardiac co-culture increased cardiogenic marker expression, Increased cell fusion and cell-to-cell interaction, and MSC production of cytokines for anti-inflammatory, anti-apoptotic, and upregulation of myoangiogenic differentiation.	[109]

Random and Aligned ES/Electrospray	Fibrous; Fiber Diameter: < 200 nm	PU/Chitosan/CNT	Rat CM H9C2	Improved proliferation on scaffolds containing CNT, aligned scaffolds exhibited a higher degree of organization than random.	Anisotropic nature of scaffold improves cardiomyocyte organization; Conductive additive improves cell proliferation.	[136]
Salt Leeching Casting	Porous; Pore Size: > 90%	PU-GNT/NW	Rat CM H9C2	Cell alignment was significantly improved in GNT/NW scaffolds and upregulated ANF, Nkx2.5, Mef2c, and NPPB in PU-GNT/NW scaffolds.	Electrical stimulation of scaffolds aided in cellular alignment and decreased the progression of hypertrophy.	[133]
Film Casting/Gell formation	Thin Film/Hydrogel	XSi-PU	Rat CM, HL-1	Upregulation of Cx-43, Troponin-T, and SERCA in XSi-PU scaffolds compared to TCP, increase intracellular calcium concentration.	Improved cell communication between cell clusters does not alter the intrinsic electrical characteristics of cells and improves cell-to-cell communication in the fibrotic area.	[134]
Salt Leeching Casting	Porous; Porosity: 80-95%, Pore Size: 80-200 µm	PU-PCL	Rat CM, H9C2	Increase in metabolic activity on PU-PCL (1:1) scaffold, Significant increase in proliferation of H9C2 (Ki67 upregulated), Upregulation of alpha-actin, and more elongation of cells on PU-PCL scaffold, Upregulation and cytoplasm distribution of Gata4 in PU-PCL scaffold, and Upregulation of cTnI and Cx-43.	Indications of more mature cell development on PU-PCL scaffold compared to other blends, Cells exhibited gene expression that mimicked normal cells rather than hypertrophic, increased differentiation into a cardiomyocyte.	[126]
Random and Aligned ES	Fibrous; Fiber Diameter: < 400 nm	PU-rGO	Mice skeletal muscle satellite cells	Upregulation of Troponin-I in aligned PU-rGO scaffold, Cell more organized on aligned scaffolds.	The better expression of cardiac gene markers in aligned PU-rGO scaffold.	[175]
Mold UV Curing	Grooved; Groove Width: 350 – 2000 nm	PUABP-RGD	hiPSC-CM	Sarcomere lengths in 800 nm grooves are similar to mature sarcomere lengths, improved proliferation in 800 nm grooves, significantly improved cell organization in 800 nm grooves, and similar binding affinity to the fibronectin-coated scaffold.	Improved cell ECM maturity due to topographic features and quickened maturity of ECM improves viability as stem cell-based cardiac therapy.	[130]
Mold UV Curing	Nano-pillars; Height: 400 nm, bottom diameter: 150 nm, top diameter: 50 nm	PEG-DMA	Rat CM	Cells on the nanostructured scaffold grew in a 3D structure, while control and bare PEG had flat morphology, decreased bpm compared to control, increased cell proliferation compared to bare PEG, larger action potentials on the nanostructured scaffold	Improved cell morphology from 3D growth, improved contractile parameters on structured scaffold due to robust action potential, weaker beating compared to control due to weak adhesion to nanostructures.	[137]
Film Casting	Flat Film	PPy-PCL	Rat CM, HL-1	Expression of Cx-43 on peripheral cells in PPy-PCL scaffold compared to PCL scaffold, increase in calcium transient wave velocity in PPy-PCL scaffold, non-significant expression of Cx-43 in PPy-PCL compared to PCL scaffold.	Improved maturity of electrical propagation due to improved gap junction formation and decreased action potential time for improved contraction propagation.	[176]
Gelation	Hydrogel	PEG-Fibrinogen	hiPSC-CM	Encapsulation of hiPSC upregulated Cx-43 in 3D culture, and similar expression of β-MHC and cTnT, improved Cx-43 expression in cell peripheral, the 3D structure had similar calcium transient duration compared to 2D culture, 3D cultures developed align sarcomere structures over 30-day culture.	Development of highly matured cardiac tissue in 3D structure, development of mature ECM organization without electro-mechanical cues, improved cell contraction in cluster cell encapsulation compared to single cell encapsulation.	[140]
Gelation	Hydrogel	GelMA	hiPSC-CM	Encapsulated cells upregulated Cx-43, cTnT, and β-MHC over 70-day culture, upregulation of MLC2v on days 20 and 70, Cx-43 on peripheral of cells, increase of maximum relaxation velocity of contractions, development of highly organized and aligned sarcomeres.	Improved contraction strength, mature contractions with increased culture time, and slower contraction times compared to cultures with mechanical or electrical stimulation.	[155]

Patterned Gelation	Patterned Hydrogel; Groove spacing: 15 µm	Gelatin-GO	Rat CM	Upregulation of cTnT and Cx-43 in patterned Gel-GO scaffold, upregulation of α-actinin in non-patterned Gel-GO, increase in sarcomere length in patterned Gel-GO scaffold, improved striation of α-actinin in patterned Gel-GO scaffold at both 3 and 5 days of culture.	The beating velocity of the Gel-GO patterned scaffold was increased compared to other scaffolds, with synchronous beating in the patterned Gel-GO scaffold.	[155]
Random and Aligned ES	Fibrous; Fiber Diameter: 400-700 nm	PCL-Graphene	mESC-CM	Upregulation of MHC, Cx-43, cTnT, β-actin, mature sarcomere formation in the aligned scaffold, increased fractional release compared to 2D culture, and synchronous beating in PCL-Graphene scaffolds.	More mature cardiac tissue formation in aligned PCL-Graphene scaffold, improved calcium transient of aligned PCL-Graphene scaffolds.	[177]
3D Printing	Hydrogel; Straight line, Bowtie, and Hilbert's Curve	$Ti_3C_2T_x$ MXene-PEG	hiPSC-CM	Upregulation of MYH7, cTnT, and Cx-43 in MXene-containing scaffolds with mRNA expression quantification, Western blotting showed no significant difference, improved sarcomere length in patterned MXene scaffolds, and non-significant impact on cell viability compared to control.	Improved contractility and fiber alignment in MXene patterned scaffold, improved Ca^{2+} handling in MXene-containing scaffolds, prolonged decay duration in MXene patterned scaffold, and increased beating cell area percentage.	[144]
Gelation	Hydrogel	Fibrinogen-PEG	HL-1	A higher fibrinogen concentration decreased cell spread, cell viability unaffected by scaffold stiffness, and more compliant gels improved spontaneous contractions. 3D culture of cells had irregular and slower calcium perfusion.	Cells in 2D culture with the most compliant gel expressed the best contraction profiles, 3D culturing of cells impeded functionality and formed cell aggregates, and layered 2D cultures improved functionality compared to 3D culture.	[142]
Aligned and Random ES	Fibrous; Fiber Diameter: 750 – 1800 nm	PLA-PEG-Collagen	H9C2	Scaffolds containing collagen improved cell viability, high concentrations of PEG had cytotoxic effects, aligned scaffolds arranged cells into an organized orientation	Homogenous growth of cells on aligned scaffolds, alterations to CM proliferation, stiffness, and alignment affected by collagen.	[143]
Decellularization	Tissue slice	Decellularized Porcine Myocardium	None	Implanted scaffolds of de-cellular ECM scaffold increased wall thickness compared to control, formation of new vessels into defect area in scaffold treated animals, and increased M2 macrophages in the treated group.	Improved LV ejection fraction for treated groups compared to control and improved fractional shortening in treated groups compared to the control group.	[148]
Decellularization	Tissue slice	Decellularized Porcine Myocardium	Bone marrow mononuclear cells	Positive staining for α-actinin, MHC, and cTnT on the scaffold after seeding of cells, deep infiltration of seeded cells into the scaffold	Reseeded cells exhibited phenotypes like cardiomyocytes, formation of vessel-like structures in the scaffold over the study	[75]
Lyophilized	Porous scaffold; Pore size: 10-70 µm	Decellularized ECM-Chitosan	hCPCs	Increase in cell proliferation with increased ECM content, optimal cell growth in scaffolds with chitosan due to mechanics	Enhanced ability for cells to attach when ECM is included, mechanics of scaffold revealed to influence cell proliferation behavior	[146]
Gelation	Hydrogel	Decellularized ECM–Chitosan	Neonatal rat CM	Significant increase in attached cells on heart matrix scaffold compared to control, a significant increase in MYH6 and Cx-43 expression in heart matrix scaffold	Increased conduction velocity for heart matrix scaffold compared to gelatin, increase in contractile stress from cells in heart matrix scaffold compared to gelatin scaffold, improved cell maturity from ECM-based scaffold.	[147]

Decellularization	Tissue slice	Decellularized Rat Ventricle Wall	hiPSC-CM	Cells grown on ECM were capable of spontaneous beating after 5 days, presence of laminin, Cx-43, and cTnT expressed on seeded cells, seeding of nonmyocytes improved cardiac development and function, and upregulation of cTnT and MYH6 found in cells ceded on ECM compared to cell only aggregates, increase in MYH7/MYH6 and MYL2/MYL7 ratio indicating maturation of tissue.	Spontaneous contractions of scaffolds were comparable to regular heart activity. Constructs were responsive to drug treatments altering beating habits, significant improvements in LV ejection fraction and fractional shortening in scaffold-treated animals, decrease in infarct size with construct treatment.	[178]
Decellularization	Whole heart	Decellularized Rat Heart	iPSC	Reduction of seeded cell pluripotency indicated induced differentiation from ECM, upregulation of cardiac gene expression, and improved proliferation of seeded cells compared to control.	Decrease possibility of teratomas formation in vivo with a decrease in pluripotency, induction of cardiac differentiation with ECM components.	[151]
Decellularization	Tissue slices and Whole heart	Decellularized Human Heart	hiPSC-CM	Upregulation of MHC in myocardial seeded cells, improved proliferation of cells in scaffolds, capable of long-term culturing (120 days) with spontaneous contractions, the recellularized whole heart had detectable depolarization across the heart. The whole heart was metabolically active, and multicellular contractile tissue formed of myocardial slices.	The formation of spontaneous beating in both myocardium slices and whole indicated the formation of functional tissues. Cardiac fiber formation had significantly higher contractile force generation, an indication of mature CM formation due to the functional activity of constructs.	[152]
Gelation	Hydrogel	GelMa-rGO	Neonatal Rat CM	Scaffolds with 5 mg/ml rGO had higher DNA concentrations than other scaffolds on days 5 and 9, high sporadic beating rates in 5 mg/ml compared to control, more uniform distribution of cells in rGO containing scaffolds, evidence of Cx-43 expression on cell peripherals in rGO containing scaffolds.	rGO-containing scaffolds curled up in response to beating forces on one side, rGO-containing scaffolds contractions were visible to the naked eye, and only rGO-containing scaffolds responded to electrical stimulation.	[156]
Random ES	Fibrous; Fiber diameter: 130-300 nm	Gel-Fibrinogen	Human CM	An increased presence of α-actinin and cTnI, a significant increase in proliferation in Fib/Gel (1:4) compared to the control (TCP).	Improved hydrophilicity via the inclusion of gelatin improved cell proliferation. Cardiac gene expression indicates maturing cell cultures.	[157]
Random ES	Fibrous; Fiber Diameter: <1000 nm	Silk Fibroin-PLA-CQD	Rat CM, H9C2	Scaffolds with CQDs exhibited higher viability compared to the control, CQDs improved elongation and attachment of cells, a significant increase in Cx-43 gene expression from scaffolds with CQDs, increase in Tnnc1, Tnnc2, Anf, and Atpa2a.	Improved maturity of seeded cells phenotype, improved gap junction formation due to increase in Cx-43, improved calcium management with Atpa2a expression, and homogenous cell distribution throughout the construct.	[159]
Random and Aligned ES	Fibrous; Fiber Diameter: 225-290 nm	Calcium Silicate-Chitosan	Neonatal Rat CM	Inclusion of CS improved proliferation of cells by day 7, significant upregulation of TnnT2, Cacna1a, and Gja genes compared to control, upregulation of Cx-43 with CS containing scaffolds, elongated cells on aligned scaffolds.	Synchronous beating in aligned CS-containing scaffolds, multiple scaffolds of parallel rhythmic beating cells in CS-containing scaffolds, and in vivo experiments indicated improvements in FS, EF, LVIDd, and LVIDs for CM-laden CS-containing scaffolds, a significant decrease in infraction area when treated with the scaffold.	[179]
Spray Drying and Compression	Porous	Silk Fibroin-Hyaluronic acid	Rat MSC	SF-HA scaffolds upregulated cardio marker gene expression of Tnnt2, Nkx2.5, and Actc1, CD44 blockage decreased cardiac differentiation, increased cell growth in SF/HA scaffold, and increased fluorescent intensity of fibronectin.	Reliable differentiation of MSC into cardiac marker expressing cells indicates an improved beating profile with improved Cx-43 expression.	[160]

The heart muscle is electrically active, relying on a timed electrical pulse carried through a complex pathway to initiate contractions. Conductive scaffolds transmit these electrical signals more effectively [180]. They can deliver electromechanical and electrochemical cues that mediate cardiomyocyte growth and differentiation [181]. Electrical stimulation of cardiomyocytes has shown enhanced gene expression for cardiac markers, specifically Cx-43, emphasizing the importance of electrically active biomaterials [182, 183]. Cx-43 is the main protein for gap junction formation, upregulation of Cx-43 is associated with improved cell-to-cell signaling and mature CM development [144, 181, 183-185]. Scaffolds incorporating conductive additives or polymers were better at forming synchronous beating throughout the studies [134, 144, 183, 185]. Baheiraei et al. saw communication between distant cell clusters via electrical signaling through their conductive scaffold [134]. The improved cellular communication within the scaffold allows for better integration with host tissues due to increased communication between seeded cells and host cells [186, 187]. To fully mimic the native ECM, Kharaziha et al. conducted a study using PGS/gelatin and multi-walled carbon nanotubes, which enhanced uniformity of cardiomyocyte contractions, decreased excitation threshold, and increased Cx-43 expression in the peripheral cells [188]. Few studies attempted to incorporate bioactive and conductive elements into a synthetic polymeric scaffold [136, 188, 189]. Most studies that aimed to improve the conductivity of scaffolds do little to include bioactive components in their scaffolding [190-192]. An exploration of scaffolds incorporating a bioactive ingredient found in native ECM and a conductive element should be investigated to see if the two components further emphasize the therapeutic effects.

Our research addresses the critical gap in incorporating bioactive and electrically conductive components into a polymeric fibrous scaffold and their effects on cell behavior. Firstly, we explore the incorporation of digested decellularized ECM from the LV of an adult porcine heart to fabricate and optimize a scaffold that is elastic and mechanically supportive containing essential biomolecules found in the native tissue. Decellularized ECM includes many structural proteins with different biological cues on cardiomyocyte development [15]. Using this novel combination of digested ECM blended directly with our

PU, we assess the optimal scaffold composition that is physiologically like native tissue with improved cell maturity due to biochemical stimuli from the digested ECM. Most studies focus on incorporating only specific proteins found in ECM, mainly collagen, or a derivative, into their scaffolds. It was rarely reported to include diverse proteins from the native tissue [193, 194]. Incorporating the full spectrum of ECM proteins into polymeric scaffolds would reveal the effects native ECM has on cardiomyocyte behavior. Morphological and physiological comparisons between increasing ECM concentrations determine the effects of ECM on the properties of the scaffold and how it compares to the native tissue. Characterizing the effects of ECM on the fabrication of PU scaffolds allows for creating more complex biomaterial blends in the future.

Secondly, investigate the effects of varying concentrations of reduced graphene oxide (rGO) in the scaffold on its morphological and physiological effects and the response of cardiomyocytes. Graphene and its derivatives were popularly investigated as doping agents for TE targeting electrically active niches in the body [195-197]. Nervous system scaffolds have encouraged regeneration with conductive scaffolds compared to non-conductive scaffolding [195, 196]. The heart, an electrically dynamic organ, should benefit similarly. Nano-fibrous scaffolds containing rGO and thermoplastic polyurethane have been investigated at a low concentration of rGO (0.025% w/w) with cardiac muscle cells [175]. Conductivity characterizations were not reported; such characterization provides insight into material behavior [175]. Similarly, they examined one concentration of rGO, failing to optimize the biomaterial blend, lacking a systematic investigation of rGO and PU's effects on cardiomyocyte behavior. Investigation into concentrations of rGO and its impact on the morphological and physiological characteristics reveal the effectiveness as a potential new biomaterial blend. Optimization in rGO concentration quantifies the trade-off mechanically and conductively. Reduced graphene oxide's effect on cytotoxicity is essential in determining the potential benefits and harms to cardiomyocytes.

The most bioactive electrical scaffolds are collagen fibers with conductive doping agents [105-107]. Cardiac scaffolds that rely on conductive doping agents with purely synthetic polymers fail to mimic a proper supportive matrix [108]. Optimizing a polymeric scaffold blended with bioactive proteins and conductive doping agents can address the shortcomings of other bioactive conductive scaffolds. We propose combining the previous optimizations of ECM and rGO with PU to form a comprehensive cardiac scaffold. A conductive, biocompatible, biodegradable, elastic, and mechanically supportive cardiac scaffold is generated and characterized *in vitro*. Morphological characterizations via scanning electron microscope (SEM) with uniaxial and biaxial testing quantify the differences compared to native tissue, while cell studies evaluate the effects the fabricated scaffolds have on cardiomyocytes. The growth and maturity of cardiomyocytes on this multifaceted scaffold indicate an amplifying effect of having an electro/bioactive scaffold more than a strictly bioactive or electroactive environment.

Following the previous background, the notable gaps in knowledge, and the variety of rationales, we investigate these three aims.

AIM 1: Fabricate and optimize a hybrid biodegradable polyurethane and extracellular matrix blended biomaterial for cardiomyocyte culture.

We characterized and optimized a hybrid biodegradable polyurethane/ECM scaffold and investigated its potential as a scaffold for cardiomyocyte culturing. We blended PU with digested decellularized ECM collected from the myocardium of adult pigs' left ventricle at varying concentrations before electrospinning aligned nanofibrous scaffolds. We hypothesized that combining complete ECM with PU would create a scaffold containing the various biomolecules. The exact composition of natural polymers that are physiologically and biologically relevant to the native tissue is re-enforced by an elastic biodegradable synthetic polymer, providing an optimal environment for cardiomyocyte culturing. Natively relevant biomolecules aid in cardiomyocyte signaling and offer binding sites for cells to attach. The surface morphology was characterized to see how hybridization could alter the scaffolds. Hydrophilicity measurements show how ECM content changes the physical characteristics of the scaffold compared to a purely synthetic scaffold. Cell viability and immunofluorescence staining were used to determine the effects of polymer hybridization on cell behavior and growth.

AIM 2: Optimization and characterization of a biodegradable polyurethane and reduced graphene oxide blended scaffold for skeletal muscle cell and cardiomyocyte growth

We hypothesized that the doping of PU with rGO would create a conductive scaffold with robust mechanical characteristics ideal for cardiac applications. In this aim, we optimized reduced graphene oxide doped polyurethane, using ultra-sonication for dispersion, and investigated its potential as a scaffold for culturing electrically active cells. The rGO doped scaffolds were fabricated using an aligned electrospinning technique with a custom-built rotating mandrel. The scaffolds of varying rGO concentrations had their morphological, chemical, electrical, and mechanical properties characterized and compared to the left ventricle myocardium of a porcine heart. Cytocompatibility of scaffolds was investigated with muscle cells. The protein expression was characterized with immunofluorescent staining to see how the scaffold affects differentiation. Studies were repeated with neonatal rat cardiomyocytes to evaluate the effects of scaffolds on cardiac cell protein expression of viability.

AIM 3: Developing a nanofibrous conductive bioactive polyurethane scaffold for cardiomyocyte growth.

We combine what was learned from prior aims to fabricate a conductive hybrid polymer consisting of biodegradable polyurethane, digested decellularized ECM, and reduced graphene oxide—taking from the optimized parameters found in the previous chapters. A scaffold that is highly tailored towards myocardium growth should be obtained. We characterized the new doped hybrid scaffold and compared it to the previous scaffold composition. The morphological, chemical, conductive, mechanical properties, and cytocompatibility changes were determined. Furthermore, we investigate the protein expression of seeded cardiomyocytes to observe how the novel scaffold affected cardiomyocyte behavior.

CHAPTER II: Electrospun Elastic Polyurethane/Extracellular Matrix Nanofiber Scaffold for Cardiomyocyte Culture

2.1 Introduction

Around the world and in the United States cardiovascular diseases (CVD) are the main cause of death, responsible for 1 in 4 deaths [198]. Following a myocardial infarction (MI), the victim experiences mass muscle cell death causing left ventricular (LV) remodeling and functionality loss due to the inability to regenerate cardiomyocytes effectively [199]. Treatment options for MI and heart failure are limited to only saving residual cardiomyocytes and do not address fibrosis during LV remodeling. Tissue engineering (TE) aims to overcome the regenerative barriers of cardiomyocytes through scaffolding that encourages cell retention and differentiation. Scaffold materials used in cardiac tissue engineering are biomimetic, provide an environment like the native extra-cellular matrix (ECM), and are biodegradable. Scaffolds that promote bio-signaling for cell migration and integration with host tissue are ideal. They also need to provide mechanical support with some elasticity to handle the physical demands of the heart to function and compensate for the loss in structural integrity due to MI.

Reviewing native ECM can provide insight into the mechanical and structural needs an effective scaffold must mimic [200]. Proteins in the ECM are highly aligned and structured to deliver specific mechanical stresses and signals for healthy myocardium cells to form [200, 201]. Cardiomyocytes grow along the aligned protein structure, with numerous binding points for the cells to latch on. Robust and efficient uniform contractions are a side effect of alignment. Electrospinning (ES) is a popular scaffold fabrication technique for cardiac tissue engineering applications. A micron to nano range network that mimics the native ECM structure can be formed from ES, offering a way to fabricate polymeric blends to tailor the scaffolding for its specific application. It is possible to manufacture fibrous scaffolds with a rotating mandrel target where the fibers are aligned uniformly. Fabrication of an aligned fibrous scaffold mimics this natural structure, guiding seeded cells to organize uniformly [202, 203]. The uniform dispersal of cells offers equal opportunities for cell binding, leading to one-directional contraction. The alignment of nanofibrous scaffolds has shown its effects on cardiomyocyte behavior [202, 203]. When seeded on aligned scaffolds, cardiomyocytes expressed higher cardiac muscle-specific protein markers than random ES scaffolds; however, more than just alignment is needed to fully mature cardiomyocytes [202-204]. The material used for scaffold production plays an equally important role.

There are multiple available biomaterials used as scaffolding in cardiac tissue repair applications. Ranging from natural polymers, like gelatin [98, 205, 206], collagen [185, 207, 208], and fibrinogen [124, 209] to synthetic polymers like polyurethane (PU) [133, 210-214], polycaprolactone (PCL) [87, 92, 215, 216], polyglycerol sebacate (PGS) [217-220], and poly(lactic-co-glycolic acid) (PLGA) [98, 221, 222]. PU is a major category of applied elastomers in cardiac tissue engineering because of its biodegradability, biocompatibility, and elastic mechanical properties [223]. Elasticity is an important property originating from soft tissue solid matter and is one of the key considerations in scaffold design and development. Some groups focus on blending PU with a natural polymer and additives to tailor the scaffolds characteristics more towards cardiac tissue engineering [212]. Blending PU with cellulose enabled the creation of ultrathin-aligned fiber scaffolds that were mechanically supportive and adjusted to the deformation of contractions [212]. Zahra et al. focused on improving the conductivity of PU via blending with carbon nanotubes to see its effects on scaffold fabrication and cell behavior [213]. Including carbon nanotubes at minimal concentrations impacted the fiber size and the mechanical characteristics. The highest concentration decreased the elasticity and mechanical strength [213]. Hybridized PU and natural polymer scaffolds enable improved cellular compatibility with the natural polymers while also providing good structural support due to PU.

Decellularized myocardium ECM as a scaffolding material offers a scaffold with near identical polymeric composition and morphology to native ECM [125, 148]. Various biochemical components in the ECM aid in bio-signaling for cell migration and differentiation [148, 224-228]. Specifically, cardiac ECM has collagens (Col I, III, and IV), fibronectin, elastin, and laminins [153, 226-228]. Each component is critical in regulating and signaling various parts of the cardiomyocyte life [153, 228, 229]. Cardiac ECM provides chemical and physiological cues to form mature functional cardiomyocytes [153, 229]. Scaffolds that contain digested decellularized ECM in their blending lead to a homogenous dispersion of bioactive molecules and protein content [230, 231]. Equal distribution throughout the scaffold leads to closer mimicking of the native tissue microenvironment, providing many binding points for cells [125, 226, 229, 231, 232]. Homogenous distribution of ECM avoids introducing structural weaknesses. Injecting ECM gel into scaffolding can create stressor points [231]. ECM-containing scaffolds also benefit from including the exact composition of natural polymers as native tissue compared to scaffolds that only incorporate one type of natural polymer [201]. Incorporating only one naturally occurring polymer from the cardiac ECM fails to provide the other natural polymers' biological cues [201].

Taking these structural and biological needs for optimal cardiac tissue engineering, we proposed that blending PU with decellularized ECM offers a novel biomaterial blend. Elastic and mechanically robust while delivering bioactive biomolecules throughout scaffolding [230]. Other literature reported incorporating a digested ECM hydrogel in PU scaffolds with a layer-by-layer structure for cardiac scaffold use [125, 214]. However, there is a need to explore digested ECM and PU blends on cardiomyocyte growth and maturation.

This study fabricates a biodegradable PU (PU) and decellularized native ECM scaffold for a cardiac tissue engineering application. Fabrication of aligned electrospun scaffold where digested ECM is dispersed throughout the scaffolds offers a unique morphologically and mechanically similar scaffold to native ECM structure and provides all relevant biological cues. We hypothesized that incorporating PU and ECM leads to a scaffold that exhibit bioactive signaling to improve cell function and provides mechanical support. The study focused on assessing material characteristics with various concentrations of digested decellularized ECM in the scaffold and its effects on cardiomyocyte behavior. Material characterization of scaffolds can help assess similarities of scaffolding to native tissue mechanically. In vitro cellular studies monitoring the effects on HL-1 cardiomyocytes and neonatal rat cardiomyocyte behavior determine the effectiveness as a potential cardiac scaffold.

2.2 Materials and Methods

2.2.1 Materials

All materials were obtained from Sigma unless stated otherwise. Polycaprolactone diol (PCL, Mn = 2000) was dried in a vacuum oven at 60°C overnight. Hexamethylene diisocyanate (HDI) and putrescine were purified via distillation. Stannous octoate ($Sn(Oct)_2$), isopropanol, 1,1,1,3,3,3-hexafluoro-2-propanol (HFIP, Oakwood Products), anhydrous dimethyl sulfone (DMSO), and pepsin (EMD Millipore Corp) were used as purchased. Hydrochloric acid (HCl, 35% solution) was diluted to form a 0.01M solution for pepsin activation. Sodium hydroxide (NaOH, 25% solution) was diluted to create a 0.1M solution to neutralize the digestion solution. Sodium dodecyl sulfate (SDS) (Abcam) was measured and put in DI water to make a 1% SDS solution. Phosphate buffer saline (PBS) (Sigma) was made using tablets in DI water. Porcine hearts were kindly donated from a local butcher (Fischer Meat Market, Muenster, Texas) and received either fresh or frozen.

2.2.2 Biodegradable Polyurethane Synthesis

PU was synthesized as previously published [233]. Briefly, PCL (Mn=2000) was dissolved in DMSO under nitrogen protection in a flask and then HDI, and 3 droplets of Sn $(Oct)_2$, were added. The solution was stirred for 3 hours at 70 °C, and then it was left to cool down to room temperature before adding a putrescine/DMSO solution under constant magnetic stirring. The final molar ratio achieved was 1:2:1 of PCL/HDI/putrescine. After it was left overnight at 70 °C, polymers were precipitated in DI water and rinsed. Polymers were submerged in isopropanol, which can remove unreacted monomers and oligomers. The resulting PU is dried at 60 °C in a vacuum oven for three days.

2.2.3 ECM Extraction and Digestion

Decellularized ECM is obtained by dissecting the left ventricle from porcine hearts. The left ventricle is cut into thin slices before placing into a 1% SDS solution. After 6 hours, a filter collected the slices. Slices were re-suspended in a 1% SDS solution. The solution was replaced after 24 hours and then once every 48 hours until the coloration of samples was lost. Slices are then washed with DI water and freeze-dried for 48 hours. Pieces are submerged in liquid nitrogen and crushed into a fine powder using a mortar and pestle. 150 mg of decellularized ECM was weighed with 10 mg of pepsin in a vial with a magnetic stirrer to digest ECM. 10 mL of 0.01 M HCl were added to activate pepsin and left to stir at high speed for 72 hours until ECM was fully digested. The acidic solution was neutralized using 1 mL of 0.1 M of NaOH before filtering the solution with a fine mesh strainer to remove any undigested ECM particulates. The sample was freeze-dried for 48 hours to obtain digested ECM. The ECM is submerged in liquid nitrogen, frozen, and crushed with a mortar and pestle before polymer solutions.

2.2.4 Electrospun Aligned, Hybrid Scaffold Fabrication

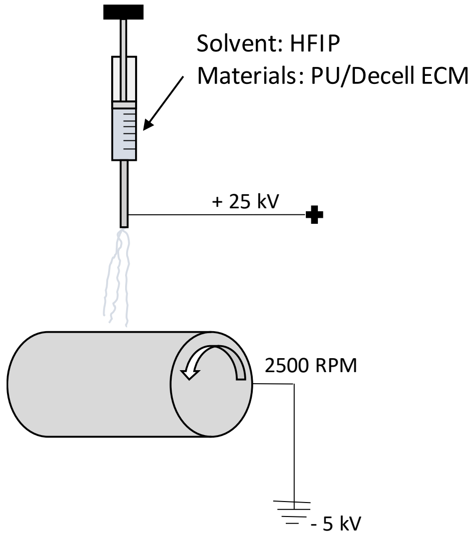

Figure 2.1: Schematic of aligned electrospinning setup; electrospinning took place over 8 hours with an extrusion rate of 1 ml/hr. The rotating mandrel was 15 cm away from the blunt tip rotating at 2500 rpm.

Hybrid scaffolds were fabricated using a standard electrospinning process with a rotating mandrel. The steel rotating mandrel (D = 150 mm, L = 40 mm) was wrapped with aluminum foil before collection (**Figure 2.1**). PU was weighed (0.64 g), cut into small pieces, and dissolved in HFIP (4 mL) for 8 hours. The digested ECM (0.032 g, 0.064 g, 0.128 g) was dissolved in HFIP (4 mL) for 1 hour with magnetic stirring. The ECM solution was transferred to the dissolved PU solution and vortexed for 10 minutes or until homogeneous. The vortexed solution was loaded into a 10 ml syringe and infused at 1 ml/hour. The distance between the tip and the collector was 15 cm. The blunt tip was connected to a DC power supply and charged with 25kV. The collection mandrel was kept at 2500 rpm with a -5 kV charge. After the 8 mL of solution was completely extruded, the syringe pump, the power supply, and the mandrel were turned off. The scaffold was left on the mandrel overnight in the fume hood, with the scaffold cut and gently peeled off the mandrel. Scaffolds were laid flat mandrel side down on aluminum foil for storage until use.

2.2.5 Scaffold Characterization

2.2.5.1 Attenuated Total Reflectance-Fourier Transform Infrared

Attenuated Total Reflectance-Fourier Transform Infrared (ATR-FTIR) was performed for each fabricated scaffold and digested ECM. A Thermo Nicolet 6700 FTIR Spectrometer was used to record spectra with a wavelength range of 4000-600 cm^{-1}. Spectrum peaks were found and recorded for comparisons between scaffolds and pure ECM.

2.2.5.2 Scaffold Morphology Analysis

Morphological analysis of the scaffolds was performed with a scanning electron microscope (SEM) (Hitachi S-4800 II FE-SEM) after scaffolds were coated with gold/platinum (Au/Pt) using a Hummer VI sputtering system. The scaffold’s fiber diameter and alignment were measured with ImageJ (n=120) using the SEM scale bar as a reference. The fiber orientation histogram and normalized curve were calculated in Excel with the imported angles from ImageJ (n=120). Scaffold shrinkage was performed by immersion of samples (8 mm diameter, n = 5) in PBS for 24 hours in a 37 °C incubator. The scaffold size was measured using a caliper to quantify shrink. Scaffolds were freeze-dried, and morphological analysis was performed as described above.

2.2.5.3 Contact Angle

The surface hydrophilicity was quantified with a custom-built instrument controlled by FTA32 software. Scaffold samples 3 cm × 1 cm (n = 2) were mounted with double-sided tape to glass slides and placed on the instrument platform with a camera positioned to view the scaffolds from a side view. A 5 µL

DI water droplet was applied to the sample with a micro-pipette. Droplet placement was repeated three times, with the droplets applied 1 cm apart for a total of n = 6 for each group. Images were captured at 15, 30, 60, 90, and 120 seconds after droplet application. The contact angle was calculated by placing points following the curve of the droplet using the FTA32 software.

2.2.5.4 In vitro Enzymatic Degradation

Weighed polymer scaffolds (W_0) were submerged in 2 mL lipase/PBS solution (100 U/mL, enzymatic degradation) at 37 °C. The PBS solution was replaced every three days. Samples on days 3, 7, and 14 were weighed (W_1) after a deionized water rinse and freeze dried (n = 3 for each sample at each time point). The mass remaining was calculated as with the following equation:

$$\% \, Degradation = \frac{W_1}{W_0} \times 100 \qquad [1]$$

2.2.5.5 Mechanical Testing

2.2.5.5.1 Uniaxial Mechanical Testing

A universal testing system performed uniaxial mechanical testing on the fabricated scaffolds and native tissue (n = 5) (Test Resources, MN). Scaffolds were cut into 5 mm × 30 mm strips, aligned with the fibers, and perpendicular to the fiber's directions. The LV of the porcine hearts were cut to 1-2 mm thick strips (5 mm × 30 mm) containing both epicardium and myocardium. Scaffolds were soaked in PBS at 37°C for 24 hours before uniaxial testing. Native tissue samples were tested at room temperature. With 10 ~15 mm between grips, samples were loaded for testing. Tests performed were stress-relaxation, creep, cyclic loading and unloading, and failure tests (20 samples/second). The target load for stress relaxation and creep was 100 g with a jogging rate of 10 mm/minutes. Cyclic testing was done using a rate of 10 mm/min and pulled until 30% strain was reached for ten cycles. Test to failure was measured at a 10 mm/min speed until the sample broke and testing was stopped.

2.2.5.5.2 Biaxial Mechanical Testing

Biaxial mechanical testing was performed on fabricated scaffolds and native tissue (n = 3). Samples were cut into 1 cm × 1 cm squares and marked to know fiber direction. Native tissue samples were collected by dissecting a 1-2 mm thick square (1 cm × 1 cm) sheet of the epicardium and myocardium. All samples were tested when at room temperature. A black tape was used to track deformation; samples were marked using a custom biaxial machine with a LabView program. Loading was set to 60 N/m:60 N/m, and data were processed using Excel.

2.2.6 Cell Compatibility and Behavior

Scaffolds tested in HL-1 cell studies were PU, PU-5%ECM, PU-10%ECM, and PU-20%ECM with a control group on a tissue culture polystyrene (TCP). Studies using neonatal rat cardiomyocytes (NNRCM) only used PU, PU-10%ECM, PU-20%ECM, and the control TCP.

2.2.6.1 *In vitro* Culture of HL-1 Cells on Scaffolds

Scaffolding for each group of samples was cut into 15 mm × 15 mm squares, taped onto glass cover slides, placed on a 24-well plate, pressed with stainless steel rings, and sterilized via UV for 60 minutes on each side. Electrospun scaffolds were washed with PBS thrice at 15 min intervals to remove any residual solvent and then soaked in Claycomb media before seeding for 2 hours. The proliferation and differentiation of HL-1 cells were seeded with a density of 3×10^4 and 5×10^5 cells/well, respectively. Cells were cultured in the same media in both proliferation and differentiation studies. Scaffolds were incubated for seven days at 37°C with 95% air and 5% CO_2 at high humidity for growth studies. Media was replaced every other day. For differentiation studies, the cells were cultured for 14 days. The media used was Claycomb media supplemented with 10% fetal bovine serum (FBS), 0.1 mM norepinephrine, 2mM L-glutamine, and 100 U/mL penicillin and streptomycin.

2.2.6.2 *In vitro* Culture of Rat Neonatal Cardiomyocyte on Scaffolds

Neonatal rat cardiomyocytes (NNRCM) (Lonza, R-CM-561) were resuscitated two days before scaffold preparation and seeding and cultured in a T25 flask with rat cardiac myocyte growth media BulletKit™ (RCGM) (Lonza, CC-4515). RCGM BulletKit™ was composed of Rat Cardiac Myocyte Basal Medium (Lonza, CC-3275) and RCGM SingleQuots™ Kit (Lonza, CC-4516). After four hours, 80% of the media was replaced with RCGM BulletKit™ supplemented with 200 µM bromodeoxyuridine (BrdU) (Lonza, CC-4519). Each group's scaffold was cut using a metal press to obtain circles with a diameter of 5 mm (n=8). Scaffolds were subjected to UV light for an hour on each side before placement into a 96-well plate, with plastic rings used to hold the scaffolds down. Scaffolds were washed with PBS thrice at 15-minute intervals before replacing with rat cardiac myocyte growth media BulletKit™ for 2 hours before seeding cells. A cell density of 1.0×10^5 cells/well was used for seeding, with scaffolds kept in an incubator for seven days at 37°C with 95% air and 5% CO_2 at high humidity for the duration of the study, replacing 50% media every 3 days with fresh RCGM BulletKit™ supplemented with 200 µM BrdU. At set time points, live/dead staining and CCK-8 were performed to determine the growth of cells on scaffolds, with immunofluorescent staining occurring on day 7.

2.2.6.3 Live/Dead Staining

Cell viability on nano-fibrous scaffolds was assessed on days 1, 4, and 7 of culture using a live/dead viability kit (Sigma). An inverted fluorescent microscope (Nikon Eclipse Ti) was used to observe cells. Live cells are stained green with calcein-AM, and dead cells are red with ethidium homodimer-1 (EthD-1). Samples were washed with PBS twice after removal from the growth medium and then treated with 2 µM calcein AM and 4 µM EthD-1 in Dulbecco's modified eagle medium (DMEM) for 30 minutes at 37°C.

2.2.6.4 CCK-8

A cell counting kit, CCK-8 (Sigma), was used to help assess cell viability on scaffolds, performed on days 1, 4, and 7 of culture (n = 3). Cell media was removed from the wells and replaced with 100 µL of DMEM and 10 µL of CCK-8 solution before continued incubation, with one well used as a blank filled with DMEM and CCK-8 solution with no cells. After one hour of incubation, the media was removed and placed in a new 96-well plate for plate reading, with the cell samples washed with PBS twice before replenished with the respective cell medium dependent on cell type. The harvested CCK-8 solution was read using a microplate reader (Tecan Spark 10M) at 450 nm and 650 nm wavelengths to measure the absorption. The OD was calculated by the measured absorption minus the blank for each well.

2.2.6.5 Cell Morphology

Cells seeded on the scaffold in differentiation media were fixed and imaged with SEM to characterize cell alignment on days 7 and 14 for HL-1 culture under differentiation conditions. Neonatal cardiomyocytes were fixed and imaged with SEM for morphology characterization on days 1, 4, and 7. The medium was removed from wells, and scaffolds were washed twice with PBS. Cells were then fixed using a 2.5% glutaraldehyde solution for 15 minutes, after which scaffolds were washed with PBS. Samples were dehydrated using increasing ethanol concentration solutions (50%, 70%, 80%, 90%, 95%, and 100%) for 5 minutes, except for 100% ethanol which was used twice for a total of 10 minutes. Scaffolds were then placed on a dry mat and left to air dry for 24 hours. After air-drying, samples were prepared for SEM using the same protocol described above.

2.2.6.6 Immunofluorescence Staining

Immunofluorescence staining was performed on cell-seeded scaffolds in differentiation conditions after 7 and 14 days for α-actinin and F-actin for Hl-1 cells. NNRCM had immunofluorescence staining only on day 7 for α-actinin and Cx-43. Media was removed from wells, and scaffolds were washed with PBS twice and fixed using 4% paraformaldehyde for 15 minutes. Scaffolds were then rewashed with PBS three times before permeabilized with a 0.3% Triton X-100 in PBS for 10 minutes under incubation. Scaffolds were washed with PBS three times before adding a 2% bovine serum album (BSA) in PBS solution for an hour. The BSA solution was removed and replaced with the primary antibodies (monoclonal anti-α-actinin (sarcomeric), 1:200, Santa Cruz; anti-connexin-43 rabbit antibody, 1:200, Santa Cruz) in 1% BSA solution incubated at 4°C overnight. Scaffolds were washed with PBS three times before incubating with the secondary antibody (goat anti-mouse IgG (H+L) Highly Cross-Adsorbed Secondary Antibody, Alexa Fluor Plus™ 488, 1:1000 for α-actinin; Alexa Fluor™ 594 goat anti-rabbit IgG (H+L) for Cx-43) in 1% BSA solution for 1 hour in the dark at room temperature. After they were washed with PBS, F-actin staining was done using tetramethyl rhodamine isothiocyanate (TRITC) labeled phalloidin (1:400) in a 1% BSA solution. Scaffolds spent 20 minutes at room temperature in the dark with F-actin stain. 4', 6 - Diamidino-2-Phenylindole (DAPI) (300nm) was used to counterstain the nuclei. Scaffolds were washed with PBS three more times before imaging. A confocal laser fluorescence microscope (Nikon A1R HD25 Confocal Microscope) was used to image cells. ImageJ was used to measure cell length, width, fluorescent intensity, sarcomere length, and Z-line length [234, 235]. Five representative images per sample were calculated and averaged. The following equations were used for calculation.

$$Aspect\ Ratio = \frac{Length\ of\ Cell}{Width\ of\ Cell} \qquad [2]$$

$$Fluorescent\ Intensity = Cell\ Mean\ Intensity - (Cell\ Area\ \times Background) \qquad [3]$$

2.2.7 Statistical Analyses

Experimental data were reported as mean ± standard deviation. For comparison between two groups, a two-tailed Student's t-test was used; for more than two groups, a one-way analysis of variance (ANOVA) test was used for statistical significance when P-value was less than 0.05. A Tukey test was performed on ANOVA tests with significance to determine significance between all groups. All analyses were calculated using Excel.

2.3 Results

2.3.1 Sample fabrication

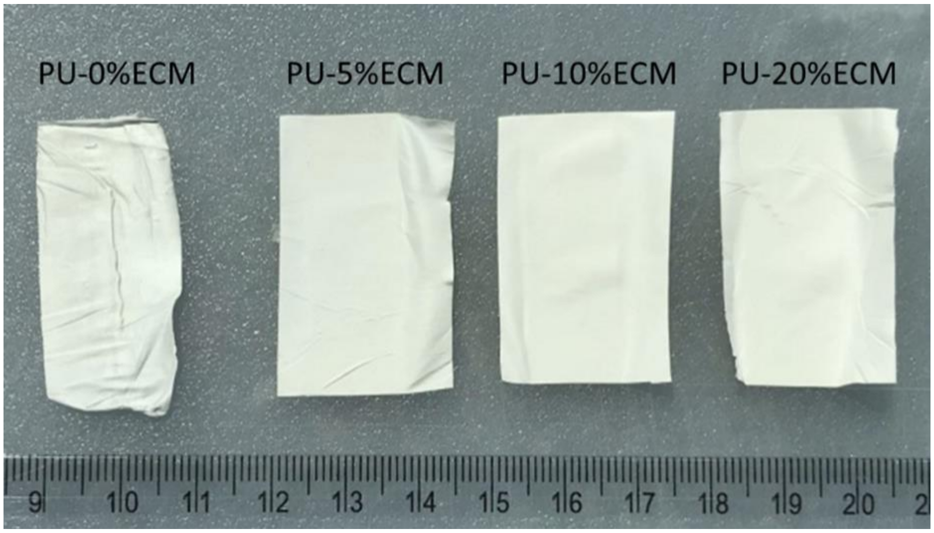

Figure 2.2: Electrospun PU, PU-5%ECM, PU-10%ECM, and PU-20%ECM scaffolds. PU was the smoothest. Roughness increased with ECM.

PU scaffold had a silkier texture that felt rougher as ECM concentration increased (**Figure 2.2**). Scaffolds with higher concentrations of ECM also exhibited more noticeable bunching after releasing the circular tension when removed from the spinning mandrel.

2.3.2 ATR-FTIR Surface Characterization

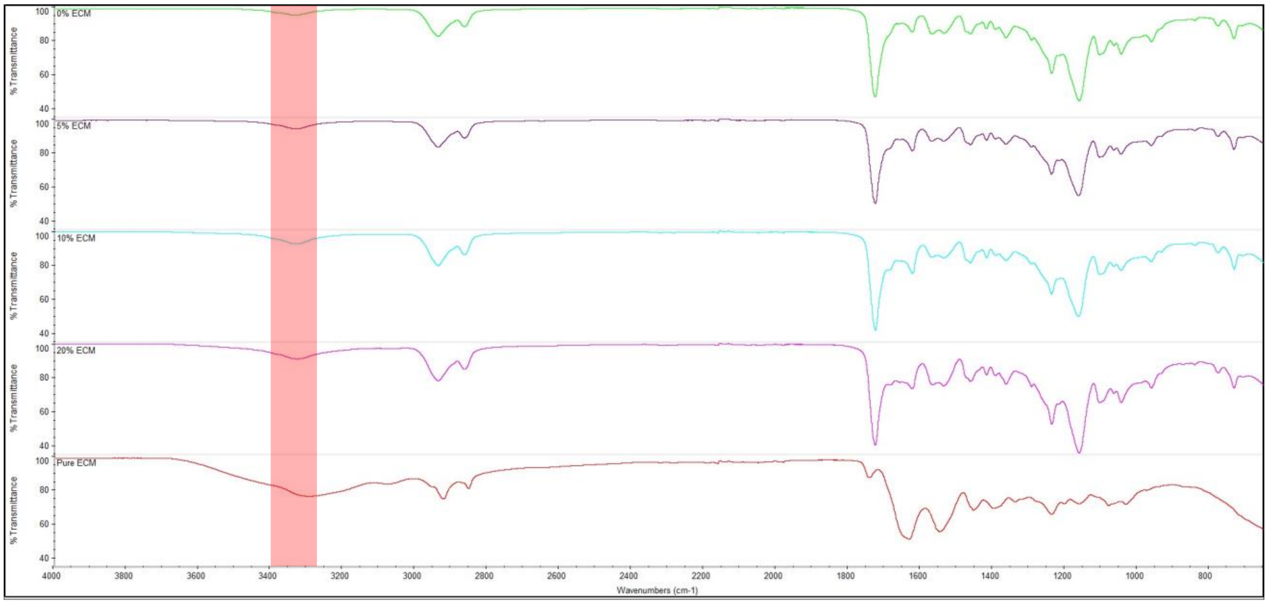

Figure 2.3: ATR-FTIR of PU, PU-5%ECM, PU-10%ECM, PU-20%ECM scaffolds, and digested ECM. The wavelength range was 4000-600 cm^{-1}.

The FTIR spectra obtained for the scaffolds showed the different characteristic peaks for PU and PU-ECM scaffolds (**Figure 2.3**). PU spectra showed a small peak around 3300 cm^{-1}, increasing peak visibility with increasing ECM concentration in the scaffold. The pure ECM spectrum displayed a prominent broad peak around 3300 cm^{-1}, with a visible peak correlating to increased ECM content in the scaffold. 3300 cm^{-1} is characteristic of the O-H function on alcohol functional groups, which are more present in the ECM. The broad peak of the pure ECM spans from around 3200 cm^{-1} to 3600 cm^{-1}, representing C-H stretching, covering a wide range of C-H stretching from the ECM. Many peaks are overlapped due to PU and ECM containing similar functional groups. This overlapping could be why O-H presence is slightly more noticeable in higher concentrations of ECM due to the overlapping effect of the C-H stretching from the ECM.

2.3.3 Scaffold Morphology Analysis

Table 2.1: Summary of shrinkage of PU, PU-5%ECM, PU-10%ECM, and PU-20%ECM after immersion in PBS at 37°C for 24 hours.

% ECM	XD (mm)	PD (mm)	% Shrink along XD	% Shrink along PD
0%	7.6 ± 0.39^{a,b}	5.35 ± 0.05^{a}	5.0 ± 4.9^{a,b}	33.1 ± 0.6^{a}
5%	7.9 ± 0.28^{a,b}	5.58 ± 0.19^{a,b}	0.1 ± 3.5^{a,b}	30.2 ± 2.4^{a,b}
10%	7.6 ± 0.09^{a}	5.42 ± 0.08^{a}	5.0 ± 1.2^{a}	32.2 ± 1.0^{a}
20%	7.9 ± 0.06^{b}	5.12 ± 0.12^{b}	0.5 ± 0.7^{b}	36.0 ± 1.5^{b}

*a, b represent significantly different groups for each characteristic

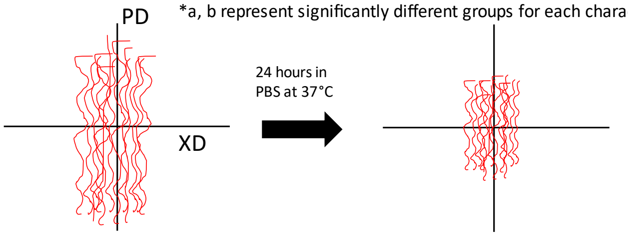

XD: Cross Preferred Fiber Direction
PD: Preferred Fiber Direction

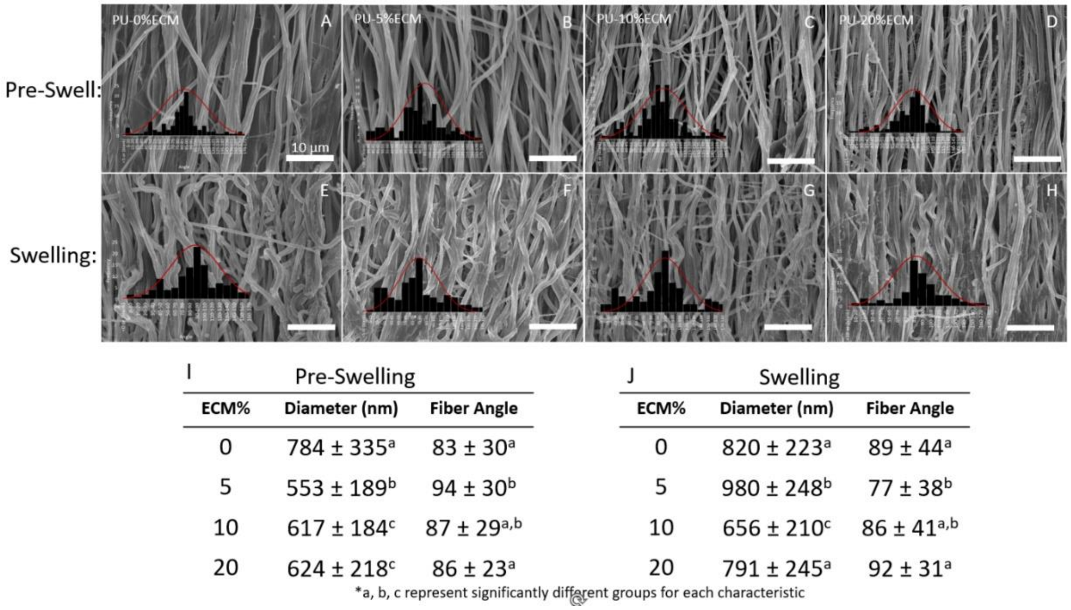

I

Pre-Swelling

ECM%	Diameter (nm)	Fiber Angle
0	784 ± 335^{a}	83 ± 30^{a}
5	553 ± 189^{b}	94 ± 30^{b}
10	617 ± 184^{c}	87 ± 29^{a,b}
20	624 ± 218^{c}	86 ± 23^{a}

J

Swelling

ECM%	Diameter (nm)	Fiber Angle
0	820 ± 223^{a}	89 ± 44^{a}
5	980 ± 248^{b}	77 ± 38^{b}
10	656 ± 210^{c}	86 ± 41^{a,b}
20	791 ± 245^{a}	92 ± 31^{a}

*a, b, c represent significantly different groups for each characteristic

Figure 2.4: A-D) PU, PU-5%ECM, PU-10%ECM, and PU-20%ECM SEM images before and E-H) after immersion in PBS. I) Summary of fiber analysis PU, PU-5%ECM, PU-10%ECM, and PU-20%ECM before immersion in PBS and J) after immersion in PBS at 37°C for 24 hours. Scale bar length is 10 µm.

Continuously aligned nanofibers were revealed with SEM. No beads were observed (**Figure 2.4**). PU and PU-ECM blends were all nano-sized. There was no increase in fiber diameter with the inclusion of ECM compared to the PU. The PU average fiber diameter was 784 ± 335 nm, while the PU-5%ECM, PU-10%ECM, and PU-20%ECM were 553 ± 189 nm, 617 ± 184 nm, and 624 ± 218 nm, respectively. PU fiber diameter was significantly larger than PU-ECM scaffolds, with a p-value of < 0.01. PU-5%ECM exhibited the smallest fiber diameter with a p-value of < 0.01; statistically, PU-10%ECM and PU-20%ECM were the same. PU-20%ECM had micro-net structures which were not present in other scaffolds. Scaffolds exhibited similar distributions of fiber angle. PU had an average fiber angle of 83 ± 30°, while PU-5%ECM, PU-10%ECM, and PU-20%ECM were 94 ± 30°, 87 ± 29°, and 86 ± 23°, respectively. ECM in the scaffold had no discernible effect on the alignment. Only PU-5%ECM had significantly different fiber angles than PU and PU-20%ECM, with a p-value of < 0.05. PU-5%ECM possibly had statistically different angles due to the slightly skewed orientation to the reference axis. Swelling from PBS immersion showed an increase in fiber size compared to non-immersed scaffolds (**Figure 2.4J**). Swollen PU measured an average fiber diameter of 820 ± 223 nm. PU-5%ECM, PU-10%ECM, and PU-20%ECM measured 980 ± 248 nm, 656 ± 210 nm, and 791 ± 245 nm, respectively. PU and PU-20%ECM had significantly similar diameters. PU-5%ECM and PU-10%ECM diameters were different from PU and PU-20%ECM with a p-value < 0.01. Fiber alignment of the swollen PU fibers was 89 ± 44°, while the PU-5%ECM, PU-10%ECM, and PU-20%ECM was 77 ± 38°, 86 ± 41°, and 92 ± 31°, respectively. There were significant differences between PU and PU-5%ECM and differences between PU-5%ECM and PU-20%ECM, with a p-value < 0.05 and < 0.01. ECM didn’t contribute significantly to fiber swelling. Scaffold shrinkage is shown in **Table 2.1**. The scaffolding shrank unevenly based on fiber orientation in the scaffold—scaffolds in the PD shank 30~36% of the original size. The XD shrank 0.1~5% of its original size. Along the PD, there were significant differences between PU and PU-20%ECM, and between PU-10%ECM and PU-20%ECM, with a p-value < 0.05. The only significant difference for the XD was between PU-10%ECM and PU-20%ECM, with a p-value < 0.05.

2.3.4 Contact Angle

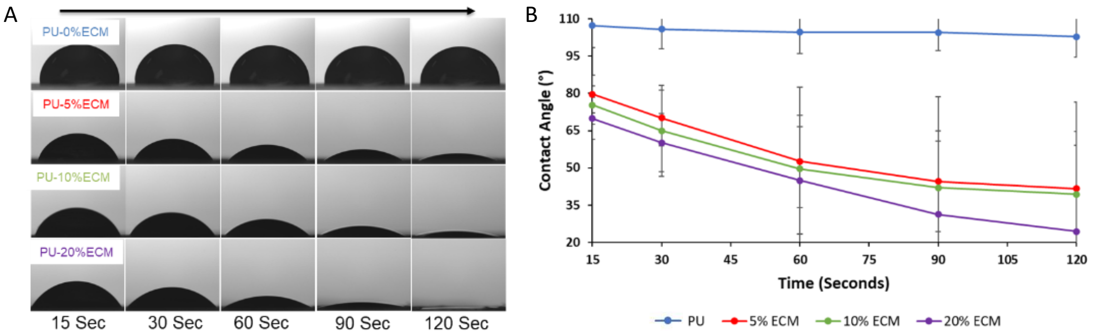

C

%ECM	CA (°) 15 Sec	CA (°) 30 Sec	CA (°) 60 Sec	CA (°) 90 Sec	CA (°) 120 Sec
0	107 ± 9^a	106 ± 8^a	105 ± 9^a	105 ± 7^a	103 ± 8^a
5	80 ± 8^b	70 ± 11^b	53 ± 19^b	45 ± 20^b	42 ± 23^b
10	75 ± 8^b	65 ± 18^b	50 ± 33^b	42 ± 37^b	39 ± 7^b
20	70 ± 9^b	60 ± 12^b	45 ± 22^b	31 ± 29^b	24 ± 34^b

*a, b represent significantly different groups for each characteristic

Figure 2.5: A) PU, PU-5%ECM, PU-10%ECM, and PU-20%ECM contact angle images at time points of 15, 30, 60, 90, and 120 seconds after water droplet application B) Dynamic contact angle for PU, PU-5%ECM, PU-10%ECM, and PU-20%ECM. C) Summary of contact angles for PU, PU-5%ECM, PU-10%ECM, and PU-20%ECM at each time point.

PU and PU-ECM scaffolds are intended for implantation for cardiac tissue regenerations and need to have hydrophilicity investigated due to exposure to body fluids. The contact angle of the PU scaffold was 107 ± 9°, following a trend of decreasing contact angle with increasing ECM content (**Figure 2.5**). The contact angle of PU-5%ECM, PU-10%ECM, and PU-20%ECM was 80 ± 8°, 75 ± 8°, and 70 ± 8°, respectively, after 15 seconds of droplet placement. As shown in **Figure 2.5B**, an apparent increase in hydrophilicity is noted with an increase in ECM concentration in the scaffold. There was a faster decrease in contact angle over 120 seconds in scaffolds with higher amounts of ECM. In some cases, the higher concentrations of ECM (10% and 20%) absorbed the droplet before the two minutes of testing was completed. PU was significantly higher at all time points than all ECM-containing scaffolds, with a p-value < 0.05.

2.3.5 In Vitro Enzymatic Degradation

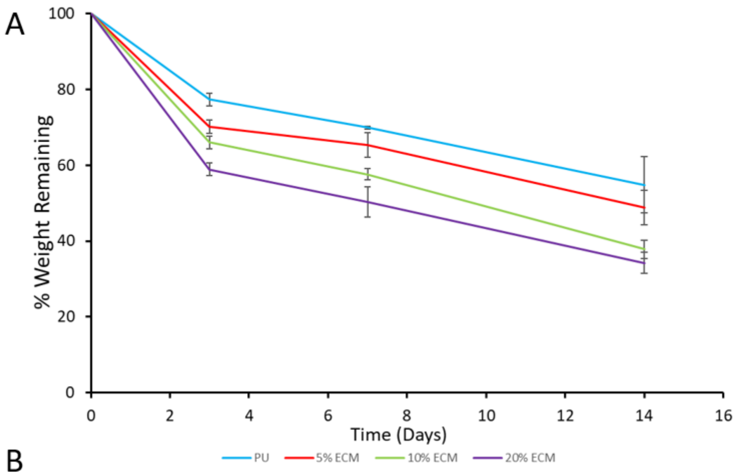

*a, b, c, and d represent significantly different groups for each characteristic

B

%ECM	0	5	10	20
Day 3	77.3 ± 1.7^{a}	70.2 ± 1.7^{b}	66.0 ± 1.7^{c}	58.9 ± 1.7^{d}
Day 7	69.9 ± 0.4^{a,c}	65.4 ± 3.3^{a}	57.6 ± 1.5^{b,c}	50.3 ± 4.0^{c}
Day 14	54.8 ± 7.3^{a}	48.8 ± 4.5^{a}	37.8 ± 2.4^{b}	34.2 ± 2.8^{c}

Figure 2.6: *In vitro* Enzymatic Degradation of PU, PU-5%ECM, PU-10%ECM, and PU-20%ECM. A) % remaining weight over the 14-day study. B) Summary of % remaining weight at each time point. The degradation solution was composed of PBS and 100 U/mL lipase; samples were incubated with the solution for 14 days.

Degradation of the scaffold due to enzymatic activity within the body causes morphological changes and weakens the scaffold's structural integrity. A 100 U/mL lipase in PBS solution replicated the body's enzymatic activity to determine the degradation rate within the body. **Figure 2.6A** depicts the decrease in mass over the study. The PU scaffold retained 54.8 ± 7.3% of its initial weight over 2 weeks when incubated with the lipase solution. PU-5%ECM, PU-10%ECM, and PU-20%ECM retained 48.8 ± 4.5%, 37.8 ± 2.4%, and 34.2 ± 2.8%, weight respectively (**Figure 2.6B**). Statistical difference between groups at each time point was indicated via ANOVA testing, with PU statistically different than all scaffolds on day 3 and only statistically different from the PU-20%ECM on day 14.

2.3.6 Mechanical Testing

2.3.6.1 Stress-relaxation Behavior

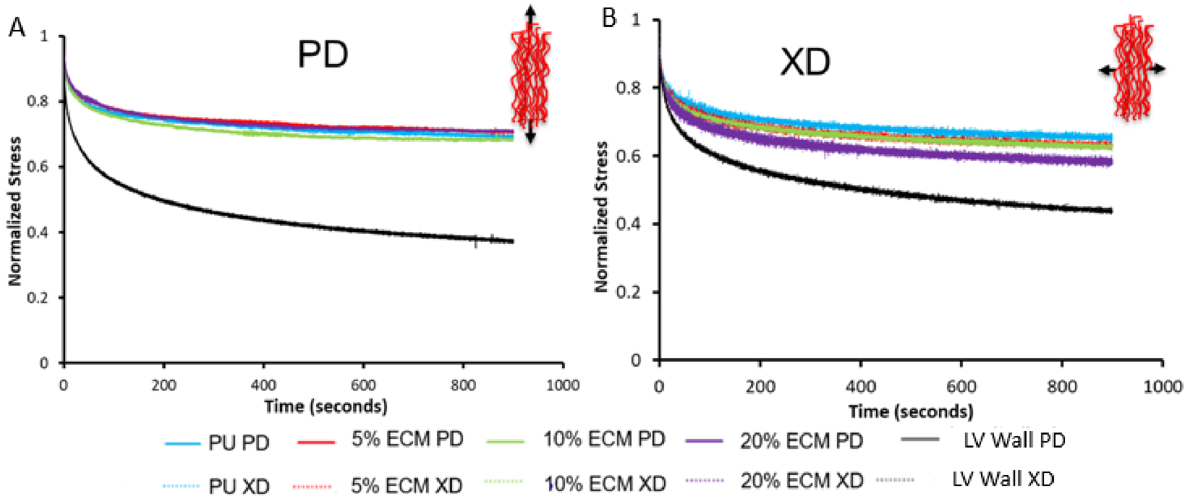

C

% ECM	0%	5%	10%	20%	LV
SR: PD (%)	30.7 ± 5.4^{a}	29.7 ± 3.6	31.4 ± 2.7^{a}	29.2 ± 2.3^{a}	63.0 ± 5.6^{b}
SR: XD (%)	34.1 ± 1.9^{a}	37.0 ± 1.2^{a,b}	36.8 ± 0.8^{b}	42.9 ± 1.6^{c}	56.2 ± 3.3^{d}

*a, b, c, and d represent significantly different groups for each characteristic

Figure 2.7: A) Stress relaxation in PD for PU, PU-5%ECM, PU-10%ECM, PU-20%ECM, and LV porcine wall B) Stress relaxation in XD for PU, PU-5%ECM, PU-10%ECM, PU-20%ECM, and LV porcine wall C) Stress relaxation summary PU, PU-5%ECM, PU-10%ECM, PU-20%ECM, and LV porcine wall.

Fatigue, elasticity, and failure are some of the cardiac scaffolds' most important material characteristics due to the constant mechanical action and pressure on the heart. Stress-relaxation is a good measure of how efficiently the scaffolds can release the applied load (**Figure 2.7**). Native tissue in the PD direction could release 63 ± 5.6% of the stress applied over 15 minutes, while the PD of PU with a stress decay at 30.7 ± 5.4%. The composite scaffolds were roughly like PU with stress decay at 29.7 ± 3.6%, 31.4 ± 2.7%, and 29.2 ± 2.3% for PU-5%ECM, PU-10%ECM, and PU-20%ECM, respectively. All scaffolds were significantly different than the native tissue, with p values < 0.001. When looking at the XD direction, the native tissue released 56.2 ± 33% of stress while the PU released 34.1 ± 1.9% of the applied stress in the XD. The stress decay of PU-ECM scaffolds in the XD increased with the increasing ECM concentration. The PU-5%ECM, PU-10%ECM, and PU-20%ECM had a stress decay at 37.0 ± 1.2%, 36.8 ± 0.8%, and 42.9 ± 1.6%, respectively. PU-20%ECM exhibited significantly higher stress decay than the other scaffolds, with a p-value < 0.01. Native tissue's ability to release stress was significantly higher than all other scaffolds, with a p-value < 0.01.

2.3.6.2 Creep

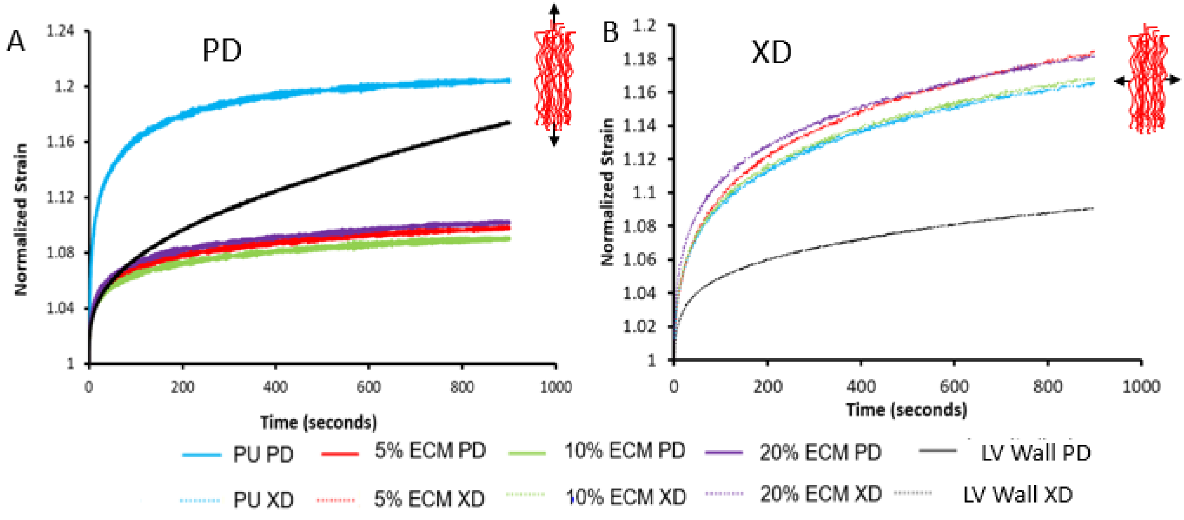

C

% ECM	0%	5%	10%	20%	LV
Creep: PD (%)	20.4 ± 9.3^{a,b}	9.8 ± 1.6^{a}	9.0 ± 1.1^{a}	10.2 ± 4.3^{a,b}	17.4 ± 6.0^{b}
Creep: XD (%)	16.4 ± 3.9^{a}	18.3 ± 2.6^{a}	16.8 ± 2.3^{a}	18.2 ± 3.1^{a}	9.1 ± 2.9^{b}

*a and b represent significantly different groups for each characteristic

Figure 2.8: A) PD Creep for PU, PU-5%ECM, PU-10%ECM, PU-20%ECM, and LV porcine wall B) XD creep for PU, PU-5%ECM, PU-10%ECM, PU-20%ECM, and LV porcine wall C) Summary of creep values for PU, PU-5%ECM, PU-10%ECM, PU-20%ECM, and LV porcine wall.

Continuing deformation of material along with time under a persistent load is measured by creep; in other words, the creep testing can track how much the scaffold can keep deforming along with time under a constant load (**Figure 2.8**). Native tissue in the PD direction had the second-largest creep under constant stress, stretching 17.4 ± 6.0% of its original length over the 15 minutes. PD PU scaffolds stretched to 20.4 ± 9.3% of their original length, which was the largest creep. The PU-5%ECM, PU-10%ECM, and PU-20%ECM had 9.8 ± 1.6%, 9.0 ± 1.1%, and 10.2 ± 4.3% respectively. There were only significant differences between the native tissue and the PU-5%ECM and PU-10%ECM, with p values < 0.05. The native tissue stretched to 9.1 ± 2.9% in the XD direction, comparatively less than in the PD direction. The XD PU stretched to 16.4 ± 3.9% of its original length. The PU-5%ECM, PU-10%ECM, and PU-20%ECM stretched

18.3 ± 2.6%, 16.8 ± 2.3%, and 18.2 ± 3.1% respectively. There were no statistical differences between all scaffolds. The only significant difference was between the native tissue and all scaffolds, with p values < 0.05.

2.3.6.3 Failure Testing

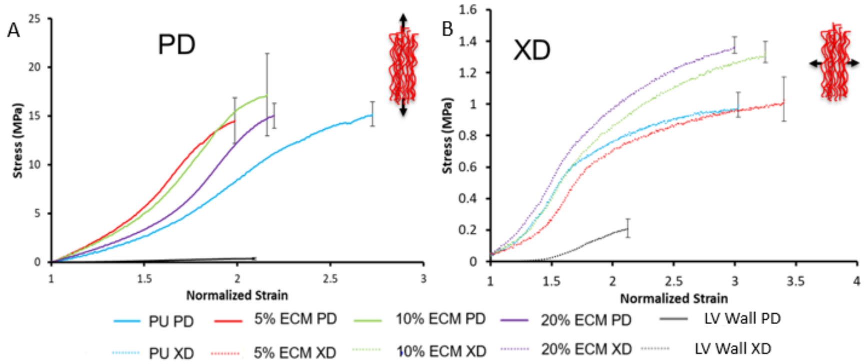

C

% ECM	0%	5%	10%	20%	LV
Failure Stress PD (MPa)	15.2 ± 1.3^{a}	14.5 ± 2.3^{a}	17.2 ± 4.2^{a}	15.0 ± 1.3^{a}	0.36 ± 0.095^{b}
Failure Strain PD	2.73 ± 0.15^{a}	1.99 ± 0.08^{b}	2.16 ± 0.18^{c}	$2.20 \pm 0.13^{b,c}$	$2.09 \pm 0.22^{b,c}$
Failure Stress XD (MPa)	1.00 ± 0.08^{a}	$1.03 \pm 0.14^{a,b}$	1.33 ± 0.07^{c}	1.38 ± 0.05^{c}	0.21 ± 0.06^{d}
Failure Stain XD	$3.02 \pm 0.50^{a,b}$	$3.40 \pm 0.51^{a,b}$	3.24 ± 0.35	3.00 ± 0.20^{a}	2.13 ± 0.15^{c}
Initial Modulus PD (KPa)	3648 ± 741^{a}	$6153 \pm 1056^{b,c}$	6183 ± 141^{c}	$5242 \pm 1112^{a,c}$	82 ± 39^{d}
Initial Modulus XD (KPa)	464 ± 47^{a}	365 ± 92^{a}	439 ± 66^{a}	612 ± 77^{b}	32 ± 11^{c}

*a, b, c, and d represent significantly different groups for each characteristic

Figure 2.9: A) PD failure testing for PU, PU-5%ECM, PU-10%ECM, PU-20%ECM, and LV porcine wall B) XD failure testing for PU, PU-5%ECM, PU-10%ECM, PU-20%ECM, and LV porcine wall. C) Failure stress and strain values for PU, PU-5%ECM, PU-10%ECM, PU-20%ECM, and LV porcine wall.

Failure testing of scaffolds was done to measure the failure stress and strain of the scaffolds and how digested ECM affected these stresses and strains (**Figure 2.9**). Pull to failure indicated the maximum stress the scaffolds withstood and determined if it is comparable to native tissue. Native tissue in the PD direction failed around 0.36 ± 0.095 MPa, significantly lower than all tested scaffolds. The native tissue's failure strain was around 2.09 ± 0.22. The PD PU had a failure stress of 15.2 ± 1.3 MPa and a strain of 2.73 ± 0.15. PD Scaffolds containing ECM exhibited failure stresses of 14.5 ± 2.3, 17.2 ± 4.2, and 15.0 ± 1.3 MPa for PU-5%ECM, PU-10%ECM, and PU-20%ECM, respectively. Failure strains were 1.99 ± 0.08, 2.16 ± 0.18, and 2.20 ± 0.13 of the original lengths. Including digested ECM into the scaffolds did not affect the failure stress across all ECM concentrations while increasing the failure stress for the 10%ECM scaffold. Failure strains of all PD PU-ECM scaffolds greatly decreased compared to the PU samples, with a p-value < 0.05. PD PU had the highest stain across all scaffolds and native tissue, with a p-value < 0.05. When looking at the XD direction of the native tissue, the failure stress was 0.21 ± 0.06 MPa, while the failure strain was 2.13 ± 0.15. The XD PU had a failure stress of 1.00 ± 0.08 MPa, and the strain was 3.02 ± 0.50. The XD PU-5%ECM, PU-10%ECM, and PU-20%ECM had failure stresses of 1.03 ± 0.14, 1.33 ± 0.07, and 1.38 ± 0.05 MPa, respectively, failure strains were 3.40 ± 0.51, 3.24 ± 0.35, and 3.00 ± 0.20, respectively. ECM increased the XD failure stress of scaffolds, while the failure strain increased at the lower ECM concentration and slightly decreased at higher concentrations. XD PU had significantly lower failure stress than PU-10%ECM and PU-20%ECM, with a p-value < 0.01. All scaffolds exhibited significantly higher failure stresses than the native tissue, with a p-value < 0.001. The only significant difference between scaffolds in failure strains was PU-10%ECM and PU-20%, with a p-value < 0.05. All scaffolds exhibited significantly higher failure strains than the native tissue, with p values < 0.01. There was a significant increase in initial modulus in PD and XD with the inclusion of ECM. The native tissue exhibited the significantly lowest initial modulus.

2.3.6.4 Cyclic Testing

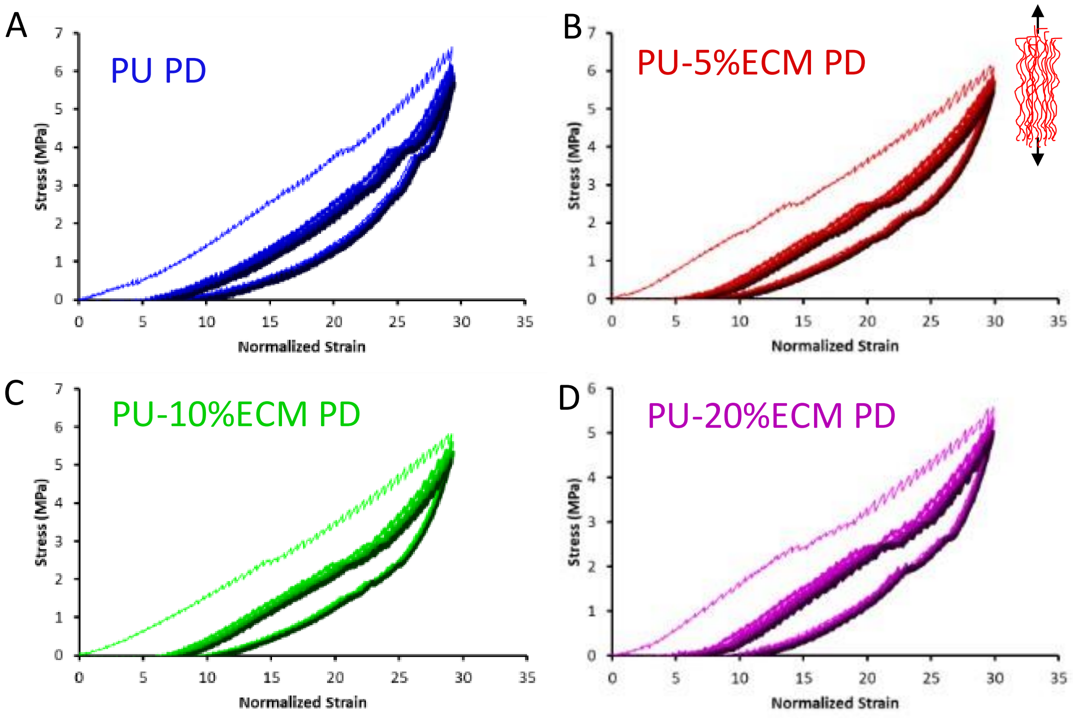

Figure 2.10: Cyclic test to 30% strain over 10 cycles for A) PU B) PU-5%ECM C) PU-10%ECM D) PU 20%. The darker coloration denotes later cycles of testing, with the darkest representing the tenth cycle.

Examining the scaffold's mechanical response to the cyclic test is a good indicator of scaffold pseudoelasticity. After the first testing cycle, all scaffolds quickly exhibited repetitive loading and unloading curves. All scaffolds exhibited similar trends when undergoing a cyclic strain of 30% of their original length (**Figure 2.10**).

2.3.6.5 Biaxial Mechanical Testing

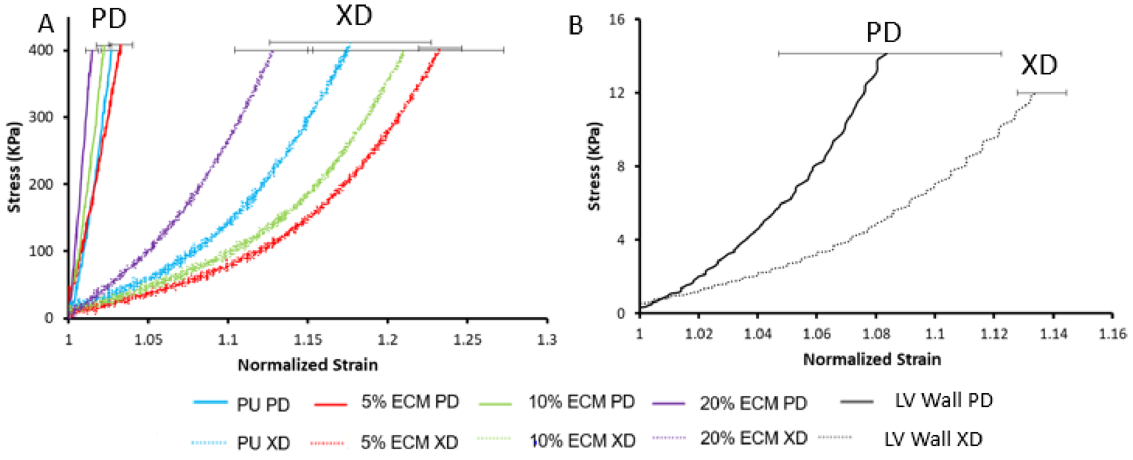

Figure 2.11: A) PD and XD biaxial testing of PU, PU-5%ECM, PU-10%ECM, PU-20%ECM, and B) LV porcine wall in the PD and XD direction. Scaffolds and LV porcine walls exhibited apparent anisotropic properties.

Biaxial testing of samples was performed to determine if the scaffolds exhibited anisotropic behavior (**Figure 2.11**). Native tissue in the PD direction had less extensibility than in the XD direction. Results were indicative of nonlinear anisotropic behavior. Scaffolds had nonlinear behavior in the XD and a more linear trend in the PD. PU and all scaffolds with varying ECM concentrations exhibited similar trends anisotropic trends.

2.3.7 *In vitro* Cell Compatibility and Behavior

2.3.7.1 HL-1 *in vitro* Studies

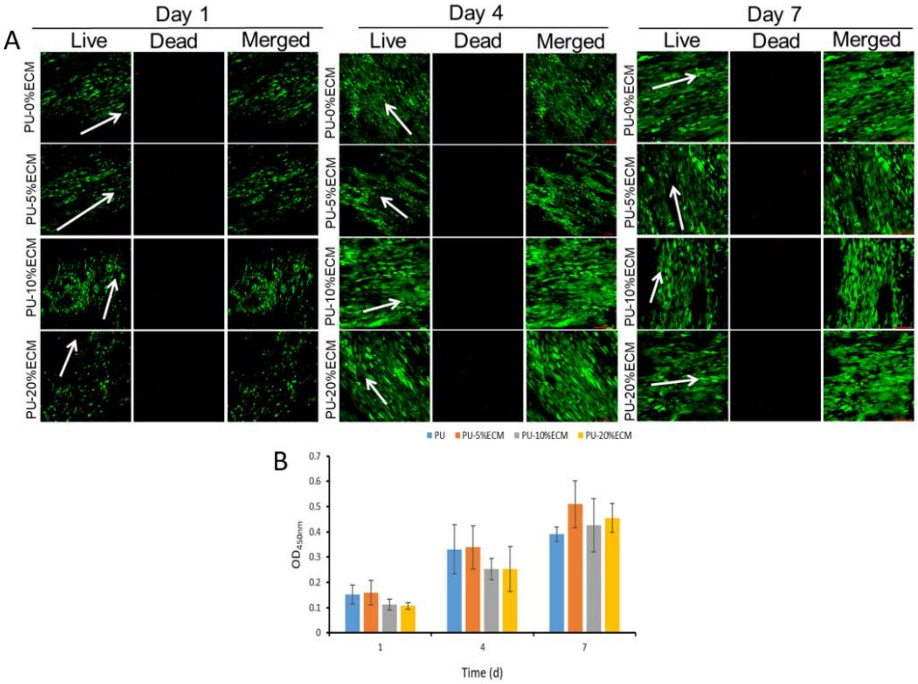

Figure 2.12: A) Live/Dead Staining of HL-1 cells on scaffolds on days 1, 4, and 7 for PU, PU-5%ECM, PU-10%ECM, PU-20%ECM, and B) Cell count from CCK-8 of HL-1 cells on days 1, 4, and 7 for PU, PU-5%ECM, PU-10%ECM, PU-20%ECM

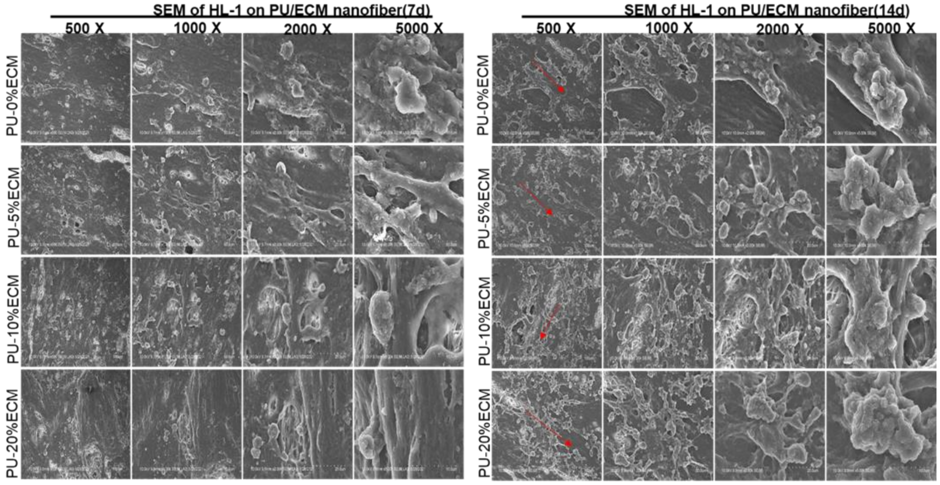

Figure 2.13: HL-1 cell morphology at 500x, 1000x, 2000x, and 5000x on days 7 and 14 of culture on PU, PU-5%ECM, PU-10%ECM, and PU-20%ECM obtained by SEM.

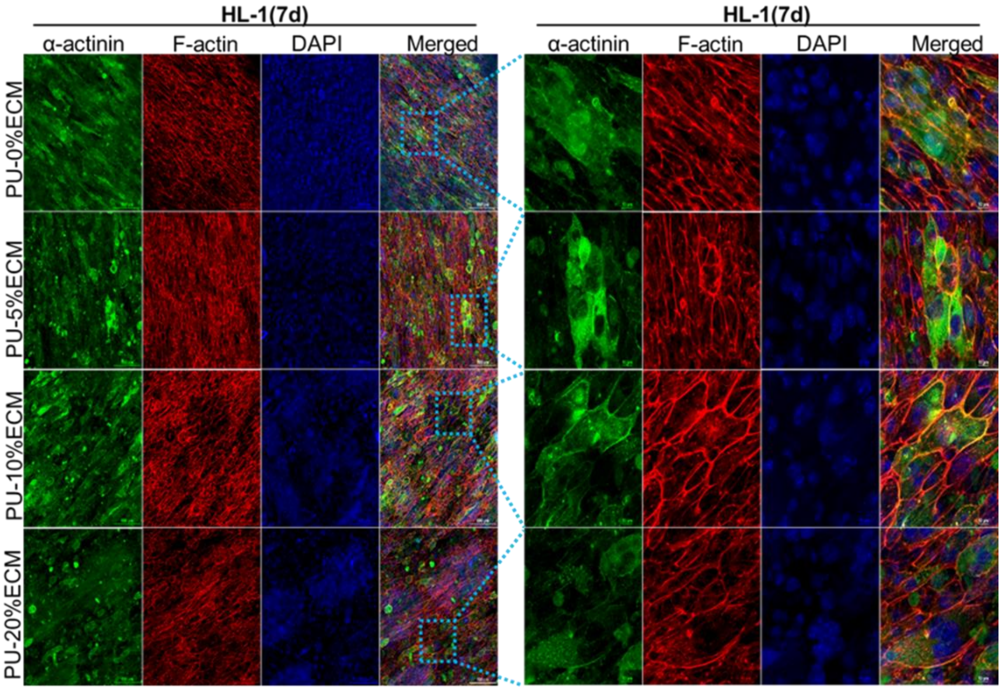

Figure 2.14: Immunofluorescence staining for α-actinin, F-actin, DAPI, and the merged images at day 7 of differentiation of HL-1 cells seeded on PU, PU-5%ECM, PU-10%ECM, and PU-20%ECM.

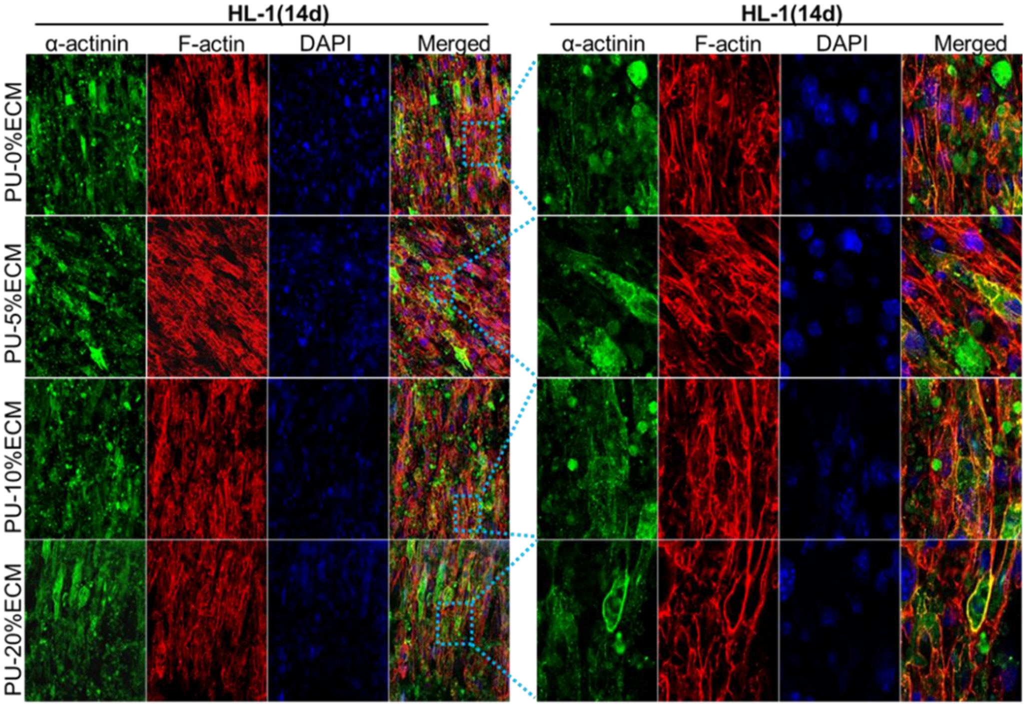

Figure 2.15: Immunofluorescence Staining for α-actinin, F-actin, DAPI, and the merged images at day 14 of differentiation of HL-1 cells seeded on PU, PU-5%ECM, PU-10%ECM, and PU-20%ECM.

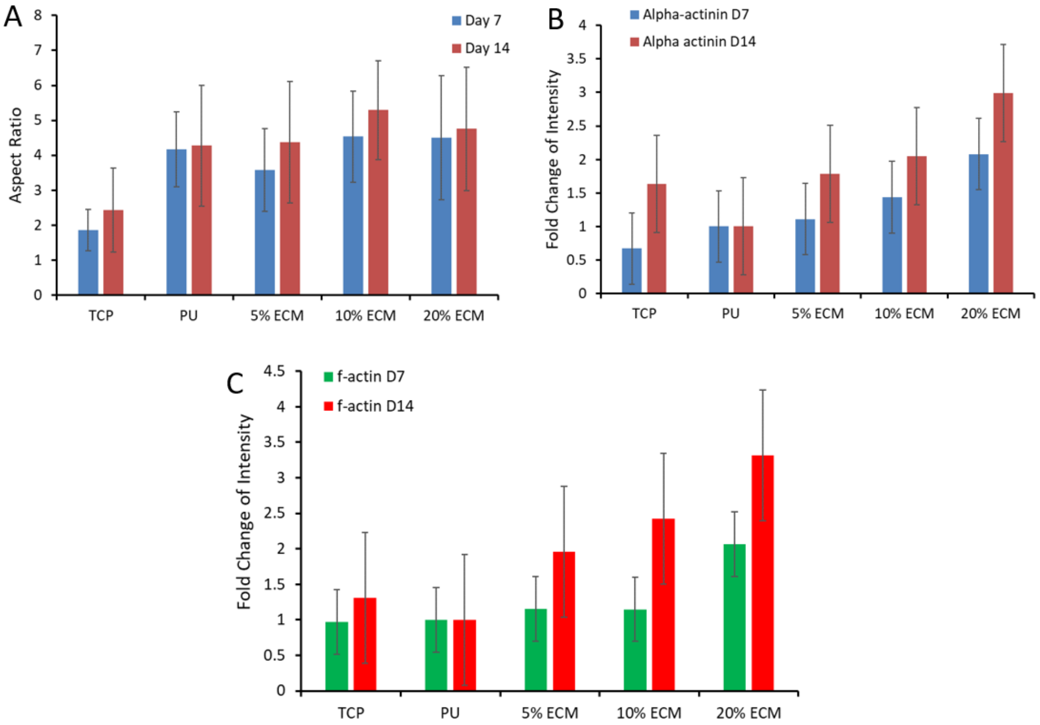

Figure 2.16: A) Aspect ratio and immunofluorescence intensity of B) α-actinin and C) F-actin of HL-1 cells on TCP, PU, PU-5%ECM, PU-10%ECM, and PU-20%ECM.

Culturing HL-1 cells on all scaffolds was successful, with cells capable of growing on all scaffolds. From live dead staining (**Figure 2.12**), all scaffolds showed little cell death over the seven days. Cells were aligned along the fibers, with apparent alignment occurring on the first day. Cell alignment was maintained throughout the seven days. On day four, cells were densely packed on the PU-10%ECM scaffold and PU-20%ECM scaffold. All scaffolds on day 7 showed similar trends of dense growth and a good dispersal of cells.

Cell alignment was evident on all scaffolds on days 7 and 14 of the culture with SEM (**Figure 2.13**). All scaffolds exhibited similar morphologies for α-actinin and F-actin (**Figure 2.14, 2.15**). The aspect ratio of HL-1 cells on aligned scaffolds had enhanced cell elongation compared to the TCP control (**Figure 2.16**). Fluorescence intensity of α-actinin and F- actin quantified cytoskeletal protein production, PU-20%ECM scaffolds had a 2-to-3-fold increase compared to PU scaffolds on days 7 and 14 of the study. A trend of more remarkable fold changes with increasing ECM content in scaffolds was observed (**Figure 2.16**).

2.3.7.2 *In vitro* culture of Rat Neonatal Cardiomyocyte on scaffolds

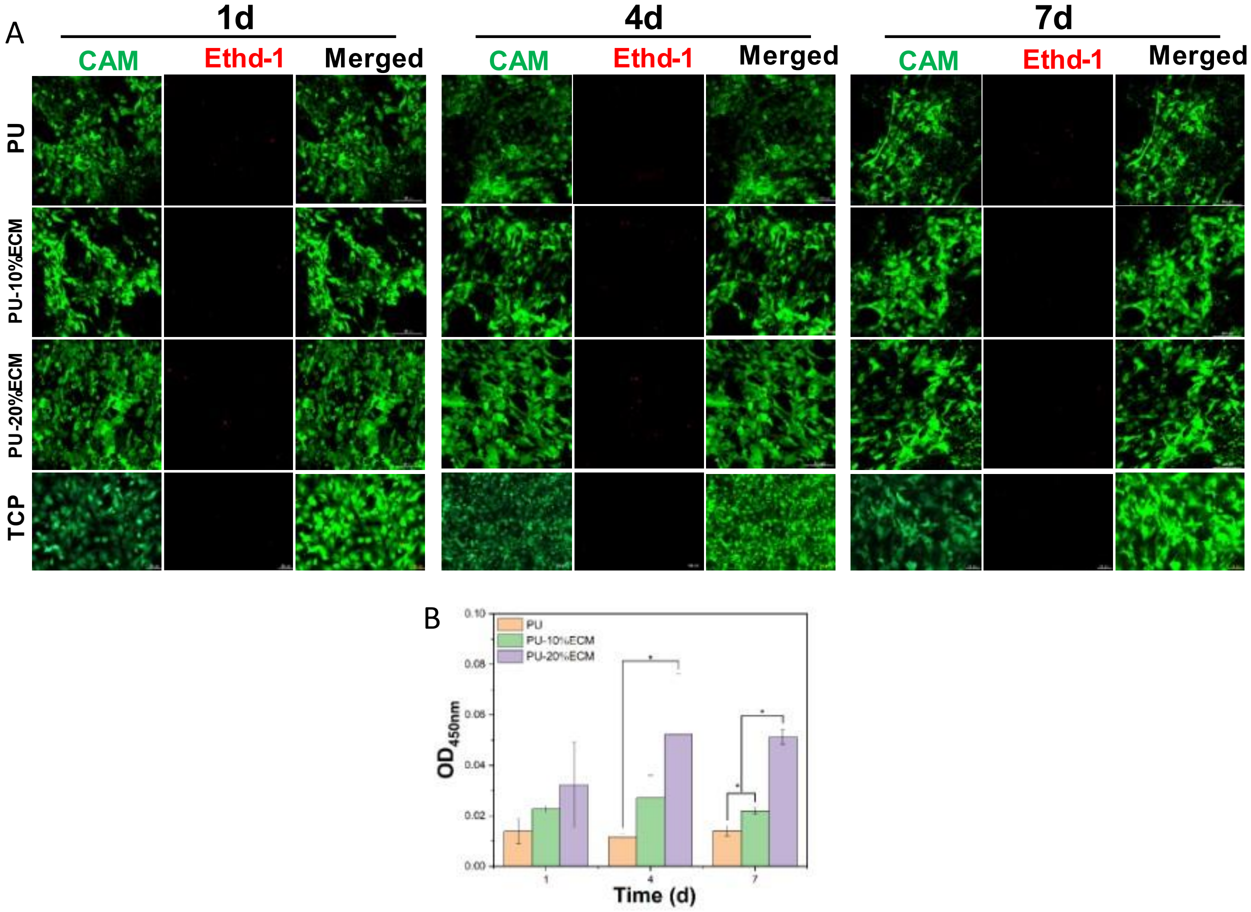

Figure 2.17: Cell viability of NNRCM on PU, PU-10%ECM, and PU-20%ECM, with A) Live/Dead staining and B) cell counting from CCK-8 results on days 1, 4, and 7.

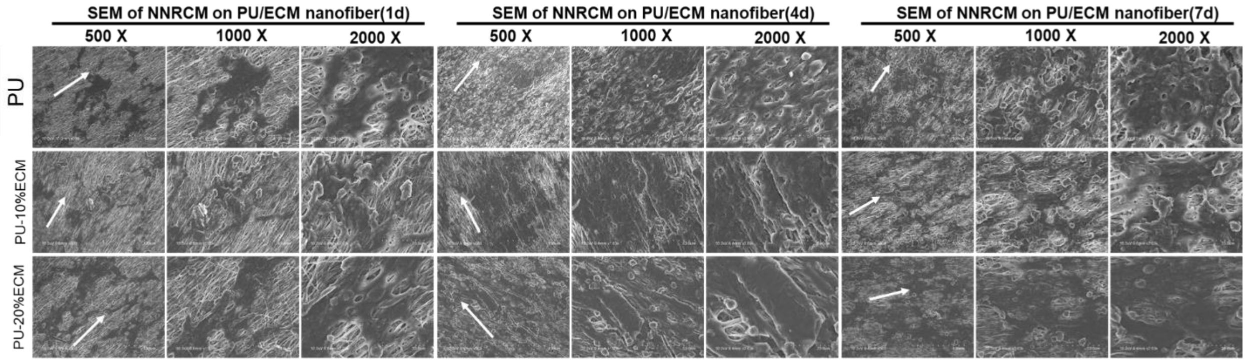

Figure 2.18: Morphology of NNRCM on PU, PU-10%ECM, and PU-20%ECM on days 1, 4, and 7. Variable magnifications of 500x, 1000x, and 2000x were used during SEM.

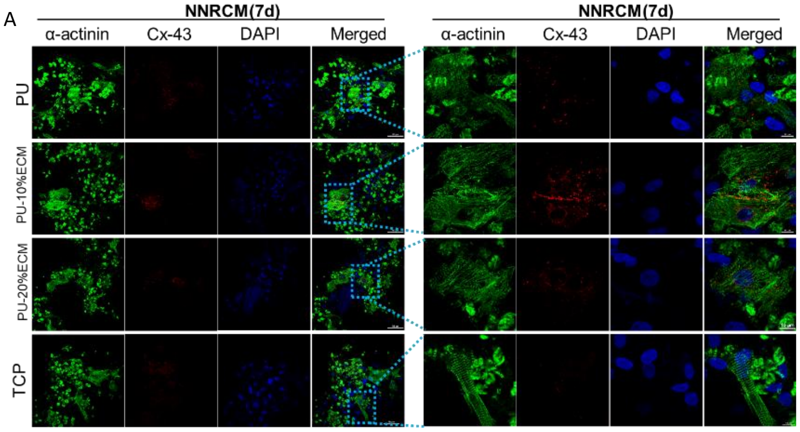

B

Sample	Sarcomere Length (μm)	Z-line Length (μm)	Aspect Ratio
TCP	1.40 ± 0.23[a]	1.79 ± 0.34[a]	2.63 ± 1.20[a]
PU	1.52 ± 0.30[a,b]	1.89 ± 0.45[a]	3.69 ± 1.29[b]
PU-10%ECM	1.56 ± 0.31[b]	2.97 ± 0.64[b]	4.42 ± 1.08[b]
PU-20%ECM	1.80 ± 0.24[c]	3.26 ± 0.70[c]	4.23 ± 1.22[b]

*a, b, and c represent significantly different groups for each characteristic

Figure 2.19: A) Immunofluorescence staining for α-actinin, Cx-43, and DAPI on PU and PU-5%ECM, PU-10%ECM, and PU-20%ECM on day 7. B) Table summary of sarcomere length, Z-line length, and aspect ratio of NNRCM on scaffolds.

Culturing neonatal rat cardiomyocytes (NNRCM) on the tested scaffolds exhibited favorable growth of cells over the study. Notably, there was a significant increase in growth exhibited by the PU-20%ECM scaffold compared to the PU scaffold on day 4. Growth on PU-20%ECM significantly increased compared to PU and PU-10%ECM on day 7 (**Figure 2.17B**). Similarly, PU-10%ECM exhibited a significant increase in growth compared to PU on day 7. Across all time points' precise alignment of cells was exhibited on all aligned scaffolds compared to the control TCP (**Figure 2.17A**). Cell elongation was noted after one day of culture on aligned scaffolds (**Figure 2.18**). All fibrous scaffolds exhibited striation of α-actinin on cells, with gap junction formation from Cx-43 expression (**Figure 2.19A**). There was an apparent increase in sarcomere length, Z-line length, and aspect ratio (**Figure 2.19B**).

2.4 Discussion

Fabrication of bio-hybridization synthesized polymers with tissue-derived polymers is an efficient, low-cost way to produce new potential biomaterials that harmonizes the strengths of synthetic polymers (mechanically robust properties) and tissue-derived polymers (native tissue composition and bioactive properties) [214]. Particularly in electrospinning fabrications, co-electrospinning, and concurrent electrospinning, its widely investigated nature provides proof of concept for its success [236, 237]. The researched methods of co-electrospinning with natural and synthetic polymers have failed to incorporate native cardiac ECM into its blends aimed at cardiac tissue engineering. Previously our group has investigated incorporating ECM-based hydrogels into PU based scaffolding [214]. Hence, direct incorporation of ECM into PU scaffolding to measure the effects ECM has on PU's properties is a novel investigation.

Fiber morphology and hydrophilicity of the scaffold are essential in cardiac cell growth due to the physiological cues cardiac cells rely on to proliferate and differentiate appropriately. In contrast, hydrophilicity encourages cellular attachment to the scaffold [86]. Electrospinning is popular due to the degree of customization it offers a high degree of control over the scaffolding's morphology is obtainable [238]. There was a decrease in fiber diameter compared to PU across all PU-ECM scaffolds. There was no discernible change in fiber diameter between PU-10%ECM and PU-20%ECM. This decrease in fiber diameter across all ECM concentrations with no difference between the higher concentrations allows for reasonable size control through modifying electrospinning parameters [86]. At the higher concentration of ECM inclusion, the formation of microstructures called 'nanonets' started to appear [239]. These net structures do little to impact the overall morphology and are thought to be caused by the increased presence of PBS from digested ECM forming complex molecules with components of ECM [239]. Saudi et al., investigating PCL-chitosan scaffolds, suggest that ionic salts can cause this [239]. Fiber swelling from PBS immersion was also examined to determine how the fibers would react to similar physiological conditions. The swelling was evident across all scaffolds; no trend was associated between swelling and ECM concentration. The alignment of fibrous scaffolds was unaffected by the swelling. Shrinkage of the scaffoldings was anisotropic, with shrinkage depending on fiber orientation. PU-20%ECM shrank the most in PD and XD compared to PU-10%ECM. The PD shrank significantly more than XD. As the fibers are stretched across the mandrel tension is built up in the fibers. As the fibers are heated during incubation the tension is released, causing shrinkage [240].

The contact angle of the scaffolds indicated a stark change in hydrophilicity with the inclusion of ECM into scaffolds. When only 5%ECM was included, its initial drop in contact angle was comparable to the 10% and 20% ECM concentrations. Native ECM contains lots of GAG, which are highly water absorbent to provide lubrication for smoother muscle contraction [21]. With higher concentrations of ECM, the initial drop in the contact angle is more pronounced. When examining the dynamic contact angle, scaffolds with ECM showed an apparent decrease in contact angle due to water absorbance. The higher concentrations of ECM accelerated the reduction over the two minutes, with the PU scaffold maintaining a relatively unchanged over the two minutes. Studies have indicated that more hydrophilic scaffolding has improved cellular attachment [112, 241]. Considering relatively small amounts of ECM need to be included to improve the scaffolds' hydrophilicity drastically, a small amount of ECM is required to provide benefits for cells' biocompatibility [86].

Scaffold degradability is essential in tissue engineering to maintain structural support and allow cells to grow without hindrance. Polymeric scaffolds, mainly synthetic, are less susceptible to degradation due to their resistance to degradation via hydrolysis to break their chemical bonds and enzyme degradation [68]. Incorporating natural polymers into scaffolds would increase the degradation due to the increased potential of hydrolysis acting on the susceptible natural polymers in the scaffolds [224]. Incorporating ECM into our scaffolds exhibited a similar trend, with the PU-20%ECM scaffold exhibiting the highest degree of degradation compared to all other scaffolds at each time point. Another critical aspect of scaffold degradation is the toxicity of the by-products through degradation; within the typical MI pathology, degradation of existing ECM around the area of defect releases pro-MMP factors attracting macrophages and neutrophils, which act as a conduit for cell migration [149, 242]. Incorporating ECM into our polymeric scaffold enables this aspect to be present within the scaffolding. Other ECM hydrogels documented the benefits of their gel degradation with cell viability [149, 243]. The degradation of our scaffold enables for degradation of the scaffold to pave the way for cell ingrowth and the release of pro-MMPs factors to attract host cells for integration.

The mechanical properties of scaffolds for cardiac tissue engineering applications are fundamental due to the physical demands of the heart, and the mechanical cues myocytes depend on to promote proper differentiation and maturation [68, 214]. Scaffolds that are physiologically like native tissue provides an optimal outlet for good cell growth and differentiation [64, 72]. Typically, synthetic scaffolds are much stiffer than the native tissue, which phenotypically inhibits the maintenance of cardiomyocytes, leading to impaired functions [214]. Brower et al. noted that the mechanics of infarct tissue demonstrated a stark increase in stiffness compared to the healthy native tissue [244]. Cardiac tissue scaffolds need to replace the defective tissue caused by the infarction, emphasizing the importance of physiological and biomechanical similarities. Comparisons to porcine heart tissue were performed due to the structural and mechanistic similarities between human and porcine hearts [245, 246]. Stress relaxation of the PD native LV wall showed a steep decrease in stress over 15 minutes, releasing 63 ± 5.6% of the stress. At the same time, all tested PD scaffolds could release around 30% of the applied stress, with a slight variation in stress between ECM concentrations. Most of the stress loss occurred within the first two minutes of the test. Native tissue ECM, compiled of GAGs and collagen networks, readily underwent conformational changes to compensate for sustained stress [247, 248]. The rigidity of polymeric scaffold structures limited conformational changes. Similar trends were exhibited in the XD for the scaffold and the XD native tissue. The XD PU-20%ECM demonstrated the most significant decrease, releasing 42.9 ± 1.6% of the stress, while the XD LV native tissue released 56.2 ± 3.3% of the stress. Increased ECM content improved the effectiveness of releasing stress in the XD. Creep testing is used to examine the continuing deformation of the material along with time under a constant load. Interestingly native tissue, like the scaffolds, exhibited an exponential increase in strain initially before transitioning into a slow linear growth, with indications of plateauing out near the end of the 15-minute test. Scaffolds exhibited a similar exponential increase in strain before rapidly transitioning to a shallow slope and plateauing characteristics. The initial trend of native tissue is most closely mimicked by the PU-20%ECM scaffold. The presence of collagen and other natural polymers in the ECM provides for potential conformational changes before the slower deformation of the elastic PU [247, 248]. The sizeable slow increase in strain for native tissue is due to the reorganization of collagen bundles from constant loading [247, 248]. At the same time, the polymeric scaffolds are incapable of undergoing extreme conformational changes past the initial straightening out of any wavy fibers. XD native tissue had less creep than all XD scaffolds. This drastic difference in creep is due to restrictions in the possible conformational changes derived from its inherent anisotropic nature [246]. Scaffolding exhibited a significant initial increase in creep and later a slow increase and plateauing due to the time-dependent kinematic adjustment of constitutive fibers. Failure tests of native tissue in PD and XD directions exhibited less failure stress than all scaffolds. The PD failure strains of scaffolds and native tissue were comparable for the ECM-containing scaffolding, while the PU exhibited a statistically higher failure strain. PD failure stresses across all scaffolds were statistically similar. The ECM containing scaffolds showed failure strains like native tissue. Similar strains are likely due to the reorganized collagen within the PU-ECM scaffolds [247, 248]. XD PU-20%ECM had statistically higher failure stresses compared to all scaffolds except PU-10%ECM. XD failure strains were similar, with only PU-10%ECM and PU-20%ECM statistically different. Cyclic testing for scaffoldings exhibited similar trends of viscoelastic materials. Biaxial testing revealed similar non-linear anisotropic properties. Examining the mechanical properties, the most likely scaffold to match native tissue parameters is the PU-20%ECM scaffolding. The scaffold could replicate the initial responses in stress-relaxation and creep behavior while exhibiting a similar failure strain to native tissue.

Cell studies on scaffolds were largely promising, with cells capable of growing on the scaffold and aligning themselves with the fiber orientation. Cardiac function (contractibility and consistent contractions) can be heightened when the cells can grow in an aligned formation [249]. Cell count improved among all scaffolds over time. There was a 3-fold increase in α-actinin and f-actin fluorescent intensity on the PU-20%ECM compared to PU. Wang et al. saw improvements in α-actinin and f-actin expression on their ECM-based scaffold [75]. Improvements to expression are likely due to biomolecules found within the incorporated ECM. Neonatal cardiomyocytes revealed improved cell morphologies with increasing ECM content, as shown by aspect ratio, sarcomere length, and Z-line length. Morris et al. showed that improved contraction strengths are associated with increased sarcomere and Z-line lengths [250]. The morphology of cells seeded on the aligned scaffolds reflects results obtained by Kai et al., confirming the effectiveness of our aligned nanofibrous scaffold at guiding cell development [89]. CCK-8 results demonstrate higher cell counts of NNRCM PU-20%ECM scaffolds. Tamimi et al. demonstrated similar results with increased ECM content exhibiting superior cell counts compared to their polymeric scaffold [251]. Incorporating digested ECM into polymeric scaffolds improved hydrophilicity, directly affecting cell adhesion, with improved growth rates indicating higher cellular attachment. Furthermore, the incorporation of ECM has been shown to improve functionality of cells [125, 251]. Improved aspect ratios and α-actinin structure demonstrated by sarcomere length and Z-line lengths reflect mature cell development [130]. Based on the mechanical and morphological characterizations of the scaffolds, PU-20%ECM scaffolding is most likely to be revealed as the most effective for cardiomyocyte cell growth and differentiation.

Further exploration of higher ECM content scaffolds should be considered. Results obtained, while indicative of promising results, could express improved functionality from higher ECM concentrations. Mechanically the scaffolds weren’t compromised by high levels of ECM content; further addition of ECM could be explored without compromising the mechanics. Similarly, improved *in vitro* parameters could be further improved if the trend continues.

2.5 Conclusions

An array of PU-ECM bio-hybrid nanofibrous scaffolds were synthesized via a co-electrospinning technique. The scaffolds morphology and mechanical properties were investigated via SEM, image analysis, uniaxial testing, and biaxial testing to optimize the scaffold to mechanically match the native tissue of porcine myocardium by altering ECM concentration. The scaffolding was morphological to native ECM structure with anisotropic properties. Including ECM could drastically improve the scaffolds' hydrophilicity and augment the scaffolds' mechanical properties to match that of native ECM. Further, in vitro studies of the optimized scaffolding indicate its feasibility as a cardiac scaffold. Studies with NNRCM confirm PU-20%ECM scaffolds' favorable cell interactions.

2.6 Outcomes

Based on current results, the PU-20%ECM scaffolding was comparable to all in fiber size and morphology to all other scaffolds and exhibited the highest hydrophilicity of all the scaffolds, an essential factor in cellular attachment and compatibility. The PU-20%ECM scaffold showed superior failure stresses and comparable failure strains to the LV tissue, exhibiting similar trends in creep testing as the LV tissue. These similar or excellent properties are attractive for cardiac applications, ensuring low chances for failure and providing similar physiological cues to cells. Cellular studies have indicated that HL-1's growth is viable on all scaffolds with improved protein expression in PU-20%ECM scaffolds. Similarly, NNRCM cultures display similar improvements to CM maturity on PU-20% ECM scaffolds. Currently, more studies need to be performed to conclude whether PU-20%ECM provides the best environment for myocardium growth. This project was presented at a conference at BMES and SFB.

CHAPTER III: Electrospun Elastic Nanofiber Polyurethane Scaffold Incorporated with Conductive Reduced Graphene Oxide for Muscle Cell Culture

3.1 Introduction

Electrical impulses generated by the sinoatrial node (SA) transmitted throughout the heart are needed for maintaining homeostasis within the myocardium and regular beating rhythms [252, 253]. The efficient transfer of these impulses from cardiomyocytes to surrounding cardiomyocytes enables the heart's well-timed contractions for maximal blood flow. Cell singling of electrical signals is derived from the polarization between the membrane; this polarization is vital for many cell functions and phenotypes [254]. Cardiac tissue engineering scaffolds often comprise insulative polymers, inhibiting the proper transfer of these signals throughout the scaffold [255, 256]. Cells within the insulative scaffold do not receive appropriate electrical signaling impacting their differentiation and connection to the host. Efforts to overcome this weakness have been achieved in a myriad of ways. Incorporating semiconductive polymers like polypyrrole has shown promise with increased growth of cardiomyocytes and cardiac protein marker presence [189]. Another popular technique is doping scaffolds with conductive elements. One of the main doping agents investigated has been graphene and its derivatives graphene oxide (GO) and reduced graphene oxide (rGO).

The advent of graphene and its derivatives, GO and rGO, revolutionized the material science field, leading to better sensors and high-performance transistors [257]. Graphene’s wide range of innovative properties has been quickly incorporated into the biomaterial field. The use of GO and rGO as doping agents to augment scaffolds' chemical and mechanical properties has been widely researched [175, 258, 259]. GO, and rGO have varying advantages; GO contains more hydroxyl and epoxide groups on the basal plane of the graphene sheet with edges containing carboxyl groups [260]. These oxygen groups cause GO to be more stable in aqueous solution, hydrophilic, and easy to functionalize [260]. Reduced graphene oxide is synthesized by reducing GO, lowering the number of oxygen groups on the carbon sheet. [260]. Reduction of GO makes rGO less stable in aqueous solutions, increasing difficulties in dispersal and lowering hydrophilicity; however, rGO regains its conductive properties and can be tuned depending on surface oxygen content [260]. Investigations have shown that the inclusion of GO and rGO stimulates the proliferation and maturation of neuronal and cardiac cells [184, 261]. The chemical mechanism for GO and rGO stimulation of growth is not fully understood, requiring further investigation [261, 262]. Some rGO doped scaffolding experiments have shown increased angiogenetic factors stimulation [156, 263]. In various studies of scaffolds doped with GO and rGO, the mechanical properties of the construct were strengthened, indicating a structural re-enforcing property [184, 258, 259]. Conductive doping has been vastly explored with graphene oxide (GO) or reduced graphene oxide (rGO) [260, 264-270]. Park et al. investigated rGO's effects on cardiac cell growth reporting stimulation of angiogenetic growth factor expression and increased gap junction protein from the mesenchymal stem, improving cardiac repair and function restoration [268]. An improvement in cell-to-cell communication was reported from growth on the rGO sheets due to the electrically conductive properties [263, 268].

As indicated in the literature, the plethora of benefits rGO has on tissue-engineered scaffolds leaves little doubt about its need for further exploration. Our group has extensive experience investigating biodegradable polyurethane (PU) as a tissue engineering scaffold due to its elasticity and mechanical properties [214, 233, 271]. Doping PU with rGO would create an extensible, structurally resilient, semi-conductive scaffolding material, providing optimal conditions for cardiomyocyte cell growth. A prior study that incorporated PU and rGO used thermoplastic PU (TPU) and a shallow concentration of rGO (0.025% (w/w)) in their scaffolding [175]. No attempt at conductivity measurement was documented in this study, leaving room for further investigation into the PU/rGO blend. Nazari et al. investigated the incorporation of rGO into PU and used functionalized graphene-silver further to augment the physical and chemical properties [259]. Like the previous study, TPU was used and only explored two concentrations of rGO-Ag (1% and 2%). Both previous studies investigated a non-biodegradable-based PU. A systematic investigation of rGO's effect on PUs mechanics and determining the optimal concentration to produce a conductive scaffold provides a deeper insight. Obtaining a complete understanding of the effects of rGO on myocardial cell growth helps validate rGO as an effective additive for cardiac tissue engineering.

This study aims to fabricate a PU and rGO composite scaffold for cardiac tissue engineering applications. Based on prior investigations on rGO, we hypothesize that incorporating rGO into PU creates a biocompatible, conductive, elastic scaffold that can withstand the heart's physiological demands and improve the seeded growth and differentiation cells. We focused on examining varying concentrations of rGO (w/w) compared to PU to fabricate a scaffold with optimal mechanical and biocompatible parameters. Characterizing the scaffold’s morphology and mechanical properties can determine the similarity to native tissue in its innate chemical and physical characteristics. In vitro cellular studies assess the scaffold's effects on C2C12 growth, differentiation, and gene expression, indicating if the scaffold would be a viable muscle scaffold. Studies with neonatal rat cardiomyocytes have been performed for viability, growth, and gene expression, investigating our scaffolds' effects on cardiac muscle development.

3.2 Materials and Methods

3.2.1 Materials

Polycaprolactone diol (PCL, Mn = 2000) was dried in a vacuum oven at 60°C overnight. Hexamethylene diisocyanate (HDI) and putrescine were purified via distillation. Stannous octoate (Sn (Oct)2), isopropanol, 1,1,1,3,3,3-hexafluoro-2-propanol (HFIP, Oakwood Products), anhydrous dimethyl sulfone (DMSO), and reduced graphene oxide (rGO). All materials were obtained from Sigma unless stated otherwise.

3.2.2 Biodegradable Polyurethane Synthesis

Previously published literature was referenced to synthesize biodegradable PU [43]. Briefly, a three-neck round bottom flask full of DMSO PCL diol (Mn = 2000) was dissolved under N_2. HDI and 3 droplets of $Sn(Oct)_2$ were stirred into the DMSO solution and heated to 70 °C for 3 hours. Putrescine dissolved in DMSO was stirred into the initial solution once it cooled to room temperature until a final molar ration of 1:2:1 of PCL: HDI: putrescine was achieved. The mixture was left overnight at 70 °C, and DI water precipitated the polymer. Isopropanol was used to purify the polymer to remove unreacted monomers and oligomers. The PU was then placed to dry at 60 °C for three days in a vacuum oven.

3.2.3 Electrospun rGO Doped Scaffold Fabrication

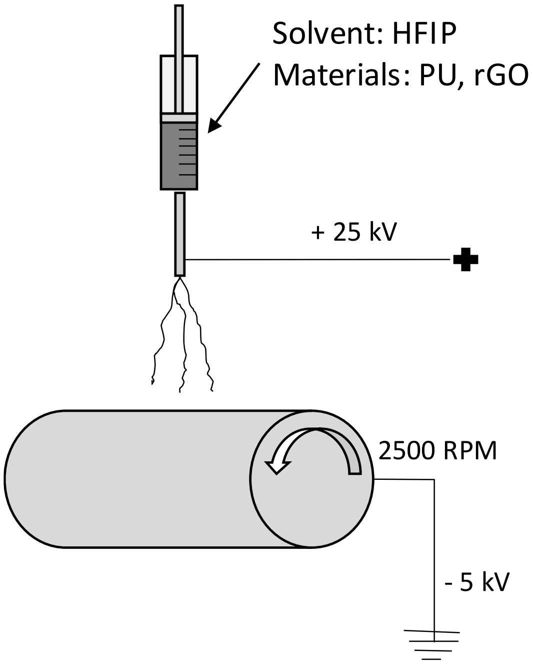

Figure 3.1: Schematic of aligned electrospinning setup

Reduced graphene oxide doped scaffolds were fabricated using a standard electrospinning process with a rotating mandrel as the collection target (**Figure 3.1**). The steel rotating mandrel (D = 150 mm, L = 40 mm) was wrapped with aluminum foil before collection. To a vial HFIP (8 mL) and rGO (0.0032g, 0.0064g, 0.0128, 0.256g) was added and stirred for 24 hours. The solution was then sonicated (25% amp) for 1 hour in an ice bath. After sonication PU (0.64g) was stirred into the solution overnight. It was sonicated once more for 1 hour in an ice bath before the solution was loaded into a 10 mL syringe, extruded at 1 ml/hour, from 15 cm, and 25 kV charge for 8 hours. The collection mandrel was kept at 2500 rpm with a -5 kV charge. After electrospinning finished, samples remained on the mandrel overnight. Samples were collected by cutting across the sheet and gently peeling off the aluminum foil. Samples were transferred to another aluminum sheet mandrel side down and stored until used.

3.2.4 Scaffold Characterization

3.2.4.1 ATR-FTIR

ATR-FTIR was performed for each fabricated scaffold using a Thermo Nicolet 6700 FTIR Spectrometer to record spectra with a wavelength range of 4000-600 cm^{-1}. Spectrum peaks were found and recorded for comparisons between scaffolds.

3.2.4.2 Scaffold Morphology Analysis

A sputter coater (Hummer VI Sputtering system) coated scaffolds with a thin gold/platinum (Au/Pt) layer. A scanning electron microscope (SEM) (Hitachi S-4800 II FE-SEM) was then used for morphological analysis of the scaffolds. The software ImageJ was used to determine fiber diameter and the degree of fiber alignment (n=120). The SEM scale bar was used as the reference bar for ImageJ analysis. Fiber angle data were exported to Excel to form a histogram and normalized curve (n=120). Scaffold shrinkage was quantified by scaffold size measurement with calipers after immersion in PBS for 24 hours in a 37 °C incubator (8 mm diameter, n = 5). After immersed samples were freeze-dried and SEM analysis was performed as before on freeze-dried samples, effects of swelling on fiber diameter and alignment were determined.

3.2.4.3 Contact Angle

A custom-built instrument controlled by FTA32 software was used to quantify the surface hydrophilicity of scaffolds. Samples were cut into 3 cm × 1 cm (n = 2) and mounted on glass slides with double-sided tape. Slides were placed on the instrument platform and adjusted for the camera focus on the side of the scaffolds. A micropipette was positioned above the scaffold. 5 µL of DI water was applied to the sample. The scaffolds were slid over; a new droplet was applied to a dry area for new images to be taken. Photos of the droplet were taken at 15, 30, 60, 90, and 120 seconds after droplet application; this was repeated three times. Droplets were applied to each sample for a total of n = 6 for each group. The FTA32 software was used to calculate the contact angle. Calculations occurred by outlining the edge of the droplet on the droplet picture.

3.2.4.4 *In vitro* Enzymatic Degradation

Scaffold samples were cut and weighed (W_0), with W_0 at least 25 mg, and were then immersed in 2 mL of a lipase/PBS solution (100 U/mL) at 37 °C. Samples at days 3, 7, and 14 (n = 3 for each time point) after immersion, with the solution, refreshed every 3 days. After collection, samples were washed in DI water and freeze dried. The samples were then reweighed (W_1), and % degradation was calculated using the following equation:

$$\% \, Degradation = \frac{W_1}{W_0} \times 100 \qquad [1]$$

3.2.4.5 Conductivity Measurement

Films were produced using the same solution preparation method for electrospinning as above; however, solutions were poured into dishes. Dishes were covered with aluminum foil, poked with holes, and left overnight for evaporation. Films were cut into 8 mm diameter circle samples (n = 3) to perform conductivity testing. Scaffolds were placed on a glass slide and a 4-point probe (Four-Point Probe, Ossila) for measurement recording. The current was measured over a sweeping voltage of 0 to 10V; sheet resistance measurements were taken 100 times once the target current of 10 µamps was achieved. The software calculated the average conductivity and resistivity of the scaffolds. Testing was also performed on scaffolds after soaking in PBS at 37°C for 24 hours. Scaffolds had excess PBS removed by blotting with a paper towel before measurements were taken.

3.2.4.6 Mechanical Testing

3.2.4.6.1 Uniaxial Mechanical Testing

Fabricated scaffolds and native tissue (n = 5) were cut into 5 mm × 30 mm strips to perform uniaxial testing (Test Resources, MN). Native tissue samples were harvested from the LV of porcine hearts. The LV wall composed of both epicardium and myocardium was cut into samples of 1-2 mm thick strips (5 mm × 30 m). Scaffolds were cut in the PD and XD. Scaffolds were soaked in PBS at 37 °C for 24 hours before testing. LV tissue samples were tested when at room temperature. The grip-to-grip length of the loaded samples was about 10 – 15 mm. Stress relaxation, creep, cyclic, and test to failure testing were run on samples with a sampling rate of 20 samples/second. For stress relaxation and creep, 100 g was used as the target load and a jogging speed of 10 mm/min, with each testing lasting for 15 minutes once the target load was achieved. Cyclic testing required samples to be stretched to 30% strain for ten cycles. Failure testing was ended once samples broke. Data was exported to Excel for stress and strain calculations and graphing.

3.2.4.6.2 Biaxial Mechanical Testing

Like uniaxial preparation of LV porcine wall, samples were cut into 1-2 mm thick squares (1 cm × 1 cm) and tested at room temperature. Fabricated scaffold (n = 3) samples were cut into 1 cm × 1 cm squares and marked to know the orientation for biaxial testing. Four markers made of white tape were added to the samples to track deformation, and sutures were used to load samples into a custom biaxial instrument. The load was set to 60 N/m:60 N/m, and data was processed in Excel.

3.2.5 Cell Compatibility and Behavior

Scaffolds used in C2C12 studies consisted of PU, PU-1%rGO, PU-4%rGO, PU-10%rGO, and tissue culture plastic. Neonatal rat cardiomyocyte cultures occurred on PU, PU-4%rGO, PU-10%rGO, and tissue culture polystyrene (TCP).

3.2.5.1 *In* vitro C2C12 Cell Culture on PU-rGO Scaffolds

Investigating the impact scaffolds have on cell behavior was analyzed with the following groups: PU, PU-1%rGO, PU-4%rGO, PU-10%rGO, and tissue culture plastic (TCP). The samples were cut into 15 mm × 15 mm squares. They were taped onto circular glass cover slides. In a 24-well plate the samples were placed and held with stainless steel rings. They were sterilized via UV light for 60 minutes on both sides. Scaffolds were submerged in sterile PBS 3 times at 15-minute intervals to remove any residual solvent. DMEM is added to the wells and placed in the incubator for 2 hours before seeding cells. Scaffolds were prepared similarly for proliferation and differentiation, with a cell density of 5×10^4 and 1×10^5 cells/well, respectively. Differentiation studies began with growth media for the first 24 hours before shifting to the differentiation media till the end of the study. Cells cultured for growth studies remained in the growth media the entire study. Cells were incubated for seven days at 37 °C with 95% air and 5% CO_2 at high humidity. Growth media was composed of DMEM supplemented with 10% fetal bovine serum (FBS), 100 U/mL penicillin and streptomycin, and two mM L-glutamine. Differentiation media consisted of DMEM supplemented with two mM L-glutamine, 100 U/mL penicillin and streptomycin, and 1% FBS.

3.2.5.2 *In vitro* Culture of Neonatal Rat Cardiomyocytes on PU-rGO Scaffolds

Ventricular neonatal rat cardiomyocytes (NNRCM) (Lonza, R-CM-561O were cultured for two days in a T25 flask before seeding on scaffolds. After resuscitating the cells, they were cultured in cardiac myocyte growth media (RCGM) BulletKit™ (Lonza, CC-4515) for four hours before replacing 80% of the media with RCGM BulletKit™ supplemented with 200 µM bromodeoxyuridine (BrdU) (Lonza, CC-4519). Scaffolds (n = 8) were prepared by cutting the scaffolds into 5 mm diameter circles with a press cut, with UV sterilization lasting for 60 minutes on each side before affixing to the bottom of a 96 well plate with plastic holders. Scaffolds were washed with PBS thrice at 15-minute intervals and then incubated with RCGM BulletKit™ for two hours before seeding with CM. Cells were seeded with a 1×10^5 cells/well density in the RCGM BulletKit™ supplemented with 200µM BrdU, replacing 50% of the media every three days. Seeded scaffolds were incubated at 37°C with high humidity and 95% air and 5% CO_2 for the seven-day study. RCGM Bulletkit™ is composed of rat cardiac myocyte basal medium (Lonza, CC-3275) and RCGM SingleQuots™ Kit (Lonza, CC4516).

3.2.5.3 Live/Dead Staining on PU-rGO Scaffolds

Live/dead staining was performed on days 1, 4, and 7 of culture in growth media to assess the cell viability of cells on nanofibrous scaffolds. Cells were stained green with calcein-AM to indicate live cells, while ethidium homodimer-1 (EthD-1) was used to stain dead cells red. Samples were removed from the media and washed with PBS twice before treatment with two µM calcein AM and four µM EthD-1 in DMEM for 30 minutes at 37 °C. An inverted fluorescent microscope (Nikon Eclipse Ti) was utilized to capture images of cells.

3.2.5.4 CCK-8 Cell Counting on PU-rGO Scaffolds

A cell counting kit, CCK-8 (Sigma), was used to measure cell viability. It was performed on days 1, 4, and 7. Briefly, cell media was removed from target wells and replaced with 100 µL of DMEM and 10 µL of CCK-8 solution, and one blank well was also filled with the same solution before they were placed in the incubator for 1 hour (n = 3). After incubation, the media was removed from wells and placed in a new 96-well plate for microplate reading. The media-filled 96-well plate was placed in a microplate reader (Tecan Spark 10M) with a target wavelength of 450 nm and a reference wavelength of 650 nm. The cell-laden wells were washed with PBS twice before filling with their required cell media for continued use in the study. Obtained absorption values from wells were used to calculate the OD by subtracting the blank absorbance from the obtained values.

3.2.5.5 Cell Morphology on PU-rGO Scaffolds

Differentiation cultures were fixed and imaged with SEM to assess cellular alignment on the scaffold on days 3 and 7. Wells had their differentiation media removed and replaced with PBS twice to wash scaffolds. A 2.5% glutaraldehyde solution was introduced for 15 minutes to fix the cells, after which it was washed with PBS. Ethanol solutions with increasing concentrations (50%, 70%, 80%, 90%, 95%, and 100%) were added to the wells for 5 minutes, except for 100% ethanol which was done twice, to dehydrate the samples. Scaffolds were left to dry on a mat for 24 hours to air dry before SEM, following the same protocol previously described.

3.2.5.6 Immunofluorescence Staining on PU-rGO Scaffolds

C2C12 seeded on scaffolds in differentiation media after 3 and 7 days had immunofluorescence staining for myosin heavy chain (MHC) and F-actin. NNRCM seeded scaffolds stained on day 7 for α-actinin and Cx-43. Scaffolds were washed with PBS twice before fixing with a 4% paraformaldehyde solution for 15 minutes. The 4% paraformaldehyde solution was washed off the scaffold using PBS before submerging in a 0.3% Triton X-100 in PBS to permeabilize cells for 10 minutes under incubation. A 2% bovine serum albumin (BSA) in PBS solution was introduced to the scaffolds at room temperature for 60 minutes before treatment with the primary antibody (Myosin Heavy Chain (MHC) antibody,1:50-1:100, Santa Cruz; monoclonal anti-α-actinin (sarcomeric), 1:50-1:100, Santa Cruz; anti-connexin-43 rabbit antibody, 1:200, Santa Cruz) in 1% BSA solution overnight at 4°C. Scaffolds were washed three times with PBS before treatment with the secondary antibody (goat anti-mouse IgG (H+L) Highly Cross-Adsorbed Secondary Antibody, Alexa Fluor™ Plus 555, 1:1000 for α-actinin; Alexa Fluor™ 594 goat anti-rabbit IgG (H+L) for Cx-43) in a 1% BSA for 1 hour in the dark at room temperature. Scaffolds were treated with tetramethyl rhodamine isothiocyanate (TRITC) labeled phalloidin (1:400) in a 1% BSA solution for 20 minutes in the dark at room temperature; cells were also counterstained with 4', 6-diamidino-2-phenylindole (DAPI, 300nM) for the cell nuclei. Scaffolds were washed three times with PBS before imaging. A confocal laser fluorescence microscope (Nikon A1R HD25 Confocal Microscope) was used to take images of the cells. ImageJ was used to measure the cell length, width, sarcomere length, and Z-line length [234, 235]. Five representative images per sample were analyzed for calculations and averages. The following equations were used for image analysis:

$$Aspect\ Ratio = \frac{Length\ of\ Cell}{Width\ of\ Cell} \qquad [2]$$

3.2.6 Statistical Analyses

Data obtained was reported as mean ± standard deviation. Comparisons between two groups used a two-tailed Student's t-test to determine statistical significance. A statistical difference was indicated with a P-value less than 0.05. A one-way analysis of variance (ANOVA) test was used for comparisons between more than two groups. Similarly, when the P-value was less than 0.05, then statistical significance was indicated. A Tukey test was performed on ANOVA results which with statistical significance. Excel did the calculation for all analyses

3.3 Results

3.3.1 Scaffold Fabrication

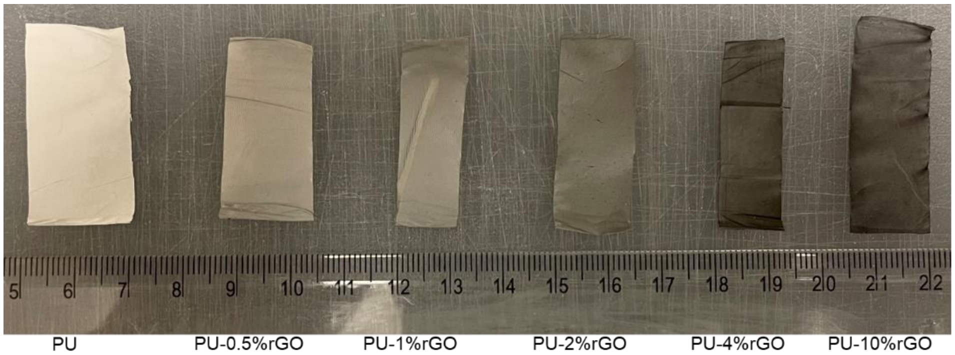

Figure 3.2: Electrospun image of PU, PU-0.5%rGO, PU-1%rGO, PU-2%rGO, PU-4%rGO, and PU-10%rGO. Scaffolds retained a shine across all rGO concentrations and darker coloration with increasing rGO.

All scaffolds were silky to the touch (**Figure 3.2**). Scaffolds took on a darker color with the increase in rGO concentration. When removed from the mandrel, bundling up from the release of circular stress was less noticeable with increasing rGO concentration.

3.3.2 ATR-FTIR Surface Characterization

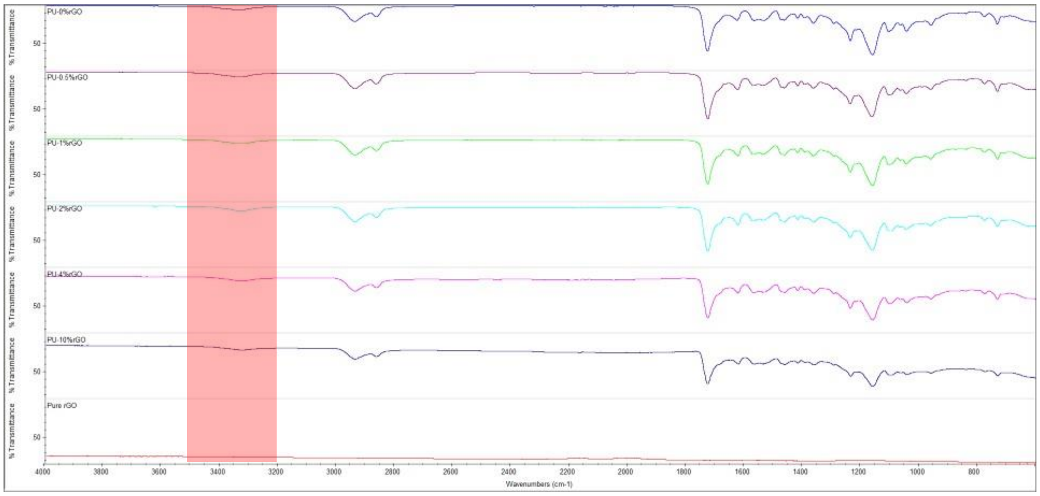

Figure 3.3: ATR-FTIR spectra of PU, PU-0.5%rGO, PU-1%rGO, PU-2%rGO, PU-4%rGO, PU-10%rGO scaffolds, and rGO flakes in the wavelength range of 4000-600 cm^{-1}.

The FTIR spectra revealed chemical interactions between rGO and the functional groups found on the PU chain (**Figure 3.3**). There was a noticeable shift across all scaffolds with increased rGO concentration. The pure rGO spectra were relatively flat with no distinct peaks. A broad peak centered around 3300 cm^{-1} displays more broadening with increasing rGO concentration. This peak corresponds to O-H bonds.

3.3.3 Scaffold Morphology Analysis

Table 3.1: Summary of shrinkage of PU, PU-0.5%rGO, PU-1%rGO, PU-2%rGO, PU-4%rGO, and PU-10%rGO after immersion in PBS at 37°C for 24 hours

% rGO	XD (mm)	PD (mm)	% Shrink along XD	% Shrink along PD
0	7.5 ± 0.22^{a,b}	5.53 ± 0.09^{a}	6.2 ± 2.8^{a,b}	30.8 ± 1.2^{a}
0.5	7.4 ± 0.19^{a,b}	5.46 ± 0.09^{a}	7.6 ± 2.4^{a,b}	31.7 ± 1.1^{a}
1	6.9 ± 0.26^{b}	5.35 ± 0.19^{a}	13.2 ± 3.2^{b}	33.1 ± 2.4^{a}
2	7.5 ± 0.07^{a,b}	5.64 ± 0.16^{a}	6.3 ± 0.9^{a,b}	29.5 ± 2.1^{a}
4	7.2 ± 0.23^{a,b}	6.12 ± 0.18^{b}	10.2 ± 2.9^{a,b}	23.6 ± 2.2^{b}
10	7.7 ± 0.42^{a}	6.32 ± 0.18^{c}	3.6 ± 5.2^{a}	21.0 ± 2.3^{c}

*a, b, and c represent significantly different groups for each characteristic

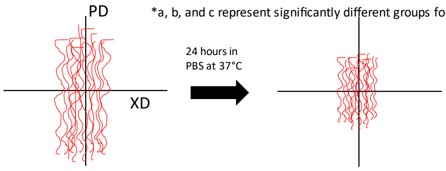

XD: Cross Preferred Fiber Direction
PD: Preferred Fiber Direction

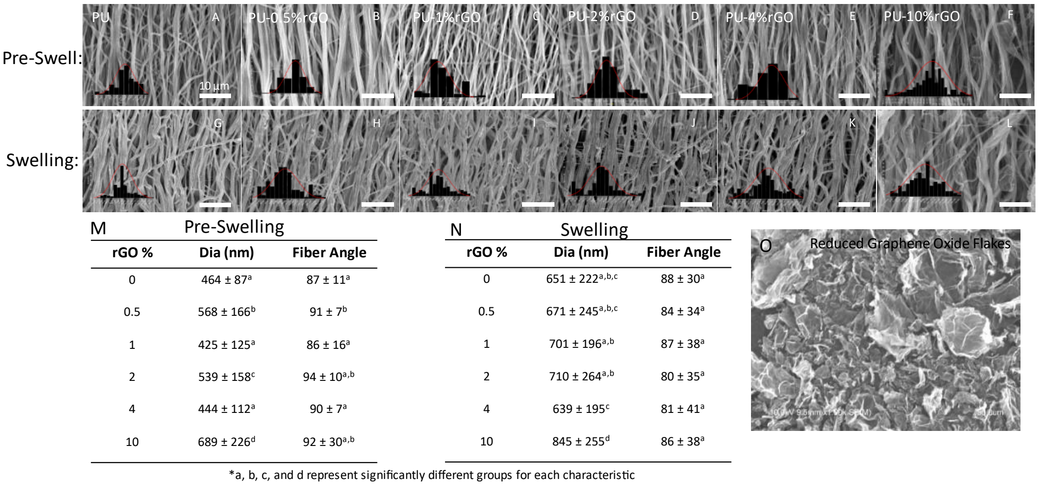

M Pre-Swelling

rGO %	Dia (nm)	Fiber Angle
0	464 ± 87^{a}	87 ± 11^{a}
0.5	568 ± 166^{b}	91 ± 7^{b}
1	425 ± 125^{a}	86 ± 16^{a}
2	539 ± 158^{c}	94 ± 10^{a,b}
4	444 ± 112^{a}	90 ± 7^{a}
10	689 ± 226^{d}	92 ± 30^{a,b}

N Swelling

rGO %	Dia (nm)	Fiber Angle
0	651 ± 222^{a,b,c}	88 ± 30^{a}
0.5	671 ± 245^{a,b,c}	84 ± 34^{a}
1	701 ± 196^{a,b}	87 ± 38^{a}
2	710 ± 264^{a,b}	80 ± 35^{a}
4	639 ± 195^{c}	81 ± 41^{a}
10	845 ± 255^{d}	86 ± 38^{a}

*a, b, c, and d represent significantly different groups for each characteristic

Figure 3.4: A-F) Images taken with SEM of PU, PU-0.5%rGO, PU-1%rGO, PU-2%rGO, PU-4%rGO, and PU-10%rGO before and G-L) after immersion in PBS at 37°C for 24 hours. M) Fiber analysis table before and N) after immersion in PBS at 37°C for 24 hours for PU, PU-0.5%rGO, PU-1%rGO, PU-2%rGO, PU-4%rGO, and PU-10%rGO and O) rGO flakes used in scaffold fabrication SEM image. Scale bar length is 10 µm.

Continuous highly aligned nanofibrous scaffolds were observed with no indication of beading between all blends of PU and rGO (**Figure 3.4A-L**). Some flakes of rGO were observable in the images, with more detectable flakes in the high concentrations of rGO scaffolds. The PU scaffold had an average fiber diameter of 464 ± 87 nm. The average fiber diameter of PU-0.5%rGO, PU-1%rGO, PU-2%rGO, PU-4%rGO, and PU-10%rGO was 568 ± 166 nm, 425 ± 125 nm, 539 ± 158 nm, 444 ± 112 nm, and 689 ± 226 nm, respectively. PU-10%rGO had significantly larger fiber diameters than all other scaffolds, with p values < 0.01. Comparatively, PU had the most petite fiber diameters compared to the other scaffolds, with p values < 0.01. There was no significant difference in diameter between PU and PU-1%rGO. Similarly, the fiber angle had no significant change between the PU and PU-rGO concentrations except PU-0.5%rGO, with a p-value < 0.01. PU scaffold exhibited a fiber angle of 87 ± 11°. Scaffolds with increasing amounts of rGO exhibited angles of 91 ± 7°, 86 ± 16°, 94 ± 10°, 90 ± 7°, and 92 ± 30° for PU-0.5%rGO, PU-1%rGO, PU-2%rGO, PU-4%rGO, and PU-10%rGO, respectively. PU-0.5%rGO was significantly different in fiber alignment than PU, PU-1%rGO, and PU-4%rGO, with p values < 0.05. The rGO flakes imaged show multilayered flakes with various sizes between flakes.

PU exhibited a fiber diameter of 651 ± 222 nm after 24 hours in PBS (**Figure 3.4G-L**). Scaffolds with increasing concentrations of rGO also exhibited swelling with PU-0.5%rGO, PU-1%rGO, PU-2%rGO, PU-4%rGO, and PU-10%rGO fiber diameters measured as 671 ± 245 nm, 701 ± 196 nm, 710 ± 264 nm, 639 ± 195 nm, and 845 ± 255 nm, respectively. PU-10%rGO exhibited a significantly larger fiber diameter than other scaffolds, with p values < 0.001. The PBS immersed PU had a fiber angle of 88 ± 30°. Scaffolds with increasing amounts of rGO exhibited angles of 84 ± 94°, 87 ± 38°, 80 ± 35°, 81 ± 41°, and 86 ± 38° for PU-0.5%rGO, PU-1%rGO, PU-2%rGO, PU-4%rGO, and PU-10%rGO, respectively. No difference was found between the fiber angle after swelling.

Shrinkage of scaffolds exhibited anisotropic properties with variations in shrinkage depending on scaffold orientation (**Table 3.1**). The PD PU scaffold shrank 30.8 ± 1.2% of the original length. Scaffolds containing rGO were 31.7 ± 1.1%, 33.1 ± 2.4%, 29.5 ± 2.1%, 23.6 ± 2.2%, and 21.0 ±2.3% for PU-

0.5%rGO, PU-1%rGO, PU-2%rGO, PU-4%rGO, and PU-10%rGO, respectively. At lower concentrations of rGO, there was little to no impact on shrinkage effects; at higher concentrations (4% and 10%), the shrinkage decreased compared to the PU sample. PU-4%rGO and PU-10%rGO shrank significantly less than all other scaffolds, with p values < 0.01. Overall, PU-10%rGO shrank the least, significantly different from PU-4%rGO with a p-value < 0.05. The shrinkage of XD scaffolds was much less than the PD. XD PU shrank 6.2 ± 2.8% of its original size. The rGO containing scaffolds shrank 7.6 ± 2.4%, 13.2 ± 3.2%, 6.3 ± 0.9%, and 10.2 ± 2.9%, and 3.6 ± 5.2% of their original size for PU-0.5%rGO, PU-1%rGO, PU-2%rGO, PU-4%rGO, and PU-10% rGO, respectively. There were no significant differences between XD scaffolds except between PU-1%rGO and PU-10%rGO, with a p-value < 0.05.

3.3.4 Contact Angle

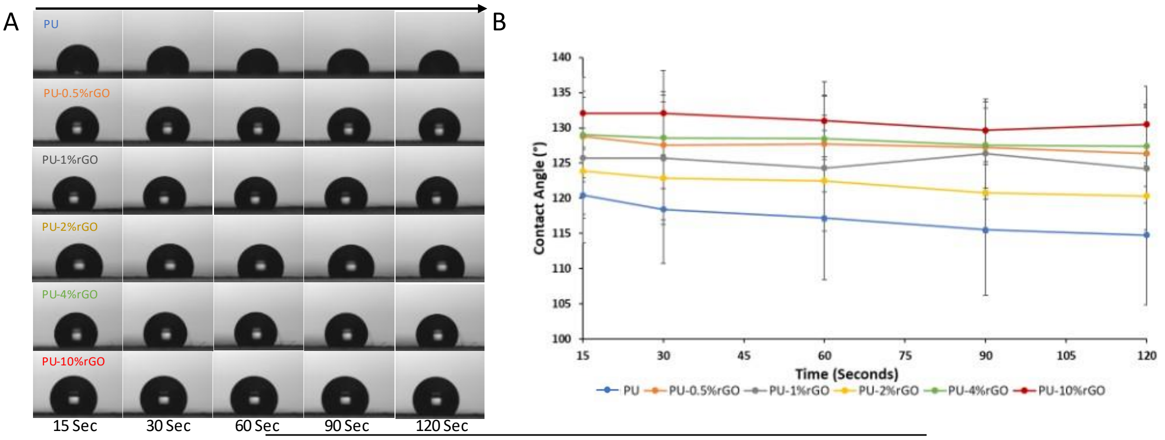

C

%rGO	CA (°) 15 Sec	CA (°) 30 Sec	CA (°) 60 Sec	CA (°) 90 Sec	CA (°) 120 Sec
0	120 ± 7^{a}	118 ± 8^{a}	117 ± 9^{a}	116 ± 9^{a}	114 ± 9^{a}
0.5	$129 \pm 6^{a,b}$	$128 \pm 6^{a,b}$	$128 \pm 7^{a,b}$	$127 \pm 7^{a,b}$	$126 \pm 7^{a,b}$
1	$126 \pm 9^{a,b}$	$126 \pm 7^{a,b}$	$124 \pm 8^{a,b}$	$126 \pm 6^{a,b}$	$124 \pm 9^{a,b}$
2	124 ± 6^{a}	123 ± 6^{a}	123 ± 7^{a}	$121 \pm 6^{a,b}$	120 ± 6^{a}
4	$129 \pm 6^{a,b}$	$129 \pm 6^{a,b}$	$128 \pm 6^{a,b}$	$128 \pm 6^{a,b}$	$127 \pm 6^{a,b}$
10	132 ± 5^{b}	132 ± 6^{b}	131 ± 6^{b}	130 ± 4^{b}	130 ± 5^{b}

*a, b, represent significantly different groups for each characteristic

Figure 3.5: A) Droplet at 15, 30, 60, 90, and 120 seconds after application for PU, PU-0.5%rGO, PU-1%rGO, PU-2%rGO, PU-4%rGO, and PU-10%rGO B) Change of contact angle with time for PU, PU-0.5%rGO, PU-1%rGO, PU-2%rGO, PU-4%rGO, and PU-10%rGO. C) Contact angle values over 120 seconds for PU, PU-0.5%rGO, PU-1%rGO, PU-2%rGO, PU-4%rGO, and PU-10%rGO.

The addition of rGO to scaffolds potentially impacts the overall hydrophilicity of the scaffold and affects the cell attachment and proliferation on the scaffold. PU scaffolds were observed to have a contact angle of 120 ± 7° 15 seconds after the droplet was placed. PU-0.5%rGO, PU-1%rGO, PU-2%rGO, PU-4%rGO, and PU-10%rGO had contact angles of 129 ± 6°, 126 ± 9°, 124 ± 6°, 129 ± 6°, and 132 ± 5° respectively. The contact angle of the scaffolds was measured over 120 seconds, with little change in the contact angle. The effect various concentrations of rGO have on the contact angle is shown in **Figure 3.5**. PU-10%rGO was significantly different from PU at all time points, with p values < 0.05. PU-10%rGO was also considerably different from PU-2%rGO at all periods except after 90 seconds, with p values < 0.05.

3.3.5 *In vitro* Enzymatic Degradation

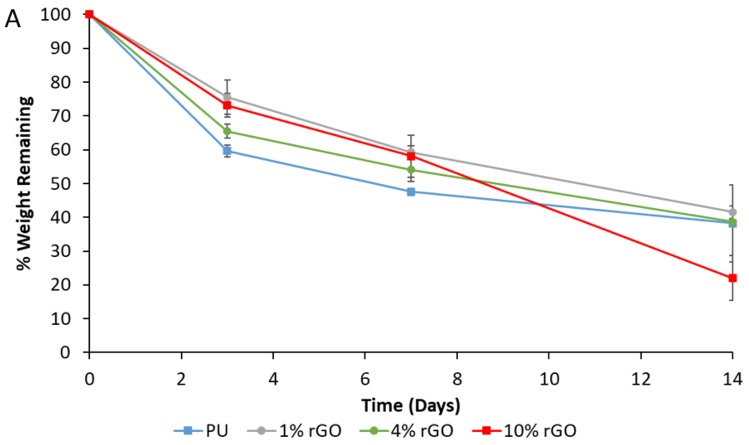

B

%rGO	0	1	4	10
Day 3	59.6 ± 1.8^{a}	75.5 ± 5.1^{b}	65.5 ± 2.1^{a,c}	73.1 ± 3.5^{b,c}
Day 7	47.5 ± 0.9^{a}	59.3 ± 2.0^{b}	54.0 ± 3.5^{a,b}	58.1 ± 6.1^{b}
Day 14	38.2 ± 11.4^{a,b}	41.6 ± 1.9^{b}	38.6 ± 0.7^{a,b}	22.0 ± 6.7^{a}

*a, b, and c represent significantly different groups for each characteristic

Figure 3.6: A) % remaining weight of *in vitro* enzymatic degradation of PU, PU-1%rGO, PU-4%rGO, and PU-10%rGO over the course of the 14-day study. B) Summary of values for % remaining weight at each time point. The degradation solution was composed of PBS and 100 U/mL lipase; samples were incubated with the solution for 14 days.

All scaffolds retained at least 20% of their weight by the end of the 14-day study (**Figure 3.6**). On day 3, the PU-1%rGO (75.5 ± 5.1%) and PU-10%rGO (73.1 ± 3.5%) scaffold degraded significantly less than the PU scaffold (59.6 ± 1.8%). This trend continued on day 7, with PU-1%rGO (59.3 ± 2.0%) and PU-

10%rGO (58.1 ± 6.2%) were still significantly different than PU (47.5 ± 0.9%). On day 14, the trend was broken, with PU-10%rGO exhibiting the highest amount of degradation, retaining only 22.0 ± 6.7% of the mass, with the only statistical difference between PU-1%rGO and PU-10%rGO, with a p-value < 0.05.

3.3.6 Conductivity

Table 3.2: Conductivity of PU, PU-1%rGO, PU-4%rGO, and PU-10%rGO film

%rGO	Dry Sheet Resistance (Ω/[])	Dry Resistivity (Ω*m)	Dry Conductivity (S/m)	Wet Sheet Resistance (Ω/[])	Wet Resistivity (Ω*m)	Wet Conductivity (S/m)
0%	Not Detectable	Not Detectable	Not Detectable	Not Detectable	Not Detectable	Not Detectable
1%	Not Detectable	Not Detectable	Not Detectable	Not Detectable	Not Detectable	Not Detectable
4%	554317 ± 203030[a]	182.9 ± 67.0[a]	0.006 ± 0.001[a]	Not Detectable	Not Detectable	Not Detectable
10%	33163 ± 21287[b]	7.3 ± 2.6[b]	0.149 ± 0.035[b]	36670 ± 8004	21.6 ± 4.7	0.049 ± 0.015

*a and b represent significantly different groups for each characteristic

Polymer composite films were used for conductivity measurement due to an inability to obtain readings using the fibrous scaffolds. At concentrations of rGO lower than 4%, no measurements were obtained, and any obtained were noise and inconsistent (data not shown). **Table 3.2** shows the lower resistivity and higher conductivity due to increased rGO doping, with PU-10%rGO having significantly higher conductivity ($p < .0001$). Similarly, sheet resistance and resistivity decreased in response to increasing the amount of rGO in the films. Resistivity is inversely related to conductivity. Wet conductivity measurements exhibited lower conductivity when measuring using the same parameters compared to the dry conductivity measurements. The decrease in conductivity was thought to be due to the bulk conductivity measurement coming from the PBS.

3.3.7 Mechanical Testing

3.3.7.1 Stress-relaxation Behavior

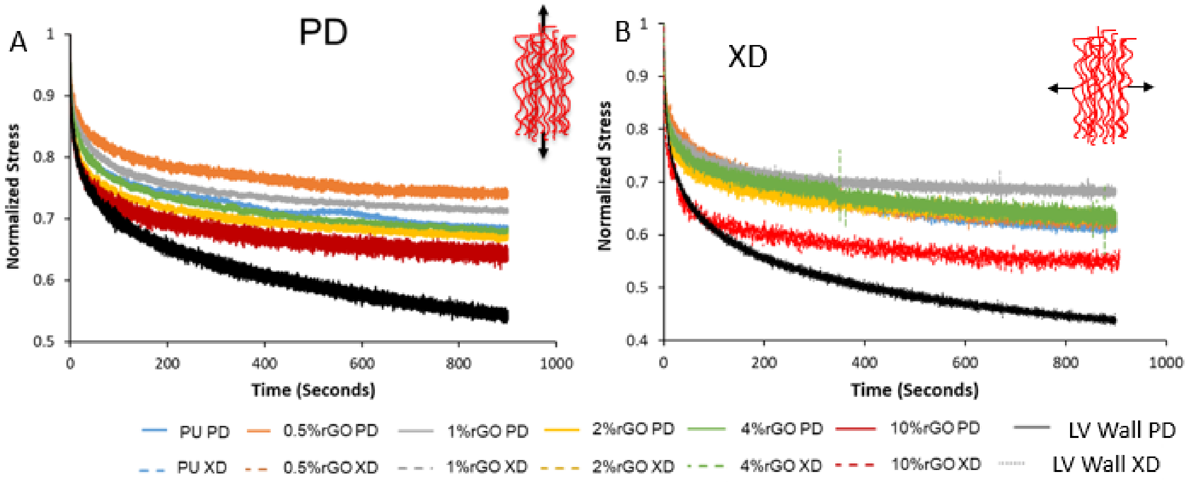

C

% rGO	0%	0.5%	1%	2%	4%	10%	LV
SR: PD (%)	31.3 ± 1.2^{a}	25.6 ± 5.4^{b}	28.6 ± 0.7^{b}	32.8 ± 2.1^{a,c}	31.7 ± 3.2^{a,b}	36.6 ± 2.6^{c}	45.6 ± 4.7^{d}
SR: XD (%)	39.0 ± 1.9^{a}	36.5 ± 1.4^{b}	32.0 ± 3.4^{b,c}	36.3 ± 2.6^{a,c}	36.3 ± 2.9^{a,c}	44.4 ± 5.2^{a}	56.2 ± 3.3^{d}

*a, b, c, and d represent significantly different groups for each characteristic

Figure 3.7: A) PD stress-relaxation of PU, PU-0.5%rGO, PU-1%rGO, PU-2%rGO, PU-4%rGO, PU-10%rGO, and LV porcine wall B) XD stress-relaxation of PU, PU-0.5%rGO, PU-1%rGO, PU-2%rGO, PU-4%rGO, PU-10%rGO, and LV porcine wall C) Table of stress relaxation values of PU, PU-0.5%rGO, PU-1%rGO, PU-2%rGO, PU-4%rGO, and PU-10%rGO and LV porcine wall in the PD and XD.

PD scaffolds were compared to PD native tissue (**Figure 3.7A**). Native tissue could release 45.6 ± 4.7% of the stress applied over the 15 minutes. The PD PU scaffold could release 31.3 ± 1.2% of the stress. PD PU-0.5%rGO, PU-1%rGO, PU-2%rGO, PU-4%rGO, and PU-10%rGO had decreases in stress measuring 25.6 ± 5.4%, 28.6 ± 0.7%, 32.8 ± 2.1%, 31.7 ± 3.2%, and 36.6 ± 2.6% respectively over a 15-minute period. PU-10%rGO released significantly more stress than the other scaffolds except for PU-2%rGO, with p values < 0.05. Native tissue was able to unload more stress than all scaffolds examined, with p values < 0.05. In the XD native tissue, 56.2 ± 3.3% of the stress was released; comparatively, XD PU released 29.0 ± 1.9% of the stress. PU-0.5%rGO, PU-1%rGO, PU-2%rGO, PU-4%rGO, and PU-10%rGO had decreases in stress measuring 36.5 ± 1.4%, 32.0 ± 3.4%, 36.3 ± 2.6%, 36.3 ± 2.9%, and 44.4 ± 5.2% respectively over a 15-minute period in the XD. When measuring the XD PU-10%rGO scaffolds, the target load had to be lowered due to the scaffold breaking. The ability of the fibrous scaffolds to release stress decreased slightly at lower concentrations of rGO (0.5% and 1%) compared to the PU scaffold, with p values < 0.05. The PU-10%rGO scaffold exhibited the best ability to release stress in the XD; however, this could be due to needing to lower the target load to obtain data. Native tissue was more efficient at releasing stress than all scaffolds tested, with p values < 0.05.

3.3.7.2 Creep Behavior

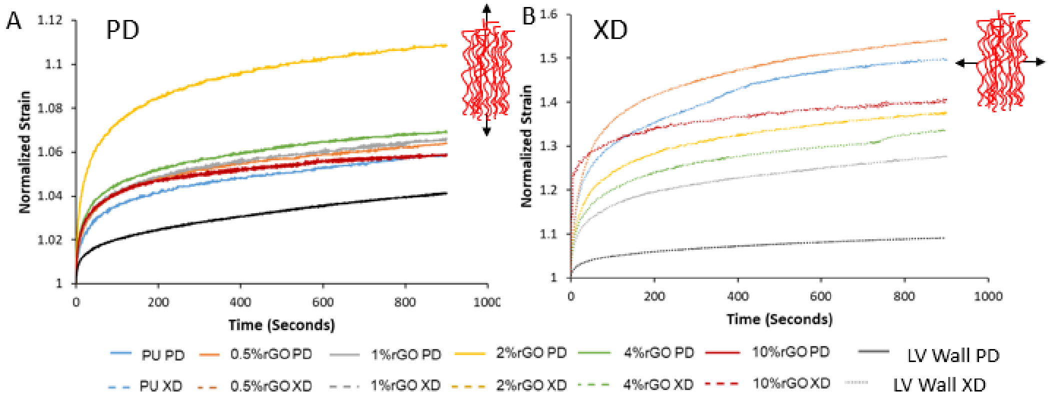

C

% rGO	0%	0.5%	1%	2%	4%	10%	LV
Creep: PD (%)	5.9 ± 0.7^{a}	6.4 ± 0.4^{a}	6.6 ± 2.0^{a,b}	10.8 ± 3.1^{b}	6.9 ± 1.1^{a}	8.7 ± 6.8^{a,b,c}	4.1 ± 1.4^{c}
Creep: XD (%)	49.6 ± 36.1^{a}	54.2 ± 33.0^{a}	27.7 ± 10.4^{a}	37.7 ± 6.7^{a}	33.6 ± 24.4^{a,b}	40.1 ± 22.2^{a}	9.1 ± 2.9^{b}

*a, b, and c represent significantly different groups for each characteristic

Figure 3.8: A) PD creep testing of PU, PU-0.5%rGO, PU-1%rGO, PU-2%rGO, PU-4%rGO, PU-10%rGO, and LV porcine wall B) XD creep testing of PU, PU-0.5%rGO, PU-1%rGO, PU-2%rGO, PU-4%rGO, PU-10%rGO, and LV porcine myocardium C) Summary table of creep testing values of PU, PU-rGO scaffolds and LV porcine wall.

The scaffolds' elasticity or stretchability and resistance to deformation were measured through creep testing, tracking how much the scaffold stretches under a constant load (**Figure 3.8**). Native tissue, with the load applied in the PD direction, stretched 4.1 ± 1.4% of its original length over the 15 minutes; comparatively, PD PU exhibited a 5.9 ± 0.7% increase in its original length. PD PU-0.5%rGO, PU-1%rGO, PU-2%rGO, PU-4%rGO, and PU-10%rGO stretched to 6.4 ± 0.4%, 6.6 ± 2.0%, 10.8 ± 3.1%, 6.9 ± 1.1%, and 8.7 ± 6.8% respectively. Native tissue exhibited significantly less creep than all scaffolds except PU-10%rGO, with p values < 0.05. PU-2%rGO exhibited significantly different creep than PU, PU-0.5%rGO, and PU-4%rGO, with p values < 0.05. The XD native tissue had stretched 9.1 ± 2.9% of its original length.

In contrast, XD PU was 49.6 ± 36.1% of its original length. XD PU-0.5%rGO, PU-1%rGO, PU-2%rGO, PU-4%rGO, and PU-10%rGO exhibited 54.2 ± 33.0%, 27.7 ± 10.4%, 37.7 ± 6.7%, 33.6 ± 24.4%, and 40.1 ± 22.2% of their original lengths, respectively. When measuring the PU-10%rGO scaffolds, the target load had to be lowered due to the scaffold breaking in the XD. Outliers present in scaffold testing caused standard deviations to be high. All scaffolds except PU-4%rGO exhibited much higher stretching than the native tissue, with p values < 0.05. No significant differences were found.

3.3.7.3 Failure Testing

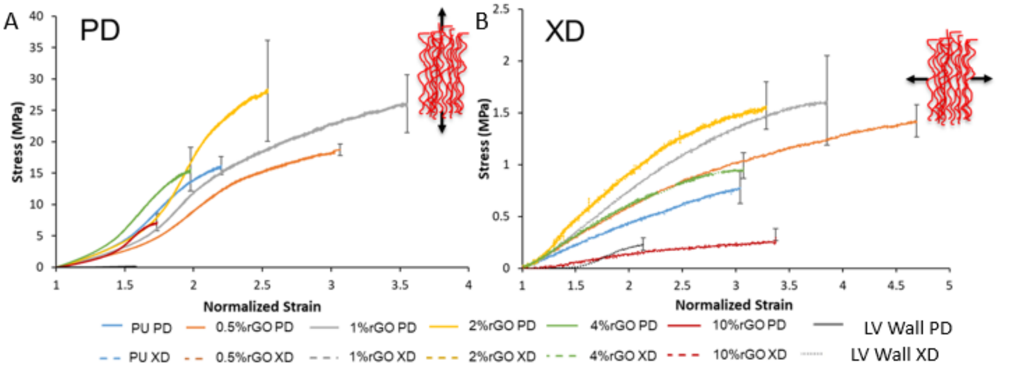

C

% rGO	0%	0.5%	1%	2%	4%	10%	LV
Failure Stress PD (MPa)	16.2 ± 1.4^{a}	18.7 ± 0.9^{b,c}	26.1 ± 4.6^{c,d}	28.1 ± 8.1^{d}	15.7 ± 3.5^{a,b}	7.2 ± 1.4^{e}	0.12 ± 0.06^{f}
Failure Strain PD	2.20 ± 0.03^{a}	3.02 ± 0.25^{b}	3.55 ± 0.57^{b,c}	2.54 ± 0.25^{b,d,c}	2.98 ± 0.20^{a,e,f}	1.73 ± 0.06^{e,f}	1.57 ± 0.08^{f}
Failure Stress XD (MPa)	0.78 ± 0.33^{a}	1.42 ± 0.34^{b}	1.62 ± 0.60^{a,b}	1.57 ± 0.70^{b,c}	0.99 ± 0.34^{a,b}	0.32 ± 0.06^{d}	0.21 ± 0.06^{e}
Failure Stain XD	3.04 ± 0.16^{a,c}	4.69 ± 0.15^{b,c}	3.85 ± 0.43^{a,c}	3.28 ± 0.23^{a,b,c}	3.07 ± 0.12^{a}	3.37 ± 1.18^{a,b,d}	2.13 ± 0.15^{d}
Initial Modulus PD (KPa)	6587 ± 626^{a,c}	4754 ± 572^{b,d}	5123 ± 510^{b,c}	7063 ± 1627^{a}	7486 ± 956^{a}	3423 ± 415^{d}	37 ± 26^{e}
Initial Modulus XD (KPa)	459 ± 162^{a}	480 ± 67^{a}	548 ± 117^{a}	427 ± 62^{a}	460 ± 95^{a}	120 ± 48^{b}	23 ± 7^{b}

*a, b, c, d, e, and f represent significantly different groups for each characteristic

Figure 3.9: A) PD failure testing of PU, PU-0.5%rGO, PU-1%rGO, PU-2%rGO, PU-4%rGO, PU-10%rGO, and LV porcine wall B) XD failure testing of PU, PU-0.5%rGO, PU-1%rGO, PU-2%rGO, PU-4%rGO, PU-10%rGO, and LV porcine wall C) Table of failure stress and strain values for PU, PU-0.5%rGO, PU-1%rGO, PU-2%rGO, PU-4%rGO, PU-10%rGO, and LV porcine wall in the PD and XD.

The failure stress and strain of tissue and scaffolds were measured by pulling on the sample until it broke to test the effects rGO has on the scaffold's mechanical properties and determine how comparable the scaffolds are to native tissue (**Figure 3.9**). The PD native tissue failed at 0.12 ± 0.06 MPa, and its failure strain was 1.57 ± 0.08; compared to all scaffolds, the native tissue had significantly lower failure stress.

Comparatively, PU failed at 16.2 ± 1.4 MPa with a failure strain of 2.20 ± 0.03 when a load was applied in the PD. While PU-0.5%rGO, PU-1%rGO, PU-2%rGO, PU-4%rGO, and PU-10%rGO had failure stresses of 18.7 ± 0.9, 26.1 ± 4.6, 28.1 ± 8.14, 15.7 ± 3.5, and 7.2 ± 1.4 MPa respectively, with failure strains of 3.02 ± 0.25, 3.55 ± 0.57, 2.54 ± 0.25, 2.98 ± 0.20, and 1.73 ± 0.06, respectively. PU-0.5%rGO, PU-1%rGO, and PU-2%rGO exhibited significantly higher failure stresses than PU, with p values < 0.03. All scaffolds exhibited significantly higher failure stresses than native tissue, with p values < 0.05. PU-10%rGO exhibited the lowest failure stress compared to the other scaffolds, with p values < 0.03. Failure strains were equally affected by rGO, with PU-10%rGO exhibiting the lowest failure strain compared to all scaffolds except PU-4%rGO, with p values < 0.03. PU-4%rGO and PU-10%rGO were the only scaffolds that did not have significantly different failure strains compared to native tissue. PU exhibited significantly different failure strains than all scaffolds except PU-4%rGO, with p values < 0.03. The failure stress and strain in the XD direction for the native tissue were 0.21 ± 0.06 MPa and 2.13 ± 0.15. The PU's XD failure stress and strain were 0.78 ± 0.33 MPa and 3.04 ± 0.16. PU-0.5%rGO, PU-1%rGO, PU-2%rGO, PU-4%rGO, and PU-10%rGO had failure stresses of 1.42 ± 0.34, 1.62 ± 0.60, 1.57 ± 0.70, 0.99 ± 0.34, and 0.32 ± 0.06 MPa respectively, with failure strains of 4.69 ± 0.15, 3.85 ± 0.43, 3.28 ± 0.23, 3.07 ± 0.12, and 3.37 ± 1.18, respectively. In a similar trend to the PD, the XD failure stress increased with rGO content until PU-4%rGO, then there is a drastic drop in failure stress, with PU-10%rGO exhibiting the lowest failure stress of all tested scaffolds, with p values < 0.03. Native tissue exhibited the lowest failure stress compared to all scaffolds, with p values < 0.03. PU-2%rGO exhibited the highest failure stress but was not significantly different from PU-0.5%rGO and PU-1%rGO. Native tissue’s failure strain was significantly different from all scaffolds except PU-10%rGO, with p values < 0.01. Only PU-0.5%rGO had a significantly different failure strain from the PU scaffold, with a p-value < 0.01. The initial modulus increased in PD and XD up to 4%rGO, with a large drop in the PU-10%rGO scaffold compared to PU. All scaffolds initial modulus was significantly higher than the native tissue.

3.3.7.4 Cyclic Mechanical Testing

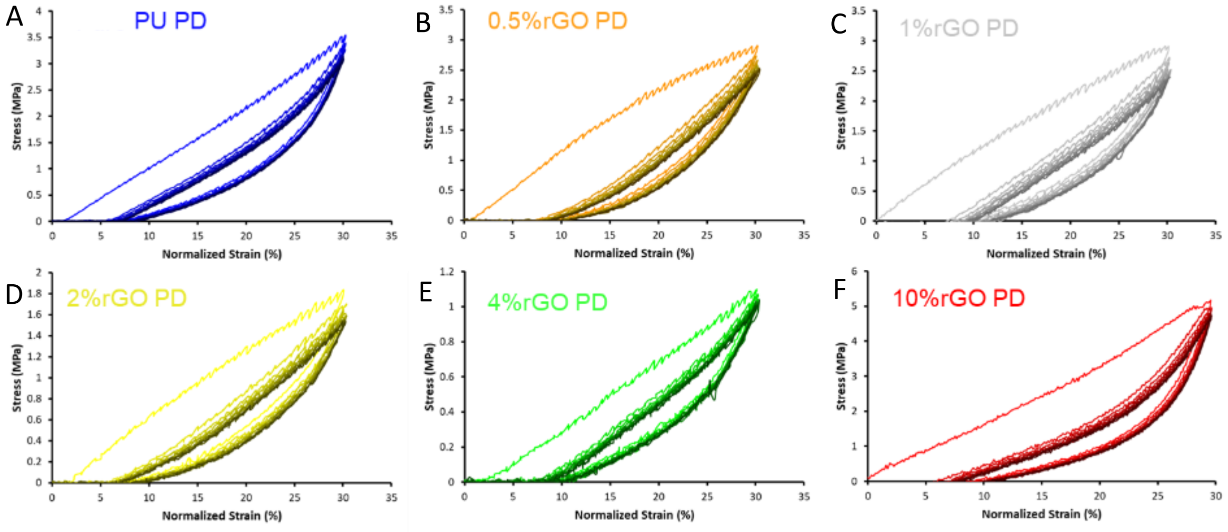

Figure 3.10: Cyclic test to 30% strain over 10 cycles with the various scaffolds; A) PU B) PU-0.5%rGO C) PU-1%rGO D) PU-2%rGO E) PU-4%rGO F) PU-10%rGO

Through cyclic loading of the scaffold and native tissue, the loading-unloading behavior of the scaffolds was measured (**Figure 3.10**). The stress borne by the scaffolds decreased with increasing concentrations of rGO until PU-10%rGO. All scaffolds exhibited pseudoelastic behaviors and quickly adjusted to repetitive cyclic stress-strain behavior by the second cycle.

3.3.7.5 Biaxial Mechanical Testing

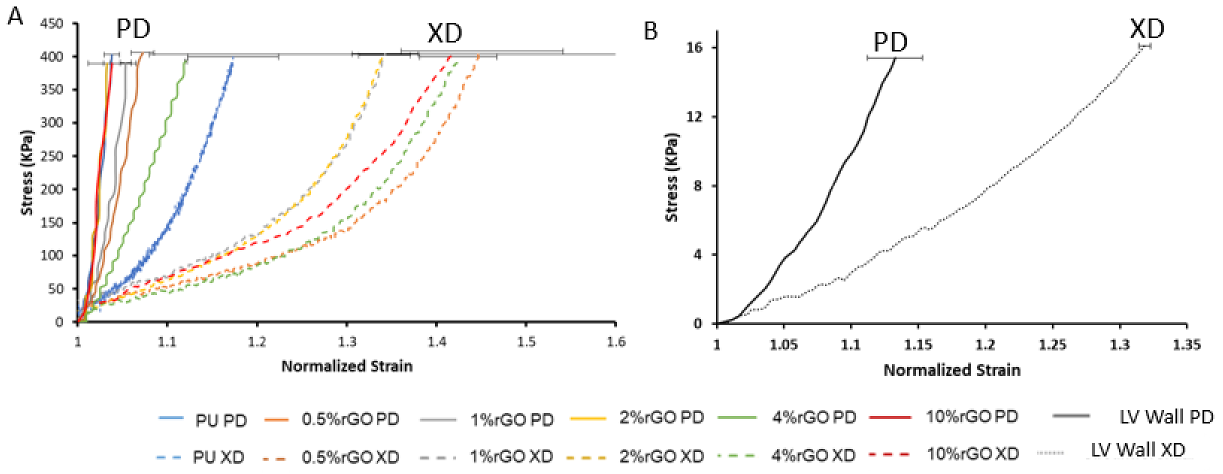

Figure 3.11: A) Biaxial testing of PU, PU-0.5%rGO, PU-1%rGO, PU-2%rGO, PU-4%rGO, PU-10%rGO, and B) LV porcine wall

Native cardiac tissue exhibited a stiffer behavior along the fiber-preferred direction than the cross fiber-preferred direction, with similar trends occurring in PD and XD of all scaffolds (**Figure 3.11**). The XD showed a more nonlinear and extensible behavior, and the PD showed a stiffer behavior. PU scaffold exhibited the stiffest curves in both PD and XD directions. Overall, along the XD direction, the scaffolds were more extensible when the rGO concentration increased. The trend in PD direction, however, is not apparent.

3.3.8 *In vitro* Cell Compatibility and Behavior

3.3.8.1 In vitro Culture of C2C12 Cells on PU-rGO Scaffolds

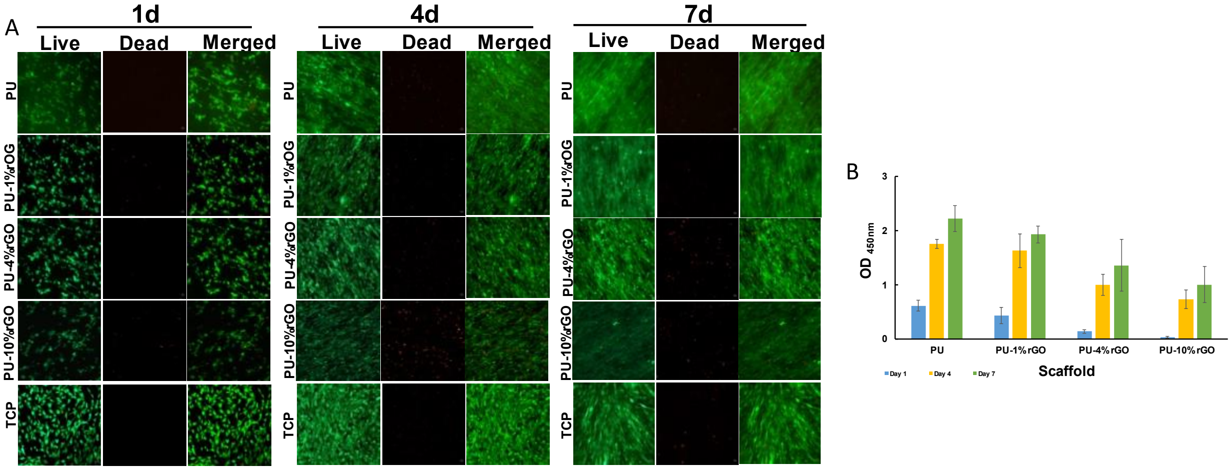

Figure 3.12: A) Live/Dead Staining of C2C12 cell seeded on PU, PU-1%rGO, PU-4%rGO, PU-10%rGO, and TCP on days 1, 4, and 7, and B) cell count from CCK-8 of C2C12 Cells on PU, PU-1%rGO, PU-4%rGO, PU-10%rGO on day 1, 4, and 7.

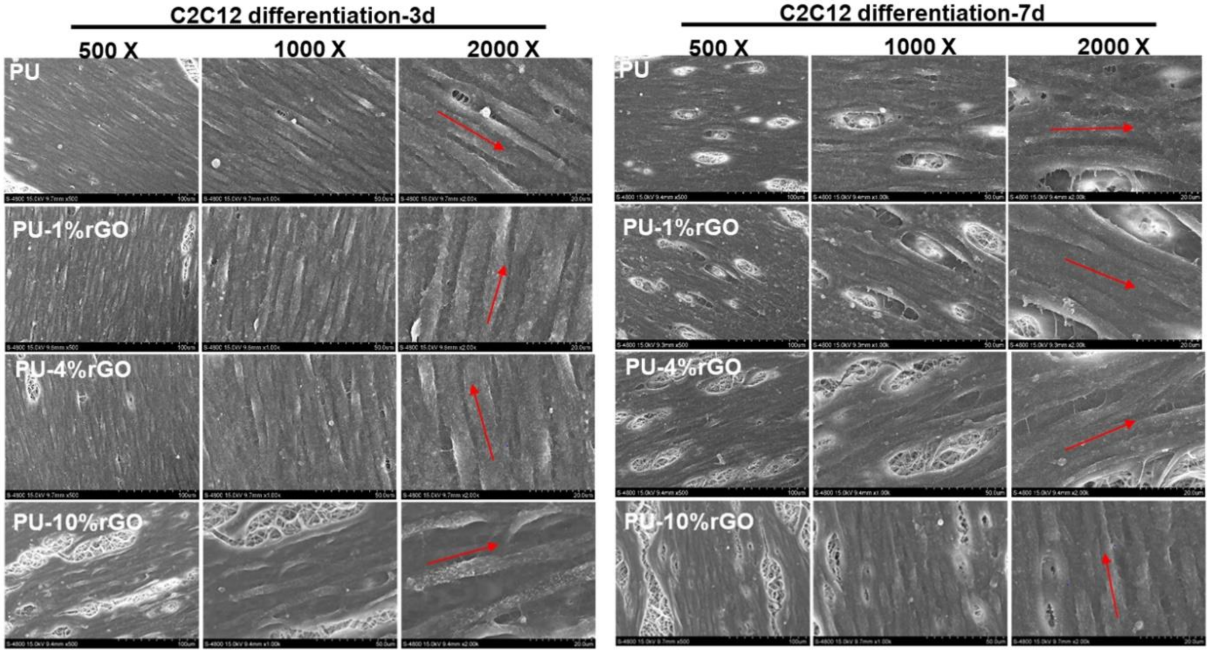

Figure 3.13: Images of C2C12 cell differentiation at 500x, 1000x, and 2000x magnification on days 3 and 7 of culture for PU, PU-1%rGO, PU-4%rGO, PU-10%rGO taken with SEM.

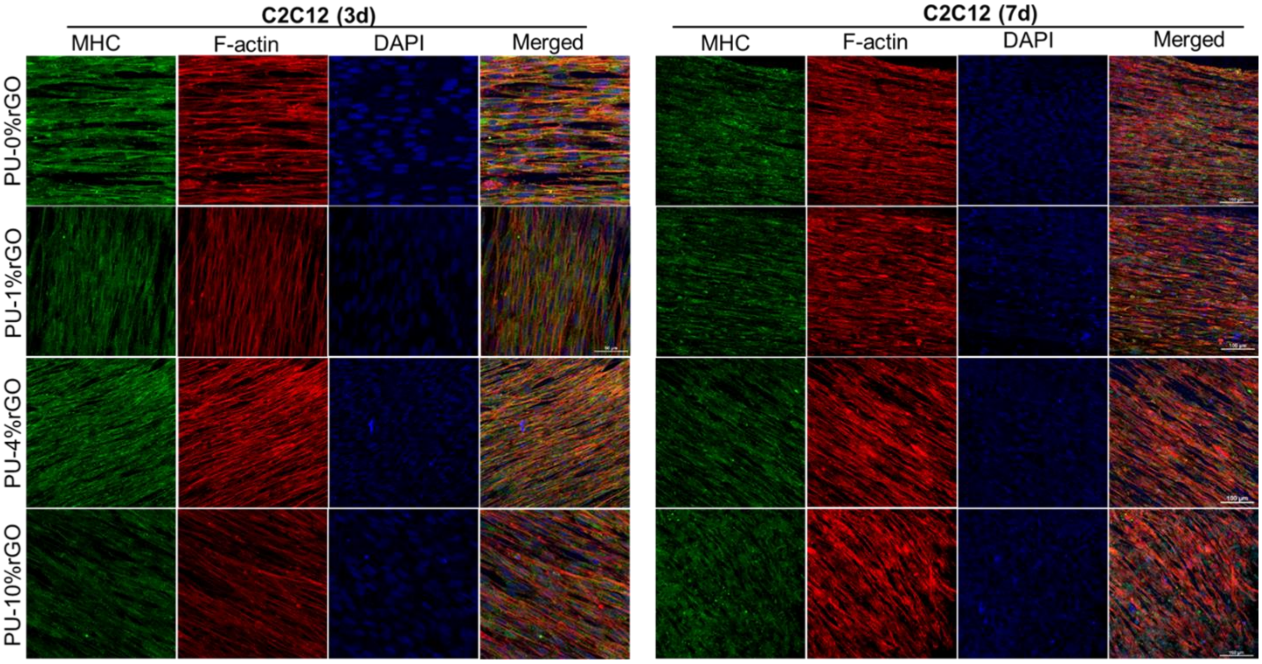

Figure 3.14: Immunofluorescence Staining for MHC, F-actin, DAPI, and the merged images on days 3 and 7 of differentiation of C2C12 cells for PU, PU-1%rGO, PU-4%rGO, PU-10%rGO.

There was nominal growth of C_2C_{12} on all scaffolds, with cells oriented along the direction of the fibers (**Figure 3.12**). Higher concentrations of rGO had a lower count of cells on day 1 due to the low cellular affinity of the hydrophobic nature of rGO. The morphology of differentiated cells had high degrees of alignment on days 3 and 7 across all scaffolds (**Figure 3.13**). Highly aligned cells indicate the scaffolds effectively cultivated cells that benefit from high degrees of structure. On day seven, a high degree of myosin heavy chain (MHC) was present in all scaffolds, with all forming highly interconnected cells. There was no indication of myotube formation (**Figure 3.14**).

3.3.8.2 *In vitro* Neonatal Rat Cardiomyocyte Culture on PU-rGO Scaffolds

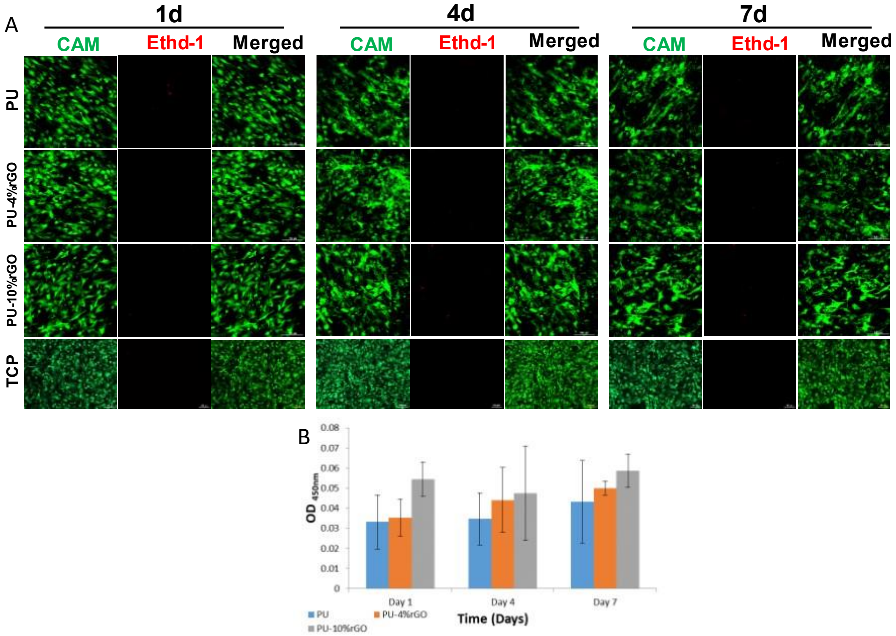

Figure 3.15: Cell viability of NNRCM for PU, PU-4%rGO, PU-10%rGO, and TCP, A) Live/dead staining of NNRCM on PU, PU-4%rGO, 10%rGO, and TCP, B) Cell counting results from CCK-8 of PU, PU-4%rGO, and PU-10%rGO scaffolds.

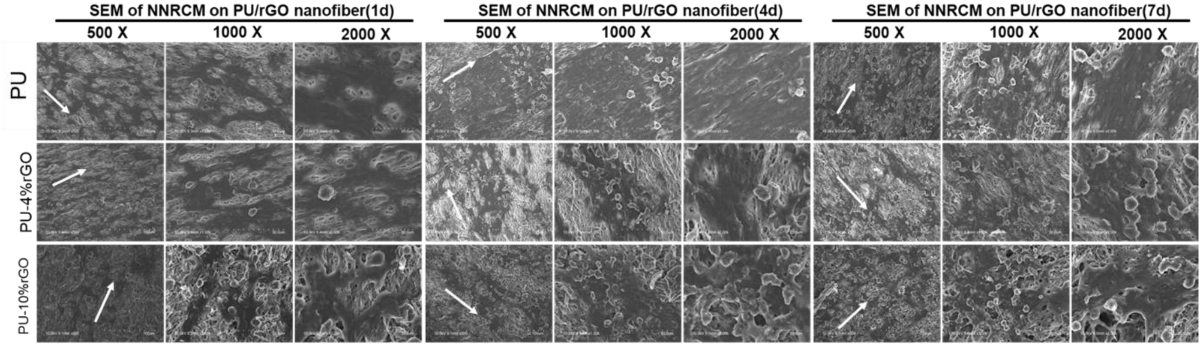

Figure 3.16: NNRCM morphology on PU, PU-4%rGO, and PU-10%rGO scaffolds, at 500x, 1000x, and 2000x magnification. Images were taken on days 1, 4, and 7 with SEM.

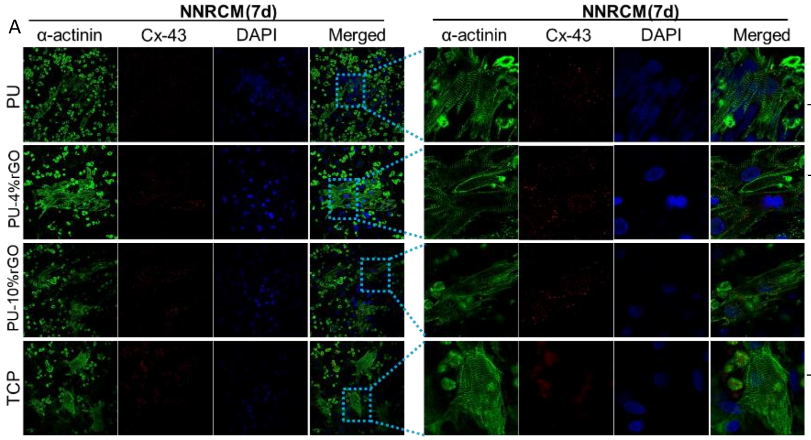

B

Sample	Sarcomere Length (μm)	Z-line Length (μm)	Aspect Ratio
TCP	1.49 ± 0.24[a]	2.72 ± 0.52[a]	2.13 ± 0.82[a]
PU	1.45 ± 0.20[a]	3.57 ± 1.06[b]	4.13 ± 1.21[b]
PU-4%rGO	1.96 ± 0.21[b]	4.07 ± 0.56[c]	5.22 ± 1.74[b,c]
PU-10%rGO	1.99 ± 0.21[b]	5.11 ± 1.33[d]	6.12 ± 1.50[c]

*a, b, c, and d represent significantly different groups for each characteristic

Figure 3.17: A) Immunofluorescence staining of NNRCM for a-actinin, Cx-43, and DAPI on PU, PU-4%rGO, PU-10%rGO, and TCP on day 7. B) Summary table of sarcomere length, Z-line length, and aspect ratio of NNRCM on scaffolds.

All scaffolds exhibited good cell viability, with CCK-8 indicating superior cell count on conductive scaffolds compared to PU (**Figure 3.15B**). No results obtained from the CCK-8 were significant. However, a clear trend of increased cell count is present in the PU-10% rGO scaffold, though nonsignificant. Morphologically there were highly organized aligned cells along the preferred direction of the fibers (**Figure 3.16**). There was mature production of cytoskeletal structures forming on all scaffolds, with the α-actinin forming distinct Z-lines (**Figure 3.17**). PU-10% rGO exhibited the most extensive sarcomere length and Z-line length, with a trend of lengths increasing correlating with rGO concentration (**Figure 3.17B**). Cell clusters on all scaffolds exhibited gap junction formation with Cx-43 expression on the peripheral of the cells. There was more peripheral production of Cx-43 on rGO-containing scaffolds compared to TCP and PU. Cx-43 expression suggested that the conductive environment encouraged gap junction formation.

3.4 Discussion

Fabrication of electrically conductive scaffolds has been highly investigated for myriad tissue engineering applications (i.e., skeletal muscle, neuron, and cardiac) along with biosensors [257, 261, 272]. Rapid fabrication of these scaffolds has often used electrospinning to reply to doping agents or synthesize conductive polymers [270]. The blending of graphene and its derivatives into polymeric scaffolds has gained much popularity from the graphene's potential mechanical augmentations and conductive properties [200, 217, 262, 269]. Although common, conductive doping agents in polymeric scaffolds still require vast exploration to identify an optimal agent and concentration for its intended purpose. Only one paper investigates polyurethane doped with reduced graphene oxide for cardiac tissue applications [175]. Their explored doping combination used thermoplastic polyurethane rather than a more biodegradable elastic type and analyzed shallow levels of rGO doping [175]. Systematic investigation of varying concentrations of rGO into polyurethane better fit for cardiac tissue engineering offers a unique insight into rGO's effects on muscle and cardiac cell growth.

Scaffolds were able to be produced with no bead formation, as evident by SEM analysis. All scaffolds were highly aligned, indicating that rGO content did not affect the overall morphology of the scaffolds. All scaffolds were nanofibrous regardless of rGO concentration, with PU-10%rGO exhibiting the largest fiber diameter. There were no discernable trends between diameter and rGO concentration. Post-PBS immersion showed a similar trend, with PU-10%rGO exhibiting the largest fiber diameter; other scaffolds exhibited similar diameters. Morphology was unchanged by PBS immersion; the shrink study showed how high concentrations of rGO lead to less shrinkage from the scaffold, causing less bunching of fibers within the scaffold. Both PU-4%rGO and PU-10%rGO exhibited significantly less shrink than other scaffolds. PU-10%rGO showed substantially less shrinkage in the fiber preferred direction compared to PU-4%rGO. Contact angle measurements reinforce this trend. Typically, graphene oxide improves the hydrophilicity of scaffolding because of oxygen-containing functional groups on the parallel plane of GO, allowing for more interaction with water molecules [260, 273]. Reduction removes some functional groups, making rGO more hydrophobic than GO [260, 273]. This increase in hydrophobic nature was evident by contact angle measurements, showing prolonged water absorption over the two-minute test. This hydrophobic property allowed scaffolds to minimize water absorption, shrinking less and maintaining their morphology more easily. PU-10%rGO exhibited a significantly higher contact angle to PU across all time points. The anisotropic nature of the aligned scaffolds confirmed asymmetric shrink and the aligned formation of the scaffolds.

The conductivity of the scaffolds is a critical factor in the reasoning for the rGO doping of PU. A conductive environment has been shown to significantly increase cell-to-cell communication of electrically active cells and promote the growth and proliferation of these cells [184, 258]. Reported skeletal and ventricular cardiac muscle conductivity values range from 0.3-0.6 S/m [274]. Previous studies using rGO exhibited superior increases in conductivity with 4-8% rGO concentration [275, 276]. The rGO used in scaffold fabrication are flakes rather than monolayer sheets; this difference leads to the need for a high concentration of rGO to measure conductive effects. The flake aggregation diminishes the electrical charge's ability to be carried continuously throughout the film [156]. Methods to avoid aggregation of rGO rely on either post fabrication reduction of GO to rGO, leading to better dispersal due to GO having better stability in organic solvents [177, 263, 277]. Obtained conductive values fall well within the reported native tissue conductance [274]. Wet conductivity measurements exhibited an exciting result of significantly decreasing conductivity compared to the dry films. The proposed reason for the decrease in conductivity is because the PBS is responsible for the bulk conductivity [278]. Martins et al. experienced a similar decrease in their conductive scaffold for this reason [278]. Degradation of the scaffolds is an equally important study. Cell growth and penetration into the scaffold require a balanced degradation rate so new cells and ECM can replace the degrading scaffold [68]. For optimal tissue engineering applications of the scaffolds, a constant structural and electrical support of the cells ensures that the scaffolding failure does not occur once implanted in the body. Results from degradation indicate that rGO-containing scaffolds initially retained more mass on days 3 and 7 of the study than PU. The PU-10%rGO scaffold was extremely delicate on day 14. The rGO doesn't contribute to maintaining the structure of the scaffold, allowing for various fragments to easily break off.

The mechanical properties of the fabricated scaffolds were extensively compared to the native tissue of the LV of a porcine heart. Porcine hearts were used due to their mechanical and structural similarities to human hearts [245, 246]. Optimizing mechanical properties ensures proper structural support of the heart. At the same time, the matched mechanical properties allow appropriate mechanical cues to be applied to the cells for proliferation and differentiation. Compared to PU scaffolds, lower concentration graphene oxide addition was shown to reduce the stress relaxation, while higher concentration graphene oxide addition increased the stress relaxation. PU-0.5%rGO and PU-1%rGO exhibited significantly less stress release than the PU scaffold. The crystalline structure of PU might explain the alteration of stress relaxation. When lower concentrations of rGO are added, the rGO sheets can diffuse through the fiber network due to van der Waal's forces, improving the fibrous interaction [279]. When in high concentrations, stacking of rGO sheets can occur, interfering with the crystalline structure of PU and decreasing its interaction [279]. PU-10%rGO was shown to have significantly higher stress decay than the other scaffolds except for PU-2%rGO. The XD exhibits a less obvious trend with rGO concentration. The main significant differences were shown between PU and the PU-0.5%rGO and PU-1%rGO, further confirming that lower concentrations of rGO reduced the stress decay.

The PD creep testing showed a similar trend, with low to medium concentrations of PU having superior mechanics. PU-2%rGO showed statistically highest creep compared to PU, PU-0.5%rGO, and PU-4%rGO. Creep testing exhibited no statistically significant differences in the XD across all scaffolds. It is important to note that the PU-10%rGO scaffold required a lower target load due to breakage, further adding to the idea that the scaffolds' continuous internal structure was interrupted due to rGO saturation. Failure stresses and strains showed the same trend with increasing the failure stress and strain at the lower concentrations and starting to decrease once over-saturated with rGO. In all failure testing cases, the PU-10%rGO scaffold was still mechanically superior to the native tissue, indicating that the weakening of the scaffold is not too extreme to prevent its use as a cardiac scaffold. Cyclic stretching showing the quick adjustment and resistance to cyclic stress indicates that the scaffold maintains its viscoelastic properties even with the stiffening from lower concentrations of rGO. Biaxial testing showed comparable anisotropic properties to a pig's LV myocardium.

Cellular studies with skeletal muscle cells, a similarly electroactive tissue as cardiac tissue, indicated that cells could grow and form an aligned structure on all tested scaffolds. Low cellular attachments based on lower cell counts on the higher concentrations of rGO are reinforced by the alterations in hydrophilicity from the rGO particles [280]. SEM analysis of cells morphology showed a high degree of alignment of the cells at both time points, required for optimal skeletal muscle and cardiac tissue engineering. These results mimic other studies testing improved conductive scaffolds [281, 282], suggesting that the scaffolding and presence of rGO positively impact the cultured cells. PU-10%rGO fibrous scaffolds exhibited similar protein staining as PU-4%rGO. Studies using NNRCM on our scaffolds exhibited favorable growth and maturity across all scaffolds, with PU-10%rGO exhibiting the highest aspect ratio, sarcomere, and Z-line length. Live/dead staining across all scaffolds exhibited a low presence of dead cells; furthermore, CCK-8 revealed an increasing amount of viable NNRCM with increased rGO concentration. Scaffolds containing rGO displayed higher presence of Cx-43 peripherally compared to TCP and PU. Increased expression of Cx-43 is tied to gap junction formation [283, 284]. The improved conductive environment promoted the formation of gap junctions between cells for better signaling action potentials [284].

3.5 Conclusions

Various rGO doped PU nanofibrous scaffolds with anisotropic properties were fabricated using a co-electrospinning technique. The scaffolds morphology and physical characteristics were investigated with SEM and contact angle to determine how it is affected by varying concentrations of rGO. Mechanical properties were determined with uniaxial and biaxial testing to compare with LV porcine tissue to determine if the scaffolds could mimic the mechanical properties of cardiac tissue. Ongoing investigations into the degree rGO affect scaffolds' conductivity help determine optimal concentrations to balance its effects on the mechanical and conductive properties to be better suited for cardiac tissue engineering. Scaffolds exhibited promising results with skeletal muscle in vitro studies to understand rGO's effects on electrically active cells. NNRCM seeded on PU-rGO scaffolds had positive signs of enhanced development with improved sarcomere lengths and Z-line lengths.

3.6 Outcomes

We have produced nanofibrous scaffolds that are all comparable in morphology regardless of rGO content. The hydrophilicity of scaffolds was shown to be impacted slightly by rGO concentration, with no significant difference between all scaffolds at all time points. Mechanically all scaffolds exhibited improved mechanical characteristics compared to native LV tissue. Considering the small changes shown from the PU-0.5%rGO, PU-1%rGO, and PU-2%rGO, future testing should not include PU-0.5%rGO and PU-2%rGO. A diverse exploration into different methods to measure conductivity needs to be made from difficulties in testing conductivity. Preliminary cell studies using C2C12 cells have indicated the need for further studies with PU-4%rGO and PU-10%rGO before deciding the optimal scaffold. PU-rGO scaffolds' effects on NNRCM also provide promising results as a potential cardiac scaffold. PU-10%rGO scaffolds displayed the highest sarcomere, Z-line, and aspect ratio. Expression of Cx-43 was notably increased in rGO-containing scaffolds supporting the beneficial effects of conductive environments on CM development. This work has been presented at a conference for the SFB.

CHAPTER IV: Fabrication of an Elastic Conductive Bioactive Electrospun Nanofiber Scaffold for Cardiomyocyte Culture

4.1 Introduction

Over the years, cardiac scaffold development has grown more complex to fulfill cardiac tissue engineering demands better. Synthesis of new complex biomaterials has shown great promise to be more bioactive or conductive through augmentation. The promise of these new biomaterials has been demonstrated that more complex biomaterials can even further improve treatment. Plenty of research has shown that the hybridization of synthetic polymers with natural polymers creates a biomaterial that incorporates the structural benefits of synthetic polymers while also improving biocompatibility by providing binding sites for cells that occur in nature [124, 212, 221]. Other studies have shown the benefits of incorporating electrically active components with synthetic polymers to create a mechanically sturdy scaffold that can efficiently deliver electrical impulses for cell singling [93, 213, 261, 264]. Creating more complex scaffolds that combine these bioactive and electrically active components stands to benefit from both aspects. The development of cardiac scaffolds that provide biochemical cues and are electrically conductive has indicated this [265]. [285]. Norahan et al. investigated a collagen scaffold doped with rGO exemplifying the benefits of these blends [258]. Scaffolds displayed high levels of biocompatibility due to collagen, with structural reinforcement from rGO, and exhibited a degree of electric activity. Tondnevis et al. investigated a PU/gelatin/carbon nanotube blend [286]. This blend was proven to be effective. Gelatin gave the scaffold softness, compensating for the stiffening carbon nanotubes caused. It was mechanically robust due to PU. Integrations with this variety of materials have shown complementary effects on the scaffolds, compensating for any potential downsides one material might exhibit because of the benefits another material provides. The tri-blended scaffold showed significantly increased cardiomyocyte proliferation compared to scaffolds containing PU/gelatin and PU/carbon nanotubes. Further proving these new complex materials are beneficial.

Various investigations into decellularized porcine myocardium have promising therapeutic effects on cardiac regeneration [75]. Often these fabricated scaffolds are hydrogels, which, while showing favorable therapeutic effects lack proper mechanical support for more extensive treatment [68, 80]. These studies lack the incorporation of conductive properties into the PU hybridized scaffolds. Similarly, studies investigating conductive additives such as rGO have shown promising results [184, 258, 259]. In contrast, they lack the incorporation of biologically relevant natural polymers or biomolecules. Using our group's previous investigation into PU blends of PU-ECM and PU-rGO, an inquiry into a scaffold containing elements from both potential scaffolds reveals any potential additive benefits. Since no other group has been found to incorporate conductive additives, specifically rGO, into a PU based scaffold augmented by the addition of digested ECM, a novel biomaterial composition is proposed.

This study aims to fabricate a PU-based scaffold incorporating the optimal blends of de-cellularized ECM and rGO to produce a bioactive and conductive scaffold. Based on literature search and prior investigations, we hypothesize that a conductive, bioactive, and mechanically comparable scaffold to native cardiac tissue should improve cardiac differentiation compared to individually blended scaffolds. We characterize a composite scaffold's morphology, hydrophilicity, mechanics, and cellular compatibility in this study. Through characterizations and comparisons to previously formed scaffolds and native tissue, we determine if this complex amalgamation is better suited as a potential cardiac scaffold.

4.2 Material and Methods

4.2.1 Materials

Materials were obtained from Sigma unless stated otherwise. Polycaprolactone diol (PCL, Mn = 2000) was placed in a vacuum oven at 60°C overnight to be dried. Hexamethylene diisocyanate (HDI) and putrescine underwent distillation for purification. Stannous octoate ($Sn(Oct)_2$), isopropanol, 1,1,1,3,3,3-hexafluoro-2-propanol (HFIP, Oakwood Products), anhydrous dimethyl sulfone (DMSO), pepsin, porcine stomach mucosa (EMD Millipore Corp., USA), and reduced graphene oxide (rGO) were used as purchased. Hydrochloric acid (HCl, 35% solution) and sodium hydroxide (NaOH, 25% solution) were diluted to form a 0.01M and 0.1M solution for pepsin activation and neutralization. Porcine hearts were donated from a local butcher shop (Fischer Meat Market, Muenster, Texas). Lipase from Thermomyces lanuginosus (50mL) was diluted with PBS to achieve a 100 U/mL solution for degradation studies.

4.2.2 Biodegradable Polyurethane Synthesis

The synthesis procedure for biodegradable polyurethane was found and replicated in the literature [43]. Briefly, PCL diol (Mn = 2000) was dissolved with DMSO in a three-neck round bottom flask under nitrogen protection. DHI and Sn $(Oct)_2$ (3 drops) were added and stirred in the DMSO solution under heating (70°C) for 3 hours. Putrescine was first dissolved in DMSO before the solution was added to the three-neck round bottom flask once it reached room temperature to achieve a final molar ratio of 1:2:1 (PCL: HDI: putrescine). The mixture was then heated to 70°C and left overnight to react. Before it was transferred to isopropanol, DI water was used to precipitate the polymer to remove unreacted monomers and oligomers. PU was then dried via vacuum at 60°C for three days.

4.2.3 ECM Extraction and Digestion

Dissected left ventricle tissue from porcine hearts was used to make the decellularized ECM. Left ventricle tissue was thinly sliced and immersed in a 1% SDS with vigorous stirring. The SDS solution was removed after 6 hours, with the tissue retained using a filter before replenishing with a new SDS solution. After 24 hours, the SDS solution was replaced every 48 hours until all tissue lost coloration. Samples were thoroughly washed with DI water before freeze-drying. Once fully dried (24-48 hours), the tissue was crushed into a fine powder with a mortar, pestle, and liquid nitrogen. For digestion, 150 mg of fine powder was weighed with 10 mg of pepsin and stirred in 10 mL of 0.01 HCl until the solution became gelatinous, and the powder was fully dissolved (48 to 72 hours). 1 mL of 0.1M NaOH was added to neutralize the solution and quickly mixed before it was freeze-dried until thoroughly dried (24 to 48 hours). Digested ECM was crushed into a fine powder in liquid nitrogen. The ECM powder was weighed out for their respective scaffolds before they were dissolved in HFIP for electrospinning.

4.2.4 Electrospun Conductive Hybrid Scaffold Fabrication

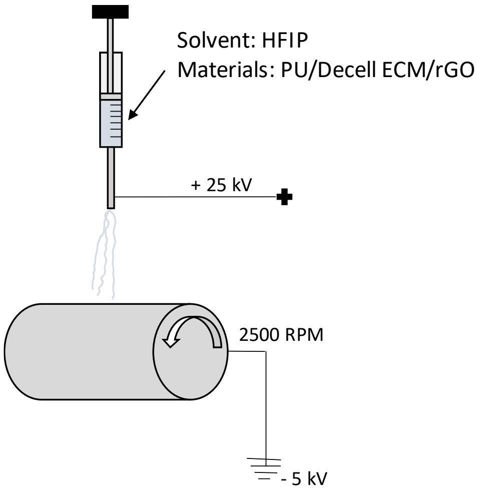

Figure 4.1: Schematic of aligned electrospinning setup

A standard aligned electrospinning process was used to fabricate the conductive hybrid scaffold (**Figure 4.1**). Before electrospinning, the steel rotating mandrel (D = 150 mm, L = 40 mm) target was wrapped with aluminum foil. In a vial, 8 mL of HFIP and rGO was added and sonicated with an ultrasonic tip for 1 hour in an ice bath for dispersal. After sonication, 4 mL of solution was removed to be used later to dissolve ECM. PU was added to the other 4 mL and left to dissolve with stirring overnight. One hour before electrospinning, the 4 mL solution of rGO is added to the vial of ECM to be dissolved. The rGO/ECM solution is added to the PU/rGO solution and mixed with sonication for 10 minutes. Once wholly integrated, the solution was loaded into a 10 mL syringe for electrospinning. Extrusion of solution occurred at 1 mL/hour, with needle tip 15 cm from mandrel, +25 kV charge on the needle for 8 hours. The mandrel was kept at a constant 2500 rpm, and a -5kV charge was applied. After electrospinning, fibrous scaffolds remained on the mandrel overnight in the fume hood for any residual solvent to evaporate. The scaffolds were removed from the mandrel by making one cut across the mat, gently peeling the scaffold free, and transferred to aluminum foil with the mandrel side facing down. Scaffolds were stored in the foil until used for characterization or cell studies.

4.2.5 Scaffold Characterization

4.2.5.1 ATR-FTIR

Attenuated total Fourier Transform Infrared spectroscopy (ATR-FTIR) was performed on each scaffold using a Thermo Nicolet 6700 FTIR Spectrometer. The wavelength range was 4000-600 cm -1. Spectrum peaks were found and compared between scaffolds.

4.2.5.2 Scaffold Morphology Analysis

The morphology of scaffolds was assessed with a scanning electron microscope (SEM) (Hitachi S-4800 FE-SEM) after scaffolds were coated with gold/platinum (Au/Pt) with a Hummer VI sputtering system. Obtained images were analyzed with ImageJ to measure fiber diameter and angle to assess alignment (n = 120). The scale bar from SEM images was used to calibrate the ImageJ pixel to µm ratio for analysis, with excel was used to calculate the fiber angle histogram and normalized curve. Shrinkage of scaffolds was obtained by immersing samples (8 mm diameter, n =5) for 24 hours in PBS at 37°C. The samples were removed and measured with a caliper to measure the lengths. Samples were then quickly washed with DI water before freeze-drying, to be analyzed by SEM following the same procedure to quantify scaffold swelling.

4.2.5.3 Contact Angle

The contact angle of samples was obtained using a custom-built instrument controlled by FTA32 software. Scaffolds were cut into 3 cm × 1 cm (n = 2) and mounted to a glass microscope slide with double-sided tape. Slides were placed on an adjustable platform. Once the side of the sample slide was in focus, a micropipette filled with DI water applied a 5 µL drop to the sample, with images were taken 15, 30, 60, 90, and 120 seconds after the drop was applied. The sample was then slid over 1 cm before the next reading was taken, for 3 drops per sample. Using the built-in software, the contact angle was calculated by outlining the droplets from the obtained images. There was a total of n = 6 for each scaffold group.

4.2.5.4 In vitro Enzymatic Degradation

Scaffolds were cut into samples that were weighed (W_0, at least 25 mg), immersed in 2 mL (100 U/mL lipase/PBS solution) in physiological conditions (37°C). Every 3 days, the lipase solution was removed and replenished with a new solution. At time points 3, 7, and 14 days ((n = 3) for each time point), scaffolds were removed from the lipase solution and thoroughly washed with DI water. Scaffolds were freeze-dried and weighed (W_1) to calculate the % degradation using the following equation:

$$\%\,Degradation = \frac{W_1}{W_0} \times 100 \qquad [1]$$

4.2.5.5 Conductivity

Films were fabricated for conductivity testing. Sample solutions were prepared in the same method described above. Solutions were poured into a PTFE dish. The dishes were covered with aluminum foil that had holes in them and left to evaporate overnight. Samples (8 mm diameter, n =3) were placed on a glass slide for conductivity testing. The slide was placed on a 4-point probe stand (Four-Point Probe, Ossila), and the stand was moved until the probes were in contact with the sample. The current through the samples was measured over a sweeping voltage of 0 to 10V. Once the target current was measured, the sheet resistance measurements were taken 100 times. The software calculated the average resistivity and conductivity. The conductivity of scaffolds in wet conditions was also tested by submerging samples in PBS for 24 hours at 37°C. Before testing excess, PBS was removed from scaffolds with paper towels. Measurements were then taken in the same manner as the dry samples.

4.2.5.6 Mechanical Testing

4.2.5.6.1 Uniaxial

Native tissue and fabricated scaffolds (n = 5) were cut into 5 mm × 30 mm strips to perform uniaxial testing (Test Resources, MN), with samples from PD and the XD. The outer wall of a porcine LV was dissected and cut into 5 mm × 30 mm strips that were 1-2 mm thick. Polymer samples were soaked in PBS at 37°C for 24 hours before testing. LV tissue was tested when at room temperature. The samples were loaded in the grips, with the grip-to-grip length around 10 – 15 mm. Scaffolds have stress relaxation, creep, failure testing, and cyclic testing performed on them. Tests had 20 samples/second and 10 mm/min jogging rates. The target load for stress relaxation and creep testing was 100 g, after which 15 minutes of data was recorded. Cyclic testing lasted for 10 cycles with a target strain of 30%. Failure testing was conducted by pulling the sample until it broke, after which the test ended. All data were exported to excel for calculations and to make the graphs.

4.2.5.6.2 Biaxial

Scaffolds and native tissue were cut into 1 cm × 1 cm squares and marked to indicate scaffold direction (n = 3). Dissected porcine LV outer walls were cut into 1 cm × 1 cm squares that were 1-2 mm thick. Four markers using white tape were applied to the sample and loaded into a custom biaxial machine controlled by a LabView program with sutures. Loading was set to 60 N/m at a jogging rate of 0.5 mm/second, and data processing was performed in Excel.

4.2.6 Cell Compatibility and Behavior

Scaffolds tested for cell studies were PU, PU-20%ECM, PU-10%rGO, and PU-20%ECM-10%rGO. A tissue culture polystyrene (TCP) was used as a control.

4.2.6.1 Neonatal Cardiomyocyte Culture

Nano-fibrous scaffolds for neonatal cardiomyocyte (Lonza, R-CM-561) culture were prepared by cutting 5 mm diameter circles with a steel cut press (n = 8), with sterilization with UV light occurring for 60 minutes on each side before they were fixed to the bottom of a 96 well plate with plastic holders. Scaffolds were washed thrice in 15-minute intervals with PBS and then incubated for 2 hours in rat cardiac myocyte growth media BulletKit™ (Lonza, CC-4515) before seeding with CM. Two days before seeding scaffolds, cells were resuscitated and cultured in a T25 flask, with the initial 4 hours of culturing occurring in RCGM BulletKit™ before replacing 80% of the media with RCGM BulletKit™ supplemented with 200 µM bromodeoxyuridine (BrdU) (Lonza, CC-4519). Cells were seeded with a density of 1×10^5 cells/well for 7 days, with 50% of the media replaced every three days with RCGM BulletKit™ supplemented with 200 µM BrdU. RCGM BulletKit™ is composed of rat cardiac myocyte basal medium (Lonza, CC-3275) and RCGM SingleQuots™ (Lonza, CC-4519). Cell seeded scaffolds were incubated at 37°C with 95% air and 5% CO_2 high humidity for the 7-day study.

4.2.6.2 Live/Dead Staining

A live/dead viability kit (Sigma) assessed cell viability of scaffolds on days 1, 4, and 7 of culture in the growth media. Live cells were stained green with calcein-AM, while the dead cells were stained red with ethidium homodimer-1 (EthD-1). Samples were washed using PBS twice before treatment with 2 µM calcein AM and 4 µM EthD-1 in DMEM for 30 minutes in an incubator at 37°C. An inverted fluorescent microscope (Nikon Eclipse Ti) was used to take the images.

4.2.6.3 CCK-8

The use of a cell counting kit, CCK-8 (Sigma), helped assess cell viability on scaffolds, performed on days 1, 4, and 7 of the study (n = 3). Cell-laden wells had their media removed and replaced with 100 µL of DMEM and 10 µL of the CCK-8 kit solution, with one blank well plate filled with the solution. Cells were left to incubate for one hour after introducing the cell counting solution before transferring the media to a new 96-well plate to be used in a microplate reader. The new well plate was read in a microplate reader (Tecan Spark 10M) with a target wavelength of 450 nm and a reference wavelength of 650 nm. Obtained absorption values were subtracted by the blank to remove background noise to calculate the OD. Cells were washed with PBS twice before refilling with the necessary cell media for continued use in the study.

4.2.6.4 Cell Morphology

Neonatal cardiomyocytes fixed on days 1, 4, and 7 of the culture were imaged with SEM to characterize the morphology of cells on the scaffold. Scaffolds were washed with PBS twice before fixing with a 2.5% glutaraldehyde solution for 15 minutes. After the 15 minutes, scaffolds were washed twice with PBS before dehydration. To dehydrate the samples, they were submerged in increasing ethanol concentration solutions (50%, 70%, 80%, 90%, 95%, and 100%) for 5 minutes in each solution and twice for 5 minutes in the 100% solution. Scaffolds were placed on tissue paper to air dry for 24 hours. Samples were then prepared for viewing with SEM using the same protocol previously described.

4.2.6.5 Immunofluorescence Staining

Immunofluorescence staining was performed on differentiation cultures on day 7 for the neonatal cardiomyocytes. Scaffolds were stained for α-actinin, Cx-43, and DAPI. Before staining, scaffolds were washed twice with PBS and fixed in a 4% paraformaldehyde solution. After 15 minutes, the scaffolds were rewashed with PBS before permeabilization in 0.3% Triton X-100 in PBS solution for 10 minutes in an incubator. After 10 minutes, samples were washed 3 times with PBS. A 2% bovine serum album (BSA) in PBS solution was added and left at room temperature. After an hour, the primary antibodies (Monoclonal anti-α-actinin (sarcomeric), 1:200, Santa Cruz; Anti-Connexin-43 antibody, 1:200, Santa Cruz) in 1% BSA solution were added to the scaffolds and left overnight at 4°C. The following day scaffolds were washed with PBS three times. The secondary antibodies (goat anti-mouse IgG (H+L) Highly Cross-Adsorbed Secondary Antibody, Alex Fluor™ Plus 488 for α-actinin; Alexa Fluor™ 594 goat anti-rabbit IgG (H+L) for Cx-43) in 1% BSA solution were added to the scaffolds in the dark at room temperature for 1 hour. Counter-stain 4’,6-diamidino-phenylindole (DAPI) was used to stain the nuclei. Scaffolds were then washed with PBS 3 times before imaging. A confocal laser fluorescence microscope (Nikon A1R HD25 Confocal Microscope) imaged the cells. Images were processed through ImageJ to characterize the cells, using five representative images per sample. Cell length, width, sarcomere length, and Z-line length were measured with ImageJ. The aspect ratio was calculated using the following equation [234, 235]:

$$Aspect\ Ratio = \frac{Length\ of\ Cell}{Width\ of\ Cell} \qquad [2]$$

4.2.7 Statistical Analyses

Reported experimental data was reported as the mean ± standard deviation. A two-tailed Student’s t-test was used for two group comparisons. More than two group comparisons used a one-way analysis of variance (ANOVA) test, with statistical significance indicating if the P-value was less than 0.05. A Tukey-Kramer test was performed on ANOVA results that returned statistical significance to find significance between each group. All analyses were calculated using Excel.

4.3 Results

4.3.1 Scaffold Fabrication

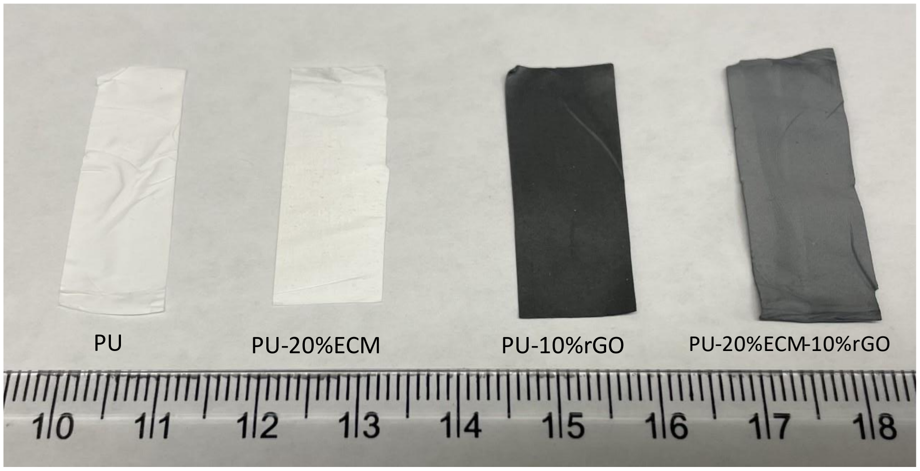

Figure 4.2: The obtained electrospun PU, PU-20%ECM, PU-10%rGO, and PU-20%ECM-10%rGO, with evident changes in color due to rGO and ECM inclusion.

Including ECM in the scaffolds caused the scaffold to take on a rougher texture than PU and PU-10%rGO (**Figure 4.2**). The inclusion of rGO darkened the scaffold. The PU-10%rGO scaffold was darker than the PU-20%ECM-10%rGO scaffold. The lighter color of PU-20%ECM-10%rGO compared to PU-10%rGO was due to the inclusion of ECM.

4.3.2 ATR-FTIR

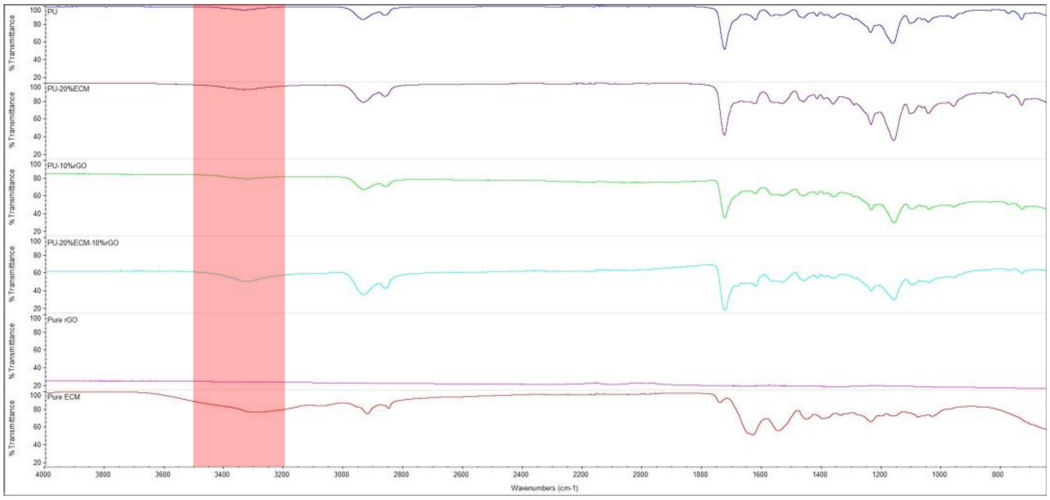

Figure 4.3: ATR-FTIR Surface Characteristics of PU, PU-20%ECM, PU-10%rGO, and PU-20%ECM-10%rGO scaffolds with pure ECM and rGO flakes in the wavelength range of 4000-600 cm^{-1}.

The ATR-FTIR spectra obtained for the scaffolds showed the different characteristic peaks for PU, PU-20%ECM, PU-10%rGO, PU-20%ECM-10%rGO scaffolds, and pure ECM and rGO (**Figure 4.3**). The obtained spectra for PU-20%ECM-10%rGO are noticeably shifted down, with a more pronounced broad peak from 3200 – 3500 cm^{-1} (O-H) from the inclusion of ECM and rGO.

4.3.3 Scaffold Morphology

Table 4.1: Summary of shrinkage of PU, PU-20%ECM, PU-10%rGO, and PU-20%ECM-10%rGO after immersion in PBS at 37°C for 24 hours.

Scaffold	XD (mm)	PD (mm)	% Shrink along XD	% Shrink along PD
PU	7.7 ± 0.09^{a}	6.2 ± 0.07^{a,b}	3.4 ± 1.2^{a}	22.4 ± 0.9^{a,b}
PU-ECM	7.8 ± 0.07^{a}	6.2 ± 0.07^{b,c}	2.0 ± 0.9^{a}	22.0 ± 0.8^{b,c}
PU-rGO	7.4 ± 0.29^{b}	6.6 ± 0.19^{a}	7.3 ± 3.7^{b}	17.0 ± 2.4^{a}
PU-ECM-rGO	7.5 ± 0.15^{b}	6.6 ± 0.12^{a}	6.4 ± 2.0^{b}	17.6 ± 1.5^{a}

*a, b, and c represent significantly different groups for each characteristic

XD: Cross Preferred Fiber Direction
PD: Preferred Fiber Direction

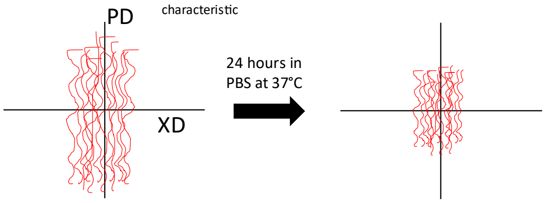

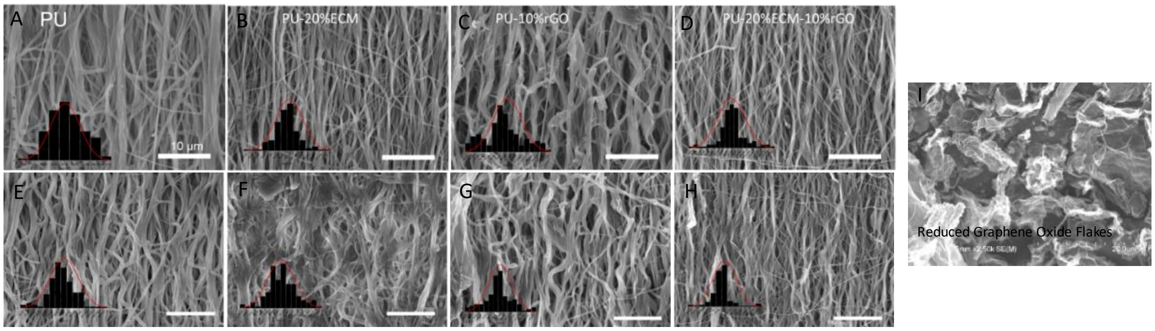

J Pre-Swelling

Scaffold	Diameter (nm)	Fiber Angle
PU	517 ± 199^{a}	88 ± 9^{a}
PU-20%ECM	367 ± 155^{b}	90 ± 12^{a}
PU-10%rGO	572 ± 297^{a}	86 ± 35^{a}
PU-20%ECM-10%rGO	438 ± 158^{c}	88 ± 17^{a}

K Swelling

Scaffold	Diameter (nm)	Fiber Angle
PU	512 ± 176^{a}	85 ± 13^{a}
PU-20%ECM	424 ± 142^{b}	91 ± 15^{a}
PU-10%rGO	375 ± 87^{c}	86 ± 30^{a}
PU-20%ECM-10%rGO	356 ± 110^{c}	90 ± 19^{a}

*a, b, and c represent significantly different groups for each characteristic

Figure 4.4: A-D) Images of PU, PU-20%ECM, PU-10%rGO, and PU-20%ECM-10%rGO before immersion and E-H) after submersion in PBS at 37°C for 24 hours taken with SEM. I) rGO flakes used in scaffold fabrication. J) Table of fiber analysis of PU, PU-20%ECM, PU-10%rGO, and PU-20%ECM-10%rGO scaffolds before immersion in PBS and K) after submersion in PBS at 37°C for 24 hours. Scale bar length is 10 µm.

All scaffolds contained continuously aligned nanofibers from SEM images; no beads were visible with all composite scaffolds (**Figure 4.4**). All composite blend scaffolds were nano-sized, with a decrease in fiber diameter and inclusion of ECM into the scaffolds compared to the PU and PU/rGO scaffolds. The PU average fiber diameter was 517 ± 199 nm, while the PU-20%ECM, PU-10%rGO, and PU-20%ECM-10%rGO was 367 ± 155 nm, 572 ± 297 nm, and 438 ± 158 nm, respectively. PU fiber diameter was significantly larger than the PU-20%ECM and PU-20%ECM-10%rGO. PU-20%ECM exhibited the smallest fiber diameter; statistically, PU and PU-10%rGO were alike. For all samples, fiber alignment was maintained with similar distributions of fiber angle. PU was measured to have an average fiber angle of 88 ± 9°, while for PU-20%ECM, PU-10%rGO, and PU-20%ECM-10%rGO was 90 ± 12°, 87 ± 36°, and 88 ± 17°, respectively. The inclusion of ECM into the scaffold had no discernible effect on the alignment, with the inclusion of rGO increasing the deviation of alignment. There were no statistical differences between all scaffolds in fiber alignment. Effects of swelling from PBS submersion were determined via SEM and showed similar fiber diameter compared to non-submerged scaffolds (**Figure 4.4K**). PU measured an average fiber diameter of 512 ± 176 nm. PU-20%ECM, PU-10%rGO, and PU-20%ECM-10%rGO measured 424 ± 142 nm, 375 ± 87 nm, and 356 ± 110 nm, respectively. All scaffolds except PU-10%rGO and PU-20%ECM-10%rGO had significantly different sizes. Fiber alignment of the immersed PU scaffolds was 85 ± 13°, while the PU-20%ECM, PU-10%rGO, and PU-20%ECM-10%rGO was 91 ± 15°, 86 ± 30°, and 90 ± 19°, respectively. There was no statistical difference between any submerged scaffold fiber angles. Scaffold shrinkage in response to PBS immersion was recorded and shown in **Table 4.1**. The scaffolding shrank in an anisotropic nature, with the amount of shrinkage depending on the orientation of the fibers. Across all scaffolds, the PD shrinkage was around 17~22% of the original size. The XD remained much closer to the original length, with all shrinkages around 2~7% of their original size. In the PD, there were significant differences between non-rGO-containing scaffolds and rGO-containing scaffolds. The only significant difference for XD was between PU-20%ECM and rGO-containing scaffolds. Images of rGO flakes confirm a multilayer morphology with various sizes between flakes.

4.3.4 Contact Angle

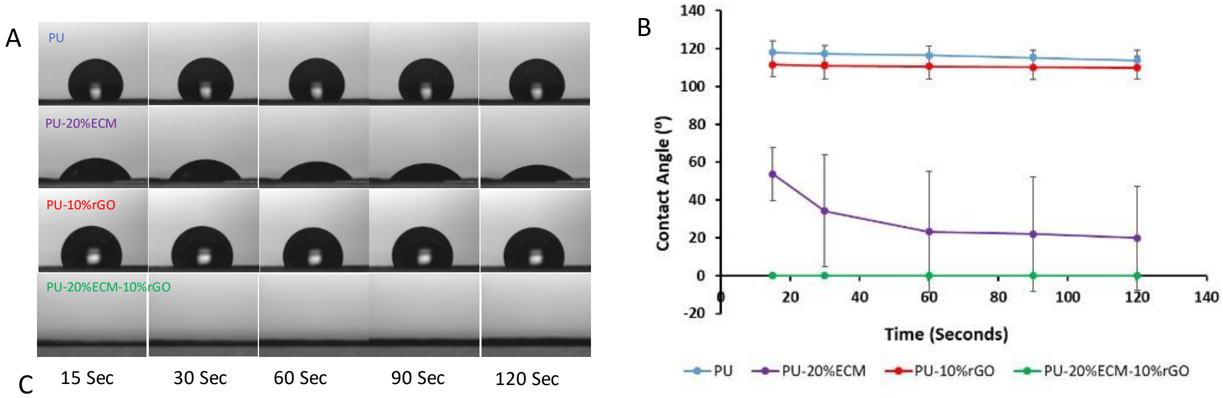

C

Scaffold	CA (°) 15 Sec	CA (°) 30 Sec	CA (°) 60 Sec	CA (°) 90 Sec	CA (°) 120 Sec
PU	118 ± 6^{a}	117 ± 4^{a}	116 ± 5^{a}	115 ± 4^{a}	113 ± 5^{a}
PU-20%ECM	54 ± 14^{b}	34 ± 30^{b}	23 ± 31^{b}	22 ± 30^{b}	20 ± 27^{b}
PU-10%rGO	111 ± 6^{a}	111 ± 6^{a}	110 ± 7^{a}	110 ± 6^{a}	110 ± 6^{a}
PU-20%ECM-10%rGO	0 ± 0^{c}	0 ± 0^{c}	0 ± 0^{b}	0 ± 0^{b}	0 ± 0^{b}

*a, b, and c represent significantly different groups for each characteristic

Figure 4.5: A) Contact angle images for PU, PU-20%ECM, PU-10%rGO, and PU-20%ECM-10%rGO scaffolds at time points of 15, 30, 60, 90, and 120 seconds after water droplet application B) Dynamic contact angle measurement for PU, PU-20%ECM, PU-10%rGO, and PU-20%ECM-10%rGO. C) Table of contact angles for PU, PU-20%ECM, PU-10%rGO, and PU-20%ECM-10%rGO at each time point.

Surface hydrophilicity quantified by contact angle revealed a clear pattern of inclusion of ECM significantly improving hydrophilicity (**Figure 4.5**). The PU scaffold exhibited a contact angle of 118 ± 6°, with the PU-20% ECM scaffold exhibiting a 54 ± 14°. The PU-10%rGO scaffold exhibited a similar contact angle to the PU scaffold of 111 ± 6°, with the PU-20% ECM- 10% rGO exhibiting a significantly lower angle of 0 ± 0° compared to the PU and PU-10%rGO scaffolding. PU-20%ECM-10%rGO exhibited the best hydrophilicity, with the droplet absorbed within the first 15 seconds of placement. PU-20%ECM could also fully absorb the droplet within the first minute of placement. The ECM-containing scaffolds were statistically different from the PU and PU-10%rGO scaffolds. PU-20%ECM and PU-20%ECM-10%rGO were considered statistically similar after 60 seconds of droplet placement.

4.3.5 In vitro Enzymatic Degradation

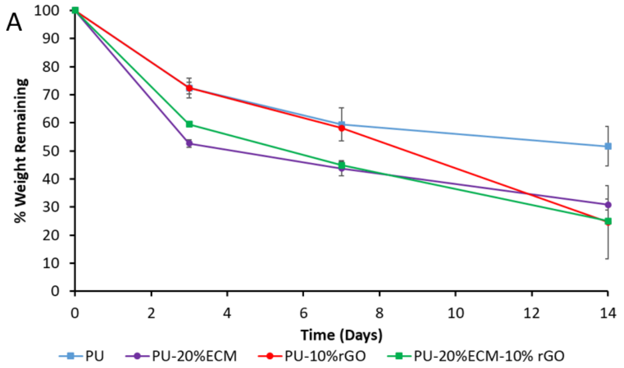

B

Sample	PU	PU-20%ECM	PU-10%rGO	PU-20%ECM-10%rGO
Day 3	72.4 ± 3.5[a]	52.6 ± 1.3[b]	72.4 ± 2.1[a]	59.4 ± 1.0[c]
Day 7	59.4 ± 5.9[a]	43.8 ± 2.8[b]	58.2 ± 0.2[a]	44.9 ± 1.1[b]
Day 14	51.6 ± 7.0[a]	30.8 ± 2.0[b]	24.6 ± 13.1[b]	25.0 ± 0.8[b]

*a, b, and c represent significantly different groups for each characteristic

Figure 4.6: A) The % remaining weight of *in vitro* enzymatic degradation for PU, PU-20%ECM, PU-10%rGO, and PU-20%ECM-10%rGO over the course of the 14-day study. B) Table of % remaining weight at each time point for PU, PU-20%ECM, PU-10%rGO, and PU-20%ECM-10%rGO. The degradation solution was composed of PBS and 100 U/mL lipase; samples were incubated with the solution for 14 days.

A 100 U/mL lipase solution in PBS was used to investigate the scaffolds' response, recapitulating the enzymatic environment of the body. The PU scaffold retained 51.6 ± 7.0% of its initial weight over the two-week study, retaining significantly more mass than the composite scaffolds by the end of the study. The PU-20%ECM, PU-10%rGO, and PU-20%ECM-10%rGO retained only 30.8 ± 2.0%, 24.6 ± 13.1%, and 25.0 ± 0.8% mass at the end of the two-week study (**Figure 4.6**). Statistical analysis with ANOVA revealed that all scaffolds deviated from each other except for PU and PU-10%rGO, remaining statistically similar from the first time point. The second time point exhibited similar results; however, PU-20%ECM and PU-20%ECM-10%rGO were considered statistically similar along with PU and PU-10%rGO.

4.3.6 Conductivity

Table 4.2: Conductivity of PU, PU-20%ECM, PU-10%rGO, and PU-20%ECM-10%rGO Films

Sample	Dry Sheet Resistance (Ω/□)	Dry Resistivity (Ω*m)	Dry Conductivity (S/m)	Wet Sheet Resistance (Ω/□)	Wet Resistivity (Ω*m)	Wet Conductivity (S/m)
PU	Not Detectable	Not Detectable	Not Detectable	Not Detectable	Not Detectable	Not Detectable
PU-20%ECM	Not Detectable	Not Detectable	Not Detectable	Not Detectable	Not Detectable	Not Detectable
PU-10%rGO	19144 ± 510[a]	5.7 ± 0.15[a]	0.174 ± 0.005[a]	51837 ± 4885[a]	19.7 ± 1.9[a]	0.051 ± 0.005[a]
PU-20%ECM-10%rGO	1724 ± 79[b]	1.1 ± 0.1[b]	0.92 ± 0.038[b]	24468 ± 2050[b]	14.4 ± 1.2[b]	0.070 ± 0.006[b]

*a and b represent significantly different groups for each characteristic

The conductivity of composite films was measured rather than fibrous scaffolds due to an inability to obtain results (data not shown). Interestingly the PU-20%ECM-10%rGO film exhibited a 5-fold increase in conductivity compared to the PU-10%rGO film (**Table 4.2**). Similarly, the sheet resistance and resistivity of PU-20%ECM-20%rGO are 11 to 5 times lower than the PU-10%rGO counterpart. Wet conductivity measurements were significantly less than the dry film measurements. A possible reason for this decrease is the conductivity of the PBS masking the bulk conductivity measurement rather than the film.

4.3.7 Mechanical Testing

4.3.7.1 Stress Relaxation Behavior

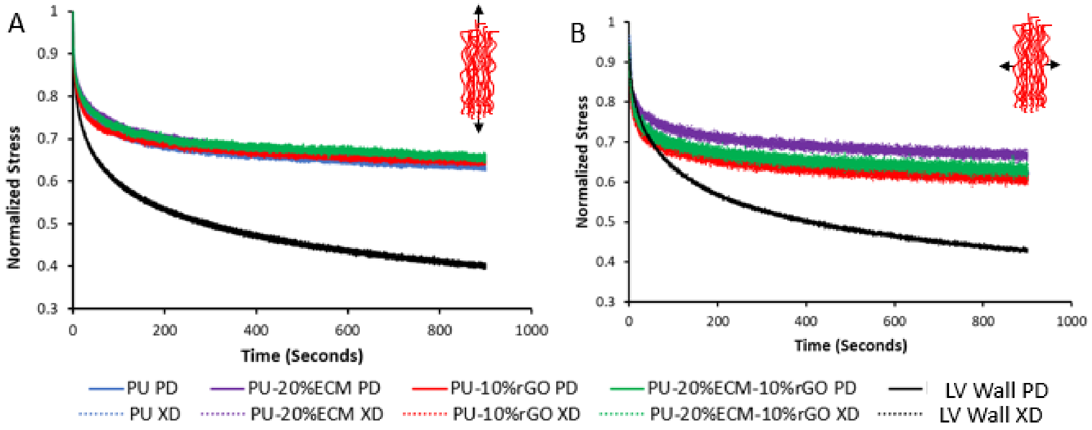

C

Scaffold	PU	PU-20%ECM	PU-10%rGO	PU-20%ECM-10%rGO	LV
SR: PD (%)	36.7 ± 2.6^{a}	35.9 ± 4.3^{a}	35.6 ± 1.4^{a}	34.3 ± 2.6^{a}	60.2 ± 2.5^{b}
SR: XD (%)	40.6 ± 3.9^{a}	34.2 ± 2.2^{a}	37.9 ± 4.1^{a}	36.3 ± 2.3^{a}	56.8 ± 8.4^{b}

*a, b represent significantly different groups for each characteristic

Figure 4.7: A) PD stress-relaxation for PU, PU-20%ECM, PU-10%rGO, PU-20%ECM-10%rGO, and LV porcine wall B) XD stress-relaxation for PU, PU-20%ECM, PU-10%rGO, PU-20%ECM-10%rGO, and LV porcine wall C) Table of stress-relaxation values for PU, PU-20%ECM, PU-10%rGO, PU-20%ECM-10%rGO, and LV porcine wall

The PD direction of the LV wall was able to release 60 ± 2.5% of the stress over 15 minutes, while the PU scaffold along the PD released 36.7 ± 2.6% (**Figure 4.7**). The composite scaffolds were roughly like PU, releasing 36 ± 4.3%, 35.6 ± 1.4%, and 34.3 ± 2.6% for PU-20%ECM, PU-10%rGO, and PU-20%ECM-10%rGO, respectively. All scaffolds were significantly different than the native tissue. In the XD direction, the native tissue released 56.8 ± 8.4% of stress while the PU released 40.6 ± 3.9% of the applied stress in the XD. The PU-20%ECM, PU-10%rGO, and PU-20%ECM-10%rGO released 34.2 ± 2.2%, 37.9 ± 4.1%, and 36.3 ± 2.3%, respectively. All fabricated scaffolds released similar amounts of stress; the native tissue's ability to release stress was significantly higher than all other scaffolds due to the higher amount of available conformational changes within the structure of the ECM.

4.3.7.2 Creep

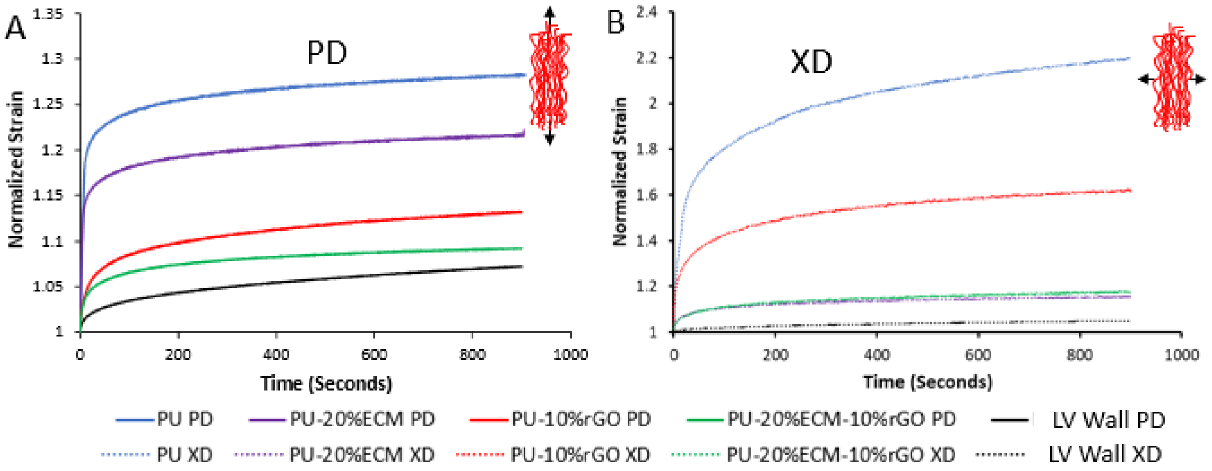

C

Scaffold	PU	PU-20%ECM	PU-10%rGO	PU-20%ECM-10%rGO	LV
Creep: PD (%)	28.3 ± 2.5^{a}	22.1 ± 2.4^{a}	13.2 ± 7.9^{b}	9.2 ± 0.8^{b}	7.2 ± 2.8^{b}
Creep: XD (%)	118.6 ± 46.2^{a}	15.4 ± 2.6^{b,c}	61.9 ± 12.9^{b}	17.8 ± 4.0^{b,c}	5.7 ± 6.2^{c}

*a and b represent significantly different groups for each characteristic

Figure 4.8: A) PD creep for PU, PU-20%ECM, PU-10%rGO, PU-20%ECM-10%rGO, and LV porcine wall B) XD creep for PU, PU-20%ECM, PU-10%rGO, PU-20%ECM-10%rGO, and LV porcine wall C) Table of creep values for PU, PU-20%ECM, PU-10%rGO, PU-20%ECM-10%rGO, and LV porcine wall

Native tissue in the PD direction had the lowest creep under constant stress, stretching 7.2 ± 2.8% of its original length over 15 minutes (**Figure 4.8**). PU scaffolds along the PD stretched to 28.3 ± 2.5% of their original length, which was the largest creep. The PU-20%ECM, PU-10%rGO, and PU-20%ECM-10%rGO had 22.1 ± 2.4%, 13.2 ± 0.9%, and 9.2 ± 2.8% respectively. PU and PU-20%ECM samples had statistically higher creep over the 15 minutes than all other tested samples. rGO containing samples were statistically like the native LV tissue. In the XD direction, the native tissue stretched to 5.7 ± 6.2% of the original length. The XD PU stretched to 118.6 ± 46.2% of its original length. The XD PU-20%ECM, PU-10%rGO, and PU-20%ECM-10%rGO stretched 15.4 ± 2.6%, 61.9 ± 12.9%, and 17.8 ± 4.0% respectively. Statistically, PU had the highest amount of creep in the XD, while all other scaffolds except PU-10%rGO were statistically like the XD native LV tissue.

4.3.7.3 Pull to Failure

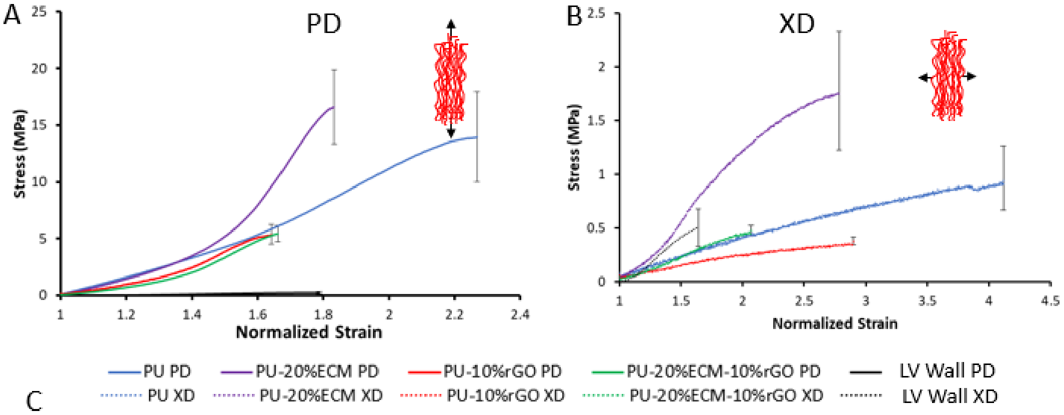

C

Scaffold	PU	PU-20%ECM	PU-10%rGO	PU-20%ECM-10%rGO	LV
Failure Stress PD (MPa)	14.0 ± 4.0^{a}	16.6 ± 3.3^{a}	5.4 ± 0.8^{b}	5.4 ± 0.7^{b}	0.25 ± 0.097^{c}
Failure Strain PD	2.26 ± 0.36^{a}	1.83 ± 0.09^{b}	1.64 ± 0.06^{b}	1.66 ± 0.02^{b}	1.79 ± 0.15^{b}
Failure Stress XD (MPa)	0.96 ± 0.29^{a}	1.78 ± 0.55^{b}	0.38 ± 0.05^{c}	0.48 ± 0.05^{a,c}	0.50 ± 0.17^{a,c}
Failure Stain XD	4.11 ± 0.90^{a}	2.78 ± 0.37^{b}	2.90 ± 0.41^{b}	2.07 ± 0.11^{b,c}	1.64 ± 0.37^{c}
Initial Modulus PD (KPa)	7191 ± 602^{a}	6157 ± 605^{a}	3161 ± 903^{b}	2863 ± 550^{b}	98 ± 25^{c}
Initial Modulus XD (KPa)	317 ± 84^{a}	592 ± 118^{b}	203 ± 47^{a}	289 ± 96^{a}	30 ± 14^{c}

*a, b, and c represent significantly different groups for each characteristic

Figure 4.9: A) PD failure testing for PU, PU-20%ECM, PU-10%rGO, PU-20%ECM-10%rGO, and LV porcine wall B) PD failure testing for PU, PU-20%ECM, PU-10%rGO, PU-20%ECM-10%rGO, and LV porcine wall C) Table of failure stress and strain values for PU, PU-20%ECM, PU-10%rGO, PU-20%ECM-10%rGO, and LV porcine wall

Native tissue in the PD failed around 0.24 ± 0.097 MPa, significantly lower than all tested scaffolds (**Figure 4.9**). The native tissue had a failure strain of around 1.79 ± 0.15. The scaffold had a failure stress of 14.0 ± 3.95 MPa for PD PU and a failure strain of 2.27 ± 0.36. Scaffolds containing ECM and rGO exhibited failure stresses of 16.6 ± 3.3 MPa, 5.4 ± 0.9 MPa, and 5.4 ± 0.10 MPa for PD PU-20%ECM, PU-10%rGO, and PU-20%ECM-10%rGO, respectively. Failure strains were 1.83 ± 0.09, 1.64 ± 0.06, and 1.66 ± 0.02 of the original lengths. The inclusion of ECM slightly improved the failure stress; however, it was statistically like PU. The inclusion of rGO significantly decreased the failure stress of the scaffold compared to both PU and PU-20%ECM. Failure strains of all composite scaffolds greatly decreased compared to the PU samples. PD PU had the highest stain across all scaffolds and native tissue. In the XD direction of the native tissue, the failure stress was 0.50 ± 0.17 MPa, while the failure strain was 1.64 ± 0.37. The XD for PU had a failure stress of 0.96 ± 0.30 MPa, while the failure strain was 4.11 ± 0.90. The XD PU-20%ECM, PU-10%rGO, and PU-20%ECM-10%rGO had failure stresses of 1.78 ± 0.55 MPa, 0.38 ± 0.04 MPa, and 0.48 ± 0.05 MPa, respectively, failure strains were 2.78 ± 0.67, 2.90 ± 0.41, and 2.07 ± 0.11, respectively. A noticeable trend of including ECM in the scaffold improved failure stresses. Inversely inclusion of rGO significantly decreased the failure stress. PU-20%ECM-10%rGO exhibited improved failure stress compared to PU-10%rGO. The only sample significantly different from the native LV tissue was PU-20%ECM; all other samples were statistically the same. All scaffolds except PU-20%ECM-10%rGO had statistically higher failure strains than the native LV tissue. The composite scaffolds initial modulus was heavily influenced by the rGO, with the PU-10%rGO and PU-20%ECM-10%rGO exhibiting similar moduli in the PD and XD.

4.3.7.4 Cyclic Stretching at 30% Strain

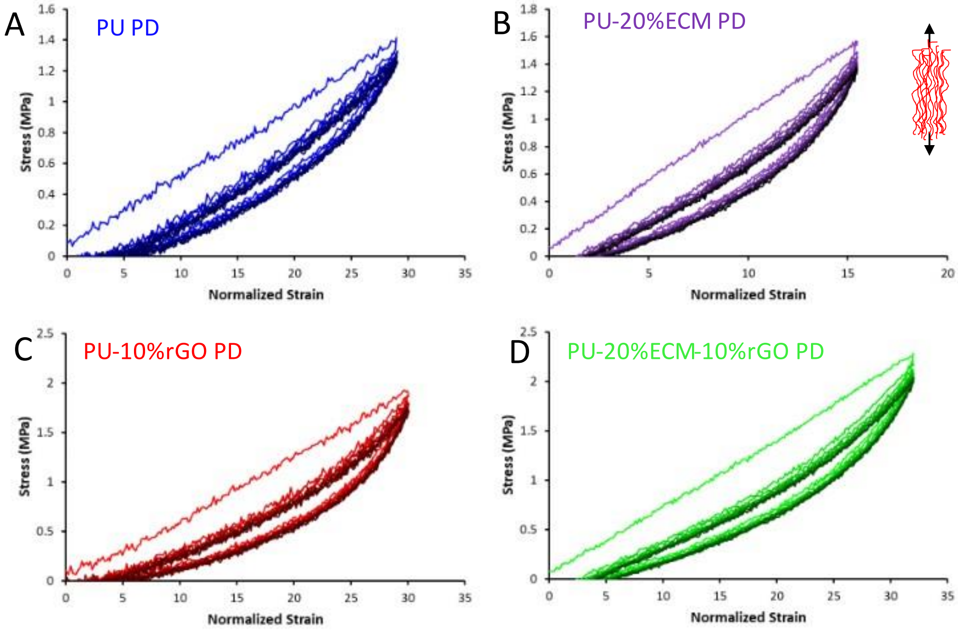

Figure 4.10: Cyclic test to 30% strain over 10 cycles for A) PU B) PU-20%ECM C) PU-10%rGO D) PU-20%ECM-10%rGO. The darker coloration denotes later cycles of testing, with the darkest representing the tenth cycle.

All scaffolds quickly adjusted to the cyclic stress after two cycles, with later cycles overlapping (**Figure 4.10**). All scaffolds exhibited similar max stresses over the testing, and all maintained a viscoelastic graph.

4.3.7.5 Biaxial

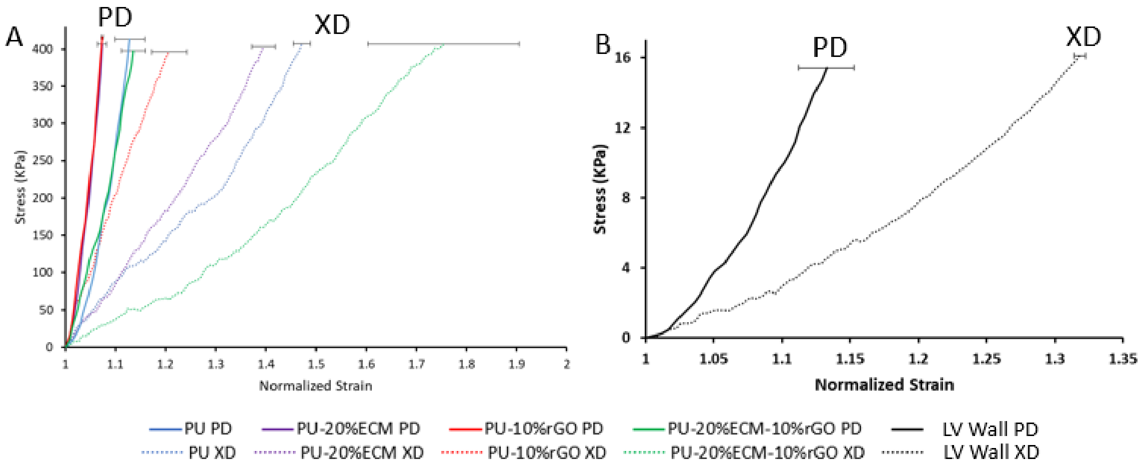

Figure 4.11: A) Biaxial testing in the PD and XD of PU, PU-20%ECM, PU-10%rGO, PU-20%ECM-10%rGO, and B) the porcine left ventricle wall in PD and XD direction.

The native tissue exhibited stiffer load curves in the PD than in the XD; similarly, scaffolds exhibited stiffer loading curves along the PD than in the XD. The trends obtained were indicative of anisotropic behavior (**Figure 4.11**).

4.3.8 *In vitro* Cell Compatibility and Behavior

4.3.8.1 *In vitro* Culture of Neonatal Rat Cardiomyocyte on PU-ECM-rGO scaffolds

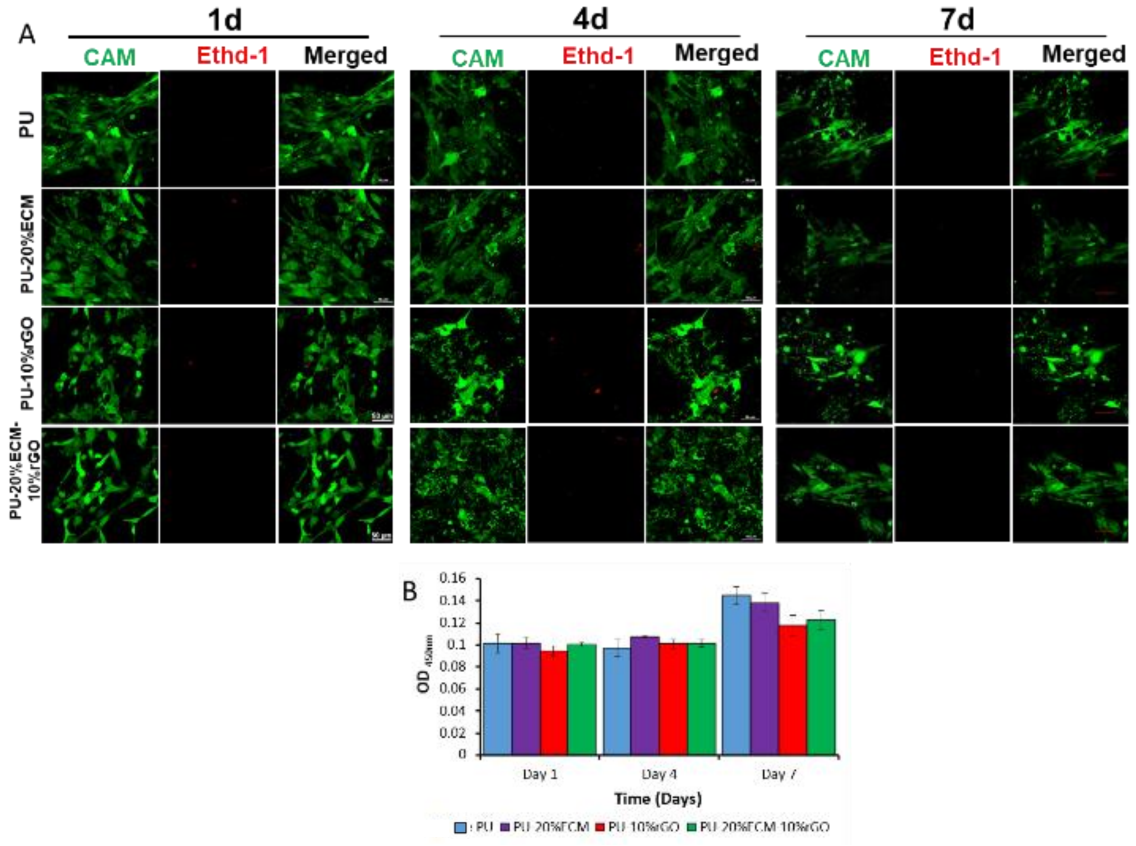

Figure 4.12: Cell viability on PU, PU-20%ECM, PU-10%rGO, PU-20%ECM-10%rGO scaffolds, A) Live/Dead staining, and B) cell counting from CCK-8 on days 1, 4, and 7.

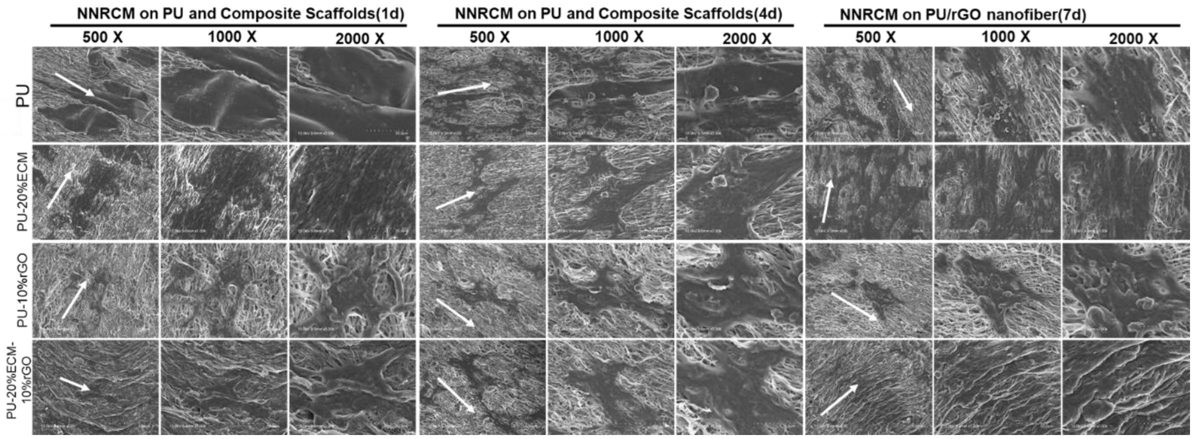

Figure 4.13: NNRCM morphology on PU, PU-20%ECM, PU-10%rGO, PU-20%ECM-10%rGO scaffolds, at 500x, 1000x, and 2000x magnification taken with SEM.

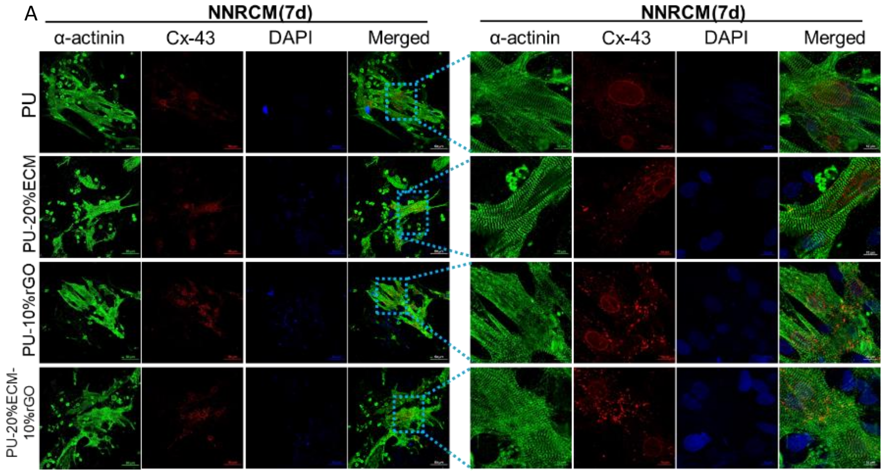

B

Sample	Sarcomere Length (μm)	Z-line Length (μm)	Aspect Ratio
PU	1.70 ± 0.23^{a}	3.54 ± 0.61^{a}	6.07 ± 2.26^{a}
PU-20%ECM	1.84 ± 0.26^{b}	3.94 ± 0.57^{b}	4.08 ± 1.14^{b}
PU-10%rGO	$1.82 \pm 0.30^{a,b}$	3.30 ± 0.46^{a}	$4.94 \pm 1.32^{a,b}$
PU-20%ECM-10%rGO	2.15 ± 0.34^{c}	3.80 ± 0.48^{b}	4.64 ± 1.21^{b}

*a, b, and c represent significantly different groups for each characteristic

Figure 4.14: A) Immunofluorescence staining of NNRCM for α-actinin, Cx-43, and DAPI on PU, PU-20%ECM, PU-10%rGO, PU-20%ECM-10%rGO scaffolds on day 7. B) Summary table of sarcomere length, Z-line length, and aspect ratio of NNRCM on scaffolds.

Cell viability on fibrous scaffolds exhibited good viability across all scaffolds (**Figure 4.12A**). There were no significant differences in cell count among scaffolds on days 1 and 4, with day 7 exhibiting a significant difference between PU and PU-10%rGO (**Figure 4.12B**). PU-20%ECM-10%rGO exhibited cell counts between PU-20%ECM and PU-10%rGO scaffolds on day 7. No noticeable trends can be inferred from the collected data. Across all scaffolds, NNRCM were organized mostly uniformly along the fibrous direction. Morphology results from SEM confirmed the alignment of cells, with evident elongation along the direction of the fibers **(Figure 4.13**). There was evident sarcomere striation and Z-line formation across all scaffolds (**Figure 4.14A**). PU-20%ECM-10%rGO exhibited superior sarcomere length to all scaffolds (**Figure 4.14B**). A similar trend was noted in Z-line length, with PU-20%ECM-10%rGO exhibiting significantly higher lengths than PU and PU-10%rGO. Improvements in these parameters suggest it improved development, with possible synergistic effects occurring from ECM and rGO influence on cells to improve sarcomere length. PU exhibited the most considerable aspect ratio, statistically more significant than PU-20%ECM and PU-20%ECM-10%rGO (**Figure 4.14C**).

4.4 Discussion

Bio-memetic biomaterials were investigated for cardiac tissue repair by including bioactive or conductive properties [114, 144, 177]. In many articles, improvements to potential tissue engineering constructs have been found through the fabrication of new composite biomaterials, which capture bioactivity and conduciveness to recapitulate the native cell niche [102, 136, 272]. This work aims to build upon our works to pioneer new bioactive, conductive, and elastic scaffolding that may be useful in cardiac tissue engineering applications. Fabricating the PU-ECM composite scaffold doped with rGO offered a novel biomaterial composite as a gestalt, with each component's weakness minimized when blended. Previous works exploring bioactive and conductive scaffolds conclude superior scaffold performance compared to scaffolds exhibiting only one of the properties [86, 100, 287]. Following in the footsteps of others, our novel PU-ECM-rGO scaffold offers superior properties compared to its base composites.

The surface morphology of scaffolding directly impacts how cells grow and organize themselves, specifically with cardiomyocytes requiring a highly organized and hierarchal structure for effective contractions [9, 88, 204]. Obtained morphology of all composite scaffolds exhibited the desired highly aligned nanofibers, with no noticeable impact on alignment due to the inclusion of ECM, rGO, or both. Fiber diameter was significantly affected by additives, namely ECM, with the inclusion of ECM decreasing the diameter of the fibers compared to the PU, while there was a non-significant increase in fiber diameter due to the inclusion of rGO. The increased fiber diameter from rGO inclusion was likely due to the aggregation of rGO within the fibers. ECM effects on fiber diameter likely occurred from ECM molecules interacting with the trace ionic salts resulting in the formation of nano-nets, further spreading the polymer out and shrinking the fibers [239]. These effects were exhibited in the PU-20%ECM-10%rGO composite scaffold, with smaller fiber diameters than PU and PU-10%rGO but larger than PU-20%ECM; a proposed mechanism for this effect is the interactions between ECM and rGO, with ECM interacting with the trace amounts of oxygen groups on the rGO [239]. In response to PBS immersion, all scaffolds maintained their highly aligned organization. PU exhibited the largest fiber diameter; the PU-20%ECM were the second largest. PU-20%ECM exhibited minor swelling due to the presence of GAGs throughout the scaffold, acting as a storage place for water [288]. Interestingly, rGO-containing scaffolds exhibited smaller fiber sizes from swelling than PU and PU-20%ECM scaffolds. The PU-20%ECM-10%rGO exhibited the slightest swelling but remained statically similar to PU-10%rGO. The rGO may act as pockets of highly hydrophobic pores within the scaffolding, shielding sections of PU from water exposure [257, 277]. The composite of both ECM and rGO have synergistic effects with reservoirs for water from GAGs and shielding PU from interacting with water due to rGO inclusion [268, 289, 290]. Shrinkage of fibrous scaffolds in PBS was noted, with an anisotropic shrinkage due to the alignment of the fiber. There was significantly more shrinkage in the PD than in the XD. Shrinkage or crimping of aligned electrospun scaffolds is a well-known occurrence originating from swelling, and the residual stress in the fibers stretched across the rotating mandrel [240]. In incubation, the residual stress can be released, causing crimping or shrinkage of the scaffolds, doping with rGO redirects some of the residual stress found within the scaffolds, decreasing the degree of shrinkage along the PD. In response to this redirection of residual stress in the XD experienced a higher degree of shrinkage, which is reflected by the observed data.

Hydrophilicity is another crucial aspect of a successful TE scaffold due to a direct correlation between the degree of cell adhesion with how hydrophilic the scaffold is [241, 291]. Our previous investigation into our scaffolds showed a clear trend that including ECM into PU vastly enhanced the hydrophilicity, while the inclusion of rGO either has no impact or decreased hydrophilicity. This trend continued in this study. Interestingly, the composite scaffold of PU-20%ECM-10%rGO exhibited improved hydrophilicity despite including the hydrophobic rGO, with all droplets absorbed within 15 seconds of application. The possible mechanism behind this phenomenon is the scaffold's interaction between ECM and rGO. Literature indicates that the oxygen groups in GO interact with the ECM to improve its colloidal stability and hydrophilicity [289]. Similarly, the digested ECM interacts with the residual oxygen groups on the rGO flakes, improving in hydrophilicity of the composite scaffold.

The longevity of the fibrous scaffolds within the host is an essential aspect of both mechanical support and integration. As cells mature and grow on the scaffold, their expansion and proliferation require more space to be made available. The slow degradation of the fibrous scaffolds allows the cells to proliferate and produce new ECM to replace the fibrous scaffold [127, 292]. Balancing the production of new ECM with the degradation of scaffolds to maintain proper mechanical stability requires ample time to tune, with our experimentation focusing on the length of time the scaffolds can survive in the enzymatic environment found in the body. Degraded scaffolds revealed PU retained the most mass compared to all the composite scaffolds, matching previously obtained results from aims 1 and 2. PU-10%rGO exhibited similar degradation rates until day 14 when fragments of the scaffold broke off during collection. Similarly, PU-20%ECM exhibited accelerated degradation, matching previously obtained results, while PU-20%ECM-10%rGO exhibited an average degradation between the PU-20%ECM and PU-10%rGO, showing the retention of rGO and accelerated degradation of ECM carried over to the composite scaffold.

Another critical aspect of the heart is the reliance on complex, timely electrical stimulation for coordinated contractions for efficient blood flow [133, 175, 263]. Integration of cell-laden scaffolding into this electrical stimulation necessitates conductive constructs to transmit unhindered signals to cells within the scaffold. The conductivity must be around the same conduciveness as the native heart, 0.03 – 0.6 S/m, or above to achieve optimal formulations of scaffolds [274, 293]. Tested films of our composite scaffolds exhibited either similar or superior conductivity in dry conditions, with the optimal composite, PU-20%ECM-10%rGO, exhibiting 5-fold better conductivity than PU-10%rGO. It is essential to distinguish that the films are not the same as the fabricated fibrous scaffolds, with no reliable readings obtained with the fibrous scaffolds. The likely reason for this deficiency in data collection is from the means of data retrieval, with the 4-point probe measuring surface conductivity; due to such limitations, films were used to receive reasonable measurements. The higher conductivity from PU-20%ECM-10%rGO compared to PU-10%rGO is likely due to the interactions between functional groups found in the digested ECM and the residual oxygen groups on the rGO [268, 290]. The amphiphilic digested ECM may interact with the amphiphilic rGO flakes for better rGO dispersal [156]. GO is highly prone to protein absorption of many globular proteins and glycoproteins. The GAGs in the PU-20%ECM-10%rGO scaffold might interact with rGO to spread more effectively throughout the film enabling higher conductivity than the PU-10%rGO scaffold [290, 294]. Better dispersal of rGO flakes ensures continuous electrical signal transfer throughout the film leading to higher conductivity measurements. Wet conductivity exhibited decreased conductivity compared to the measured dry membranes. A proposed reason for this decrease in conductance is the absorbed PBS masking the conductance of the film [278]. The liquid of the PBS heavily influences conductivity; the microscopic conductivity of the composite membrane would still be present on a cellular level [278].

The mechanical parameters of the tested scaffolding are essential indicators for its viability as a mechanically supportive wrap to diminish the adverse effects from LV remodeling post-MI. Cardiomyocyte maturity and growth are regulated through mechanical stimuli propagated by the surrounding ECM during development; mimicking these mechanical conditions promotes proper differentiation and maturation [64, 214, 295]. The stark difference in stiffness between healthy and infarcted hearts illustrates the need for elastic ‘soft’ scaffolding [244]. With difficulty obtaining human hearts for mechanical comparison, often, porcine hearts are used as an alternative model due to the similarities both mechanically and structurally [245, 246]. For constant stress exposure, stress-relaxation models the scaffoldings' ability to adapt and minimize loaded stress over continuous load. Native tissue samples exhibited superior adaptability compared to all scaffold composites, with the ability to diminish stress by 55~60% in PD and XD, while tested scaffolds were only able to diminish stress by 35-40%. This stark difference in adaptability originates from the high degree of crimping and potential conformational adaptation the interconnected native ECM can undergo, whereas the polymeric fibers have less structural freedom for the extensive morphological changes to diminish similar degrees of load [247, 248]. The noted benefit of native tissue ECM reorganization is the negligible creep during prolonged stress exposure, with the collagen network forming stiffer bundles leading to the low degrees of creep exhibited from creep testing [247]. Scaffoldings containing rGO exhibited similar creep to native tissue in the PD, this change exhibited by the rGO-containing scaffolds is noted in the literature and hypothesized to be caused by the interaction of rGO with the crystalline structure of the PU chains [279, 296]. Examining the XD, only PU-20%ECM and PU-20%ECM-10%rGO exhibited similar creep to the native tissue. The inclusion of ECM stiffened the scaffolds and allowed for side-to-side fiber interaction through the presence of the ‘micro-net’ structures. PU exhibited the highest degree of creep in PD and XD, owing to its elasticity and the lack of resistance to creep through either reorganization of polymer chains. Trends of failure stresses and strains followed similar patterns noted from the stress-relaxation and creep testing. PU exhibited the highest failure strain, with the doping or rGO and ECM inclusion stiffening the scaffold and lowering failure strains. The inclusion of ECM strengthened fibrous scaffolds by increasing the failure stress, with a statistically significant increase in stress in the XD, while the inclusion of rGO significantly decreased failure stresses. The addition of rGO particles throughout scaffolding would cause stark decreases in failure stress; however, rGO-containing scaffolds still exhibited similar or superior failure stresses compared to the native tissue, suggesting that the addition of rGO did not deteriorate the mechanical strength of scaffolds and the blends were feasible mechanically [279]. Cyclic testing of materials suggests the composite scaffolds can produce repetitive stress-strain curves, with a high degree of overlap occurring after 2 cycles, duplicating the pseudoelasticity of soft tissues. Further validation of mechanical similarities with native tissue from biaxial testing exhibited an apparent anisotropic behavior, with the PD exhibiting less strain than the XD, which was much more extensible.

In vitro studies with NNRCM exhibited promising results for the composite scaffolds, and exploration of composite scaffolds demonstrated no detrimental effects on cell viability. The only notable difference from cell counting was between PU and PU-10%rGO. Integrating ECM and rGO in the PU-20%ECM-10%rGO counteracted the possible detriment of rGO inclusion. Furthermore, sarcomere length was further improved compared to the stand compositions, and this may suggest synergistic signaling to the cells from the bioactivity and improved cell-to-cell communication derived from a conducive environment [112]. Smith et al. and Kharaziha et al. saw improved sarcomere lengths and Z-line formation with conductive and bioactive composite scaffolds, respectively [112, 283]. Z-line length in PU-20%ECM-10%rGO was comparable to PU-20%ECM while exhibiting superior lengths compared to PU and PU-10%rGO. There was a spread expression of Cx-43 throughout the cells and the peripherals in rGO-containing scaffolds. Cx-

43 is a protein related to gap junction formation; peripheral expression allows for faster cell-to-cell electrical communication [156]. PU-20%ECM exhibited some peripheral expression. However, PU-20%ECM-10%rGO expression appears like PU-10%rGO.

4.5 Conclusions

The fabrication of a novel biomaterial as a potential cardiac scaffold was successfully done with tunable characteristics depending on the fabrication procedure. The composite scaffold PU-20%ECM-10%rGO exhibited superior characteristics compared to the other fabricated scaffolds, exhibiting the unique interaction between digested ECM and rGO that was not seen in PU-20%ECM or PU-10%rGO scaffolds. Integration of bioactive and conductive aspects enabled closer mimicking of native tissue conditions. Preliminary *in vitro* studies with NNRCM demonstrated promising results, with PU-20%ECM-10%rGO cells having superior sarcomere lengths compared to PU-20%ECM and PU-10%rGO. Further optimization of scaffold fabrication with varied ECM and rGO content is promising for heart repair.

CHAPTER V: Summary and Future Studies

5.1 Summary

Myocardial infarctions are the prevalent cause of death worldwide, causing many complications and making treatment equally tricky. Relying on the body's natural regeneration further exacerbates difficulties and the risk of death. Conventional treatment options for patients who suffer from MI cater to the prevention of future complications. To overcome the hurdles in MI treatments, innovation in cardiac tissue engineering must occur to fill the current gaps. This thesis seeks to develop new blends of biomaterials and process them into scaffolds targeted toward cardiac tissue applications. We modify existing polymers used in cardiac tissue engineering, focusing on providing biologically relevant cues and a conducive environment to make a biomaterial blend tailored to myocardium regeneration. Through the following chapters, modifications and optimizations of elastic biodegradable polyurethane were done to address these needs.

5.1.1 Chapter II: Electrospun Elastic Polyurethane/Extracellular Matrix Nanofiber Scaffold for Cardiomyocyte Culture

Throughout this chapter, we investigated the novel polymer blend of biodegradable polyurethane. Through investigations, we have determined the viability of hybridizing biodegradable polyurethane with decellularized ECM. We digested decellularized ECM from the left ventricle of a porcine heart to craft a mechanically robust scaffold containing biomolecules found in the native tissue. Nanofibrous scaffolds were consistently obtainable through electrospinning. Physical characterizations of the scaffolds revealed a consistent trend in improving hydrophilicity with increasing ECM content. The fibrous scaffolds were mechanically comparable to cardiac tissue, verified through various mechanical testing, at higher concentrations of ECM content. Good cell compatibility for HL-1 and neonatal rat cardiomyocytes on the scaffolds was noted. More α-actinin and F-actin were expressed based on fluorescent intensity on PU-20%ECM scaffolds. Positive signs of improved development were noted in the higher ECM scaffolds. Neonatal rat cardiomyocytes provided promising results with improved maturity characteristics. PU-20%ECM had significantly more viable counted cells after 7 days than other scaffolds. Sarcomere and Z-line length maturity markers were significantly higher on PU-20%ECM scaffolds than on other scaffolds.

5.1.2 Chapter III: Electrospun Elastic Nanofiber Polyurethane Scaffold Incorporated with Conductive Reduced Graphene Oxide for Muscle Cell Culture

Aiming to create a scaffold with conductive properties to improve cell signaling and growth, we doped biodegradable polyurethane with reduced graphene oxide. Exhaustive optimization of rGO concentrations in PU was performed to find a blend ideal for electrically active cells to grow. Morphological and chemical characterizations of scaffolds verified that rGO content had no significant effect on the morphology of electrospun scaffolds. Hydrophilicity tests indicated potential limitations of rGO, slightly increasing the hydrophobic nature of the scaffolding. Conductive quantification of scaffolding was performed and determined that 10% rGO exhibited several magnitudes of improved conductivity compared to PU-4%rGO. Mechanical characterizations displayed a clear shift in properties corresponding to rGO content, with lower concentrations strengthening the scaffolds and a steep decrease in mechanical strength at high concentrations. Despite the reduction in mechanical compliance at higher concentrations of rGO, the scaffolds maintained superior mechanics to the native tissue. Muscle cells had lower growth at higher concentrations of rGO, with enhanced expression of MHC. *In vitro* studies with neonatal rat cardiomyocytes indicated an improvement in cell maturity parameters (sarcomere, Z-line length, and aspect ratio). Staining of Cx-43 suggested enhanced expression of Cx-43 in rGO-containing scaffolds.

5.1.3 Chapter IV: Fabrication of an Elastic Conductive Bioactive Electrospun Nanofiber Scaffold for Cardiomyocyte Culture

In this chapter, we investigated the viability of combining the previous two chapters' works to fabricate a biologically active and conductive scaffold, providing a highly tailored biomaterial blend for cardiac tissue repair. A PU-20%ECM-10%rGO fibrous scaffold was successfully fabricated and characterized. PU-20%ECM-10%rGO was compared to PU-20%ECM and PU-10%rGO to note any changes in morphology and physical properties. The addition of ECM counteracted the hydrophobic nature of rGO, and PU-20%ECM-10%rGO scaffolds were more hydrophilic than PU-20%ECM scaffolds. Improved conductive effects may have resulted from the interaction between ECM and rGO. PU-20%ECM-10%rGOs' mechanical properties are superior or comparable to the native tissue. The ECM in the PU-20%ECM-

10%rGO scaffold slightly improved the mechanics compared to the PU-10%rGO scaffold. Finally, ECM and rGO blends exhibited synergistic effects on NNRCM culture, increasing the expression of Cx-43 and maturity parameters like sarcomere and Z-line length.

5.2 Limitations

Throughout the studies, future works should address some limitations for improved results. Production of digested decellularized ECM from porcine hearts was all obtained from slaughterhouse-destined animals. Vecerek et al. noted cardiac pathoanatomical issues in about 7% of slaughterhouse-bound pigs [297]. Possible variations from various ECM batches would impact the effectiveness of scaffolding. A possible workaround would be sourcing porcine hearts from known vendors, with one large, produced ECM batch for all scaffold fabrication to minimize variation. Sourced rGO flakes were non-monolayer and required high concentrations to obtain noticeable effects on conductivity. Sourcing of monolayer rGO would overcome the decrease in mechanical strength from the aggregation of rGO. Improved conductivity characterization would be gained from the testing of fibrous scaffolds rather than films. Similarly, higher resolution 4-point probe instruments could test fibrous scaffolds or measure the voltage across the scaffolds when a known voltage is applied to calculate the resistivity of the scaffolds. Limited cell studies performed on scaffolds fail to characterize cell behavior effects completely. PCR would quantify gene expression for various muscle or cardiac markers. Targeting genes like Nkx2.5 and Gata4 would provide insight into the degree of early cardiac differentiation markers between scaffolds. Similarly, gene expression of TNNT2, Cx-43, and Actc1 would quantify the expression of proteins used in contractions, which can later be correlated with functionality evaluations to provide insight. Evaluating contraction strength, frequency of spontaneous contractions, conduction velocity, and calcium flux imaging would quantify how bioactive and conductive elements affected contraction behavior.

5.3 Future Works and Preliminary Study

Promising results from our work in these studies offer a strong basis for further exploration and characterization of these scaffolds. Expanding upon these works would involve more intensive *in vitro* studies. Recommendations for future directions of research are suggested in the following sections below.

5.3.1 *In vitro* Cell Functionality Quantification

Involving extensive in vitro functional tests for cell-laden scaffolds would document the idiosyncratic differences between scaffold iteration on cell behavior. Early cardiac markers like Nkx2.5 and Gata4 require quantification to indicate if seeded cells are predisposed to cardiac differentiation on composite scaffolds [298]. Nkx2.5 and Gata4 are essential in early heart development, regulating many cardiac-specific proteins [299]. The expression of cardiac contraction-associated proteins and gap junction-associated proteins like TNNT2, Cx-43, and Actc1 would give empirical data for the degree of expression [300, 301]. Increased gene expression correlates to improved CM maturity development [300, 301]. Similarly, functional tests like contraction strength on scaffolds would examine the direct effects the scaffolds have on function. Measured contraction strength would correlate α-Actinin striation and structure and its effects on the force [235]. Calcium flux imaging would quantify and visualize the transmittance of action potential between cardiomyocytes. Intracellular calcium (Ca^{2+}) oscillation is characteristic of functional CM, tracking Ca^{2+} movement provides insight on contraction [302]. Correlating gap junction formation from immunostaining and conductance of cells would confirm if upregulation of Cx-43 improved electrical cell-to-cell coupling [303]. Examining the electrical coupling of cells would confirm if expressed Cx-43 are functional gap junctions or ineffective hemichannels [304]. Furthermore, the number of spontaneous contractions exhibited from cells on scaffolds would characterize cell behavior with little effort. Overall, evaluating the cell behavioral and functional response to their scaffold would provide much-needed insight into scaffold effectiveness as a heart repair tool.

5.3.2 Mechanical and Electrical Stimulation Bioreactor

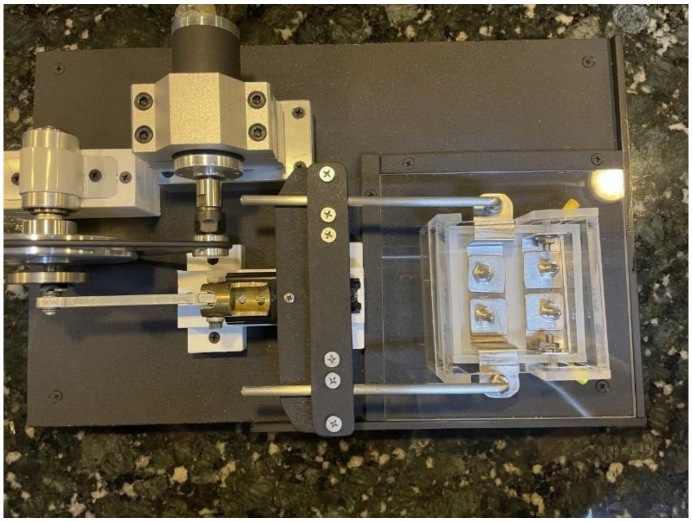

Figure 5.1: Bioreactor capable of mechanical stretch and electronic stimulation.

A bioreactor capable of performing mechanical and electrical stimulation was fabricated (**Figure 5.1**). A bioreactor, especially one that applies electrical stimulus, would help validate the effects a conductive scaffold has on cardiac cell differentiation [305]. Similarly, the continuous mechanical stimulation would simulate similar stresses scaffolds undergo to examine how scaffolds hold up under extended fatigue. Validation testing of loading scaffold samples into the reactor to undergo mechanical stretching has been explored to calibrate the Hz for the controller. To test the effectiveness of mechanical and electrical stimulation *in vitro,* studies utilizing muscle cells would provide good indicators of muscle cell growth due to their resilient nature as a cell line. Cell studies investigating the degree of contractibility cultured cells exhibit would provide valuable insight into the strength and uniformity of contractions on the scaffolds in response to mechanical and electrical stimulation.

5.3.3 Annealing of Aligned Electrospun Scaffolds

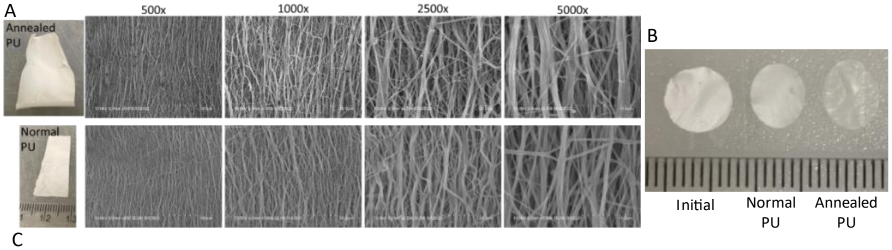

C

Scaffold	XD (mm)	PD (mm)	% Shrink along XD	% Shrink along PD
PU	7.7 ± 0.09	6.2 ± 0.07	3.4 ± 1.2	22.4 ± 0.9
PU Annealed	7.8 ± 0.26	6.6 ± 0.13	2.5 ± 3.3	17.0 ± 1.6

Figure 5.2: A) Annealed PU and PU scaffolds with SEM images at 500x, 1000x, 2500x, and 5000x magnification. B) Comparison of PU to annealed PU scaffold shrinkage. C) Summary of % shrinkage for PU and annealed PU scaffolds.

Diminishing shrinkage from aligned scaffolds has been explored through annealing [306]. Annealing can release the residual stress from aligned electrospinning by subjecting the scaffolds on the mandrel to heat to reach the T_m of PU (37°C, 24 hours). When removed from the mandrel, annealed fibrous scaffold had little to no shrinkage immediately after removal. Interestingly the edge of the fibrous sheet along the XD curled inwards (**Figure 5.2**). Morphological imaging with SEM (**Figure 5.2A**) showed that annealed scaffolds retained a high degree of alignment and are nanoscale. A shrink study by submersion in PBS at 37°C exhibited less shrink than non-annealed scaffolds. Annealed scaffolds shrank 17.0 ± 1.6% of their length in the PD and 2.5 ± 3.3% in the XD. Non-annealed scaffolds in this study exhibited 22.4 ± 0.9% shrink in the PD. Although a significant decrease in shrinkage occurred from annealing, further optimization of the annealing process is planned.

5.3.4 Increasing ECM Concentration in Hybrid Scaffolds

A vital concern of the inclusion of soft materials like ECM is the relatively weak mechanical properties they can contribute to the overall strength of the scaffold [68, 307]. Based on the mechanical data collected in Aim 2, increasing the amount of ECM in the scaffolds is possible while maintaining structural strength. The cell data collected based on the PU-20%ECM could be further improved by using a scaffold of up to 40-50% ECM [308]. Further testing with high concentrations of ECM could prove beneficial by increasing the biocompatibility of the scaffolding. Functionality improvements to cardiomyocytes could be further promoted through a more viable bonding site for integrins on the seeded CMs.

5.3.5 Exchanging Multilayer rGO Flakes for Monolayer rGO or Carbon Derivatives

In chapter 3, conductive scaffolds fabricated with high concentrations of rGO displayed significantly reduced mechanics compared to PU. The main reason for needing to include such a high concentration of rGO was due to the multilayer nature of the used rGO. Monolayer rGO requires significantly fewer concentrations for noticeable improvements in conductivity [156, 260]. Fabricating scaffolds with monolayer rGO would improve conductivity without compromising mechanical strength. Similarly, using other carbon derivatives such as carbon nanotubes has improved conductivity and mechanics. Investigations into these alternatives would provide a better understanding of possible future biomaterial blends.

5.3.6 Finite Element Analysis

Finite element analysis (FEA) and simulation of scaffolds using the mechanical properties that have been characterized would offer a unique look at how the scaffold would react in various conditions, saving time and material from actual testing of scaffolds [309-311]. Through mathematical modeling, finite element analysis would also enable predictability of the mechanical properties for other untested blended scaffolds. Simulation of scaffold responses to mechanical forces should help optimize the desired mechanical characteristics and minimize the risk of potential failure of the scaffold due to mechanical failure.

5.3.7 *In vivo* Evaluation of Cardiac Repair

Animal models are extensively used to validate the efficacy of developing treatment. Implantation of the scaffold in an animal model would provide insight into scaffold behavior in a clinical setting. Well-established protocols with Lewis rats investigating post-chronic infarction are numerous in the literature [125, 312]. Rat models are desirable compared to large animal models due to their time efficiency, lower material cost, and relatively cheap care costs [313]. The extensive validation from prior rat model protocols for MI treatment further bolsters its usefulness. Post MI treatment models allow for assessment of cardiac function in later stage MI conditions and alterations in LV remodeling with treated groups. A previously established protocol will be used in *in vivo* models. Lewis rats will be induced for MI through artery ligation; after 2 weeks, scaffolds would be sutured to the defect area after light scrapping to remove any fibrotic tissue and residual pericardium [125, 127, 310]. The rats will be divided into the following treatment groups; healthy rats as control, no treatment as a negative control, acellular PU scaffold, and acellular composite PU scaffolds (PU-20%ECM, PU-10%rGO, and PU-20%ECM-10%rGO). Electrocardiography (ECG) readings will be used to record for heart function weekly during the study [314]. Before sacrificing, hemodynamic catheterization will be performed on all rats to determine various functional parameters such as mean LV pressure, heart rate, and systolic and diastolic function [125]. Animals would be sacrificed 4 months after treatment for histological sampling. Histology samples will be analyzed with ImageJ to evaluate ECM composition between groups to determine if the composition is like the healthy control or no treatment. The area of defect, amount of fibrosis, and ventricle wall thickness will quantify the degree of remodeling between each treatment group [315]. Integration with the host will be measured by cell infiltration into the scaffold and if vascularization is present in the scaffold. Cells infiltrating the scaffold will be stained to identify cell types (macrophage, fibroblast, and myocyte). Angiogenesis will be detected by staining endothelial cell marker (CD31) and smooth muscle cell marker (α-SMA).

Appendix A

Related Publications

Conference Abstracts

1. McMahan, Sara, Katherine M Copeland, Xiaodan Shi, **Alan Taylor**, Brant Shipferling, Sammira Lakiesha Williams, Yi Hong, Pietro Bajona, Jun Liao. Biomechanical Characterization of the Neonatal Porcine Pulmonary Artery and Aorta. *World Congress of Biomechanics*, Dublin, Ireland, July 8-12, 2018.
2. Copeland, Katherine M., Sammira Rais-Rohani, **Alan Taylor**, Sarah Fitzgerald, Bryn Brazile, Victoria Messerschmidt, Richland L. Summers, Robert L. Hester, Raj Prabhu, Lakeisha N. Williams, Yi Hong, and Jun Liao. Biomechanical Characterization and Interrupted Mechanical Testing of Porcine Optic Nerve. *World Congress of Biomechanics*, Dublin, Ireland, July 8-12, 2018
3. McMahan, Sara, **Alan Taylor**, Katherine M. Copeland, Xiaodan Shi, Aneeta E. Kuriakose, Karla L. Perez, Yi Hong, Kytai T. Nguyen, Jun Liao. A Comparative Biomechanical Study of Porcine Epicardial Layer and Endocardial Layer. *Biomaterial Engineering Society,* Philadelphia, Pennsylvania, October 16-19, 2019
4. **Taylor, Alan**, Jiazhu Xu, Huikang Fu, Sara McMahan, Jun Liao, Yi Hong. Nanofibrous Biodegradable Polyurethane/Cardiac ECM Hybrid Patch. *Biomedical Engineering Society*, Online, October 14-17, 2020.
5. **Taylor, Alan**, Jiazhu Xu, Huikang Fu, Sara McMahan, Jun Liao, Yi Hong. Biodegradable Polyurethane/Reduced Graphene Oxide Fibers for C2C12 Growth. *Society for Biomaterials*, Online, April 21-24, 2021
6. **Taylor, Alan**, Jiazhu Xu, Huikang Fu, Lia Molina Cortez, Sara McMahan, Yan Chang, Zui Pan, Jun Liao, Yi Hong, Aligned Elastic Polyurethane/Extracellular Matrix Nanofibers for Cardiomyocyte Culture. *Society for Biomaterials*, Baltimore, Maryland, April 27-30, 2022.

Journal Articles

1. McMahan, Sara, **Alan Taylor**, Katherine M. Copeland, Zui Pan, Jun Liao, and Yi Hong. "Current advances in biodegradable synthetic polymer based cardiac patches." *Journal of Biomedical Materials Research Part A* 108, no. 4 (2020): 972-983.
2. McMahan, Sara, Katherine M Copeland, Xiaodan Shi, **Alan Taylor**, Brant Shipferling, Sammira Lakiesha Williams, Yi Hong, Pietro Bajona, Jun Liao. *Biomechanical Characterization of the Neonatal Porcine Pulmonary Artery and Aorta.* (In preparation)
3. Copeland, Katherine M., Sammira Rais-Rohani, **Alan Taylor**, Sarah Fitzgerald, Bryn Brazile, Victoria Messerschmidt, Richland L. Summers, Robert L. Hester, Raj Prabhu, Lakeisha N. Williams, Yi Hong, and Jun Liao. *Biomechanical Characterization and Interrupted Mechanical Testing of Porcine Optic Nerve.* (In preparation)
4. Di Zhang, Guoxun Wang, Xueliang Yu, Tuo Wei, Lukas Farbiak, Lindsay Johnson, **Alan Mark Taylor**, Jiazhu Xu, Yi Hong, Hao Zhu, Daniel Siegwart. "Enhancing CRISPR/Cas gene editing through modulating cellular mechanical properties for cancer therapy." *Nature Nanotechnology.* (Accepted)
5. **Alan Taylor**, Jiazhu Xu, Huikang Fu, Sara McMahan, Jun Liao, Yi Hong. *Electrospun Elastic Polyurethane/Extracellular Matrix Nanofiber Scaffold for Cardiomyocyte Culture*. (In preparation)
6. **Alan Taylor**, Jiazhu, Huikang Fu, Lia Molina, Karla Perez, Jun Liao, Yi Hong. *Electrospun Elastic Nanofiber Polyurethane Scaffold Doped with Reduced Graphene Oxide for muscle cell Culture*. (In preparation)
7. **Alan Taylor**, Jiazhu Xu. Huikang Fu, Lia Molina, Karla Perez, Jun Liao, Yi Hong. *Fabrication of an Elastic Conductive Electrospun Nanofiber Scaffold for Cardiomyocyte Culture*. (In preparation)

Appendix B

Abbreviations

Abbreviations

CVD	Cardiovascular Disease
HF	Heart Failure
MI	Myocardial Infarction
CM	Cardiomyocytes
ECM	Extracellular Matrix
EMT	Epithelial to Mesenchymal Transition
MMP	Metalloproteases
HA	Hyaluronic Acid
PG	Proteoglycans
GAGs	Glycosaminoglycan’s
NRG-1	Neuregulin-1
IGF-1	Insulin-like Growth Factor 1
Nf1	Neurofibromin
FgFs	Fibroblast Growth Factors
FGFR-1/2	Fibroblast Growth Factor Receptor ½
LV	Left Ventricle
LAD	Left Anterior Descending Coronary Artery
RAAS	Renin-Angiotensin-Aldosterone System
ACE	Angiotensin-Converting Enzyme

AGT	Angiotensin
PCL	Poly (ε-Caprolactone)
PLGA	Poly (Lactic-co-Glycolic acid)
PGS	Poly (Glycerol Sebacate)
PU	Polyurethane
ROP	Ring-Opening Polymerization
cTnT	Cardiac Troponin-T
PAni	Polyaniline
PLA	Poly (Lactic Acid)
PGA	Poly (Glycolic Acid)
FDA	US Food and Drug Administration
Cx-43	Connexin-43
cTnI	Cardiac Troponin I
β-MHC	β-Myosin Heavy Chain
PPy	Polypyrrole
AT	Aniline Trimer
PEUU	Poly (Ester Urethane Urea)
PECUU	Poly (Ester Carbonate Urethane) Urea
PCUU	Poly (Carbonate Urethane) Urea
PEG	Polyethylene Glycol

DMA	Dimethacrylate
PLA	Poly (Lactic acid)
MYH7	Myosin-7
TNNT2	Troponin T2 Gene
hCPCs	Human Cardiac Progenitor Cells
MYH6	Myosin-6
TCP	Tissue Culture Polystyrene
ROS	Reactive Oxygen Species
PU	Biodegradable Polyurethane
GO	Graphene Oxide
rGO	Reduced Graphene Oxide
SEM	Scanning Electron Microscope
ES	Electrospinning
HDI	Hexamethylene Diisocyanate
HFIP	1,1,1,3,3,3-Hexafluoro-2-Propanol
DMSO	Anhydrous Dimethyl Sulfone
HCl	Hydrochloric Acid
NaOH	Sodium Hydroxide
SDS	Sodium Dodecyl Sulfate
PBS	Phosphate Buffer Saline

Au/Pt	Gold/Platinum
FBS	Fetal Bovine Serum
EthD-1	Ethidium Homodimer-1
DMEM	Dulbecco’s Modified Eagle Medium
TRITC	Tetramethyl Rhodamine Isothiocyanate
DAPI	4’, 6 - Diamidino-2-Phenylindole
ANOVA	One-Way Analysis of Variance
ATR-FTIR	Attenuated Total Reflection - Fourier Transform Infrared Spectroscopy
XD	Across Preferred Fiber Direction
PD	Preferred Fiber Direction
SA	Sinoatrial Node
PCR	Polymerase Chain Reaction
NNRCM	Neonatal Rat Cardiomyocyte
Ca^{2+}	Calcium
ECG	Echocardiography

REFERENCES

1. Fryar CD, Chen T-C, Li X. Prevalence of uncontrolled risk factors for cardiovascular disease: United States, 1999-2010: US Department of Health and Human Services, Centers for Disease Control and Prevention, National Center for Health Statistics; 2012.

2. Abu-Issa R, Kirby ML. Heart field: from mesoderm to heart tube. Annual Review of Cell and Developmental Biology. 2007;23:45-68.

3. Marieb, N. E. Essentials of Human Anatomy & Physiology. 10th ed. San Francisco, CA: Pearson/Benjamin Cummings; 2009.

4. Smits AM, Dronkers E, Goumans M-J. The epicardium as a source of multipotent adult cardiac progenitor cells: Their origin, role and fate. Pharmacological Research. 2018;127:129-40.

5. Männer J, Perez-Pomares J, Macias D, Munoz-Chapuli R. The origin, formation and developmental significance of the epicardium: a review. Cells Tissues Organs. 2001;169(2):89-103.

6. Brutsaert DL, De Keulenaer GW, Fransen P, Mohan P, Kaluza GL, Andries LJ, et al. The cardiac endothelium: functional morphology, development, and physiology. Progress in Cardiovascular Diseases. 1996;39(3):239-62.

7. Mcmahan SR. The Biomechanics of Cardiac Elastin and Its Role in Bioengineering: The University of Texas at Arlington; 2020.

8. Franco D, Lamers WH, Moorman AF. Patterns of expression in the developing myocardium: towards a morphologically integrated transcriptional model. Cardiovascular Research. 1998;38(1):25-53.

9. Pagliarosi O, Picchio V, Chimenti I, Messina E, Gaetani R. Building an artificial cardiac microenvironment: A focus on the extracellular matrix. Frontiers in Cell and Developmental Biology. 2020:919.

10. Lockhart M, Wirrig E, Phelps A, Wessels A. Extracellular matrix and heart development. Birth Defects Research Part A: Clinical and Molecular Teratology. 2011;91(6):535-50.

11. Moorman AF, Lamers WH. Molecular anatomy of the developing heart. Trends in Cardiovascular Medicine. 1994;4(6):257-64.

12. Harris IS, Black BL. Development of the endocardium. Pediatric Cardiology. 2010;31(3):391-9.

13. Akerberg BN, Sarangam ML, Stankunas K. Endocardial Brg1 disruption illustrates the developmental origins of semilunar valve disease. Developmental Biology. 2015;407(1):158-72.

14. Stankunas K, Hang CT, Tsun Z-Y, Chen H, Lee NV, Wu JI, et al. Endocardial Brg1 represses ADAMTS1 to maintain the microenvironment for myocardial morphogenesis. Developmental Cell. 2008;14(2):298-311.

15. Ross RS, Borg TK. Integrins and the myocardium. Circulation Research. 2001;88(11):1112-9.

16. Ross RS. The extracellular connections: the role of integrins in myocardial remodeling. Journal of Cardiac Failure. 2002;8(6):S326-S31.

17. Chin TK, Perloff JK, Williams RG, Jue K, Mohrmann R. Isolated noncompaction of left ventricular myocardium. A study of eight cases. Circulation. 1990;82(2):507-13.

18. Bhatia NL, Tajik AJ, Wilansky S, Steidley DE, Mookadam F. Isolated noncompaction of the left ventricular myocardium in adults: a systematic overview. Journal of Cardiac Failure. 2011;17(9):771-8.

19. Engberding R, Yelbuz T, Breithardt G. Isolated noncompaction of the left ventricular myocardium. Clinical Research in Cardiology. 2007;96(7):481-8.

20. Schelbert HR. Anatomy and physiology of coronary blood flow. Journal of Nuclear Cardiology. 2010;17(4):545-54.

21. Rienks M, Papageorgiou A-P, Frangogiannis NG, Heymans S. Myocardial extracellular matrix: an ever-changing and diverse entity. Circulation Research. 2014;114(5):872-88.

22. Ferrara N, Carver-Moore K, Chen H, Dowd M, Lu L, O'shea KS, et al. Heterozygous embryonic lethality induced by targeted inactivation of the VEGF gene. Nature. 1996;380(6573):439-42.

23. Derrick CJ, Noël ES. The ECM as a driver of heart development and repair. Development. 2021;148(5):dev191320.

24. Smith TK, Bader DM, editors. Signals from both sides: Control of cardiac development by the endocardium and epicardium. Seminars in Cell & Developmental Biology; 2007: Elsevier.

25. Barry A. The functional significance of the cardiac jelly in the tubular heart of the chick embryo. The Anatomical Record. 1948;102(3):289-98.

26. Männer J, Yelbuz TM. Functional morphology of the cardiac jelly in the tubular heart of vertebrate embryos. Journal of Cardiovascular Development and Disease. 2019;6(1):12.

27. Dimarakis I, Levicar N, Nihoyannopoulos P, Gordon MY, Habib NA. In vitro stem cell differentiation into cardiomyocytes: Part 2: Chemicals, extracellular matrix, physical stimuli and coculture assays. Journal of Cardiothoracic-Renal Research. 2006;1(2):115-21.

28. Snarr BS, Kern CB, Wessels A. Origin and fate of cardiac mesenchyme. Developmental Dynamics. 2008;237(10):2804-19.

29. Person AD, Klewer SE, Runyan RB. Cell biology of cardiac cushion development. International Review of Cytology. 2005;243:287-335.

30. Kruithof BP, Duim SN, Moerkamp AT, Goumans M-J. TGFβ and BMP signaling in cardiac cushion formation: Lessons from mice and chicken. Differentiation. 2012;84(1):89-102.

31. Brannan CI, Perkins AS, Vogel KS, Ratner N, Nordlund ML, Reid SW, et al. Targeted disruption of the neurofibromatosis type-1 gene leads to developmental abnormalities in heart and various neural crest-derived tissues. Genes & Development. 1994;8(9):1019-29.

32. Frangogiannis NG. The extracellular matrix in myocardial injury, repair, and remodeling. The Journal of Clinical Investigation. 2017;127(5):1600-12.

33. Severino P, D'Amato A, Pucci M, Infusino F, Adamo F, Birtolo LI, et al. Ischemic heart disease pathophysiology paradigms overview: from plaque activation to microvascular dysfunction. International Journal of Molecular Sciences. 2020;21(21):8118.

34. Maseri A. Mechanisms of myocardial ischemia. Cardiovascular Drugs and Therapy. 1990;4(4):827-31.

35. Arras M, Höche A, Bohle R, Eckert P, Riedel W, Schaper J. Tumor necrosis factor-α in macrophages of heart, liver, kidney, and in the pituitary gland. Cell and Tissue Research. 1996;285(1):39-49.

36. Frangogiannis NG. Matricellular proteins in cardiac adaptation and disease. Physiological Reviews. 2012;92(2):635-88.

37. Bornstein P. Matricellular proteins: an overview. Journal of Cell Communication and Signaling. 2009;3(3):163-5.

38. Grauss RW, Winter EM, van Tuyn J, Pijnappels DA, Steijn RV, Hogers B, et al. Mesenchymal stem cells from ischemic heart disease patients improve left ventricular function after acute myocardial infarction. American Journal of Physiology-Heart and Circulatory Physiology. 2007;293(4):H2438-H47.

39. Goldstein S, de Jong JW. Changes in left ventricular wall dimensions during regional myocardial ischemia. The American Journal of Cardiology. 1974;34(1):56-62.

40. Anversa P, Zhang X, Li P, Olivetti G, Cheng W, Reiss K, et al. Ventricular remodeling in global ischemia. Cardioscience. 1995;6(2):89-100.

41. Salisbury PF, Cross CE, Rieben PA. Acute ischemia of inner layers of ventricular wall. American Heart Journal. 1963;66(5):650-6.

42. Gallagher K, Matsuzaki M, Koziol JA, Kemper WS, Ross Jr J. Regional myocardial perfusion and wall thickening during ischemia in conscious dogs. American Journal of Physiology-Heart and Circulatory Physiology. 1984;247(5):H727-H38.

43. Lima JA, Jeremy R, Guier W, Bouton S, Zerhouni EA, McVeigh E, et al. Accurate systolic wall thickening by nuclear magnetic resonance imaging with tissue tagging: correlation with sonomicrometers in normal and ischemic myocardium. Journal of the American College of Cardiology. 1993;21(7):1741-51.

44. D'Elia N, D'hooge J, Marwick TH. Association between myocardial mechanics and ischemic LV remodeling. JACC: Cardiovascular Imaging. 2015;8(12):1430-43.

45. Bishop J, Laurent G. Collagen turnover and its regulation in the normal and hypertrophying heart. European Heart Journal. 1995;16(suppl_C):38-44.

46. Weintraub WS, Hartigan PM, Mancini GJ, Teo KK, Maron DJ, Spertus JA, et al. Effect of coronary anatomy and myocardial ischemia on long-term survival in patients with stable ischemic heart disease. Circulation: Cardiovascular Quality and Outcomes. 2019;12(2):e005079.

47. Querejeta R, López B, González A, Sánchez E, Larman M, Martínez Ubago JL, et al. Increased collagen type I synthesis in patients with heart failure of hypertensive origin: relation to myocardial fibrosis. Circulation. 2004;110(10):1263-8.

48. Mill J, Stefanon I, Dos Santos L, Baldo M. Remodeling in the ischemic heart: the stepwise progression for heart. Brazilian Journal of Medical and Biological Research. 2011;44:890-8.

49. Lorenzen JM, Batkai S, Thum T. Regulation of cardiac and renal ischemia–reperfusion injury by microRNAs. Free Radical Biology and Medicine. 2013;64:78-84.

50. Burchfield JS, Xie M, Hill JA. Pathological ventricular remodeling: mechanisms: part 1 of 2. Circulation. 2013;128(4):388-400.

51. Sandler H, Dodge HT. Left ventricular tension and stress in man. Circulation Research. 1963;13(2):91-104.

52. Sabbah H, Goldstein S. Ventricular remodelling: consequences and therapy. European Heart Journal. 1993;14(suppl_C):24-9.

53. Ornish D, Scherwitz LW, Doody RS, Kesten D, McLanahan SM, Brown SE, et al. Effects of stress management training and dietary changes in treating ischemic heart disease. JAMA. 1983;249(1):54-9.

54. Dziedzic T, Slowik A, Pera J, Szczudlik A. Beta-blockers reduce the risk of early death in ischemic stroke. Journal of the Neurological Sciences. 2007;252(1):53-6.

55. Basoli A, Cametti C, Satriani FG, Mariani P, Severino P. Hemocompatibility of stent materials: alterations in electrical parameters of erythrocyte membranes. Vascular Health and Risk Management. 2012;8:197.

56. Choi D, Hwang K-C, Lee K-Y, Kim Y-H. Ischemic heart diseases: current treatments and future. Journal of Controlled Release. 2009;140(3):194-202.

57. Landmesser U, Drexler H. Chronic heart failure: an overview of conventional treatment versus novel approaches. Nature Clinical Practice Cardiovascular Medicine. 2005;2(12):628-38.

58. Kaba E, Thompson DR, Burnard P. Coping after heart transplantation: a descriptive study of heart transplant recipients' methods of coping. Journal of Advanced Nursing. 2000;32(4):930-6.

59. Bourge RC, Naftel DC, Costanzo-Nordin MR, Kirklin JK, Young JB, Kubo SH, et al. Pretransplantation risk factors for death after heart transplantation: a multiinstitutional study. The Transplant Cardiologists Research Database Group. The Journal of Heart and Lung Transplantation: The Official Publication of the International Society for Heart Transplantation. 1993;12(4):549-62.

60. Oh JH, Badhwar V, Mott BD, Li CM, Chiu RC-J. The effects of prosthetic cardiac binding and adynamic cardiomyoplasty in a model of dilated cardiomyopathy. The Journal of Thoracic and Cardiovascular Surgery. 1998;116(1):148-53.

61. Taguchi S, Mori A, Suzuki R, Ishida O. Technique for using pedicled latissimus dorsi muscle flaps to wrap prosthetic grafts in an infected thoracic aorta. Annals of Vascular Surgery. 2013;27(8):1223-7.

62. Nugent HM, Edelman ER. Tissue engineering therapy for cardiovascular disease. Circulation Research. 2003;92(10):1068-78.

63. Mayer J, Shin'oka T, Shum-Tim D. Tissue engineering of cardiovascular structures. Current Opinion in Cardiology. 1997;12:528-32.

64. Hirt MN, Hansen A, Eschenhagen T. Cardiac tissue engineering: state of the art. Circulation Research. 2014;114(2):354-67.

65. Enderle J. Introduction to biomedical engineering: Academic press; 2012.

66. Domenech M, Polo-Corrales L, Ramirez-Vick JE, Freytes DO. Tissue engineering strategies for myocardial regeneration: acellular versus cellular scaffolds? Tissue Engineering Part B: Reviews. 2016;22(6):438-58.

67. Moroni F, Mirabella T. Decellularized matrices for cardiovascular tissue engineering. American Journal of Stem Cells. 2014;3(1):1.

68. McMahan S, Taylor A, Copeland KM, Pan Z, Liao J, Hong Y. Current advances in biodegradable synthetic polymer based cardiac patches. Journal of Biomedical Materials Research Part A. 2020;108(4):972-83.

69. Tallawi M, Rosellini E, Barbani N, Cascone MG, Rai R, Saint-Pierre G, et al. Strategies for the chemical and biological functionalization of scaffolds for cardiac tissue engineering: a review. Journal of the Royal Society Interface. 2015;12(108):20150254.

70. Jawad H, Ali N, Lyon A, Chen Q, Harding S, Boccaccini A. Myocardial tissue engineering: a review. J Tissue Eng Regen Med. 2007;1(5):327-42.

71. Zhang D, Shadrin IY, Lam J, Xian H-Q, Snodgrass HR, Bursac N. Tissue-engineered cardiac patch for advanced functional maturation of human ESC-derived cardiomyocytes. Biomaterials. 2013;34(23):5813-20.

72. Eschenhagen T, Didié M, Heubach J, Ravens U, Zimmermann W-H. Cardiac tissue engineering. Transplant Immunology. 2002;9(2):315-21.

73. Kankala RA-O, Zhu K, Sun XN, Liu CG, Wang SB, Chen AA-O. Cardiac Tissue Engineering on the Nanoscale. ACS Biomaterials Science & Engineering. 2018;4(3):800-18.

74. Kitsara M, Joanne P, Boitard SE, Dhiab IB, Poinard B, Menasché P, et al. Fabrication of cardiac patch by using electrospun collagen fibers. Microelectronic Engineering. 2015;144:46-50.

75. Wang B, Borazjani A, Tahai M, de Jongh Curry AL, Simionescu DT, Guan J, et al. Fabrication of cardiac patch with decellularized porcine myocardial scaffold and bone marrow mononuclear cells. Journal of Biomedical Materials Research Part A. 2010;94(4):1100-10.

76. Qasim M, Haq F, Kang M-H, Kim J-H. 3D printing approaches for cardiac tissue engineering and role of immune modulation in tissue regeneration. Int J Nanomedicine. 2019;14:1311.

77. Boffito M, Sartori S, Ciardelli G. Polymeric scaffolds for cardiac tissue engineering: requirements and fabrication technologies. Polymer International. 2014;63(1):2-11.

78. Radisic M, Park H, Chen F, Salazar-Lazzaro JE, Wang Y, Dennis R, et al. Biomimetic approach to cardiac tissue engineering: oxygen carriers and channeled scaffolds. Tissue Engineering. 2006;12(8):2077-91.

79. Kapnisi M, Mansfield C, Marijon C, Guex AG, Perbellini F, Bardi I, et al. Auxetic cardiac patches with tunable mechanical and conductive properties toward treating myocardial infarction. Advanced Functional Materials. 2018;28(21):1800618.

80. Li Z, Guan J. Hydrogels for cardiac tissue engineering. Polymers (Basel). 2011;3(2):740-61.

81. Saludas L, Pascual-Gil S, Prósper F, Garbayo E, Blanco-Prieto M. Hydrogel based approaches for cardiac tissue engineering. International Journal of Pharmaceutics. 2017;523(2):454-75.

82. Tallawi M, Dippold D, Rai R, D'Atri D, Roether J, Schubert D, et al. Novel PGS/PCL electrospun fiber mats with patterned topographical features for cardiac patch applications. Materials Science and Engineering: C. 2016;69:569-76.

83. Prabhakaran MP, Kai D, Ghasemi-Mobarakeh L, Ramakrishna S. Electrospun biocomposite nanofibrous patch for cardiac tissue engineering. Biomedical Materials. 2011;6(5):055001.

84. Raina N, Pahwa R, Khosla JK, Gupta PN, Gupta M. Polycaprolactone-based materials in wound healing applications. Polymer Bulletin. 2021:1-23.

85. Gong C, Li J, Yi C, Qu S. Catalytic Regulation of Oligomers in Polycaprolactone. Molecular Catalysis. 2021;508:111594.

86. Sousa I, Mendes A, Pereira RF, Bártolo PJ. Collagen surface modified poly (ε-caprolactone) scaffolds with improved hydrophilicity and cell adhesion properties. Materials Letters. 2014;134:263-7.

87. Guex AG, Frobert A, Valentin J, Fortunato G, Hegemann D, Cook S, et al. Plasma-functionalized electrospun matrix for biograft development and cardiac function stabilization. Acta Biomater. 2014;10(7):2996-3006.

88. Rath R, Lee JB, Tran T-L, Lenihan SF, Galindo CL, Su YR, et al. Biomimetic microstructure morphology in electrospun fiber mats is critical for maintaining healthy cardiomyocyte phenotype. Cellular and Molecular Bioengineering. 2016;9(1):107-15.

89. Kai D, Prabhakaran MP, Jin G, Ramakrishna S. Guided orientation of cardiomyocytes on electrospun aligned nanofibers for cardiac tissue engineering. Journal of Biomedical Materials Research Part B: Applied Biomaterials. 2011;98(2):379-86.

90. Gil-Castell O, Ontoria-Oviedo I, Badia J, Amaro-Prellezo E, Sepúlveda P, Ribes-Greus A. Conductive polycaprolactone/gelatin/polyaniline nanofibres as functional scaffolds for cardiac tissue regeneration. Reactive and Functional Polymers. 2022;170:105064.

91. Shin M, Ishii O, Sueda T, Vacanti J. Contractile cardiac grafts using a novel nanofibrous mesh. Biomaterials. 2004;25(17):3717-23.

92. Liu Y, Xu Y, Wang Z, Wen D, Zhang W, Schmull S, et al. Electrospun nanofibrous sheets of collagen/elastin/polycaprolactone improve cardiac repair after myocardial infarction. Am J Transl Res. 2016;8(4):1678-94.

93. Borriello A, Guarino V, Schiavo L, Alvarez-Perez M, Ambrosio L. Optimizing PANi doped electroactive substrates as patches for the regeneration of cardiac muscle. Journal of Materials Science: Materials in Medicine. 2011;22(4):1053-62.

94. Loo SCJ, Tan WLJ, Khoa SM, Chia NK, Venkatraman S, Boey F. Hydrolytic degradation characteristics of irradiated multi-layered PLGA films. International Journal of Pharmaceutics. 2008;360(1-2):228-30.

95. Astete CE, Sabliov CM. Synthesis and characterization of PLGA nanoparticles. Journal of Biomaterials Science, Polymer Edition. 2006;17(3):247-89.

96. Wan Y, Qu X, Lu J, Zhu C, Wan L, Yang J, et al. Characterization of surface property of poly (lactide-co-glycolide) after oxygen plasma treatment. Biomaterials. 2004;25(19):4777-83.

97. Chen Y, Wang J, Shen B, Chan CW, Wang C, Zhao Y, et al. Engineering a freestanding biomimetic cardiac patch using biodegradable poly (lactic-co-glycolic acid)(PLGA) and human embryonic stem cell-derived ventricular cardiomyocytes (hESC-VCMs). Macromolecular Bioscience. 2015;15(3):426-36.

98. Cristallini C, Vaccari G, Barbani N, Cibrario Rocchietti E, Barberis R, Falzone M, et al. Cardioprotection of PLGA/gelatine cardiac patches functionalised with adenosine in a large animal model of ischaemia and reperfusion injury: A feasibility study. J Tissue Eng Regen Med. 2019;13(7):1253-64.

99. Yu J, Lee A-R, Lin W-H, Lin C-W, Wu Y-K, Tsai W-B. Electrospun PLGA fibers incorporated with functionalized biomolecules for cardiac tissue engineering. Tissue Engineering Part A. 2014;20(13-14):1896-907.

100. Li M, Mondrinos MJ, Chen X, Gandhi MR, Ko FK, Lelkes PI. Co-electrospun poly (lactide-co-glycolide), gelatin, and elastin blends for tissue engineering scaffolds. Journal of Biomedical Materials Research Part A. 2006;79(4):963-73.

101. Prabhakaran MP, Mobarakeh LG, Kai D, Karbalaie K, Nasr-Esfahani MH, Ramakrishna S. Differentiation of embryonic stem cells to cardiomyocytes on electrospun nanofibrous substrates. Journal of Biomedical Materials Research Part B: Applied Biomaterials. 2014;102(3):447-54.

102. Lee EJ, Lee JH, Shin YC, Hwang D-G, Kim JS, Jin OS, et al. Graphene oxide-decorated PLGA/collagen hybrid fiber sheets for application to tissue engineering scaffolds. Biomaterials Research. 2014;18(1):18-24.

103. Stout DA, Basu B, Webster TJ. Poly (lactic–co-glycolic acid): carbon nanofiber composites for myocardial tissue engineering applications. Acta Biomater. 2011;7(8):3101-12.

104. Hsiao C-W, Bai M-Y, Chang Y, Chung M-F, Lee T-Y, Wu C-T, et al. Electrical coupling of isolated cardiomyocyte clusters grown on aligned conductive nanofibrous meshes for their synchronized beating. Biomaterials. 2013;34(4):1063-72.

105. Lesman A, Habib M, Caspi O, Gepstein A, Arbel G, Levenberg S, et al. Transplantation of a tissue-engineered human vascularized cardiac muscle. Tissue Engineering Part A. 2010;16(1):115-25.

106. Wang Y, Ameer GA, Sheppard BJ, Langer R. A tough biodegradable elastomer. Nature Biotechnology. 2002;20(6):602-6.

107. Rai R, Tallawi M, Grigore A, Boccaccini AR. Synthesis, properties and biomedical applications of poly (glycerol sebacate)(PGS): A review. Progress in Polymer Science. 2012;37(8):1051-78.

108. Li Y, Cook WD, Moorhoff C, Huang WC, Chen QZ. Synthesis, characterization and properties of biocompatible poly (glycerol sebacate) pre-polymer and gel. Polymer International. 2013;62(4):534-47.

109. Ravichandran R, Venugopal JR, Sundarrajan S, Mukherjee S, Ramakrishna S. Cardiogenic differentiation of mesenchymal stem cells on elastomeric poly (glycerol sebacate)/collagen core/shell fibers. World Journal of Cardiology. 2013;5(3):28.

110. Engelmayr GC, Cheng M, Bettinger CJ, Borenstein JT, Langer R, Freed LE. Accordion-like honeycombs for tissue engineering of cardiac anisotropy. Nature Materials. 2008;7(12):1003-10.

111. Marsano A, Maidhof R, Luo J, Fujikara K, Konofagou EE, Banfi A, et al. The effect of controlled expression of VEGF by transduced myoblasts in a cardiac patch on vascularization in a mouse model of myocardial infarction. Biomaterials. 2013;34(2):393-401.

112. Kharaziha M, Nikkhah M, Shin S-R, Annabi N, Masoumi N, Gaharwar AK, et al. PGS: Gelatin nanofibrous scaffolds with tunable mechanical and structural properties for engineering cardiac tissues. Biomaterials. 2013;34(27):6355-66.

113. Ravichandran R, Venugopal JR, Sundarrajan S, Mukherjee S, Sridhar R, Ramakrishna S. Expression of cardiac proteins in neonatal cardiomyocytes on PGS/fibrinogen core/shell substrate for Cardiac tissue engineering. International Journal of Cardiology. 2013;167(4):1461-8.

114. Ravichandran R, Venugopal JR, Mukherjee S, Sundarrajan S, Ramakrishna S. Elastomeric core/shell nanofibrous cardiac patch as a biomimetic support for infarcted porcine myocardium. Tissue Engineering Part A. 2015;21(7-8):1288-98.

115. Chen Q-Z, Ishii H, Thouas GA, Lyon AR, Wright JS, Blaker JJ, et al. An elastomeric patch derived from poly (glycerol sebacate) for delivery of embryonic stem cells to the heart. Biomaterials. 2010;31(14):3885-93.

116. Zanjanizadeh Ezazi N, Ajdary R, Correia A, Mäkilä E, Salonen J, Kemell M, et al. Fabrication and characterization of drug-loaded conductive poly (glycerol sebacate)/nanoparticle-based composite patch for myocardial infarction applications. ACS Applied Materials & Interfaces. 2020;12(6):6899-909.

117. Hu T, Wu Y, Zhao X, Wang L, Bi L, Ma PX, et al. Micropatterned, electroactive, and biodegradable poly (glycerol sebacate)-aniline trimer elastomer for cardiac tissue engineering. Chemical Engineering Journal. 2019;366:208-22.

118. Fakhrali A, Nasari M, Poursharifi N, Semnani D, Salehi H, Ghane M, et al. Biocompatible graphene-embedded PCL/PGS-based nanofibrous scaffolds: A potential application for cardiac tissue regeneration. Journal of Applied Polymer Science. 2021;138(40):51177.

119. Grasl C, Bergmeister H, Stoiber M, Schima H, Weigel G. Electrospun polyurethane vascular grafts: in vitro mechanical behavior and endothelial adhesion molecule expression. Journal of Biomedical Materials Research Part A: An Official Journal of The Society for Biomaterials, The Japanese Society for Biomaterials, and The Australian Society for Biomaterials and the Korean Society for Biomaterials. 2010;93(2):716-23.

120. Jia L, Prabhakaran MP, Qin X, Kai D, Ramakrishna S. Biocompatibility evaluation of protein-incorporated electrospun polyurethane-based scaffolds with smooth muscle cells for vascular tissue engineering. Journal of Materials Science. 2013;48(15):5113-24.

121. Amna T, Hassan MS, Sheikh FA, Lee HK, Seo K-S, Yoon D, et al. Zinc oxide-doped poly (urethane) spider web nanofibrous scaffold via one-step electrospinning: a novel matrix for tissue engineering. Applied Microbiology and Biotechnology. 2013;97(4):1725-34.

122. Soletti L, Nieponice A, Hong Y, Ye SH, Stankus JJ, Wagner WR, et al. In vivo performance of a phospholipid-coated bioerodable elastomeric graft for small-diameter vascular applications. Journal of Biomedical Materials Research Part A. 2011;96(2):436-48.

123. McDevitt TC, Woodhouse KA, Hauschka SD, Murry CE, Stayton PS. Spatially organized layers of cardiomyocytes on biodegradable polyurethane films for myocardial repair. Journal of Biomedical Materials Research Part A: An Official Journal of The Society for Biomaterials, The Japanese Society for

Biomaterials, and The Australian Society for Biomaterials and the Korean Society for Biomaterials. 2003;66(3):586-95.

124. Park H-s, Gong M-S, Park J-H, Moon S-i, Wall IB, Kim H-W, et al. Silk fibroin–polyurethane blends: Physical properties and effect of silk fibroin content on viscoelasticity, biocompatibility and myoblast differentiation. Acta Biomater. 2013;9(11):8962-71.

125. D'Amore A, Yoshizumi T, Luketich SK, Wolf MT, Gu X, Cammarata M, et al. Bi-layered polyurethane - Extracellular matrix cardiac patch improves ischemic ventricular wall remodeling in a rat model. Biomaterials. 2016;107:1-14.

126. Asadpour S, Yeganeh H, Ai J, Kargozar S, Rashtbar M, Seifalian A, et al. Polyurethane-polycaprolactone blend patches: scaffold characterization and cardiomyoblast adhesion, proliferation, and function. ACS Biomaterials Science & Engineering. 2018;4(12):4299-310.

127. Hashizume R, Hong Y, Takanari K, Fujimoto KL, Tobita K, Wagner WR. The effect of polymer degradation time on functional outcomes of temporary elastic patch support in ischemic cardiomyopathy. Biomaterials. 2013;34(30):7353-63.

128. Boffito M, Di Meglio F, Mozetic P, Giannitelli SM, Carmagnola I, Castaldo C, et al. Surface functionalization of polyurethane scaffolds mimicking the myocardial microenvironment to support cardiac primitive cells. PLoS One. 2018;13(7):e0199896.

129. Tao ZW, Jarrell DK, Robinson A, Cosgriff-Hernandez EM, Jacot JG. A Prevascularized Polyurethane-Reinforced Fibrin Patch Improves Regenerative Remodeling in a Rat Right Ventricle Replacement Model. Advanced Healthcare Materials. 2021;10(23):2101018.

130. Carson D, Hnilova M, Yang X, Nemeth CL, Tsui JH, Smith AS, et al. Nanotopography-induced structural anisotropy and sarcomere development in human cardiomyocytes derived from induced pluripotent stem cells. ACS Applied Materials & Interfaces. 2016;8(34):21923-32.

131. Bahrami S, Solouk A, Mirzadeh H, Seifalian AM. Electroconductive polyurethane/graphene nanocomposite for biomedical applications. Composites Part B: Engineering. 2019;168:421-31.

132. Ganji Y, Kasra M, Kordestani SS, Hariri MB. Synthesis and characterization of gold nanotube/nanowire–polyurethane composite based on castor oil and polyethylene glycol. Materials Science and Engineering: C. 2014;42:341-9.

133. Ganji Y, Li Q, Quabius ES, Böttner M, Selhuber-Unkel C, Kasra M. Cardiomyocyte behavior on biodegradable polyurethane/gold nanocomposite scaffolds under electrical stimulation. Materials Science and Engineering: C. 2016;59:10-8.

134. Baheiraei N, Gharibi R, Yeganeh H, Miragoli M, Salvarani N, Di Pasquale E, et al. Electroactive polyurethane/siloxane derived from castor oil as a versatile cardiac patch, part II: HL-1 cytocompatibility and electrical characterizations. Journal of Biomedical Materials Research Part A. 2016;104(6):1398-407.

135. Yao Y, Ding J, Wang Z, Zhang H, Xie J, Wang Y, et al. ROS-responsive polyurethane fibrous patches loaded with methylprednisolone (MP) for restoring structures and functions of infarcted myocardium in vivo. Biomaterials. 2020;232:119726.

136. Ahmadi P, Nazeri N, Derakhshan MA, Ghanbari H. Preparation and characterization of polyurethane/chitosan/CNT nanofibrous scaffold for cardiac tissue engineering. International Journal of Biological Macromolecules. 2021;180:590-8.

137. Kim P, editor Guided Three-Dimensional Growth of Functional Cardiomyocytes Using Nanostructured PEG Scaffold. Gordon Research Conferences on Signal Transduction By Engineered Extracellular Matrices; 2006: Gordon Research Conferences.

138. Hubbell JA. Bioactive biomaterials. Current Opinion in Biotechnology. 1999;10(2):123-9.

139. Whitesides GM, Ostuni E, Takayama S, Jiang X, Ingber DE. Soft lithography in biology and biochemistry. Annual Review of Biomedical Engineering. 2001;3(1):335-73.

140. Kerscher P, Turnbull IC, Hodge AJ, Kim J, Seliktar D, Easley CJ, et al. Direct hydrogel encapsulation of pluripotent stem cells enables ontomimetic differentiation and growth of engineered human heart tissues. Biomaterials. 2016;83:383-95.

141. Dikovsky D, Bianco-Peled H, Seliktar D. The effect of structural alterations of PEG-fibrinogen hydrogel scaffolds on 3-D cellular morphology and cellular migration. Biomaterials. 2006;27(8):1496-506.

142. Geuss LR, Allen AC, Ramamoorthy D, Suggs LJ. Maintenance of HL-1 cardiomyocyte functional activity in PEGylated fibrin gels. Biotechnology and Bioengineering. 2015;112(7):1446-56.

143. Cesur S, Ulag S, Ozak L, Gumussoy A, Arslan S, Yilmaz BK, et al. Production and characterization of elastomeric cardiac tissue-like patches for Myocardial Tissue Engineering. Polymer Testing. 2020;90:106613.

144. Basara G, Saeidi-Javash M, Ren X, Bahcecioglu G, Wyatt BC, Anasori B, et al. Electrically conductive 3D printed Ti3C2Tx MXene-PEG composite constructs for cardiac tissue engineering. Acta Biomater. 2020.

145. Dobner S, Bezuidenhout D, Govender P, Zilla P, Davies N. A synthetic non-degradable polyethylene glycol hydrogel retards adverse post-infarct left ventricular remodeling. Journal of Cardiac Failure. 2009;15(7):629-36.

146. Pourfarhangi KE, Mashayekhan S, Asl SG, Hajebrahimi Z. Construction of scaffolds composed of acellular cardiac extracellular matrix for myocardial tissue engineering. Biologicals. 2018;53:10-8.

147. Pok S, Benavides OM, Hallal P, Jacot JG. Use of myocardial matrix in a chitosan-based full-thickness heart patch. Tissue Engineering Part A. 2014;20(13-14):1877-87.

148. Shah M, Kc P, Zhang G. In Vivo Assessment of Decellularized Porcine Myocardial Slice as an Acellular Cardiac Patch. ACS Applied Materials & Interfaces. 2019;11(27):23893-900.

149. Singelyn JM, Sundaramurthy P, Johnson TD, Schup-Magoffin PJ, Hu DP, Faulk DM, et al. Catheter-deliverable hydrogel derived from decellularized ventricular extracellular matrix increases endogenous

cardiomyocytes and preserves cardiac function post-myocardial infarction. Journal of the American College of Cardiology. 2012;59(8):751-63.

150. Seif-Naraghi SB, Singelyn JM, Salvatore MA, Osborn KG, Wang JJ, Sampat U, et al. Safety and efficacy of an injectable extracellular matrix hydrogel for treating myocardial infarction. Science Translational Medicine. 2013;5(173):173ra25-ra25.

151. Carvalho JL, de Carvalho PH, Gomes DA, Goes AM. Characterization of decellularized heart matrices as biomaterials for regular and whole organ tissue engineering and initial in-vitro recellularization with ips cells. Journal of Tissue Science & Engineering. 2012:002.

152. Guyette JP, Charest JM, Mills RW, Jank BJ, Moser PT, Gilpin SE, et al. Bioengineering human myocardium on native extracellular matrix. Circulation Research. 2016;118(1):56-72.

153. Traverse JH, Henry TD, Dib N, Patel AN, Pepine C, Schaer GL, et al. First-in-man study of a cardiac extracellular matrix hydrogel in early and late myocardial infarction patients. Basic to Translational Science. 2019;4(6):659-69.

154. Kerscher P, Kaczmarek JA, Head SE, Ellis ME, Seeto WJ, Kim J, et al. Direct production of human cardiac tissues by pluripotent stem cell encapsulation in gelatin methacryloyl. ACS Biomaterials Science & Engineering. 2017;3(8):1499-509.

155. Zhang F, Zhang N, Meng H-X, Liu H-X, Lu Y-Q, Liu C-M, et al. Easy applied gelatin-based hydrogel system for long-term functional cardiomyocyte culture and myocardium formation. ACS Biomaterials Science & Engineering. 2019;5(6):3022-31.

156. Shin SR, Zihlmann C, Akbari M, Assawes P, Cheung L, Zhang K, et al. Reduced graphene oxide-gelMA hybrid hydrogels as scaffolds for cardiac tissue engineering. Small. 2016;12(27):3677-89.

157. Balasubramanian P, Prabhakaran MP, Kai D, Ramakrishna S. Human cardiomyocyte interaction with electrospun fibrinogen/gelatin nanofibers for myocardial regeneration. Journal of Biomaterials Science, Polymer Edition. 2013;24(14):1660-75.

158. Herrick S, Blanc-Brude O, Gray A, Laurent G. Fibrinogen. The International Journal of Biochemistry & Cell Biology. 1999;31(7):741-6.

159. Yan C, Ren Y, Sun X, Jin L, Liu X, Chen H, et al. Photoluminescent functionalized carbon quantum dots loaded electroactive Silk fibroin/PLA nanofibrous bioactive scaffolds for cardiac tissue engineering. Journal of Photochemistry and Photobiology B: Biology. 2020;202:111680.

160. Yang M-C, Chi N-H, Chou N-K, Huang Y-Y, Chung T-W, Chang Y-L, et al. The influence of rat mesenchymal stem cell CD44 surface markers on cell growth, fibronectin expression, and cardiomyogenic differentiation on silk fibroin–hyaluronic acid cardiac patches. Biomaterials. 2010;31(5):854-62.

161. Nguyen TP, Nguyen QV, Nguyen V-H, Le T-H, Huynh VQN, Vo D-VN, et al. Silk fibroin-based biomaterials for biomedical applications: a review. Polymers (Basel). 2019;11(12):1933.

162. Alperin C, Zandstra P, Woodhouse K. Polyurethane films seeded with embryonic stem cell-derived cardiomyocytes for use in cardiac tissue engineering applications. Biomaterials. 2005;26(35):7377-86.

163. Jaganathan SK, Mani MP. Enriched mechanical, thermal, and blood compatibility of single stage electrospun polyurethane nickel oxide nanocomposite for cardiac tissue engineering. Polymer Composites. 2019;40(6):2381-90.

164. Prasath Mani M, Jaganathan SK, Prabhakaran P, Nageswaran G, Pandiyaraj Krishnasamy N. Fabrication and characterization of polyurethane patch loaded with palmarosa and cobalt nitrate for cardiac tissue engineering. International Journal of Polymer Analysis and Characterization. 2019;24(5):399-411.

165. Roylance D. Engineering viscoelasticity. Department of Materials Science and Engineering–Massachusetts Institute of Technology, Cambridge MA. 2001;2139:1-37.

166. Katz AM. Physiology of the Heart: Lippincott Williams & Wilkins; 2010.

167. Kaiser E, Jaganathan SK, Supriyanto E, Ayyar M. Fabrication and characterization of chitosan nanoparticles and collagen-loaded polyurethane nanocomposite membrane coated with heparin for atrial septal defect (ASD) closure. 3 Biotech. 2017;7(3):1-12.

168. Sridharan D, Palaniappan A, Blackstone BN, Dougherty JA, Kumar N, Seshagiri PB, et al. In situ differentiation of human-induced pluripotent stem cells into functional cardiomyocytes on a coaxial PCL-gelatin nanofibrous scaffold. Materials Science and Engineering: C. 2021;118:111354.

169. Mao M, He J, Li Z, Han K, Li D. Multi-directional cellular alignment in 3D guided by electrohydrodynamically-printed microlattices. Acta Biomater. 2020;101:141-51.

170. Torabi M, Abazari MF, Zare Karizi S, Kohandani M, Hajati-Birgani N, Norouzi S, et al. Efficient cardiomyocyte differentiation of induced pluripotent stem cells on PLGA nanofibers enriched by platelet-rich plasma. Polymers for Advanced Technologies. 2021;32(3):1168-75.

171. Horn MA, Trafford AW. Aging and the cardiac collagen matrix: Novel mediators of fibrotic remodelling. Journal of Molecular and Cellular Cardiology. 2016;93:175-85.

172. Wang X, Wu P, Hu X, You C, Guo R, Shi H, et al. Polyurethane membrane/knitted mesh-reinforced collagen–chitosan bilayer dermal substitute for the repair of full-thickness skin defects via a two-step procedure. Journal of the Mechanical Behavior of Biomedical Materials. 2016;56:120-33.

173. Meng Z, He J, Xia Z, Li D. Fabrication of microfibrous PCL/MWCNTs scaffolds via melt-based electrohydrodynamic printing. Materials Letters. 2020;278:128440.

174. Yang Y, Lei D, Huang S, Yang Q, Song B, Guo Y, et al. Elastic 3D-printed hybrid polymeric scaffold improves cardiac remodeling after myocardial infarction. Advanced Healthcare Materials. 2019;8(10):1900065.

175. Azizi M, Navidbakhsh M, Hosseinzadeh S, Sajjadi M. Cardiac cell differentiation of muscle satellite cells on aligned composite electrospun polyurethane with reduced graphene oxide. Journal of Polymer Research. 2019;26(11):1-9.

176. Spearman BS, Hodge AJ, Porter JL, Hardy JG, Davis ZD, Xu T, et al. Conductive interpenetrating networks of polypyrrole and polycaprolactone encourage electrophysiological development of cardiac cells. Acta Biomater. 2015;28(1878-7568 (Electronic)):109-20.

177. Hitscherich P, Aphale A, Gordan R, Whitaker R, Singh P, Xie Lh, et al. Electroactive graphene composite scaffolds for cardiac tissue engineering. Journal of Biomedical Materials Research Part A. 2018;106(11):2923-33.

178. Wang Q, Yang H, Bai A, Jiang W, Li X, Wang X, et al. Functional engineered human cardiac patches prepared from nature's platform improve heart function after acute myocardial infarction. Biomaterials. 2016;105:52-65.

179. Wang X, Wang L, Wu Q, Bao F, Yang H, Qiu X, et al. Chitosan/calcium silicate cardiac patch stimulates cardiomyocyte activity and myocardial performance after infarction by synergistic effect of bioactive ions and aligned nanostructure. ACS Applied Materials & Interfaces. 2018;11(1):1449-68.

180. Ahadian S, Khademhosseini A. Smart scaffolds in tissue regeneration. Regenerative Biomaterials. 2018;5(3):125-8.

181. Ashtari K, Nazari H, Ko H, Tebon P, Akhshik M, Akbari M, et al. Electrically conductive nanomaterials for cardiac tissue engineering. Advanced Drug Delivery Reviews. 2019;144:162-79.

182. Martherus RS, Vanherle SJ, Timmer ED, Zeijlemaker VA, Broers JL, Smeets HJ, et al. Electrical signals affect the cardiomyocyte transcriptome independently of contraction. Physiological Genomics. 2010;42(4):283-9.

183. Chan Y-C, Ting S, Lee Y-K, Ng K-M, Zhang J, Chen Z, et al. Electrical stimulation promotes maturation of cardiomyocytes derived from human embryonic stem cells. Journal of Cardiovascular Translational Research. 2013;6(6):989-99.

184. Norahan MH, Amroon M, Ghahremanzadeh R, Mahmoodi M, Baheiraei N. Electroactive graphene oxide-incorporated collagen assisting vascularization for cardiac tissue engineering. Journal of Biomedical Materials Research Part A. 2019;107(1):204-19.

185. Ryan AJ, Kearney CJ, Shen N, Khan U, Kelly AG, Probst C, et al. Electroconductive biohybrid collagen/pristine graphene composite biomaterials with enhanced biological activity. Advanced Materials. 2018;30(15):1706442.

186. Chen S, Hsieh M-H, Li S-H, Wu J, Weisel RD, Chang Y, et al. A conductive cell-delivery construct as a bioengineered patch that can improve electrical propagation and synchronize cardiomyocyte contraction for heart repair. Journal of Controlled Release. 2020;320:73-82.

187. He S, Song H, Wu J, Li S-H, Weisel RD, Sung H-W, et al. Preservation of conductive propagation after surgical repair of cardiac defects with a bio-engineered conductive patch. The Journal of Heart and Lung Transplantation. 2018;37(7):912-24.

188. Kharaziha M, Shin SR, Nikkhah M, Topkaya SN, Masoumi N, Annabi N, et al. Tough and flexible CNT–polymeric hybrid scaffolds for engineering cardiac constructs. Biomaterials. 2014;35(26):7346-54.

189. Kai D, Prabhakaran MP, Jin G, Ramakrishna S. Polypyrrole-contained electrospun conductive nanofibrous membranes for cardiac tissue engineering. Journal of Biomedical Materials Research Part A. 2011;99(3):376-85.

190. Baheiraei N, Gharibi R, Yeganeh H, Miragoli M, Salvarani N, Di Pasquale E, et al. Electroactive polyurethane/siloxane derived from castor oil as a versatile cardiac patch, part I: Synthesis, characterization, and myoblast proliferation and differentiation. Journal of Biomedical Materials Research Part A. 2016;104(3):775-87.

191. Al-Attabi NY, Kaur G, Adhikari R, Cass P, Bown M, Evans M, et al. Preparation and characterization of highly conductive polyurethane composites containing graphene and gold nanoparticles. Journal of Materials Science. 2017;52(19):11774-84.

192. Kim S-W, Kwon S-N, Na S-I. Stretchable and electrically conductive polyurethane-silver/graphene composite fibers prepared by wet-spinning process. Composites Part B: Engineering. 2019;167:573-81.

193. Zhu Y, Gao C, He T, Shen J. Endothelium regeneration on luminal surface of polyurethane vascular scaffold modified with diamine and covalently grafted with gelatin. Biomaterials. 2004;25(3):423-30.

194. Wong CS, Liu X, Xu Z, Lin T, Wang X. Elastin and collagen enhances electrospun aligned polyurethane as scaffolds for vascular graft. Journal of Materials Science: Materials in Medicine. 2013;24(8):1865-74.

195. Tu Q, Pang L, Chen Y, Zhang Y, Zhang R, Lu B, et al. Effects of surface charges of graphene oxide on neuronal outgrowth and branching. Analyst. 2014;139(1):105-15.

196. Chiacchiaretta M, Bramini M, Rocchi A, Armirotti A, Giordano E, Vázquez E, et al. Graphene oxide upregulates the homeostatic functions of primary astrocytes and modulates astrocyte-to-neuron communication. Nano Letters. 2018;18(9):5827-38.

197. Lee SK, Kim H, Shim BS. Graphene: an emerging material for biological tissue engineering. Carbon Letters. 2013;14(2):63-75.

198. Virani SS, Alonso A, Benjamin EJ, Bittencourt MS, Callaway CW, Carson AP, et al. Heart Disease and Stroke Statistics-2020 Update: A Report From the American Heart Association. Circulation. 2020;141(9):e139-e595.

199. Guan J, Wang F, Li Z, Chen J, Guo X, Liao J, et al. The stimulation of the cardiac differentiation of mesenchymal stem cells in tissue constructs that mimic myocardium structure and biomechanics. Biomaterials. 2011;32(24):5568-80.

200. Heydarkhan-Hagvall S, Schenke-Layland K, Dhanasopon AP, Rofail F, Smith H, Wu BM, et al. Three-dimensional electrospun ECM-based hybrid scaffolds for cardiovascular tissue engineering. Biomaterials. 2008;29(19):2907-14.

201. Badylak SF, Freytes Do Fau - Gilbert TW, Gilbert TW. Extracellular matrix as a biological scaffold material: Structure and function. Acta Biomater. 2009;5(1):1-13.

202. Kai D, Prabhakaran Mp Fau - Jin G, Jin G Fau - Ramakrishna S, Ramakrishna S. Guided orientation of cardiomyocytes on electrospun aligned nanofibers for cardiac tissue engineering. Journal of Biomedical Materials Research Part B: Applied Biomaterials.98(2):379-86.

203. Rockwood DN, Akins RE, Jr., Parrag IC, Woodhouse KA, Rabolt JF. Culture on electrospun polyurethane scaffolds decreases atrial natriuretic peptide expression by cardiomyocytes in vitro. Biomaterials. 2008;29(36):4783-91.

204. Han J, Wu Q, Xia Y, Wagner MB, Xu C. Cell alignment induced by anisotropic electrospun fibrous scaffolds alone has limited effect on cardiomyocyte maturation. Stem Cell Res. 2016;16(3):740-50.

205. C Echave M, S Burgo L, L Pedraz J, Orive G. Gelatin as biomaterial for tissue engineering. Current Pharmaceutical Design. 2017;23(24):3567-84.

206. Rosellini E, Cristallini C, Barbani N, Vozzi G, Giusti P. Preparation and characterization of alginate/gelatin blend films for cardiac tissue engineering. Journal of Biomedical Materials Research Part A: An Official Journal of The Society for Biomaterials, The Japanese Society for Biomaterials, and The Australian Society for Biomaterials and the Korean Society for Biomaterials. 2009;91(2):447-53.

207. Wu W-q, Peng S, Song Z-y, Lin S. Collagen biomaterial for the treatment of myocardial infarction: an update on cardiac tissue engineering and myocardial regeneration. Drug Delivery and Translational Research. 2019;9(5):920-34.

208. Li Y, Shi X, Tian L, Sun H, Wu Y, Li X, et al. AuNP–collagen matrix with localized stiffness for cardiac-tissue engineering: Enhancing the assembly of intercalated discs by β1-integrin-mediated signaling. Advanced Materials. 2016;28(46):10230-5.

209. Zhang G, Wang X, Wang Z, Zhang J, Suggs L. A PEGylated fibrin patch for mesenchymal stem cell delivery. Tissue Engineering. 2006;12(1):9-19.

210. Mani MP, Jaganathan SK, Faudzi AAM, Sunar MS. Engineered Electrospun Polyurethane Composite Patch Combined with Bi-functional Components Rendering High Strength for Cardiac Tissue Engineering. Polymers (Basel). 2019;11(4):705.

211. Ivanoska-Dacikj A, Bogoeva-Gaceva G, Krumme A, Tarasova E, Scalera C, Stojkovski V, et al. Biodegradable polyurethane/graphene oxide scaffolds for soft tissue engineering: in vivo behavior assessment. International Journal of Polymeric Materials and Polymeric Biomaterials. 2019:1-11.

212. Chen P-H, Liao H-C, Hsu S-H, Chen R-S, Wu M-C, Yang Y-F, et al. A novel polyurethane/cellulose fibrous scaffold for cardiac tissue engineering. RSC Advances. 2015;5(9):6932-9.

213. Eivazi Zadeh Z, Solouk A, Shafieian M, Haghbin Nazarpak M. Electrospun polyurethane/carbon nanotube composites with different amounts of carbon nanotubes and almost the same fiber diameter for biomedical applications. Materials Science and Engineering: C. 2021;118:111403.

214. Xu C, Okpokwasili C, Huang Y, Shi X, Wu J, Liao J, et al. Optimizing Anisotropic Polyurethane Scaffolds to Mechanically Match with Native Myocardium. ACS biomaterials science & engineering. 2020;6(5):2757-69.

215. Wang QL, Wang HJ, Li ZH, Wang YL, Wu XP, Tan YZ. Mesenchymal stem cell-loaded cardiac patch promotes epicardial activation and repair of the infarcted myocardium. Journal of Cellular and Molecular Medicine. 2017;21(9):1751-66.

216. Shafiq M, Zhang Y, Zhu D, Zhao Z, Kim DH, Kim SH, et al. In situ cardiac regeneration by using neuropeptide substance P and IGF-1C peptide eluting heart patches. Regenerative Biomaterials. 2018;5(5):303-16.

217. Tallawi M, Dippold D, Rai R, D'Atri D, Roether J, Schubert D, et al. Novel PGS/PCL electrospun fiber mats with patterned topographical features for cardiac patch applications. Materials Science and Engineering C. 2016;69:569-76.

218. Vogt L, Rivera LR, Liverani L, Piegat A, El Fray M, Boccaccini AR. Poly(epsilon-caprolactone)/poly(glycerol sebacate) electrospun scaffolds for cardiac tissue engineering using benign solvents. Materials Science and Engineering C. 2019;103:109712.

219. Chen QZ, Bismarck A, Hansen U, Junaid S, Tran MQ, Harding SE, et al. Characterisation of a soft elastomer poly(glycerol sebacate) designed to match the mechanical properties of myocardial tissue. Biomaterials. 2008;29(1):47-57.

220. Luginina M, Schuhladen K, Orru R, Cao G, Boccaccini AR, Liverani L. Electrospun PCL/PGS Composite Fibers Incorporating Bioactive Glass Particles for Soft Tissue Engineering Applications. Nanomaterials (Basel). 2020;10(5).

221. Cristallini C, Cibrario Rocchietti E, Gagliardi M, Mortati L, Saviozzi S, Bellotti E, et al. Micro- and Macrostructured PLGA/Gelatin Scaffolds Promote Early Cardiogenic Commitment of Human Mesenchymal Stem Cells In Vitro. Stem Cells International. 2016;2016:7176154.

222. Tsao CJ, Pandolfi L, Wang X, Minardi S, Lupo C, Evangelopoulos M, et al. Electrospun Patch Functionalized with Nanoparticles Allows for Spatiotemporal Release of VEGF and PDGF-BB Promoting In Vivo Neovascularization. ACS Applied Materials & Interfaces. 2018;10(51):44344-53.

223. Kucinska-Lipka J, Gubanska I, Janik H, Sienkiewicz M. Fabrication of polyurethane and polyurethane based composite fibres by the electrospinning technique for soft tissue engineering of cardiovascular system. Materials Science and Engineering: C. 2015;46:166-76.

224. Giraud M-N, Armbruster C, Carrel T, Tevaearai HT. Current state of the art in myocardial tissue engineering. Tissue Engineering. 2007;13(8):1825-36.

225. Jang J, Park HJ, Kim SW, Kim H, Park JY, Na SJ, et al. 3D printed complex tissue construct using stem cell-laden decellularized extracellular matrix bioinks for cardiac repair. Biomaterials. 2017;112:264-74.

226. Zhu F, Meng Q, Yu Y, Shao LA-O, Shen Z. Adult Cardiomyocyte Proliferation: a New Insight for Myocardial Infarction Therapy. Journal of Cardiovascular Translational Research. 2021;14(3):457-66.

227. Mewhort HEM, Svystonyuk DA, Turnbull JD, Teng G, Belke DD, Guzzardi DG, et al. Bioactive Extracellular Matrix Scaffold Promotes Adaptive Cardiac Remodeling and Repair. Basic to Translational Science. 2017;2(4):450-64.

228. Hall ML, Ogle BM. Cardiac Extracellular Matrix Modification as a Therapeutic Approach. Adv Exp Med Biol. 2018;1098:131-50.

229. Singelyn JM, DeQuach JA, Seif-Naraghi SB, Littlefield RB, Schup-Magoffin PJ, Christman KL. Naturally derived myocardial matrix as an injectable scaffold for cardiac tissue engineering. Biomaterials. 2009;30(29):5409-16.

230. Hong Y, Huber A, Takanari K, Amoroso NJ, Hashizume R, Badylak SF, et al. Mechanical properties and in vivo behavior of a biodegradable synthetic polymer microfiber–extracellular matrix hydrogel biohybrid scaffold. Biomaterials. 2011;32(13):3387-94.

231. Kim IG, Hwang MP, Park JS, Kim SH, Kim JH, Kang HJ, et al. Stretchable ECM Patch Enhances Stem Cell Delivery for Post-MI Cardiovascular Repair. Advanced Healthcare Materials. 2019;8(17):1900593.

232. Aamodt JM, Grainger DW. Extracellular matrix-based biomaterial scaffolds and the host response. Biomaterials. 2016;86:68-82.

233. Punnakitikashem P, Truong D, Menon JU, Nguyen KT, Hong Y. Electrospun biodegradable elastic polyurethane scaffolds with dipyridamole release for small diameter vascular grafts. Acta Biomater. 2014;10(11):4618-28.

234. Gokhin DS, Fowler VM. Software-based measurement of thin filament lengths: an open-source GUI for Distributed Deconvolution analysis of fluorescence images. Journal of Microscopy. 2017;265(1):11-20.

235. Lin Y-S, Chang T-H, Ho W-C, Chang S-F, Chen Y-L, Chang S-T, et al. Sarcomeres morphology and Z-line arrangement disarray induced by ventricular premature contractions through the Rac2/cofilin pathway. International Journal of Molecular Sciences. 2021;22(20):11244.

236. Stankus JJ, Freytes DO, Badylak SF, Wagner WR. Hybrid nanofibrous scaffolds from electrospinning of a synthetic biodegradable elastomer and urinary bladder matrix. Journal of Biomaterials Science, Polymer Edition. 2008;19(5):635-52.

237. Valentin JE, Turner NJ, Gilbert TW, Badylak SF. Functional skeletal muscle formation with a biologic scaffold. Biomaterials. 2010;31(29):7475-84.

238. Teo WE, Ramakrishna S. A review on electrospinning design and nanofibre assemblies. Nanotechnology. 2006;17(14):R89.

239. Saudi S, Bhattarai SR, Adhikari U, Khanal S, Sankar J, Aravamudhan S, et al. Nanonet-nano fiber electrospun mesh of PCL–chitosan for controlled and extended release of diclofenac sodium. Nanoscale. 2020;12(46):23556-69.

240. Xiong C, Wang L, Yu J, Qin X, Wang R, Yu J. Continuous self-crimped micro-nanofiber via one-step electrospinning. Composites Part A: Applied Science and Manufacturing. 2022;158:106959.

241. Kuo ZK, Fang MY, Wu TY, Yang T, Tseng HW, Chen CC, et al. Hydrophilic films: How hydrophilicity affects blood compatibility and cellular compatibility. Advances in Polymer Technology. 2018;37(6):1635-42.

242. Cleutjens JP, Creemers EE. Integration of concepts: cardiac extracellular matrix remodeling after myocardial infarction. Journal of Cardiac Failure. 2002;8(6):S344-S8.

243. Rane AA, Chuang JS, Shah A, Hu DP, Dalton ND, Gu Y, et al. Increased infarct wall thickness by a bio-inert material is insufficient to prevent negative left ventricular remodeling after myocardial infarction. PLoS One. 2011;6(6):e21571.

244. Brower GL, Gardner JD, Forman MF, Murray DB, Voloshenyuk T, Levick SP, et al. The relationship between myocardial extracellular matrix remodeling and ventricular function. European Journal of Cardio-Thoracic Surgery. 2006;30(4):604-10.

245. Martin C, Pham T, Sun W. Significant differences in the material properties between aged human and porcine aortic tissues. European Journal of Cardio-Thoracic Surgery. 2011;40(1):28-34.

246. Wang B, Tedder ME, Perez CE, Wang G, de Jongh Curry AL, To F, et al. Structural and biomechanical characterizations of porcine myocardial extracellular matrix. Journal of Materials Science: Materials in Medicine. 2012;23(8):1835-47.

247. Purslow PP, Wess TJ, Hukins D. Collagen orientation and molecular spacing during creep and stress-relaxation in soft connective tissues. The Journal of Experimental Biology. 1998;201(1):135-42.

248. Sethuraman V, Makornkaewkeyoon K, Khalf A, Madihally SV. Influence of scaffold forming techniques on stress relaxation behavior of polycaprolactone scaffolds. Journal of Applied Polymer Science. 2013;130(6):4237-44.

249. Liu Y, Wang S, Zhang R. Composite poly (lactic acid)/chitosan nanofibrous scaffolds for cardiac tissue engineering. International Journal of Biological Macromolecules. 2017;103:1130-7.

250. Morris TA, Naik J, Fibben KS, Kong X, Kiyono T, Yokomori K, et al. Striated myocyte structural integrity: Automated analysis of sarcomeric z-discs. PLoS Computational Biology. 2020;16(3):e1007676.

251. Tamimi M, Rajabi S, Pezeshki-Modaress M. Cardiac ECM/chitosan/alginate ternary scaffolds for cardiac tissue engineering application. International Journal of Biological Macromolecules. 2020;164:389-402.

252. Chan V, Raman R, Cvetkovic C, Bashir R. Enabling microscale and nanoscale approaches for bioengineered cardiac tissue. ACS Nano. 2013;7(3):1830-7.

253. Liu Y, Lu J, Xu G, Wei J, Zhang Z, Li X. Tuning the conductivity and inner structure of electrospun fibers to promote cardiomyocyte elongation and synchronous beating. Materials Science and Engineering: C. 2016;69:865-74.

254. Monteiro LM, Vasques-Nóvoa F, Ferreira L, Nascimento DS. Restoring heart function and electrical integrity: closing the circuit. NPJ Regenerative Medicine. 2017;2(1):1-13.

255. Vunjak-Novakovic G, Tandon N, Godier A, Maidhof R, Marsano A, Martens TP, et al. Challenges in cardiac tissue engineering. Tissue Engineering Part B: Reviews. 2010;16(2):169-87.

256. Burnstine-Townley A, Eshel Y, Amdursky N. Conductive scaffolds for cardiac and neuronal tissue engineering: Governing factors and mechanisms. Advanced Functional Materials. 2020;30(18):1901369.

257. Feng L, Liu Z. Graphene in biomedicine: opportunities and challenges. Nanomedicine. 2011;6(2):317-24.

258. Norahan MH, Pourmokhtari M, Saeb MR, Bakhshi B, Zomorrod MS, Baheiraei N. Electroactive cardiac patch containing reduced graphene oxide with potential antibacterial properties. Materials Science and Engineering: C. 2019;104:109921.

259. Nazari H, Azadi S, Hatamie S, Zomorrod MS, Ashtari K, Soleimani M, et al. Fabrication of graphene-silver/polyurethane nanofibrous scaffolds for cardiac tissue engineering. Polymers for Advanced Technologies. 2019;30(8):2086-99.

260. Compton OC, Nguyen ST. Graphene oxide, highly reduced graphene oxide, and graphene: versatile building blocks for carbon-based materials. Small. 2010;6(6):711-23.

261. Magaz A, Li X, Gough JE, Blaker JJ. Graphene oxide and electroactive reduced graphene oxide-based composite fibrous scaffolds for engineering excitable nerve tissue. Materials Science and Engineering: C. 2021;119:111632.

262. Guo R, Zhang S, Xiao M, Qian F, He Z, Li D, et al. Accelerating bioelectric functional development of neural stem cells by graphene coupling: implications for neural interfacing with conductive materials. Biomaterials. 2016;106:193-204.

263. Zhao G, Feng Y, Xue L, Cui M, Zhang Q, Xu F, et al. Anisotropic conductive reduced graphene oxide/silk matrices promote post-infarction myocardial function by restoring electrical integrity. Acta Biomater. 2021;139:190-203.

264. Shokraei N, Asadpour S, Shokraei S, Nasrollahzadeh Sabet M, Faridi-Majidi R, Ghanbari H. Development of electrically conductive hybrid nanofibers based on CNT-polyurethane nanocomposite for cardiac tissue engineering. Microscopy Research and Technique. 2019;82(8):1316-25.

265. Mehrabi A, Baheiraei N, Adabi M, Amirkhani Z. Development of a novel electroactive cardiac patch based on carbon Nanofibers and gelatin encouraging vascularization. Applied Biochemistry and Biotechnology. 2020;190(3):931-48.

266. Zhao G, Zhang X, Li B, Huang G, Xu F, Zhang X. Solvent-Free Fabrication of Carbon Nanotube/Silk Fibroin Electrospun Matrices for Enhancing Cardiomyocyte Functionalities. ACS Biomaterials Science & Engineering. 2020;6(3):1630-40.

267. Ghasemi A, Imani R, Yousefzadeh M, Bonakdar S, Solouk A, Fakhrzadeh H. Studying the potential application of electrospun polyethylene terephthalate/graphene oxide nanofibers as electroconductive cardiac patch. Macromolecular Materials and Engineering. 2019;304(8):1900187.

268. Park J, Kim YS, Ryu S, Kang WS, Park S, Han J, et al. Graphene potentiates the myocardial repair efficacy of mesenchymal stem cells by stimulating the expression of angiogenic growth factors and gap junction protein. Advanced Functional Materials. 2015;25(17):2590-600.

269. Narayanan KB, Park GT, Han SS. Electrospun poly (vinyl alcohol)/reduced graphene oxide nanofibrous scaffolds for skin tissue engineering. Colloids and Surfaces B: Biointerfaces. 2020;191:110994.

270. Blachowicz T, Ehrmann A. Conductive electrospun nanofiber mats. Materials. 2020;13(1):152.

271. Xu C, Yepez G, Wei Z, Liu F, Bugarin A, Hong Y. Synthesis and characterization of conductive, biodegradable, elastomeric polyurethanes for biomedical applications. Journal of Biomedical Materials Research Part A. 2016;104(9):2305-14.

272. Shin YC, Lee JH, Jin L, Kim MJ, Kim Y-J, Hyun JK, et al. Stimulated myoblast differentiation on graphene oxide-impregnated PLGA-collagen hybrid fibre matrices. Journal of Nanobiotechnology. 2015;13(1):1-11.

273. Park S, Ruoff RS. Chemical methods for the production of graphenes. Nature nanotechnology. 2009;4(4):217-24.

274. Potse M, Dubé B, Vinet A. Cardiac anisotropy in boundary-element models for the electrocardiogram. Medical & Biological Engineering & Computing. 2009;47(7):719-29.

275. Patel A, Xue Y, Mukundan S, Rohan LC, Sant V, Stolz DB, et al. Cell-instructive graphene-containing nanocomposites induce multinucleated myotube formation. Annals of Biomedical Engineering. 2016;44(6):2036-48.

276. Niu Y, Chen X, Yao D, Peng G, Liu H, Fan Y. Enhancing neural differentiation of induced pluripotent stem cells by conductive graphene/silk fibroin films. Journal of Biomedical Materials Research Part A. 2018;106(11):2973-83.

277. Grant JJ, Pillai SC, Hehir S, McAfee M, Breen A. Biomedical applications of electrospun graphene oxide. ACS Biomaterials Science & Engineering. 2021;7(4):1278-301.

278. Martins AM, Eng G, Caridade SG, Mano JF, Reis RL, Vunjak-Novakovic G. Electrically conductive chitosan/carbon scaffolds for cardiac tissue engineering. Biomacromolecules. 2014;15(2):635-43.

279. Seyedsalehi A, Daneshmandi L, Barajaa M, Riordan J, Laurencin CT. Fabrication and characterization of mechanically competent 3D printed polycaprolactone-reduced graphene oxide scaffolds. Scientific Reports. 2020;10(1):1-14.

280. Wang W, Caetano G, Ambler WS, Blaker JJ, Frade MA, Mandal P, et al. Enhancing the hydrophilicity and cell attachment of 3D printed PCL/graphene scaffolds for bone tissue engineering. Materials. 2016;9(12):992.

281. Palmieri V, Sciandra F, Bozzi M, De Spirito M, Papi M. 3D graphene scaffolds for skeletal muscle regeneration: future perspectives. Frontiers in Bioengineering and Biotechnology. 2020;8:383.

282. Ku SH, Park CB. Myoblast differentiation on graphene oxide. Biomaterials. 2013;34(8):2017-23.

283. Smith AS, Yoo H, Yi H, Ahn EH, Lee JH, Shao G, et al. Micro-and nano-patterned conductive graphene–PEG hybrid scaffolds for cardiac tissue engineering. Chemical Communications. 2017;53(53):7412-5.

284. You J-O, Rafat M, Ye GJ, Auguste DT. Nanoengineering the heart: conductive scaffolds enhance connexin 43 expression. Nano Letters. 2011;11(9):3643-8.

285. He Y, Ye G, Song C, Li C, Xiong W, Yu L, et al. Mussel-inspired conductive nanofibrous membranes repair myocardial infarction by enhancing cardiac function and revascularization. Theranostics. 2018;8(18):5159.

286. Tondnevis F, Keshvari H, Mohandesi JA. Fabrication, characterization, and in vitro evaluation of electrospun polyurethane-gelatin-carbon nanotube scaffolds for cardiovascular tissue engineering applications. Journal of Biomedical Materials Research Part B: Applied Biomaterials. 2020;108(5):2276-93.

287. Xiong W, Wang X, Guan H, Kong F, Xiao Z, Jing Y, et al. A Vascularized Conductive Elastic Patch for the Repair of Infarcted Myocardium through Functional Vascular Anastomoses and Electrical Integration. Advanced Functional Materials. 2022;32(19):2111273.

288. Amorim S, Reis RL, Pires RA. Hyaluronan-Based Hydrogels as Modulators of Cellular Behavior. Multifunctional Hydrogels for Biomedical Applications. 2022:217-32.

289. Rueda-Gensini L, Serna JA, Cifuentes J, Cruz JC, Muñoz-Camargo C. Graphene oxide-embedded extracellular matrix-derived hydrogel as a multiresponsive platform for 3D bioprinting applications. International Journal of Bioprinting. 2021;7(3).

290. Lee WC, Lim CHY, Shi H, Tang LA, Wang Y, Lim CT, et al. Origin of enhanced stem cell growth and differentiation on graphene and graphene oxide. ACS Nano. 2011;5(9):7334-41.

291. Kim CH, Khil Ms Fau - Kim HY, Kim Hy Fau - Lee HU, Lee Hu Fau - Jahng KY, Jahng KY. An improved hydrophilicity via electrospinning for enhanced cell attachment and proliferation. Journal of Biomedical Materials Research Part B: Applied Biomaterials. 2006;78B(2):283-90.

292. Alagarsamy KN, Yan W, Srivastava A, Desiderio V, Dhingra S. Application of injectable hydrogels for cardiac stem cell therapy and tissue engineering. Reviews in Cardiovascular Medicine. 2019;20(4):221-30.

293. Raghavan K, Porterfield JE, Kottam AT, Feldman MD, Escobedo D, Valvano JW, et al. Electrical conductivity and permittivity of murine myocardium. IEEE Transactions on Biomedical Engineering. 2009;56(8):2044-53.

294. Tang LAL, Wang J, Loh KP. Graphene-based SELDI probe with ultrahigh extraction and sensitivity for DNA oligomer. Journal of the American Chemical Society. 2010;132(32):10976-7.

295. Zhao G, Zhang X, Lu TJ, Xu F. Recent advances in electrospun nanofibrous scaffolds for cardiac tissue engineering. Advanced Functional Materials. 2015;25(36):5726-38.

296. Naz A, Riaz I, Jalil R, Afzal S. Creep strain and recovery analysis of polypropylene composites filled with graphene nano filler. Polymer. 2021;217:123423.

297. Vecerek V, Voslarova E, Semerad Z, Passantino A. The health and welfare of pigs from the perspective of post mortem findings in slaughterhouses. Animals. 2020;10(5):825.

298. Rajala K, Pekkanen-Mattila M, Aalto-Setälä K. Cardiac differentiation of pluripotent stem cells. Stem Cells International. 2011;2011.

299. Armiñán A, Gandía C, Bartual M, García-Verdugo JM, Lledó E, Mirabet V, et al. Cardiac differentiation is driven by NKX2. 5 and GATA4 nuclear translocation in tissue-specific mesenchymal stem cells. Stem Cells and Development. 2009;18(6):907-18.

300. Xing Y, Huang P, Zhang K. Cardiac troponin T and I: application in myocardial injury and forensic medicine. Fa yi xue za zhi. 2003;19(4):242-4.

301. Ramkisoensing AA, Pijnappels DA, Swildens J, Goumans MJ, Fibbe WE, Schalij MJ, et al. Gap junctional coupling with cardiomyocytes is necessary but not sufficient for cardiomyogenic differentiation of cocultured human mesenchymal stem cells. Stem Cells. 2012;30(6):1236-45.

302. Ding M, Andersson H, Martinsson S, Sabirsh A, Jonebring A, Wang Q-D, et al. Aligned nanofiber scaffolds improve functionality of cardiomyocytes differentiated from human induced pluripotent stem cell-derived cardiac progenitor cells. Scientific reports. 2020;10(1):1-14.

303. McCain ML, Desplantez T, Geisse NA, Rothen-Rutishauser B, Oberer H, Parker KK, et al. Cell-to-cell coupling in engineered pairs of rat ventricular cardiomyocytes: relation between Cx43 immunofluorescence and intercellular electrical conductance. American Journal of Physiology-Heart and Circulatory Physiology. 2012;302(2):H443-H50.

304. Himelman E, Lillo MA, Nouet J, Gonzalez JP, Zhao Q, Xie L-H, et al. Prevention of connexin-43 remodeling protects against Duchenne muscular dystrophy cardiomyopathy. The Journal of clinical investigation. 2020;130(4):1713-27.

305. LaBarge W, Mattappally S, Kannappan R, Fast VG, Pretorius D, Berry JL, et al. Maturation of three-dimensional, hiPSC-derived cardiomyocyte spheroids utilizing cyclic, uniaxial stretch and electrical stimulation. PLoS One. 2019;14(7):e0219442.

306. Tan EP, Lim C. Effects of annealing on the structural and mechanical properties of electrospun polymeric nanofibres. Nanotechnology. 2006;17(10):2649.

307. Ozdil D, Aydin HM. Polymers for medical and tissue engineering applications. Journal of Chemical Technology & Biotechnology. 2014;89(12):1793-810.

308. Wang X, Yu T, Chen G, Zou J, Li J, Yan J. Preparation and characterization of a chitosan/gelatin/extracellular matrix scaffold and its application in tissue engineering. Tissue Engineering Part C: Methods. 2017;23(3):169-79.

309. Toeg HD, Abessi O, Al-Atassi T, De Kerchove L, El-Khoury G, Labrosse M, et al. Finding the ideal biomaterial for aortic valve repair with ex vivo porcine left heart simulator and finite element modeling. The Journal of Thoracic and Cardiovascular Surgery. 2014;148(4):1739-45. e1.

310. Bosi GM, Capelli C, Khambadkone S, Taylor AM, Schievano S. Patient-specific finite element models to support clinical decisions: A lesson learnt from a case study of percutaneous pulmonary valve implantation. Catheterization and Cardiovascular Interventions. 2015;86(6):1120-30.

311. Dang AB, Guccione JM, Zhang P, Wallace AW, Gorman RC, Gorman III JH, et al. Effect of ventricular size and patch stiffness in surgical anterior ventricular restoration: a finite element model study. The Annals of Thoracic Surgery. 2005;79(1):185-93.

312. Fujimoto KL, Ma Z, Nelson DM, Hashizume R, Guan J, Tobita K, et al. Synthesis, characterization and therapeutic efficacy of a biodegradable, thermoresponsive hydrogel designed for application in chronic infarcted myocardium. Biomaterials. 2009;30(26):4357-68.

313. Ye J, Yang L, Sethi R, Copps J, Ramjiawan B, Summers R, et al. A new technique of coronary artery ligation: experimental myocardial infarction in rats in vivo with reduced mortality. The Cellular Basis of Cardiovascular Function in Health and Disease: Springer; 1997. p. 227-33.

314. Piao H, Kwon J-S, Piao S, Sohn J-H, Lee Y-S, Bae J-W, et al. Effects of cardiac patches engineered with bone marrow-derived mononuclear cells and PGCL scaffolds in a rat myocardial infarction model. Biomaterials. 2007;28(4):641-9.

315. Yin M, van der Horst IC, van Melle JP, Qian C, van Gilst WH, Silljé HH, et al. Metformin improves cardiac function in a nondiabetic rat model of post-MI heart failure. American Journal of Physiology-Heart and Circulatory Physiology. 2011;301(2):H459-H68.

Biographical Information

Alan Taylor was born in Fort Worth, Texas. He received his bachelor's degree in biomedical engineering from the University of Texas in Arlington in 2017, with honors Magna Cum Laude. His good grades allowed him to be accepted into the accelerated master's program at the University of Texas in Arlington. He worked in Dr. Jun Liao's biomechanics lab, developing an instrument to deliver traumatic brain injuries to mice and characterized the mechanics of porcine hearts. After graduating with his master's in 2018, he joined the Ph.D. program in Biomedical Engineering at the University of Texas in Arlington under Dr. Yi Hong. He was awarded the NIH T32 training grant from Dr. Kytai Nguyen for research focused on nanotechnology treatments for heart or lung health. His research focused on the fabrication of nanofibrous electrospun mats. He received the Alfred and Janet Potvin Award for Academic Excellence. His current plan after graduation is to join the biomedical industry.